Oceanologia

Official Journal of the Polish Academy of Sciences: Institute of Oceanology and Committee on Maritime Research

This journal is supported by the Ministry of Science and Higher Education, Warsaw, Poland

Indexed in: ISI Journal Master List, Science Citation Index Expanded, Scopus, Current Contents, Zoological Record, Thomson Scientific SSCI, Aquatic Sciences and Fisheries Abstracts, DOAJ

IMPACT FACTOR ANNOUNCED FOR 2016 IN THE 'JOURNAL CITATION REPORTS' IS 1.500; 5-year IF is 1.341

Publisher
Elsevier Sp. z o.o.
22, Jana Pawła II Avenue
00-133 Warsaw, Poland

Associate Publisher
Justyna Kasprzycka
j.kasprzycka@elsevier.com
+31 20 485 3846

ISSN 0078-3234

Oceanologia (2018) 60, 107—113

Available online at www.sciencedirect.com

ScienceDirect

journal homepage: www.journals.elsevier.com/oceanologia/

ORIGINAL RESEARCH ARTICLE

Total benthic oxygen uptake in two Arctic fjords (Spitsbergen) with different hydrological regimes

Lech Kotwicki [a,*], **Katarzyna Grzelak** [a,b], **Krzysztof Opaliński** [c], **Jan Marcin Węsławski** [a]

[a] *Institute of Oceanology, Polish Academy of Sciences, Sopot, Poland*
[b] *Laboratory of Polar Biology and Oceanobiology, Faculty of Biology and Environmental Protection, University of Łódź, Łódź, Poland*
[c] *Cardinal Wyszyński University, Warsaw, Poland*

Received 8 July 2016; accepted 27 November 2017
Available online 6 December 2017

KEYWORDS
Sediment oxygen uptake;
Respiration partitioning;
Carbon demand;
Svalbard fjord;
Arctic

Summary Benthic total oxygen uptake (TOU) was measured in two Arctic fjords (NW Spitsbergen shelf) with different hydrological regimes: Hornsund with "cold" coastal Arctic waters and Kongsfjorden with "warm" Atlantic shelf waters. TOU rates in Kongsfjorden were more than 50% higher than in Hornsund. This is presumably related to the relatively higher biomass of bacterial and faunal (meiobenthos and macrofauna) communities in Kongsfjorden as compared to Hornsund caused by the source of organic matter: Kongsfjorden is dominated by marine, Hornsund by terrigenous organic matter. We conclude that the quality of organic matter supplied to marine sediments influences the biomass of benthic organisms and the rate of oxygen consumption. Therefore the Kongsfjorden sea bed has much higher oxygen uptake and hence a greater carbon demand than Hornsund.

* Corresponding author at: Institute of Oceanology Polish Academy of Sciences, Powstańców Warszawy 55, 81-712 Sopot, Poland. Tel.: +48 58 7311776; fax: +48 58 5512130.
E-mail address: lechk@iopan.gda.pl (L. Kotwicki).
Peer review under the responsibility of Institute of Oceanology of the Polish Academy of Sciences.

ELSEVIER Production and hosting by Elsevier

1. Introduction

In deeper waters, where primary production does not occur, benthic parameters like oxygen or carbon demand depend on the food supply from external sources. Therefore, they are considered 'recipients' of biological processes occurring in the water column, from which valuable amounts of nutrients are received (Pusceddu et al., 2007). Present-day rises in air and ocean temperatures are well documented, especially in the

https://doi.org/10.1016/j.oceano.2017.11.005

Arctic areas. It should be assumed that such changes will intensify in the coming years (Johannessen et al., 2004). Increasing temperatures, ice cover melt and fluvial run-off growth will affect all trophic levels in ecosystems (Piepenburg, 2005). But it is unclear how these changes will impact the fjord ecosystems in the Svalbard archipelago. For this purpose, two comparable stations in two fjords in the west of Spitsbergen, differently exposed to the present-day hydrological regime, were investigated.

The measurement of oxygen consumption, i.e. total oxygen uptake (TOU), is still the standard method of estimating the flow of energy and carbon demand of organisms within marine sediments (Rowe et al., 2008). At shallow depths it is generally assumed that TOU is a direct estimate of the coupling between benthic and pelagic processes (Graf, 1992). In the Arctic region, a number of TOU measurement campaigns have been run, e.g. in the Chukchi and north Bering Seas (Grebmeier and McRoy, 1989), in Greenland fjords (Glud et al., 2000; Rysgaard et al., 1996, 1998, 2004) and in the Svalbard area (Glud et al., 1998; Hulth et al., 1994; Kostka et al., 1999; Piepenburg et al., 1995; Thamdrup and Fleischer, 1998).

The present investigation was designed to address the following questions: What is the oxygen consumption by sediments in environmentally different fjords? How is oxygen uptake related to the meio- and macrofaunal communities?

2. Material and methods

2.1. Study area

The area of west Svalbard is strongly influenced by the relatively warm and nutrient-rich water arriving from the Atlantic Ocean, whereas cold Arctic water determines the environmental conditions to the east and north of Svalbard (Jones and Anderson, 1990). Kongsfjorden and Hornsund are located at 79°N and 77°N, respectively. The Atlantic water carried by the West Spitsbergen Current (WSC) directly influences the temperature of Kongsfjorden. On the other hand, cold water masses from the Barents Sea driven by the South Cape Current (SCC) affect Hornsund farther south. Kongsfjorden and Hornsund are two glacial fjords without sills at their entrances. They are of comparable size: Hornsund is 30 km long and up to 15 km wide and has an average depth of 90 m, while Kongsfjorden is 26 km long, up to 16 km wide but is significantly deeper, over 300 m at the entrance (Fig. 1). Two sampling areas were situated in the inner part of each fjord at about 100 m depth. The sediments of the fjords consist of poorly-sorted, medium-grained silt.

The sampling stations were located in the central/inner parts of both fjords on a flat bottom where the sediment is soft. The geographical positions, bottom water temperature and oxygen content are listed in Table 1.

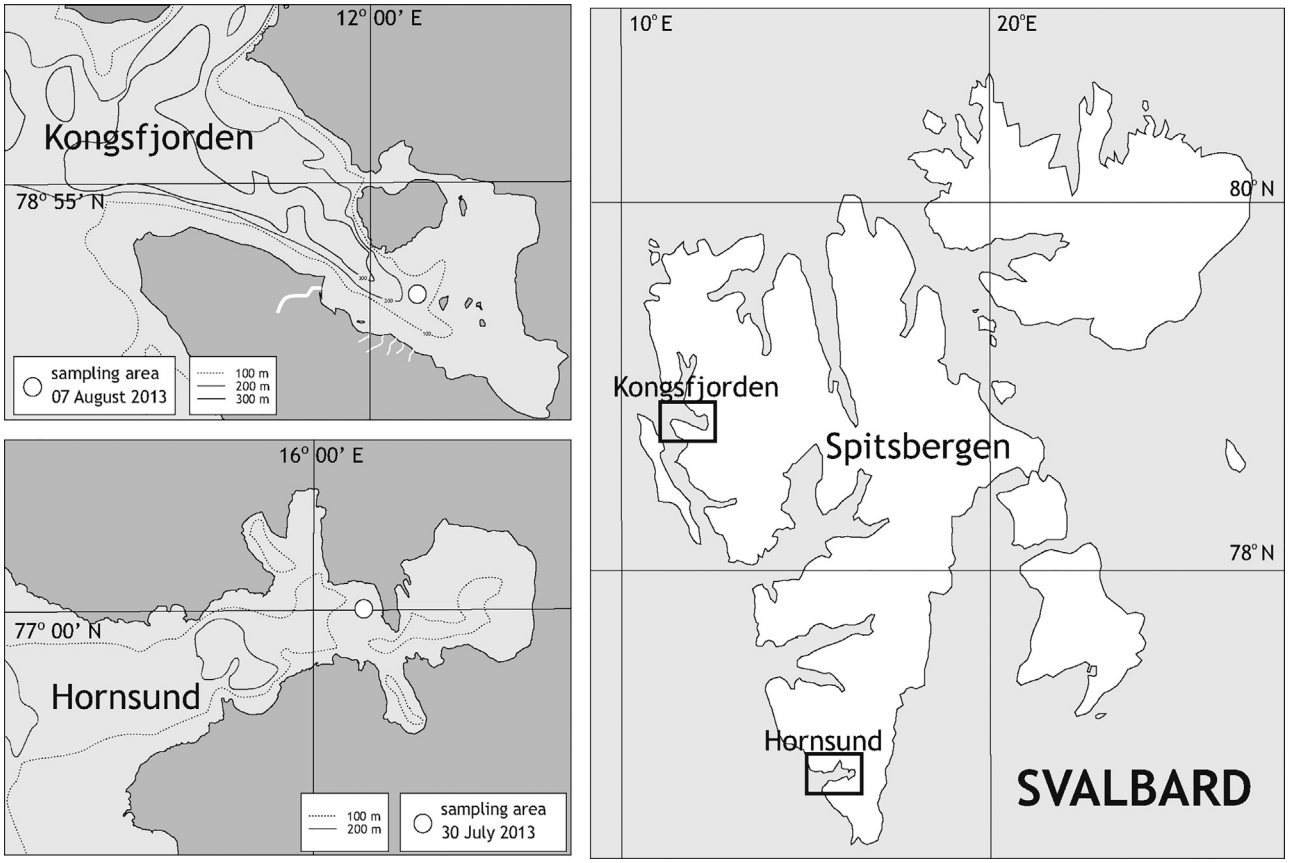

Figure 1 Localization of the investigated fjords at Svalbard archipelago (right panel) and the sampling areas in Kongsfjorden (left top panel) and Hornsund (left bottom panel).

2.2. Sediment core incubation

Total benthic oxygen uptake (TOU) was measured using incubations of surficial sediments and bottom water within chambers. Undisturbed sediment cores with ambient bottom water were collected with a box corer on 30 July 2013 at the stations in Hornsund and on 7 August 2013 in Kongsfjorden. Six cores, 11.4 cm in diameter and containing approximately 15 cm of overlying water, were collected from each cast by inserting Plexiglas tubes into the sediments. The tubes with sediment cores were placed in a container and filled with well oxygenated bottom water if necessary. The area of sediment covered approximately 100 cm^2 and the seawater volume above the interface varied from 0.85 to 1.8 dm^3. Plexiglas lids with a rubber O-ring were equipped with an electric steering motor, and Teflon-coated magnetic bars were gently placed on the core tubes without trapping any air. The incubation temperature in the container was adjusted when necessary to correspond to in-situ bottom water temperatures (2.8/3.5°C respectively). The chambers were maintained in the dark and at the in-situ temperature, during which oxygen concentration was measured over periods of about 50 h. Six replicate incubations were made in each area. Direct measurements of dissolved oxygen were carried out using a microsensor (oxygen electrode) (Unisense Denmark), an IntelliCAL LDO101 probe and an appropriate HACH multimeter.

The oxygen uptake rates [mmol m^{-2} d^{-1}] were calculated as a function of the incubation time on the basis of the oxygen concentration in the overlying water column. They were defined as Total Oxygen Uptake TOU, which includes diffusion and biologically mediated transport of oxygen into sediment. At the same time a "control" tube filled with seawater was incubated without sediments.

Additionally, oxygen profiles in the sediment were measured immediately after sampling with a high-performance microsensor (Unisense Denmark) for non-destructive measurements of oxygen. The response time of the oxygen microsensor is less than 0.3 s and it has insignificant oxygen consumption, giving fast and accurate oxygen measurements.

2.3. Laboratory analysis and calculations

Meio- and macrofauna were extracted from the sediment after incubation from each core, identified to the highest taxonomic level, counted and weighed. For this purpose a Plexiglas tube with an inner diameter of 3.6 cm was pushed into the sediment. Meiofaunal material was fixed with a 4% formaldehyde–seawater solution. LUDOX silica density gradient centrifugation (density 1.18 g cm^{-3}) was used to extract meiofaunal organisms from the sediment (Heip et al., 1985). After centrifugation, the supernatant was passed through 500 μm and 32 μm sieves. Samples retained on the 32 μm sieve were stained with Rose Bengal dye (Sigma–Aldrich). Subsequently, the meiofauna organisms were identified to the highest taxonomic level (phylum, class or order), and the abundance of particular taxa was expressed per 10 cm^2. For biomass calculation nematodes were measured individually using an image analyser (Axiocam Zeiss). The body length (L) was measured from head to tail (excluding filiform tails). The width of the nematodes (W) was measured at the thickest part of the body. Individual nematode biomass was calculated using an adjusted version of Andrassy's formula (1956): wet weight [μg] = L [μm] × W^2 [μm]/1,600,000. Macrobenthic organisms from each core were sorted, identified to the highest taxonomic level and weighed. Meiofaunal respiration was estimated using the function of Grant and Schwinghamer (1987) $R = 2.90\ V^{0.80}$, where V is the total meiofaunal biovolume. For estimating macrofaunal respiration we used the biomass of the major taxa and the mass-specific metabolic rates given by Piepenburg et al. (1995). Oxygen consumption rates were converted into carbon demand by assuming a 1:1 stoichiometric relationship between oxygen and carbon consumption. Hargrave (1973) assumed that sediment oxygen uptake could be converted to carbon release by applying a respiratory coefficient RQ value of 0.85.

Table 1 The sampling stations in Hornsund and Kongsfjorden – geographical position, bottom water temperature and oxygen content.

Site	Geographical position	Depth [m]	Bottom water temperature [°C]	Bottom oxygen content [%]
Hornsund	77°00.02′N 16°05.44′E	98	2.8	77.6
Kongsfjorden	78°55.85′N 12°08.37′E	105	3.5	88.4

2.4. Statistical analysis

To determine whether there are statistically significant differences between the two basins, the Kruskal–Wallis H test, a rank-based nonparametric test, was used to compare independent variables of oxygen consumption and faunal communities.

3. Results

3.1. What is the oxygen consumption by sediments in environmentally different fjords?

Mean total oxygen uptake TOU was 8.11 (±0.87) in Hornsund and 12.86 (±0.69) mmol m^{-2} d^{-1} in Kongsfjorden (Fig. 2). The Kruskal–Wallis test showed that these results differed significantly ($p = 0.0039$) between the fjords (Fig. 3). The variability in the measurements at both sites was low, with a relative standard deviation of 5%, reflecting the necessary precision of the method and the homogeneous variation of the benthic community on the sea floor. Finally, during the respiration experiment, 27% and 25% of the initial oxygen content were consumed in the incubation chambers.

The oxygen concentration profiles in sediment for the Hornsund and Kongsfjorden stations are illustrated in Fig. 4. The Kongsfjorden site had a higher initial value, likely reflecting a higher oxygen concentration in the water column.

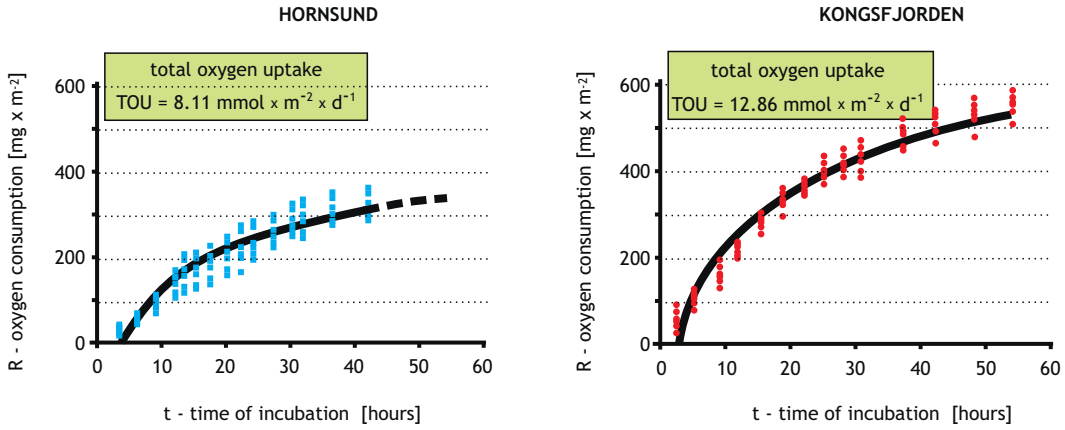

Figure 2 Total sediment oxygen consumption [mg m^{-2}] over incubation time in Hornsund (left panel) and in Kongsfjorden (right panel) for the ambient temperature in both areas; calculated total oxygen uptake (TOU) within the rectangles.

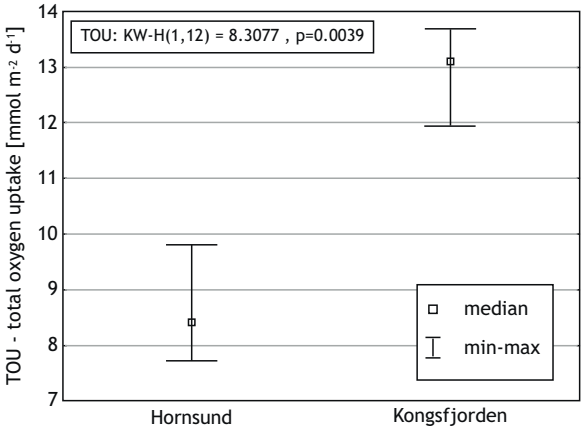

Figure 3 Total oxygen uptake in Hornsund and Kongsfjorden — Kruskal—Wallis test result.

The oxygen concentration gradients in the sediment were rather steep in both areas, despite the high bottom water O_2 concentrations: 77.6% in Hornsund and 88.4% in Kongsfjorden. In Hornsund the suboxic zone was reached at a depth of 1—2 cm, and in Kongsfjorden the thickness of the oxic sediment layer was greater, up to 2—3 cm, where oxygen was almost depleted.

3.2. How is oxygen uptake related to the meio- and macrofaunal communities?

The biomass of the macrofauna was highly variable within both areas but the meiofaunal biomass was in the same range and there was no difference with respect to nematode dominance (Table 2).

The total biomass of macrofauna (extracted from the incubated sediment cores) in Kongsfjorden was a dozen times larger than in Hornsund, which resulted in proportionate levels of oxygen consumption, i.e. 7.8% and 0.7% of the total benthic oxygen uptake, respectively. The meiofauna contributed roughly 5% of the total sediment oxygen uptake in both fjords.

4. Discussion

Hornsund and Kongsfjorden are among the best studied areas in the Svalbard archipelago (e.g. Svendsen et al., 2002). Incubation of sediment cores and monitoring dissolved oxygen concentration in the ambient water allows the energy flow through benthic communities to be estimated. The oxygen uptake of the sediment is still a widely used method for measuring total benthic mineralization, which is a proxy of total benthic ecosystem functioning, i.e. activity and benthic remineralisation (Glud, 2008; Holstein and Hensen, 2010). By benthic remineralisation we mean the degradation

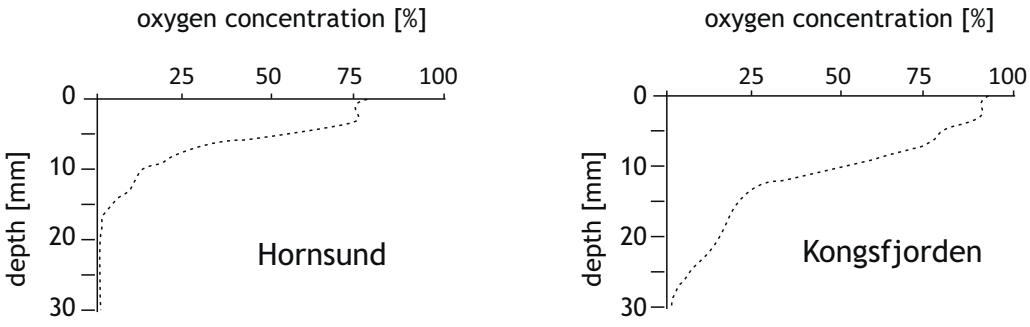

Figure 4 Oxygen concentration profiles in the 30 mm thick sediment surface layer in Hornsund (left panel) and in Kongsfjorden (right panel).

Table 2 Average biomass [g m^{-2}] of meiofauna and macrofauna (particular taxa) extracted from incubated cores and calculated respective oxygen consumption rates [mmol m^{-2} d^{-1}].

Area	Biomass wet weight [g m^{-2}]				Oxygen consumption rates [mmol m^{-2} d^{-1}]		
	Macrofauna		Meiofauna		Macrofauna		Meiofauna
Hornsund	Crustacea	–	Nematoda	0.53 ± 0.10	Crustacea	–	
	Polychaeta	3.1 ± 0.6	Polychaeta	0.01 ± 0.01	Polychaeta	0.045	
	Mollusca	2.1 ± 4.8	Harpacticoida	0.01 ± 0.01	Mollusca	0.008	0.45
	Others	0.1 ± 0.2	Others	0.02 ± 0.01	Others	0.003	
	Total	5.4 ± 5.3	Total	0.57 ± 0.21	Total	0.056	
Kongsfjorden	Crustacea	3.6 ± 3.1	Nematoda	0.40 ± 0.14	Crustacea	0.263	
	Polychaeta	32.6 ± 9.7	Polychaeta	0.01 ± 0.01	Polychaeta	0.469	
	Mollusca	25.7 ± 19.9	Harpacticoida	0.01 ± 0.01	Mollusca	0.088	0.50
	Others	3.7 ± 4.9	Others	0.01 ± 0.01	Others	0.093	
	Total	65.7 ± 27.1	Total	0.42 ± 0.16	Total	0.913	

of organic matter (OM), whereby carbon dioxide and inorganic nutrients flow from the sediments back into the water column (Link et al., 2013). Benthic communities use organic matter to grow and maintain their populations. Part of the organic matter that reaches the bottom is recycled and reused, e.g. for secondary production, while the remainder becomes buried in the sediment (Clough et al., 1997). The quantity and quality of organic matter falling to the seafloor serves as food and influences all biotic assemblages, including microbial production (Meyer et al., 2013). The total oxygen uptake of the sediments investigated in this study is close to that in other studies of Svalbard fjords at comparable depths measured by core incubation (Table 3).

These values are also similar to oxygen uptake rates in shelf sediments of temperate latitudes. The benthic respiration rate in Arctic is thus of the same magnitude as in warmer areas, indicating that the benthic Arctic system is no less productive (Glud et al., 1998).

Diverse bottom communities play a crucial role in the remineralization of the organic matter settling on the sea bed. Benthic communities consist of mega- (>4 mm), macro- (500 μm–4 mm), meio- (32 μm–500 μm) and microfauna (<32 μm) (Bluhm et al., 2011). Generally, in Arctic shelf sediments in the Barents Sea, oxygen uptake is dominated by the microbenthos (57%), followed by the macrobenthos (21%), megabenthos (15%) and meiobenthos (7%) (Piepenburg et al., 1995). In Hornsund and Kongsfjorden, there are distinct differences in both density and biomass in the standing stock of all benthic assemblages, which are reflected by different oxygen uptake rates and carbon demands. Also the total bacteria number was relatively higher in Kongsfjorden than in Hornsund, 4.27 and 3.39×10^9 cell cm^{-2}, respectively, same as bacterial biomass 2.16 and 1.56 gC m^{-2}, respectively (Jankowska, unpublished data). The measured sediment oxygen uptakes may be equivalent to total benthic carbon demands of 52 and 86 gC m^{-2} y^{-1} in Hornsund and Kongsfjorden, respectively (Table 4).

It is commonly assumed that the organic carbon which is not channelled through the pelagic food chain governs both the biomass and the production of the benthos (e.g. Danovaro et al., 1999). The amount of organic carbon reaching the benthos depends principally on the intensity of primary production in the water column (Ambrose and Renaud, 1995; Graf, 1989). On the other hand, the density, composition and activity of benthic communities, including bacteria, micro-, meio- and macrofauna, reflect processes such as pelagic-benthic coupling, mineral and organic sedimentation, freshwater input and advection of labile organic material from outside the local area (e.g. Grebmeier and Barry, 1991; Kotwicki et al., 2004). Advection seems to be an important mechanism providing food to benthic communities, especially in Kongsfjorden, where the carbon demand is relatively higher. Carbon accumulation and burial is relatively higher in Hornsund, whereas carbon mineralization is disproportionately greater in Kongsfjorden (Table 4). It appears that pelagic-benthic coupling is regulated not only

Table 3 Summary of the reports on previous total benthic oxygen uptake rates from the fjords of Svalbard archipelago.

Region	Water depth [m]	Method	Oxygen uptake rate [mmol m^{-2} d^{-1}]	Source
Eastern Svalbard	200–300	Core incubation	3.2–11.9	Pfannkuche and Thiel (1987)
Around Svalbard	170–257	Core incubation	1.85–11.2	Hulth et al. (1994)
Kongsfjorden	326	Core incubation	9.33	Hulth et al. (1994)
Hornsund, Bellsund	115–155	Sediment incubation	11.1–24.2	Kostka et al. (1999)
Hornsund	155	In situ measurement	16.4	Jørgensen et al. (2005)
Van Mijenfjord	115	In situ measurement	13.1	Jørgensen et al. (2005)
Storfjorden	175	In situ measurement	9.0	Jørgensen et al. (2005)
Hornsund	98	Core incubation	7.7–9.8	This study
Kongsfjorden	105	Core incubation	11.9–13.7	This study

Table 4 Carbon accumulation and burial values [g C m^{-2} y^{-1}] and estimated carbon demand [g C m^{-2} y^{-1}] by benthic fauna of Hornsund and Kongsfjorden.

	Hornsund	Kongsfjorden	Reference
Carbon accumulation rate	38–42	29–35	Zaborska et al., 2018
Carbon burial	35–39	15–16	Zaborska et al., 2018
Meiofauna carbon demand	1.68	1.86	This study
Macrofauna carbon demand	0.44	7.13	This study
Total benthic carbon demand	51.62	86.49	This study

by the availability of organic matter but also by its quality (Clough et al., 1997; Morata et al., 2015). The main difference between these two fjords is the source of carbon for the benthic assemblages. In Kongsfjorden most organic carbon comes from fresh, marine sources, in contrast to Hornsund where most organic carbon is of terrestrial origin (Grzelak et al., 2016; Koziorowska et al., 2016). Terrigenous organic matter is weakly mineralized in the sediments: this is reflected in the relatively low benthic density, biomass and diversity. It can be concluded that the lower sediment oxygen uptake in Hornsund reflects the quality of organic carbon delivered to marine sediments.

Benthic remineralisation is also influenced by sediment reworking and the irrigation activities of macro- and meiofauna (Bonaglia et al., 2014; Braeckman et al., 2010). Therefore, infauna is responsible for transport processes (bioturbation), including particle reworking and burrow ventilation or solute transfer (bio-irrigation), which makes them important for the oxygen and nutrient cycling process (Kristensen et al., 2012). For example, they introduce oxygen into reduced sediments, thereby promoting bacterial oxidation processes, which lead to higher respiration rates. This infaunal activity therefore contributes extensively to ecosystem functioning (Bonaglia et al., 2014; Braeckman et al., 2010; Morata et al., 2015).

In summary, the significantly higher total oxygen uptake rates in Kongsfjorden are directly related to the relatively higher biomass of the bacterial community and the greater biomass of fauna (meiobenthos and macrofauna), both resulting in the faster carbon accumulation rate in relation to Hornsund (Zaborska et al., 2018). This may be indirectly affected by organic matter in Kongsfjorden, acquired predominantly from marine sources (Grzelak et al., 2016; Koziorowska et al., 2016). We conclude that it is the quality, not the quantity of organic matter supplied to marine sediments that influences the rate of oxygen consumption in sediments of the fjord.

Acknowledgements

This study was financially supported by NCN project number 2012/04/A/NZ8/00661 (GAME project) and project number 2012/05/B/ST10/01908. Current position of dr Katarzyna Grzelak is supported by National Science Centre postdoctoral fellowship FUGA (grant number 2016/20/S/NZ8/00432). Our thanks go to Marta Głuchowska, Kajetan Deja and Mikołaj Mazurkiewicz for their assistance in the field. We also thank the crew of r/v "Oceania" for their technical support.

References

Ambrose Jr., W.G., Renaud, P.E., 1995. Benthic response to water column productivity patterns: evidence for benthic-pelagic coupling in the Northeast Water Polynya. J. Geophys. Res. 100 (C3), 4411–4421, http://dx.doi.org/10.1029/94JC01982.

Andrassy, I., 1956. The determination of volume and weight of nematodes. Acta Zool. Acad. Sci. Hungary 2, 1–15.

Bluhm, B.A., Ambrose Jr., W.G., Bergmann, M., Clough, L.M., Gebruk, A.V., Hasemann, C., Iken, K., Klages, M., MacDonald, I.R., Renaud, P.E., Schewe, I., Soltwedel, T., Włodarska-Kowalczuk, M., 2011. Diversity of the arctic deep-sea benthos. Mar. Biodivers. 41 (1), 87–107, http://dx.doi.org/10.1007/s12526-010-0078-4.

Bonaglia, S., Nascimento, F.J.A., Bartoli, M., Klawonn, I., Brüchert, V., 2014. Meiofauna increases bacterial denitrification in marine sediments. Nat. Commun. 5, 5133, http://dx.doi.org/10.1038/ncomms6133.

Braeckman, U., Provoost, P., Gribsholt, B., Van Gansbeke, D., Middelburg, J.J., Soetaert, K., Vincx, M., Vanaverbeke, J., 2010. Role of macrofauna functional traits and density in biogeochemical fluxes and bioturbation. Mar. Ecol. Prog. Ser. 399, 173–186, http://dx.doi.org/10.3354/meps08336.

Clough, L.M., Ambrose Jr., W.G., Cochran, J.K., Barnes, C., Renaud, P.E., Aller, R.C., 1997. Infaunal density, biomass and bioturbation in the sediments of the Arctic Ocean. Deep-Sea Res. Pt. II 44 (8), 1683–1704, http://dx.doi.org/10.1016/S0967-0645(97)00052-0.

Danovaro, R., Pusceddu, A., Covazzi Harriague, A., Marrale, D., Dell'Anno, A., Petrillo, M., Albertelli, G., Della Croce, N., 1999. Community experiments using benthic chambers: microbial significance in highly organic enriched sediments. Chem. Ecol. 16 (1), 7–30.

Glud, R.N., 2008. Oxygen dynamics of marine sediments. Mar. Biol. Res. 4 (4), 243–289, http://dx.doi.org/10.1080/17451000801888726.

Glud, R.N., Holby, O., Hoffmann, F., Canfield, D.E., 1998. Benthic mineralization and exchange in Arctic sediments (Svalbard, Norway). Mar. Ecol. Prog. Ser. 173, 237–251.

Glud, R.N., Risgaard-Petersen, N., Thamdrup, B., Fossing, H., Rysgaard, S., 2000. Benthic carbon mineralization in a high-Arctic sound (Young Sound, NE Greenland). Mar. Ecol. Prog. Ser. 206, 59–71.

Graf, G., 1989. Benthic-pelagic coupling in a deep-sea benthic community. Nature 341 (6241), 437–439.

Graf, G., 1992. Benthic-pelagic coupling: a benthic view. Oceanogr. Mar. Biol. Annu. Rev. 30, 149–190.

Grant, J., Schwinghamer, P., 1987. Size partitioning of microbial and meiobenthic biomass and respiration on Brown's Bank, south-west Nova Scotia. Estuar. Coast. Mar. Sci. 25 (6), 647–661, http://dx.doi.org/10.1016/0272-7714(87)90013-8.

Grebmeier, J.M., Barry, J.P., 1991. The influence of oceanographic processes on pelagic-benthic coupling in polar regions: a benthic perspective. J. Mar. Syst. 2 (3–4), 495–518, http://dx.doi.org/10.1016/0924-7963(91)90049-Z.

Grebmeier, J.M., McRoy, C.P., 1989. Pelagic-benthic coupling on the shelf of the northern Bering and Chukchi Seas. III. Benthic food supply and carbon cycling. Mar. Ecol. Prog. Ser. 53, 79—91.

Grzelak, K., Gluchowska, M., Gregorczyk, K., Winogradow, A., Weslawski, J.M., 2016. Nematode biomass and morphometric attributes as biological indicators of local environmental conditions in Arctic fjords. Ecol. Indic. 69, 368—380, http://dx.doi.org/10.1016/j.ecolind.2016.04.036.

Hargrave, B.T., 1973. Coupling carbon flow through some pelagic and benthic communities. J. Fish. Res. Board Can. 30, 1317—2132.

Heip, C., Vincx, M., Vranken, G., 1985. The ecology of marine nematodes. Oceanogr. Mar. Biol. 23, 399—489.

Holstein, J.M., Hensen, C., 2010. Microbial mediation of benthic biogenic silica dissolution. Geo-Mar. Lett. 30 (5), 477—492, http://dx.doi.org/10.1007/s00367-009-0181-3.

Hulth, S., Blackburn, T.H., Hall, P.O.J., 1994. Arctic sediments (Svalbard): consumption and microdistribution of oxygen. Mar. Chem. 46 (3), 293—316, http://dx.doi.org/10.1016/0304-4203(94)90084-1.

Johannessen, O.M., Bengtsson, L., Miles, M.W., Kuzmina, S.I., Semenov, V.A., Alekseev, G.V., Nagurnyi, A.P., Zakharov, V.F., Bobylev, L.P., Pettersson, L.H., Hasselmann, K., Cattle, H.P., 2004. Arctic climate change: observed and modeled temperature and sea-ice variability. Tellus A 56 (5), 559—560, http://dx.doi.org/10.1111/j.1600-0870.2004.00060.x.

Jones, P., Anderson, L.G., 1990. On the origin of the properties of the Arctic Ocean halocline north of Ellesmere Island: results from the Canadian Ice Island. Cont. Shelf. Res. 10 (5), 485—498, http://dx.doi.org/10.1016/0278-4343(90)90051-M.

Jørgensen, B.B., Glud, R.R., Holby, O., 2005. Oxygen distribution and bioirrigation in Arctic fjord sediments (Svalbard, Barents Sea). Mar. Ecol. Prog. Ser. 292, 85—95.

Kostka, J.E., Thamdrup, B., Glud, R.N., Canfield, D.E., 1999. Rates and pathways of carbon oxidation in permanently cold Arctic sediments. Mar. Ecol. Prog. Ser. 180 (3), 7—21.

Kotwicki, L., Szymelfenig, M., De Troch, M., Zajaczkowski, M., 2004. Distribution of meiofauna in Kongsfjorden, Spitsbergen. Polar Biol. 27 (11), 661—669, http://dx.doi.org/10.1007/s00300-004-0625-1.

Koziorowska, K., Kulinski, K., Pempkowiak, J., 2016. Sedimentary organic matter in two Spitsbergen fjords: terrestrial and marine contribution based on carbon and nitrogen contents and stable isotopes composition. Cont. Shelf Res. 113, 38—46, http://dx.doi.org/10.1016/j.csr.2015.11.010.

Kristensen, E., Penha-Lopes, G., Delefosse, M., Valdemarsen, T., Quintana, C.O., Banta, G.T., 2012. What is bioturbation? The need for a precise definition for fauna in aquatic sciences. Mar. Ecol. Prog. Ser. 446 (2), 285—302.

Link, H., Piepenburg, D., Archambault, P., 2013. Are hotspots always hotspots? The relationship between diversity, resource and ecosystem functions in the arctic. PLOS ONE 8 (9), e74077, http://dx.doi.org/10.1371/journal.pone.0074077.

Meyer, K.S., Bergmann, M., Soltwedel, T., 2013. Interannual variation in the epibenthic megafauna at the shallowest station of the HAUSGARTEN observatory (79N, 6 E). Biogeosciences 10 (6), 3479—3492, http://dx.doi.org/10.5194/bg-10-3479-2013.

Morata, N., Michaud, E., Włodarska-Kowalczuk, M., 2015. Impact of early food input on the Arctic benthos activities during the polar night. Polar Biol. 38 (1), 99—114, http://dx.doi.org/10.1007/s00300-013-1414-5.

Pfannkuche, O., Thiel, H., 1987. Meiobenthic stocks and benthic activity on the NE-Svalbard shelf and in the Nansen Basin. Polar Biol. 7 (5), 253—266, http://dx.doi.org/10.1007/BF00443943.

Piepenburg, D., 2005. Recent research on Arctic benthos: common notions need to be revised. Polar Biol. 28 (10), 733—755, http://dx.doi.org/10.1007/s00300-005-0013-5.

Piepenburg, D., Blackburn, T.H., von Dorrien, C.F., Gutt, J., Hall, P.O., Hulth, S., Kendall, M.A., Opalinski, K.W., Rachor, E., Schmid, M.K., 1995. Partitioning of benthic community respiration in the Arctic (northwestern Barents Sea). Mar. Ecol. Prog. Ser. 118 (1—3), 199—214.

Pusceddu, A., Fraschetti, S., Mirto, S., Holmer, M., Danovaro, R., 2007. Effects of intensive mariculture on sediment biochemistry. Ecol. Appl. 17 (5), 1366—1378, http://dx.doi.org/10.1890/06-2028.1.

Rowe, G.T., Morse, J., Nunnally, C., Boland, G.S., 2008. Sediment community oxygen consumption in the deep Gulf of Mexico. Deep-Sea Res. 55 (24—26), 2686—2691, http://dx.doi.org/10.1016/j.dsr2.2008.07.018.

Rysgaard, S., Finster, K., Dahlgaard, H., 1996. Primary production, nutrient dynamics and mineralisation in a northeastern Greenland fjord during the summer thaw. Polar Biol. 16 (7), 497—506, http://dx.doi.org/10.1007/s003000050081.

Rysgaard, S., Glud, R.N., Risgaard-Petersen, N., Dalsgaard, T., 2004. Denitrification and anammox activity in Arctic marine sediments. Limnol. Oceanogr. 49 (5), 1493—1502.

Rysgaard, S., Thamdrup, B., Risgaard-Petersen, N., Fossing, H., Berg, P., Christensen, P.B., Dalsgaard, T., 1998. Seasonal carbon and nutrient mineralization in a high-Arctic coastal marine sediment, Young Sound, Northeast Greenland. Mar. Ecol. Prog. Ser. 175 (17), 261—276.

Svendsen, H., Beszczynska-Moller, A., Hagen, J.O., Lafauconnier, B., Tverberg, V., Gerland, S., Ørbæk, J.B., Bischof, K., Papucci, C., Zajaczkowski, M., Azzolini, R., Bruland, O., Wiencke, C., 2002. The physical environment of Kongsfjorden—Krossfjorden, an Arctic fjord system in Svalbard. Polar Res. 21 (1), 133—166.

Thamdrup, B., Fleischer, S., 1998. Temperature dependence of oxygen respiration, nitrogen mineralization, and nitrification in Arctic sediments. Aquat. Microb. Ecol. 15 (2), 191—199.

Zaborska, A., Włodarska-Kowalczuk, M., Legeżyńska, J., Winogradow, A., Jankowska, E., Deja, K., 2018. Sedimentary organic matter sources, benthic consumption and burial in west Spitsbergen fjords — signs of warming induced maturing of high latitude fjordic systems? J. Mar. Syst. 180, 112—123, http://dx.doi.org/10.1016/j.jmarsys.2016.11.005.

Oceanologia (2018) 60, 114—127

Available online at www.sciencedirect.com

ScienceDirect

journal homepage: www.journals.elsevier.com/oceanologia/

ORIGINAL RESEARCH ARTICLE

Seasonal influence of physico-chemical parameters on phytoplankton diversity, community structure and abundance at Parangipettai coastal waters, Bay of Bengal, South East Coast of India

Manigandan Vajravelu [a], Yosuva Martin [a], Saravanakumar Ayyappan [b,*], Machendiranathan Mayakrishnan [a]

[a] *Centre of Advanced Study in Marine Biology, Annamalai University, Parangipettai, India*
[b] *Faculty of Marine Science, Centre of Advanced Study in Marine Biology, Annamalai University, Parangipettai, India*

Received 3 May 2017; accepted 25 August 2017
Available online 19 September 2017

KEYWORDS
Phytoplankton;
Nutrient;
CCA analysis;
Diversity;
Richness;
Productivity

Summary The present investigation studied the seasonal variation between physico-chemical parameters and phytoplankton diversity, community structure and abundance; quantitative samples were collected on a monthly basis from April 2015 to March 2016 at Parangipettai coast, the Bay of Bengal (BOB). Statistical analyses were performed on physico-chemical parameters such as salinity, dissolved oxygen (DO), pH, temperature, nitrate, nitrite, silicate, and inorganic phosphate (IP). The significant ($P < 0.0005$) variation among seasons as well as a high influence of these parameters was observed on phytoplankton productivity. Totally, 117 species were identified, belonging to five different classes, Coscinodiscophyceae (62%), Bacillariophyceae (17%), Fragilariophyceae (8%), Dinophyceae (8%) and Cyanophyceae (5%). Throughout the study period, the occurrence of most dominant species was observed from class Coscinodiscophyceae and Bacillariophyceae. The phytoplankton species also showed significant changes according to seasonal variations as well as the nutrient availability. Phytoplankton attained their maximum population density during premonsoon; whereas minimum population was observed during monsoon. The performed statistical analysis on phytoplankton species, the Shannon & Wiener diversity index was found to be higher during postmonsoon and lower during monsoon season. The

* Corresponding author at: Faculty of Marine Sciences, Centre of Advanced Study in Marine Biology, Annamalai University, Parangipettai 608502, Tamil Nadu, India. Tel.: +91 9443610371.
E-mail address: asarvaan@gmail.com (S. Ayyappan).

Peer review under the responsibility of Institute of Oceanology of the Polish Academy of Sciences.

ELSEVIER Production and hosting by Elsevier

http://dx.doi.org/10.1016/j.oceano.2017.08.003

Canonical Correspondence Analysis (CCA) was used, to find out the seasonal relationship between phytoplankton and physicochemical parameters. Hence, the executed CCA results revealed that temperature, salinity, silicate, DO and IP have a higher influence on phytoplankton abundance.

1. Introduction

Phytoplankton are the primary source of a food chain, which contributes to the major fishery resource around the world. They are responsible for the formulation of a biological community and regulate the food web (Falkowski et al., 2008; Field et al., 1998). Phytoplankton act as an important component of the marine ecosystem, as they liberate oxygen during photosynthesis and aid in energy exchange process (Khan, 2003). They play a crucial role in mitigating the climate change and global warming, thereby recede the global CO_2 levels (Santhosh Kumar and Perumal, 2012). Phytoplankton community structure, composition and species diversity in aquatic ecosystem are determined by several physico-chemical parameters (Sin et al., 1999). Spatial and temporal variations in phytoplankton distribution are widely affected by the hydrochemical and physical factors such as temperature, salinity, pH, nitrate, nitrite, ammonia, silicate and IP. The influence of these factors on phytoplankton community alters species composition and their diversity in the marine ecosystem (Durate et al., 2006; Madhu et al., 2007). Generally, shallow water and estuaries show seasonal fluctuations among variables depending on the regional rainfall, tidal inflow and various abiotic and biotic processes, which play substantial role in nutrient cycle (Choudhury and Panigrahy, 1991).

The relationship between phytoplankton and nutrients is highly dynamic and has always been the major focus among researchers to explicate experimental ecology (Chattopadhyay et al., 2003). Recently, various anthropogenic activities have increased, which in turn enhance the nutrient concentration thus, leads to high productivity in coastal environment (Rakhesh et al., 2013). Availability of nutrient plays an important role in phytoplankton diversity that reflects the environmental condition of the ecosystem (Dugdale, 1967; Rhyther and Dunstan, 1971; Smayda, 1980). Phytoplankton species shows wide variation in distribution due to changes in factor like hydro-chemical and physical parameters. These dramatic changes in physico-chemical parameters, exhibit differential effect in distribution and abundance of many phytoplankton species, ultimately indicating the quality of water (Shashi Shekhar et al., 2008). Phytoplankton species can be very sensitive to slight modification in its environment and hence, it provides good insight about water quality before it reaches to extreme visible condition like eutrophication (Brettum and Andersen, 2005). Eutrophication is caused by several factors such as substrate remineralization, upwelling, increase river inflow and resuspension of particulate matter (Guinder et al., 2015; Su et al., 2015). It might have both positive and negative impact on phytoplankton diversity depending on the state of an ecosystem (Crossetti et al., 2008; Marasović and Pucher-Petković, 1985; Skejić et al., 2014; Su et al., 2015). Species diversity and community composition are subjective to substantial changes by environmental parameters and eutrophication. Phytoplankton biomass increases due to eutrophication and causes uniform distribution in species composition. Simultaneously, opportunistic species start proliferating by dominating other (McQuatters-Gollop et al., 2009). The factors such as eutrophication, changes in nutrients concentration and competition between species reduce the phytoplankton species diversity (Spatharis et al., 2007). The phytoplankton biomass (chlorophyll-*a*) is used as a good indicator of water quality and eutrophication because it provides good insights of that particular area (McQuatters-Gollop et al., 2009; Ninčević-Gladan et al., 2015). Monitoring the seasonal changes in phytoplankton diversity and its community structure provides the better understanding about the state of coastal waters and they are one of the most important biological elements that provide the ecological status of the sea (Barić et al., 1992; Legović et al., 1994). A marine phytoplankton community is mostly dependent on nutrients and physical parameters in a coastal environment. The nutrient availability is frequently considered as a key factor regulating the phytoplankton abundance, growth and metabolism. Significant work has been done in relation to seasonal variation in phytoplankton species composition in the different coastal ecosystem of India (Menon et al., 2000; Sahu et al., 2012; Siva Sankar and Padmavathi, 2012; Sridhar et al., 2006). The present study area is highly influenced by seasonal changes in freshwater. In addition, aquaculture and anthropogenic activities also significantly contribute to changes in the coastal ecosystem of Parangipettai. Therefore, comprehending the dynamic environmental parameters and their influence on phytoplankton productivity is extremely important as it plays a vital role in the food web and coastal productivity. This will also aid in assessing the water quality in future. Hence, the present study aims to find out the seasonal variation in phytoplankton diversity, composition and their abundance in response to various environmental parameters.

2. Material and methods

2.1. Description of study area

The present investigation was carried out from April 2015 to March 2016 in Parangipettai coast of Tamil Nadu, Southeast Coast of India. The freshwater influence is high due to fluctuations in tide and incursion of freshwater during monsoon because of Vellar estuary debouching in the Bay of

Bengal. Sampling sites are shown in Fig. 1. Totally five sampling sites were fixed and monthly sampling was carried out.

2.2. Sampling

Monthly samples were collected at different depths using Niskin water sampler. Seawater was collected for 1 L in polypropylene bottles to analyze chlorophyll *a* and physico-chemical parameters, which were then filtered through Whatman GF/F filters for further analysis as described by (Strickland and Parsons, 1972). Physical parameters such as temperature, pH, salinity were measured on the site itself by using standard instruments (a multistem digital thermometer (accuracy $\pm$ 0.1), a hand-held refractometer (ATAGO S/Mill-E), pH pen).

Nutrients such as nitrite (NO_2), nitrate (NO_3), ammonia (NH_4), inorganic phosphate (PO_4), reactive silicate (SiO_4) were analyzed following the standard methodology described by Strickland and Parsons (1972). Chlorophyll-*a* concentration was estimated by pigment extraction method using 90% acetone. Extracted samples were kept for incubation in refrigerator under dark condition and the pigment concentration was obtained through UV–VIS spectrophotometer (Shimadzu-UV) using 5 cm cells at 630 nm, 645 nm, and 665 nm (Strickland and Parsons, 1972).

To estimate the total suspended solids (TSS) in seawater, glass filter paper (Whatmann GF/C, 0.45 μm) was weighed before filtration, the filtered paper was kept in an oven for 24 h at 75°C and weighed again to find out the TSS.

Phytoplankton were collected at monthly intervals on surface water by towing plankton net (mouth diameter – 1.5 m) made up of bolting silk cloth (mesh size 54 μm). The flow meter (Hydro-bios, Germany) was attached at the center of the net to calculate the volume of seawater passed through the net. Collected phytoplankton samples were preserved in 4% buffered formalin for further analysis. Qualitative and quantitative analysis of phytoplankton were executed using an inverted microscope. Quantification of phytoplankton was carried out using Sedgwick rafter counting chamber and phytoplankton species were identified by following standard manuals of Subramanyan (1946), Al-Kandari et al. (2009), Venkataraman (1939), Perumal et al. (1998), Santhanam et al. (1987) and Smith (1977).

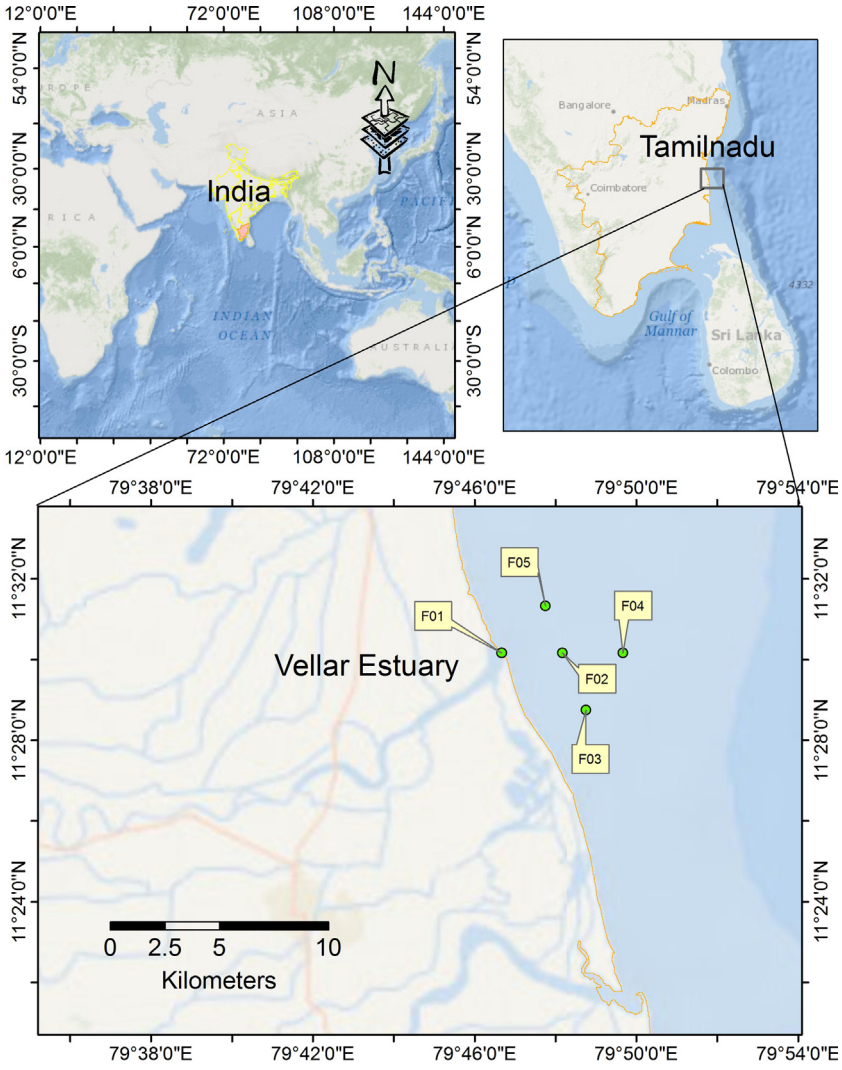

Figure 1 The GPS location of sampling sites.

2.3. Statistical analysis

Canonical Correspondence Analysis was used to determine the relationship between phytoplankton and environmental parameters. Biological diversity (H′) and richness (S) were calculated by following the equation of Shannon and Wiener (1949), and Pielou (1966). One way ANOVA was performed using Tukey's HSD test to observe the seasonal variation in nutrients. Variations in physico-chemical parameters were depicted using box plot. All of these analyses were run in R software (R Version 3.4.0, 2016), vegan: community ecology package. R (Oksanen et al., 2016) was used to run the CCA and Shannon diversity index analysis. Box plot and line diagrams were plotted using ggplot2 package (Wickham, 2009).

3. Results and discussion

3.1. Physico-chemical characteristics of water

Variation in phytoplankton distribution and abundance were mostly influenced by the seasonal changes in environmental parameters (DO, salinity, temperature, nitrate, IP, silicate). It is of paramount importance to study the hydro-chemical parameters to distinguish the difference in phytoplankton diversity on a seasonal scale in marine ecosystem (Chang, 2008). The environmental parameters which drive the succession of plankton diversity were depicted seasonally in Figs. 2 and 3. Physico-chemical parameters showed significant difference among seasons.

Temperature is an important factor for marine environment as it influences the life of organisms and physico-chemical parameters (Sukumaran et al., 2013). Temperature showed significant variations between seasons ($F = 191.9$; $P < 0.0005$) and varied from 27.15°C (November 2015; monsoon) to 32.4°C (May 2015; summer) with the mean of 29.53°C ($\pm$ 1.23). Seasonal variations in temperature may attribute with wind force, influx of freshwater and atmospheric temperature. The low temperature could be attributed to the heavy rainfall received during monsoon season. Earlier reports also stated that temperature reduction in water depends mainly on the intensity of rainfall received on monsoon and less air temperature.

Salinity reached a maximum of 34.33 ppt (May 2015) during summer and minimum was recorded as 27.11 ppt (November 2015) with the mean value of 31.80 ($\pm$1.83). Salinity showed significant difference among seasons ($F = 143$; $P < 0.0005$). Salinity plays a major role as a limiting factor since it controls the faunal and floral diversity of coastal ecosystems (Govindasamy et al., 2000; Sridhar et al., 2006; Subramanian and Mahadevan, 1999). Generally, salinity shows seasonal variation in Parangipettai coastal waters due to Vellar estuary as it brings continuous freshwater during monsoon (Soundarapandian et al., 2009). The intrusion of neritic water and high intensity of solar radiation during summer could be the reason for high salinity, and the reduced salinity during monsoon might be due to the freshwater influence and fluctuation in tides (Jyothibabu et al., 2008; Sukumaran et al., 2013). Thus the present investigation evidenced earlier reports on variation in salinity.

Hydrogen ion concentration varied from 7.5 to 8.2 with the mean of 7.97 ($\pm$0.22). Maximum pH was observed during March 2015 and minimum was recorded in November 2015. pH was alkaline during summer and showed downward pattern up to monsoon and remained alkaline during post-monsoon, significant difference was observed in between seasons ($F = 52.47$; $P < 0.0005$). Changes in pH will depend on the factor like the removal of CO_2 by photosynthesis through bicarbonate degradation, fresh water influx, reduction in salinity and temperature and decomposition of organic matter (Rajasegar et al., 2002). Higher pH in post-monsoon could be attributed to the high photosynthetic activity by phytoplankton whereas the lowered pH value in monsoon was due to freshwater influx by Vellar estuary.

Dissolved oxygen is a major component in an aquatic ecosystem which determines the quality of water and support aquatic life. Dissolved oxygen in water ranged between 4.23 mg L^{-1} and 5.5 mg L^{-1} (4.77 $\pm$ 0.34) registering the maximum value during monsoon (November 2015) and minimum in summer (April 2015). Analysis of variance showed significance difference between seasons ($F = 40.9$; $P < 0.0005$). Dissolved oxygen showed marked seasonal variation throughout the study period. During summer and premonsoon less dissolved oxygen content was recorded, this could be due to the high temperature, salinity and biological activity (Davis, 1975; Levinton, 2001). High concentration of dissolved oxygen during monsoon and postmonsoon is attributed to high fresh water input and evidenced by the maximum occurrence of phytoplankton species (Morgan et al., 2006).

Chlorophyll-*a* concentration varied from 0.35 μg L^{-1} (April 2015) to 3.72 μg L^{-1} (February, 2016) (mean = 1.28 $\pm$ 0.88) and significant variation was observed between different seasons ($F = 158.7$; $P < 0.0005$). Chlorophyll-*a*, the most principle pigment is responsible for primary production in marine water. The elevated concentration of chlorophyll-*a* in postmonsoon might be due to the availability of sufficient amount of UV radiation, pristine water condition, consumption of silicate and phosphate by primary producers, which were brought up by river runoff during monsoon (Prabhahar et al., 2011; Sardessai et al., 2007).

Total suspended solids (TSS) varied from 18.04 mg L^{-1} (February 2016) to 44.60 mg L^{-1} (November 2015) (mean = 31.28 mg L^{-1}; $\pm$5.17) and the observed TSS values showed significant variations in between seasons ($F = 43.3$; $P < 0.0005$). High terrestrial runoff, along with heavy suspended solid loads, was brought to coast during monsoon season could be responsible for the increased suspended solid concentration (Vinayachandran et al., 2002).

3.2. Nutrient dynamics

Nutrients such as nitrate, nitrite, IP, and silicate in the coastal environment would exhibit substantial seasonal variations depending on the rainfall, freshwater input, tidal ingress and consumption of nutrients by autotrophs. Nitrate concentration ranged from 1.24 μmol (August 2015) to 6.89 μmol (April 2015) and the significant difference was observed between seasons in statistical analysis (mean = 3.158 $\pm$ 1.45; $F = 42.62$; $P < 0.0005$). Nitrite concentration varied from 0.12 μmol (February 2016) to 0.88 μmol (February 2016) and varied significantly throughout the season (mean = 0.41 $\pm$ 0.17; $F = 4.08$; $P < 0.0005$). The higher concentration of nitrate during summer and

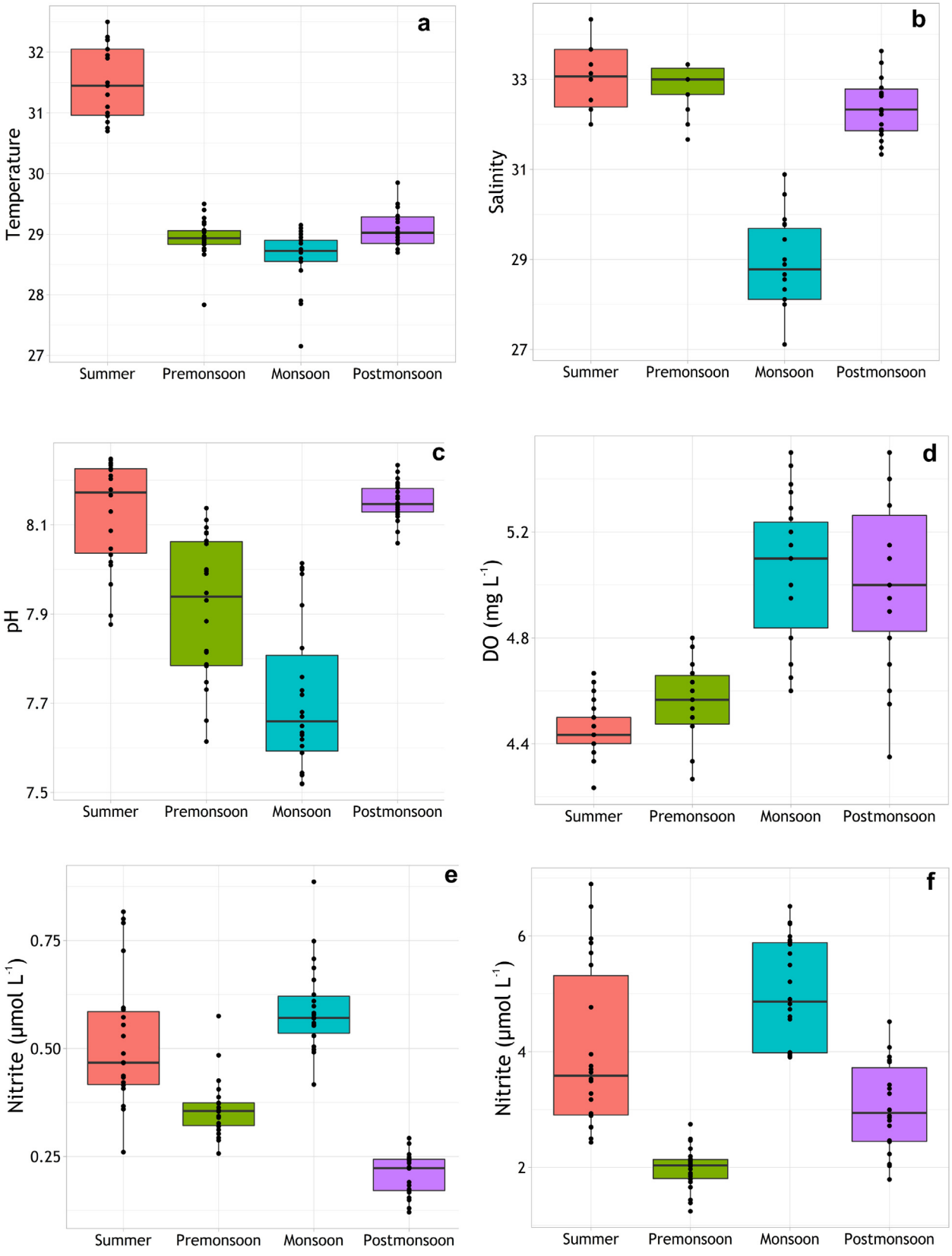

Figure 2 Seasonal variation of physico-chemical parameters during the study period. Temperature (a), salinity (b), pH (c), DO — dissolved oxygen (d), nitrite (e), nitrate (f).

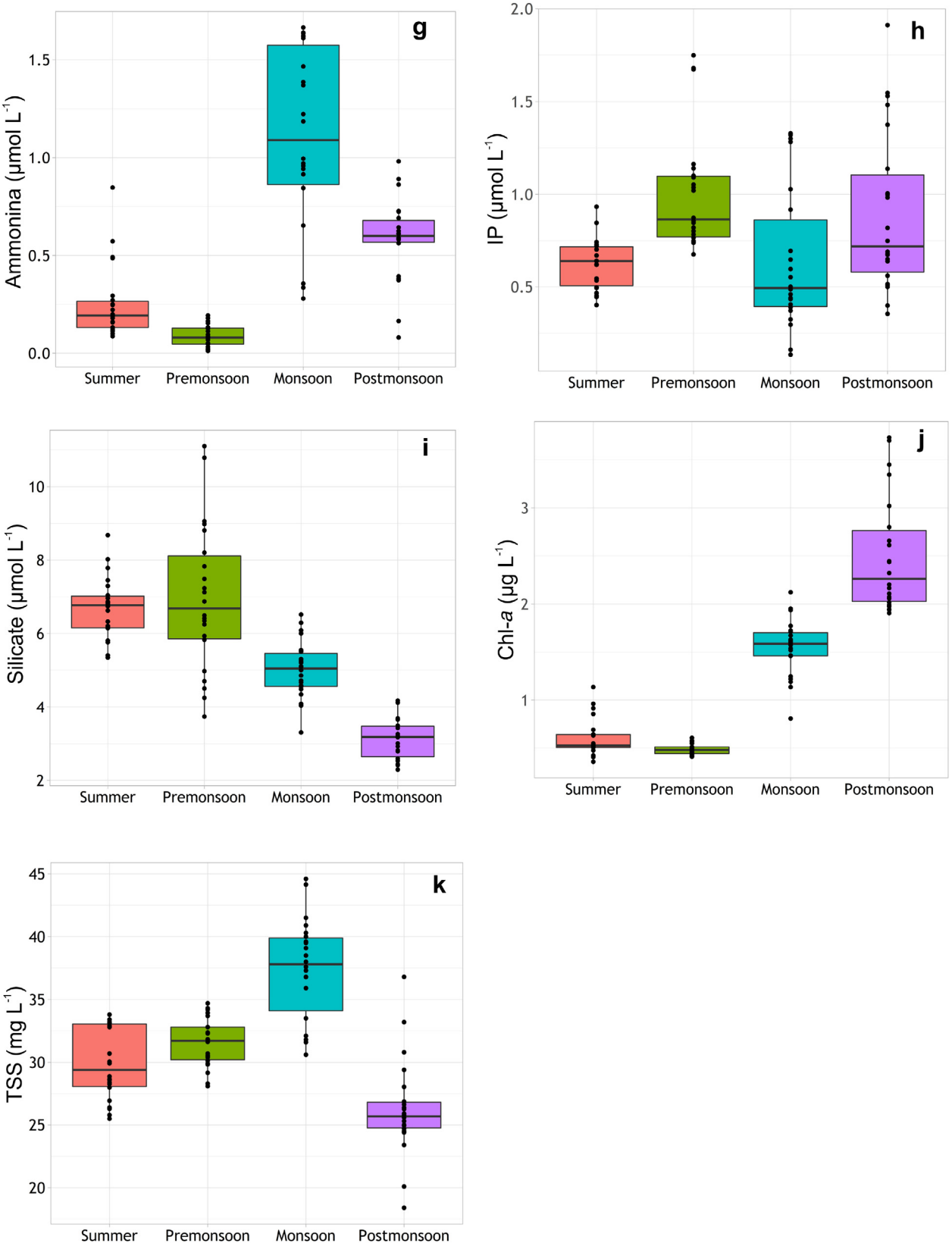

Figure 3 Seasonal variation of physico-chemical parameters during the study period. Ammonia (g), IP — inorganic phosphate (h), silicate (i), Chl-*a* — Chlorophyll-*a* (j), TSS — total suspended solids (k).

monsoon could be due to fresh water inflow, terrestrial runoff, and high rate of biological production, oxidation of ammonia, reduction of nitrate by recycling of nitrogen and also by biodegradation of planktonic detritus present in the environment (Govindasamy et al., 2000; Hutchinson, 1957; Santhanam and Perumal, 2003). The registered lower concentration of nitrate during non-monsoon period might be due to high consumption of nitrate by photosynthetic organisms and the incursion of neritic water which constitute only the smaller amount of nitrate (Das et al., 1997; Gouda and Panigrahy, 1995; Govindasamy et al., 2000).

Ammonia concentration ranged between 0.0116 μmol (August 2016) and 1.66 μmol (November 2016) with significant variation (mean = 0.509 ± 0.47; $F = 63.28$; $P < 0.0005$). Increased concentration of ammonia during monsoon season was due to the incursion of terrestrial runoff and decomposition of phytoplankton (Segar and Hariharan, 1989; Senthilkumar et al., 2008; Thangaradjou et al., 2013). Decreased ammonia concentration during summer and premonsoon, may be attributed to quick utilization of specific phytoplankton community as they prefer ammonia more than nitrate at certain environment (Dugdale et al., 2007; Lipschultz, 1995).

Phosphate plays a major role in primary productivity in an aquatic ecosystem as it promotes growth for organisms and limits the phytoplankton production (Cole and Sanford, 1989). The recorded phosphate values ranged between 0.13 μmol (June 2015) and 1.91 μmol (mean = 0.79 ± 0.36). Statistical analysis also evidenced that the dissolved inorganic phosphate concentration has a significant difference within seasons ($F = 6.899$; $P < 0.0005$). Higher concentration of inorganic phosphate might be attributed to the monsoonal intrusion due to rainfall along with terrestrial runoff (Satpathy et al., 2009) and the low value in summer might be due to utilization of phosphate by photoautotrophs and buffering process of sediment under varying environmental conditions (Perumal et al., 2009).

Variation in silicate concentration is driven by physical mixing of seawater with a freshwater addition, adsorption and sediment particles, interaction between chemicals and minerals, co- precipitation with humic components, and biological removal by phytoplankton, particularly diatoms and silicoflagellates (Satpathy et al., 2009). The minimum concentration of 2.29 μmol (February 2016) was observed during postmonsoon whereas the maximum concentration of 11.10 μmol (October 2015) was recorded during premonsoon season. The high significant difference was found with the mean value of 5.43 (±1.92) ($F = 48.55$; $P < 0.0005$). Increased concentration of silicate in premonsoon was due to the intermittent rainfall which might have brought up the terrestrial runoff to the coast. High consumption of silicate by silicoflagellates and diatoms might have contributed to the less availability of silicate concentration during postmonsoon (Satpathy et al., 2009).

3.3. Phytoplankton composition, population density, and diversity

Phytoplankton species composition, development, proliferation and quantification are majorly influenced by physicochemical parameters of that particular environment. The abundant and common species recorded during the study period are presented in Table 1. Totally 117 species of phytoplankton were identified in the present study belonging

Table 1 Checklist of dominant phytoplankton species surveyed during the study period.

No.	Species name	Summer	Premonsoon	Monsoon	Postmonsoon
	Diatoms				
	Coscinodiscophyceae (Centric diatoms)				
1	*Bacteriastrum delicatulum*	+	+	+	+
2	*B. hyalinum*	+	+	+	+
3	*B. varians*	+	+	+	
4	*Bellerochea malleus*	+	+		+
5	*Chaetoceros affinis*	+	+	+	+
6	*C. atlanticus*	+	+	+	+
7	*C. compressus*	+	+	+	+
8	*C. costatus*	+	+		+
9	*C. curvisetum*	+	+	+	+
10	*C. curvisetus*		+	+	+
11	*C. decipiens*		+	+	+
12	*C. didymus*	+	+	+	+
13	*C. diversus*	+	+	+	
14	*C. laciniosus*	+	+		+
15	*C. lorenzianus*	+	+	+	+
16	*C. messanensis*	+		+	+
17	*Coscinodiscus centralis*	+	+	+	+
18	*C. asteromphalus*		+	+	+
19	*C. concinnus*	+	+	+	+
20	*C. gigas*	+		+	+
21	*C. granii*	+	+	+	+
22	*C. marginatus*	+	+	+	+

Table 1 (*Continued*)

No.	Species name	Summer	Premonsoon	Monsoon	Postmonsoon
23	*C. oculus-iridis*	+		+	+
24	*C. wailesii*	+	+	+	+
25	*Ditylum brightwelli*	+	+	+	+
26	*Guinardia flaccida*	+	+	+	+
27	*G. striata*	+	+		+
28	*Hemiaulus membranaceus*	+		+	+
29	*Hemiaulus sinensis*	+	+	+	+
30	*Lampriscus shadboltianum*	+	+		+
31	*Lauderia annulata*	+	+		+
32	*Leptocylindrus danicus*	+		+	+
33	*Odontella mobiliensis*	+	+		+
34	*Palmeria hardmaniana*	+	+		+
35	*Proboscia alata*	+	+		+
36	*Pseudosolenia calcar-avis*	+		+	+
37	*Rhizosolenia imbricata*	+	+	+	+
38	*R. setigera*	+	+		+
39	*R. shrubsolei*		+	+	+
40	*Skeletonema costatum*	+	+	+	+
41	*Stephanopyxis palmeriana*		+	+	+
42	*Streptotheca thamensis*	+		+	+
43	*Triceratium cf. broecuii*	+	+		+
	Fragilariophyceae (Pennate diatoms)				
44	*Asterionella japonica*	+	+	+	
45	*Asterionellopsis glacialis*	+	+	+	+
46	*Thalassionema nitzschioides*	+	+	+	+
	Bacillariophycea (Pennate diatoms)				
47	*Bacillaria socialis*	+	+	+	+
48	*Nitzschia longissima*	+	+		+
49	*N. seriata (Pseudo-nitzschia seriata)*	+	+	+	
50	*N. sigma*	+	+		
51	*Pleurosigma cuspidatum*	+		+	+
	Dinoflagellates				
	Dinophyceae				
52	*Alexandrium leei*	+		+	+
53	*Ceratium breve*	+	+		+
54	*C. furca*	+	+	+	+
55	*C. fusus*		+	+	+
56	*C. massiliense*	+	+		+
57	*C. trichoceros*	+	+		+
58	*C. tripos*	+	+	+	+
59	*Dinophysis caudata*	+	+		+

to five different classes, Coscinodiscophyceae (62%), Bacillariophyceae (17%), Fragilariophyceae (8%), Dinophyceae (8%), Cyanophyceae (5%). *Chaetoceros atlanticus*, *Chaetoceros curvisetum*, *Coscinodiscus granii*, *Coscinodiscus wailesii*, *Coscinodiscus marginatus* and *Guinardia flaccida* of Coscinodiscophyceae, *Nitzschia longissima*, *Nitzschia seriata* (*peudo nitzschia seriata group*) of Bacillariophyceae, *Asterionellopsis glacialis* of Fragellariophycea and *Ceratium tripos*, *Ceratium furca* of Dinophyceae were most common group observed throughout the study period. Species composition of phytoplankton was more diverse during postmonsoon period, especially diatoms found to be more dominant group than the others. This could be due to the terrestrial runoff during monsoon season might have brought up the sufficient amount of silicate which in turn enhanced the species composition. It has been reported that the suitable environmental condition, late monsoonal effects such as land runoff and upwelling which favors the growth and proliferation of diatoms (Dehradrai and Bhargava, 1972; Dupuis and Hann, 2009).

Noticeable seasonal and spatial differences in population density were observed among phytoplankton communities and the density of phytoplankton ranged between 8771 cells L^{-1} (November 2015) and 1,303,142 cells L^{-1} (September 2015). In the present study, the phytoplankton population density was observed in the order of premonsoon > summer > postmonsoon > monsoon. Phytoplankton population density attained its maximum

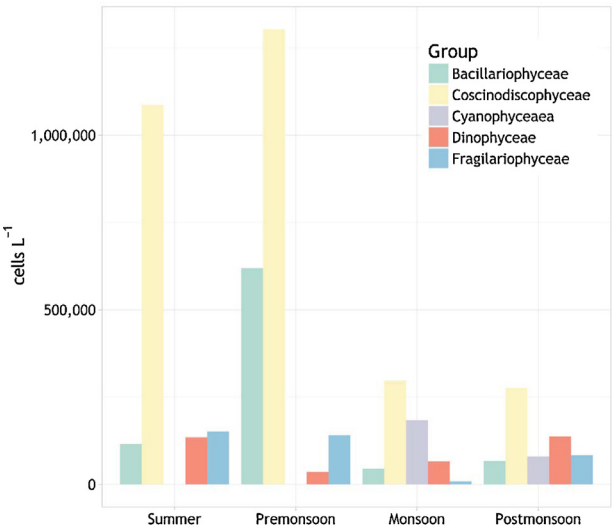

Figure 4 Seasonal variation in phytoplankton population density.

(1.303×10^6 cells L^{-1}, and 1.086×10^6 cells L^{-1}) during premonsoon (September 2015) and summer (April 2015) are shown in Fig. 4. The investigated high population density during premonsoon was due to the prevalence of *N. seriata* (*pseudo-nitzschia seriata group*) and *Skeletonema costatum*. The same phenomenon has been reported earlier with other few different species during premonsoon season (Senthilkumar et al., 2002; Thillai Rajsekar et al., 2005). The observed high density during summer might have attributed to more stable hydrographical parameters (Babu et al., 2013). However, species composition was comparatively higher in postmonsoon and summer than premonsoon. Phytoplankton abundance was low during monsoon season and this could be due to heavy rainfall, decreased salinity, temperature, pH and high turbidity (Babu et al., 2013; Rajasekar et al., 2010).

Seasonal variations in phytoplankton species diversity index and species richness is illustrated in Fig. 5. The phytoplankton diversity index and species richness ranged from 1.39 to 3.60 and 1.68 to 1.96 respectively. The highest values were found during postmonsoon and the lowest values were observed during monsoon season. The observed highest value in postmonsoon was due to high species composition observed during the study. Dupuis and Hann (2009) also reported desirable environmental condition promotes the growth of diatoms during postmonsoon season. Low species richness and diversity indices on monsoon might have associated with lower salinity and temperature as reported by Rajasegar et al. (2000) and Mani (1992).

3.4. Canonical Correspondence Analysis of phytoplankton and environmental parameters

Canonical Correspondence Analysis was intended to find out the relationship between environmental variables and phytoplankton distribution (Ariyadej et al., 2004). Important environmental variables responsible for the phytoplankton community changes were identified with CCA are represented in Fig. 6.

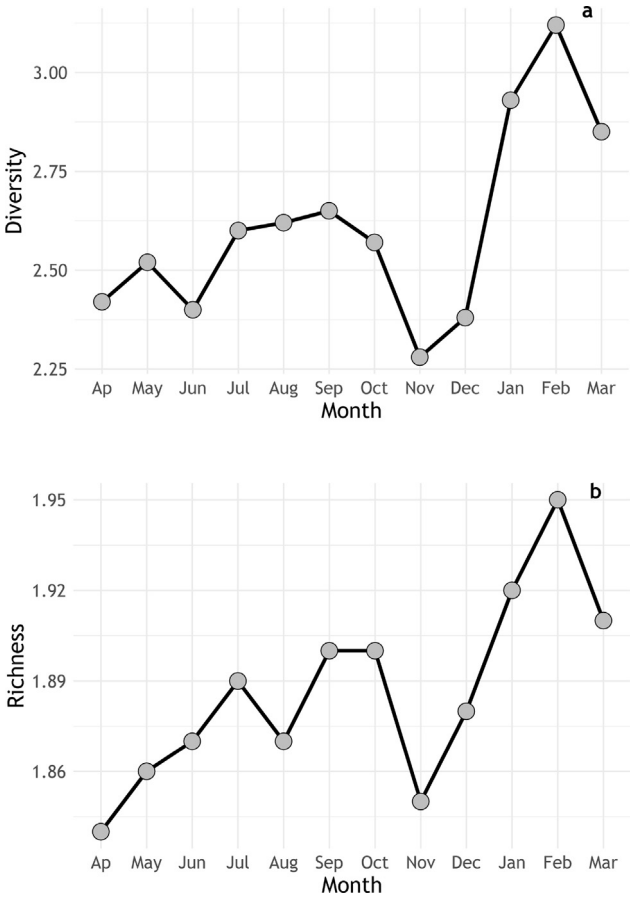

Figure 5 Shows seasonal variation in phytoplankton species diversity and richness. Phytoplankton species diversity (a), phytoplankton species richness (b).

During summer axis 1 and 2 explained 71% of the variability in the species environment biplot (Fig. 6). Temperature, DO, silicate, pH, chlorophyll-*a*, IP, and nitrite had positive correlation in axis 1 and highly associated with *A. glacialis*, *Bacteriastrum delicatalum*, *Bacteriastrum hyalinum*, *Leptocylindrus minimus*, *Chaetoceros curvisteum*, *Chaetoceros decipiens*, *Chaetoceros lorenzianus*, *S. costatum*, *Lauderia annualta*, *C. tripos* among these *A. glacialis*, *Chaetoceros curviesteum*, *C. decipiens*, *S. costatum*, *Dityum brightwelli*, *Lauderia annualata* and *C. tripos* exhibited maximum canonical values (1.246, 0.656, 1.025, 0.913, 0.938, 0.541 and 0.920). In previous studies, it has been proven that stable environmental parameters like increased salinity, pH, high temperature, high nutrients and high intensity of light penetration during summer favor these species proliferation especially *S. costatum*, *Dityum* spp., *Chaetoceros* spp., *Odontella* spp. (Gouda and Panigrahy, 1996; Rajasegar et al., 2000; Saravanakumar et al., 2008; Vengadesh et al., 2009). In axis 2 *C. furca*, *Chaetoceros tortissimum*, *Chaetoceros diversus*, and *C. granii*, had a strong positive correlation with salinity. CCA biplot explained that temperature, pH and salinity had a close relation with phytoplankton species than other variables which indicated the increased temperature in summer is responsible for its positive relationship. Concurrently DO, IP, silicate, and chlorophyll-*a* also expressed strong positive relation in both axis 1 and 2, which

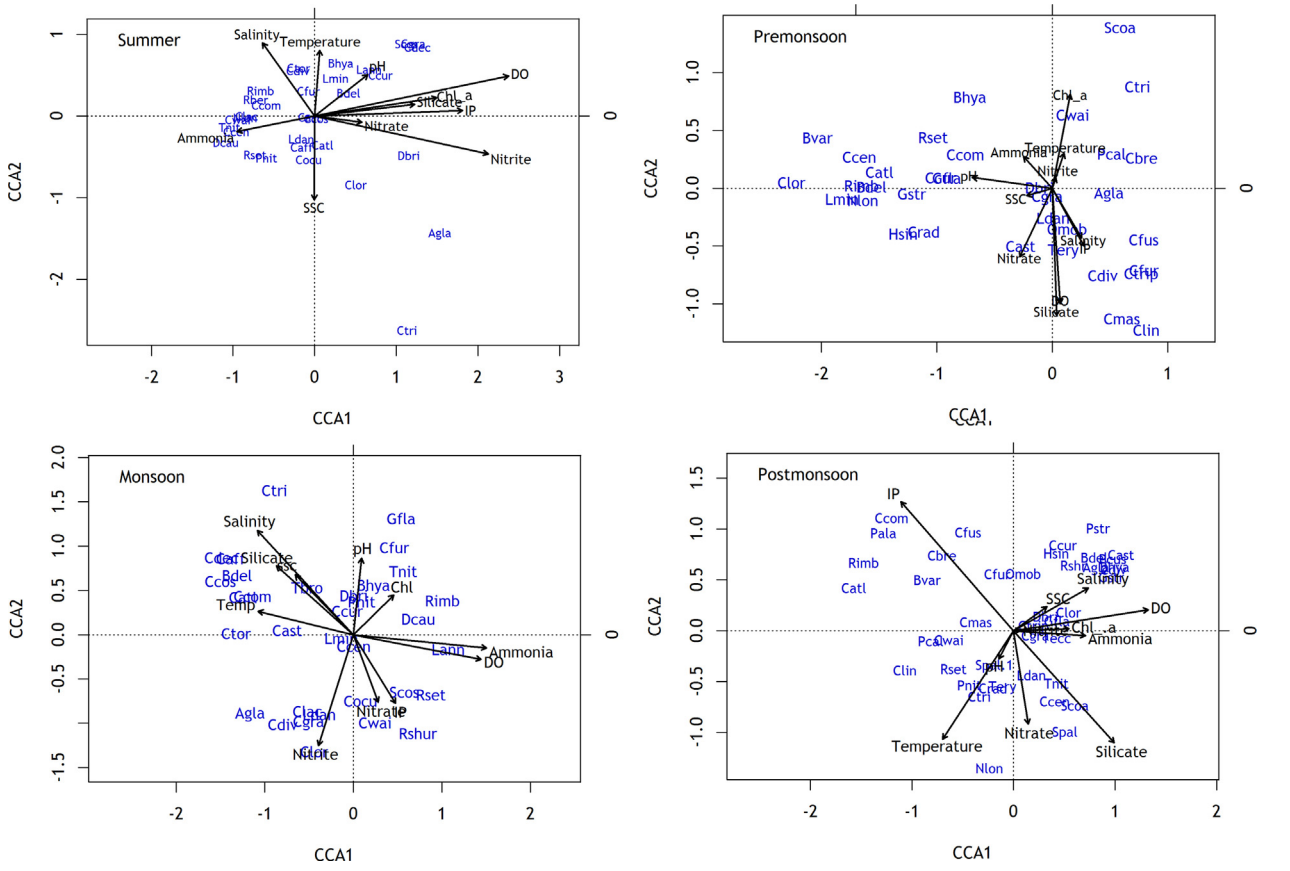

Figure 6 CCA biplot showing the seasonal variation between phytoplankton species and environmental parameters. Environmental variables are depicted by long arrows and species are given in code words. The correlation between species and environmental variables are explained by the length of the arrows. (DO — dissolved oxygen, Chl-*a* — chlorophyll-*a*, IP — inorganic phosphate: Agla — *Asterionellopsis glacialis*, Bdel — *Bacteriastrum delicatulum*,Bhya — *Bacteriastrum hyalinum*, Bvar — *Bacteriastrum varians*, Caff — *Chaetoceros affinis*, Cast — *Coscinodiscus cf. asteromphalus*, Catl — *Chaetoceros atlanticus*, Cbre — *Ceratium breve*, Ccen — *Coscinodiscus centralis*, Ccom — *Chaetoceros compressus*, Ccos — *Chaetoceros costatus*, Ccur — *Chaetoceros curvisetum*, Cdec — *Chaetoceros decipiens*, Cdiv — *Chaetoceros diversus*, Cfur — *Ceratium furca*, Cfus — *Ceratium fusus*, Cgra — *Coscinodiscus granii*, Clac — *Chaetoceros laciniosus*, Clor — *Chaetoceros lorenzianus*, Cma — *Ceratium massiliense*, Cocu — *Coscinodiscus oculus-iridis*, Crad — *Coscinodiscus radiatus*, Ctor — *Chaetoceros tortissimum*, Ctri — *Ceratium trichoceros*, Ctrip — *Ceratium tripos*, Cwai — *Coscinodiscus wailesii*, Dbri — *Ditylum brightwelli*, Gfla — *Guinardia flaccida*, Gstr — *Guinardia striata*, Hsin — *Hemiaulus sinensis*, Lann — *Lauderia annulata*, Ldan — *Leptocylindrus danicus*, Lmin — *Leptocylindrus minimus*, Nlon — *Nitzschia longissima*, Omob — *Odontella mobiliensis*).

implies the stable and favorable condition of water parameters for phytoplankton. However, temperature, pH and salinity exhibited the maximum relationship with phytoplankton species indicating that light and salinity are the major source for supporting the phytoplankton species positively during summer (Cetin and Sen, 2004; Litchman, 2000; Richardson et al., 2000).

In premonsoon the variation explained by CCA analysis was 64% (Fig. 6). The variable that positively correlated in axis 2 were nitrite, pH, ammonia and salinity, DO, silicate had a negative correlation in the same axis. Chlorophyll-*a* and temperature were in a positive relationship in both axis 1 and 2, they explained the closer association with *C. wailesii*, *C. tripos*, *Ceratium breve*, *B. hyalinum*, *S. costatum*. However, some species were negatively correlated in axis 2 with salinity and inorganic phosphate (*A. glacialis*, *C. diversus*, *Odontella mobilensis*, *C. tripos)*. In axis 1 diatoms and dinoflagellates exhibited both positive and negative correlation, especially species of dinoflagellates (*Ceratium massilensis*, *C. breve*, *C. furca*, *Ceratium fusus*, *C. tripos*, *Ceratium trichoceros*) explained very strong positive association by having high canonical values of 0.500, 0.643, 0.659, 0.677, 0.615, and 0.640 respectively. This must be due to the favorable intermediate salinity values and moderate nutrient concentrations that might have favorably increased their abundance during premonsoon (Kannan, 1980; Mani et al., 1986; Mani, 1992; Perumal et al., 1999).

As for postmonsoon, the variation explained by CCA ordination was 57% (Fig. 6), the main environmental parameters which had a positive correlation with axis 1 and 2 were salinity, DO, chlorophyll-*a*, ammonia, SSC and inorganic phosphate. Silicate showed a positive and a negative correlation in axis 1 and 2, genera like *Leptocylindrus danicus*, *Thalassionema nitzschioides*, *Coscinodiscus centralis*, *S. costatum*, *Stephanopyxis palmeriana* were in the negative relation with silicate. Species like *Guinardia striata*, *A. glacialis*, *Rhizosolenia shurbsolei*, *Bacteriastrum delicatulum*, *B. hyalinum*, *C. diversus* found to have the positive

correlation with salinity in axis 1 whereas in axis 2 species such as *Ceratium massiliense*, *C. breve*, *C. fusus*, *C. furca*, *Chaetoceros compressus*, *Bacteriastrum variance* were having a close association with IP. This result confirms with Rajkumar et al. (2012) observation with presence of similar species in abundance during postmonsoon and he also reported that high nutrient input caused by northeast monsoon rainfall might have contributed in their abundance. The same observation also reported during postmonsoon season by several authors (Kannan, 1980; Mani et al., 1986). Both diatom and dinoflagellates showed a positive and negative relationship with different environmental variable but most of the species showed a significant positive relationship in axis 2 with IP, and salinity. This confirms that IP and salinity plays a vital role in phytoplankton abundance and composition (Thangaradjou et al., 2012). On the contrary the dinoflagellate species (*C. breve*, *C. furca*, *C. fusus*, *C. tripos*, *C. trichoceros*) which had a high positive relationship in premonsoon showed a significant negative correlation in axis 2. This implies that the shift in physico-chemical parameters can dramatically change the species composition and abundance.

During monsoon the variation explained by CCA in first two axes was 53% (Fig. 6) ammonia, DO, nitrate, IP in axis 1 and temperature, salinity, silicate in axis 2 had positive and negative correlations in CCA biplot, implying the influence of freshwater on contributing hydrochemical parameters. Species such as *Coscinodiscus cf. asteromphalus*, *C. diversus*, *C. lorenzianus*, *C. centralis*, *C. granii*, *L. minimus* were positively correlated with temperature, silicate, nitrite in axis 1, and few species of phytoplankton (*T. nitzschioides*, *D. brightwelli*, *Triceratium cf. broecii*) were negatively correlated with salinity in the same axis. In axis 1 most of the species were in negative correlation with high canonical values especially genera like *A. glacialis* (−0.921), *B. delicatulum* (−1.038), *C. tripos* (−0.703), *Chaetoceros affinis* (−1.091), *C. atlanticus* (−0.986), *C. compressus* (−0.898), *C. decipiens* (−1.174), *C. diversus* (−0.627), *Chaetoceros tortissum* (−1.047), and *Coscinodiscus asteromphaus* (−0.588). This pattern clearly shows that less temperature and salinity results in scarce phytoplankton diversity and abundance. The revealed results coincide with the earlier investigation as monsoon season causes dramatic changes in environmental parameters due to heavy freshwater discharges and high turbidity thereby reduces the phytoplankton diversity and abundance (Rajkumar et al., 2009; Vengadesh et al., 2009). Similarly, high positive association with DO and ammonia indicates the freshwater influence and high organic matters.

The CCA executed on the phytoplankton data in the preset study revealed that the abundance of phytoplankton was dynamic and was controlled mainly by temperature, DO, salinity, inorganic phosphate and silicate. In CCA analysis, several phytoplankton species showed a significant positive relationship with environmental parameters irrespective to season specifically centric diatoms such as *A. glacialis*, *B. delicatulum*, *B. hyalinum*, *C. decipiens*, *C. diversus*, and *S. costatum* implying their persistent nature and high tolerance to wide variation in environmental parameters. Similarly, earlier investigations also reported the occurrence of these diatom species in all the season (Kobayashi and Takahashi, 2002; Paul et al., 2008). In the present investigation phytoplankton showed a positive correlation with salinity during summer and had a negative correlation in premonsoon and monsoon, implying that the estuarine regions are subjected to considerable fluctuations in environmental parameters, which enable phytoplankton to adapt such dynamic environment (Lionard et al., 2005). Phosphate and nitrogen are crucial chemical elements for phytoplankton survival (Dawes, 1981). In CCA, inorganic phosphate showed a high positive correlation in all the seasons except, premonsoon. This could be due to less concentration of IP or rapid recycling. Similar results have been stated by Steinhart et al. (2002), Hergenrader (1980). However, certain species restricted their abundance to a particular season. For example *pseudo nitzschia seriata* species proliferated abundantly during premonsoon season which implies that suitable nutrient availability for their growth on premonsoon. Similarly, CCA result for dinoflagellate species showed a positive and negative correlation in premonsoon and postmonsoon season implying the seasonal shift of physico-chemical parameters influence their occurrence and abundance. A similar scenario was observed in the Bay of Bengal with particular species as it appeared to be seasonally dominant (Paul et al., 2008). In addition, it had a high tolerance to large variation in environmental parameters (Bonilla et al., 2005). It is evidenced from CCA results that the environmental parameters played a vital role in phytoplankton abundance and species composition and influence the occurrence of phytoplankton species with respect to seasonal changes in physico-chemical parameters.

4. Conclusion

The present investigation summarizes the seasonal fluctuations in physico-chemical parameters and phytoplankton diversity at Parangipettai coastal waters seasonally. Parangipettai waters are highly subjective to riverine freshwater influence as the Vellar estuary debouches in the Bay of Bengal. The addition of nutrients such as nitrate and silicate to the coastal waters are mainly during monsoon season. Introduction of the high organic load during monsoon season containing phosphate, silicate, and nitrate plays the substantial role in phytoplankton growth in the forthcoming seasons, which helps the phytoplankton to avail the nutrients and proliferate. It is clearly evidenced from ANOVA that the nutrients have significant variation between seasons and substantially influenced the phytoplankton diversity and abundance. Phytoplankton diversity is highly dynamic depending on the nutrient availability which is clearly explained by Canonical Correspondence Analysis in the present study. From CCA biplot, it is clear that temperature, salinity, silicate, DO and IP played a tremendous role in phytoplankton growth and abundance. Thus, the overall study gives a good outline of the seasonal dynamic relationship between phytoplankton and environmental parameters.

Funding

This study was funded by Indian National Centre for Ocean Information Service (grant number: INCOIS:F&A: XII:A1:028).

Acknowledgments

The authors would like to thank Dean and Director of CAS in Marine Biology and authorities of Annamalai University for providing facilities. We would like to express deep gratitude to Indian National Centre for Ocean Information Service for providing us financial support.

References

Al-Kandari, M., Al- Yamani, F.Y., Al-Rifaie, K., 2009. Marine Phytoplankton Atlas of Kuwait's Waters. Kuwait Inst. Sci. Res., Safar, 351 pp.

Ariyadej, C., Tansakul, R., Tansakul, P., Angsupanich, S., 2004. Phytoplankton diversity and its relationships to the physicochemical environment in the Banglang reservoir, Yala province. Songklahnakarin J. Sci. Technol. 26 (5), 595—607.

Babu, A., Varadharajan, D., Vengadesh, P.N., Thilagavathi, B., Manikandarajan, T., Sampathkumar, P., Balasubramanian, T., 2013. Diversity of phytoplankton in different stations from Muthupettai, South east coast of India. J. Mar. Sci.: Res. Dev. 3 (3), http://dx.doi.org/10.4172/2155-9910.1000128 128 pp.

Barić, A., Marasović, I., Gačić, M., 1992. Eutrophication phenomenon with special reference to the Kaštela Bay. Chem. Ecol. 6 (1—4), 51—68, http://dx.doi.org/10.1080/02757549208035262.

Bonilla, S., Conde, D., Aubriot, L., Perez, M.D.C., 2005. Influence of hydrology on phytoplankton species composition and life strategies in a subtropical costal lagoon periodically connected with the Atlantic Ocean. Estuaries 28 (6), 884—895, http://dx.doi.org/10.1007/BF02696017.

Brettum, P., Andersen, T., 2005. The Use of Phytoplankton as Indicators of Water Quality. NIVA Rep. SNO 4818-2004, 33 pp.

Cetin, A.K., Sen, B., 2004. Seasonal distribution of phytoplankton in Orduzu Dam Lake (Malatya, Turkey). Turk. J. Bot. 28 (3), 279—285.

Chang, H., 2008. Spatial analysis of water quality trends in the Han River basin, South Korea. Water Res. 42 (13), 3285—3304, http://dx.doi.org/10.1016/j.watres.2008.04.006.

Chattopadhyay, J., Sarkar, R.R., Pal, S., 2003. Dynamics of nutrient—phytoplankton interaction in the presence of viral infection. Biosystems 68 (1), 5—17.

Choudhury, S.B., Panigrahy, R.C., 1991. Seasonal distribution and behavior of nutrients in the Greek and coastal waters of Gopalpur, East coast of India. Mahasagar — Bull. Natl. Inst. Oeanogr. 24 (2), 88—91.

Cole, C.V., Sanford, R.L., 1989. Biological aspects of the Phosphorus cycle. In: Proceedings of a Symposium "Phosphorous requirements for sustainable agriculture in Asia and Oceania March 6—10 1989". SCOPE/UNEP, 1989, Int. Rice Res. Inst. 497 pp.

Crossetti, L.O., Bicudo, D.C., Bicudo, C.E.M., Bini, L.M., 2008. Phytoplankton biodiversity changes in a shallow tropical reservoir during the hypertrophication process. Braz. J. Biol. 68 (4), 1061—1067, http://dx.doi.org/10.1590/S1519-69842008000500013.

Das, J., Das, S.N., Sahoo, R.K., 1997. Semidiurnal variation of some physicochemical parameters in the Mahanadi estuary, east coast of India. Indian J. Mar. Sci. 26 (3), 323—326.

Davis, J.C., 1975. Minimal dissolved oxygen requirements of aquatic life with emphasis on Canadian species. Rev. J. Fish. Res. Board Canada 32 (12), 2295—2332.

Dawes, C.J., 1981. Marine Botany. Wiley & Sons, New York, 496 pp.

Dehradrai, P.V., Bhargava, R.M.S., 1972. Distribution of chlorophyll, carotenoids and phytoplankton in relation to certain environmental factors along the central west coast of India. Mar. Biol. 17 (1), 30—37.

Dugdale, R.C., 1967. Nutrient limitation in the sea: dynamics, identification, and significance. Limnol. Oceanogr. 12 (4), 685—695, http://dx.doi.org/10.4319/lo.1967.12.4.0685.

Dugdale, R.C., Wilkerson, Hogue, V.E., Marchi, A., 2007. The role of ammonium and nitrate in spring bloom development in San Francisco Bay. Est. Coast. Shelf. Sci. 73 (1—2), 17—29, http://dx.doi.org/10.1016/j.ecss.2006.12.008.

Dupuis, A., Hann, B.J., 2009. Warm spring and summer water temperatures in small eutrophic lakes of the Canadian prairies: potential implications for phytoplankton and zooplankton. J. Plankton. Res. 31 (5), 489—502, http://dx.doi.org/10.1093/plankt/fbp001.

Durate, P., Macedo, M.F., Da Fonseca, L.C., 2006. The relationship between phytoplankton diversity and community function in a coastal lagoon. Hydrobiologia 183, 3—18, http://dx.doi.org/10.1007/1-4020-4697-9_1.

Falkowski, P.G., Fenchel, T., Delong, E.F., 2008. The microbial engines that drive Earth's biogeochemical cycles. Science 320 (5879), 1034—1039, http://dx.doi.org/10.1126/science.1153213.

Field, C.B., Behrenfeld, M.J., Randerson, J.T., Falkowski, P., 1998. Primary production of the biosphere: integrating terrestrial and oceanic components. Science 281 (5374), 237—240, http://dx.doi.org/10.1126/science.281.5374.237.

Gouda, R., Panigrahy, R.C., 1995. Seasonal distribution and behavior of nitrate and phosphate in Rushikulya estuary, East coast of India. Indian J. Mar. Sci. 24 (4), 233—235.http://nopr.niscair.res.in/handle/123456789/37362.

Gouda, R., Panigrahy, R.C., 1996. Ecology of phytoplankton in coastal waters off Gopalpur, east coast of India. Indian J. Mar. Sci. 25 (2), 81—84.http://nopr.niscair.res.in/handle/123456789/37094.

Govindasamy, C., Kannan, L., Jayapaul, A., 2000. Seasonal variation in physico-chemical properties and primary production in the coastal water biotopes of Coramandal coast, India. J. Environ. Biol. 21 (1), 17.

Guinder, V.A., López-Abbate, M.C., Berasategui, A.A., Negrin, V.L., Zapperia, G., Pratolongo, P.D., Fernández Severini, M.D., Popovich, C.A., 2015. Influence of the winter phytoplankton bloom on the settled material in a temperate shallow estuary. Oceanologia 57 (1), 50—60, http://dx.doi.org/10.1016/j.oceano.2014.10.002.

Hergenrader, G.L., 1980. Eutrophication of the salt valley reservoirs, 1968—1973 II. Changes in physical and chemical parameters of eutrophication. Hydrobiologia 74 (3), 225—240, http://dx.doi.org/10.1007/BF00008756.

Hutchinson, G.E., 1957. Concluding remarks. CSH Sympos. 22, 415—457, http://dx.doi.org/10.1101/SQB.1957.022.01.039.

Jyothibabu, R., Madhu, N.V., Maheswaran, P.A., Jayalakshmy, K.V., Nair, K.K.C., Achuthankutty, C.T., 2008. Seasonal variation of microzooplankton (20200 μm) and its possible implications on the vertical carbon flux in the western Bay of Bengal. Cont. Shelf. Res. 28 (6), 737—755.

Kannan, L., 1980. Hydrobiological studies in nearshore and estuarine waters of Portonovo (India) with special reference to diatoms. (Ph.D. thesis). Annamalai Univ., India, 120 pp.

Khan, T.A., 2003. Limnology of four saline lakes in western Victoria, Australia. Limnologica 33 (4), 327—339, http://dx.doi.org/10.1016/S0075-9511(03)80027-0.

Kobayashi, F., Takahashi, K., 2002. Distribution of diatoms along equatorial transect in the western and central Pacific during La Niña conditions. Deep-Sea Res. Pt. II 49 (13—14), 2801—2821, http://dx.doi.org/10.1016/S0967-0645(02)00059-0.

Legović, T., Žutić, V., Gržetić, Z., Cauwet, G., Precali, R., Viličić, D., 1994. Eutrophication in the Krka estuary. Mar. Chem. 46 (1—2), 203—215, http://dx.doi.org/10.1016/0304-4203(94)90056-6.

Levinton, J.S., 2001. Marine Biology. Chapter 4 — The Chemical and Physical Environment. Oxford Univ. Press, New York, 560 pp.

Lionard, M., Muylaert, K., Gansbeke, V., Vyverman, W., 2005. Influence of changes in salinity and light intensity on growth of phytoplankton communities from the Scheldt River and estuary (Belgium/The Netherlands). Hydrobiologia 540 (1—3), 105—115, http://dx.doi.org/10.1007/s10750-004-7123-x.

Lipschultz, F., 1995. Nitrogen- specific uptake rates of marine phytoplankton isolated from natural populations of particles by flow

cytometry. Mar. Ecol.-Prog. Ser. 123, 245—258, http://dx.doi.org/10.3354/meps123245.

Litchman, E., 2000. Growth rates of phytoplankton under fluctuating light. Freshw. Biol. 44 (2), 223—235, http://dx.doi.org/10.1046/j.1365-2427.2000.00559.x.

Madhu, N.V., Jyothibabu, R., Balachandran, K.K., Honey, U.K., Martin, G.D., Vijay, J.G., Shiyas, C.A., Gupta, G.V.M., Achuthankutty, C.T., 2007. Monsoonal impact on planktonic standing stock and abundance in a tropical estuary (Cochin Backwaters—India). Estuar. Coast. Shelf Sci. 73 (1—2), 54—64.

Mani, P., 1992. Natural phytoplankton communities in Pichavaram mangroves. Indian J. Mar. Sci. 21 (4), 278—280.http://nopr.niscair.res.in/handle/123456789/38123.

Mani, P., Krishnamurthy, K., Palaniappan, R., 1986. Ecology of phytoplankton blooms in the Vellar estuary, east coast of India. Indian J. Mar. Sci. 15 (1), 24—28.http://nopr.niscair.res.in/handle/123456789/38590.

Marasović, I., Pucher-Petković, T., 1985. Effect of eutrofication on the structure of the coastal phytoplankton community. Rapp. Comm. Int. Mer. Medit. 29 (9), 137—139.

McQuatters-Gollop, A., Gilbert, A.J., Mee, L.D., Vermaat, J.E., Artioli, Y., Humborg, C., Wulff, F., 2009. How well do ecosystem indicators communicate the effects of anthropogenic eutrophication? Estuar. Coast. Shelf Sci. 82 (4), 583—596, http://dx.doi.org/10.1016/j.ecss.2009.02.017.

Menon, N.N., Balchand, A.N., Menon, N.R., 2000. Hydrobiology of the Cochin backwater system — a review. Hydrobiologia 430 (1—3), 149—183, http://dx.doi.org/10.1023/A:10040334.

Morgan, A.M., Royer, T.V., David, M.B., Gentry, L.E., 2006. Relationships among nutrients, chlorophyll-*a*, and dissolved oxygen in agricultural streams in Illinois. J. Environ. Qual. 35, 1110—1117, http://dx.doi.org/10.2134/jeq2005.0433.

Ninčević-Gladan, Ž., Bužančić, M., Kušpilić, G., Grbec, B., Matijević, S., Skejić, S., Marasović, I., Morović, M., 2015. The response of phytoplankton community to anthropogenic pressure gradient in the coastal waters of the eastern Adriatic Sea. Ecol. Indic. 56, 106—115, http://dx.doi.org/10.1016/j.ecolind.2015.03.018.

Oksanen, J., Blanchet, F.G., Friendly, M., Kindt, R., Legendre, P., McGlinn, D., Minchin, P.R., O'Hara, R.B., Simpson, G.L., Solymos, P., Stevens, M.H.H., Szoecs, E., Wagner, H., 2016. R Package Version 2.4-0. Vegan: Community Ecology Package, https://cran.r-project.org.

Paul, J.T., Ramaiah, N., Sardessai, S., 2008. Nutrient regimes and their effect on distribution of phytoplankton in the Bay of Bengal. Mar. Environ. Res. 66 (3), 337—344, http://dx.doi.org/10.1016/j.marenvres.2008.05.007.

Perumal, P., Sampathkumar, P., Santhanam, P., 1998. Zoopalnkton of Parangipettai Coastal Waters. Monogr. Ser., Vol. 1: UGC-SAP, CAS in Marine Biology. Annamali Univ., Parangipettai, 31 pp.

Perumal, P., Sampathkumar, P., Karuppasamy, P.K., 1999. Studies on the bloom forming species of phytoplankton in the Vellar estuary, southeast coast of India. Indian J. Mar. Sci. 28 (4), 400—403.

Perumal, N.V., Rajkumar, M., Perumal, P., Rajasekar, K.T., 2009. Seasonal variations of plankton diversity in the Kaduviyar estuary, Nagapattinam, southeast coast of India. J. Environ. Biol. 30 (6), 1035—1046.

Pielou, E.C., 1966. Species-diversity and pattern-diversity in the study of ecological succession. J. Theor. Biol. 10 (2), 370—383.

Prabhahar, C., Saleshrani, K., Dhanasekaran, D., Tharmaraj, K., Baskaran, K., 2011. Seasonal variations in physico-chemical parameters of Nagapattinam Coastal area, Tamil nadu, India. Int. J. Curr. Life Sci. 1 (6), 29—32.

Rajasegar, M., Srinivasan, M., Rajaram, R., 2000. Phytoplankton diversity associated with the shrimp farm development in Vellar estuary, south India. Seaweed Res. Utiln. 22 (1—2), 125—213.

Rajasegar, M., Sirnivasan, M., Ajmal Khan, S., 2002. Distribution of sediment nutrients of Vellar estuary in relation to shrimp farming. Indian J. Mar. Sci. 31 (2), 153—156.

Rajasekar, K., Thillai, R.M., Jun, S., Ashok Prabu, V., Perumal, P., 2010. Seasonal variations of phytoplankton diversity in the Coleroon coastal waters, southeast coast of India. Acta Oceanol. Sin. 29 (5), 97—108.

Rajkumar, M., Perumal, P., Ashok, P.V., Vengadesh, Perumal, N., Thillai Rajasekar, K., 2009. Phytoplankton diversity in pichavaram mangrove waters from south east coast of india. J. Environ. Biol. 30 (4), 489—498.

Rajkumar, M., Jankinson, I.R., Sun, J., Pachiappan, P., 2012. Phytoplankton diversity in the Parangipettai coastal waters, southeast coast of India. J. Environ. Biol. 33 (6), 1115—1125.

Rakhesh, M., Raman, A.V., Ganesh, T., Chandramohan, P., 2013. Small copepods structuring mesozooplankton community dynamics in a tropical estuary-coastal system. Estuar. Coast. Shelf Sci. 126 (7), 7—22, http://dx.doi.org/10.1016/j.ecss.2013.03.025.

Rhyther, J.H., Dunstan, W.M., 1971. Nitrogen, phosphorous and eutrophication in the coastal marine environment. Science 171 (3975), 1008—1013.

Richardson, T.L., Gibson, C.E., Heaney, S.I., 2000. Temperature, growth and seasonal succession of Phytoplankton in Lake Baikal, Siberi. Freshw. Biol. 44 (3), 431—440, http://dx.doi.org/10.1046/j.1365-2427.2000.00581.x.

Sahu, G., Satpathy, K.K., Mohanty, A.K., Sarkar, S.K., 2012. Variations in community structure of phytoplankton in relation to physicochemical properties of coastal waters, southeast coast of India. Indian J. Geo-Mar. Sci. 41 (3), 223—241.

Santhanam, P., Perumal, P., 2003. Diversity of zooplankton in Parangipettai coastal waters, Southeast coast of India. J. Mar. Biol. Assoc. India 45 (2), 144—151.

Santhanam, R., Ramanathan, N., Venkataramanuja, K.V., Jegatheesan, G., 1987. Phytoplankton of the Indian Seas: An Aspect of Marine Botany. Daya Publ., House, Delhi, 127 pp.

Santhosh Kumar, C., Perumal, P., 2012. Studies on phytoplankton characteristics in Ayyampattinam coast. Indian J. Environ. Biol. 33 (3), 585—589.

Saravanakumar, A., Rajkumar, M., Serebiah, J.S., Thivakaran, G.A., 2008. Seasonal variations in physico-chemical characteristics of water, sediment and soil texture in arid zone mangroves of Kachchh-Gujarat. J. Environ. Biol. 29 (5), 725—732.

Sardessai, S., Ramaiah, N., Prasanna Kumar, S., De Souza, S.N., 2007. Influence of environmental forcings on the seasonality of dissolved oxygen and nutrients in the Bay of Bengal. J. Mar. Res. 65 (2), 301—316. http://drs.nio.org/drs/handle/2264/623.

Satpathy, K.K., Sahu, G., Mohanty, A.K., Prasad, M.V.R., Panigrahy, R.C., 2009. Phytoplankton community structure and its variability during southwest to northeast monsoon transition in the coastal waters of Kalpakkam, east coast of India. Int. J. Oceans Oceanogr. 3 (1), 43—74.

Segar, K., Hariharan, V., 1989. Seasonal distribution nitrate, nitrite, ammonia and plankton in effluent discharge area of Mangalore, west coast of India. Indian J. Mar. Sci. 18 (3), 170—173. http://nopr.niscair.res.in/handle/123456789/38360.

Senthilkumar, S., Santhanam, P., Perumal, P., 2002. Diversity of phytoplankton in Vellar estuary, southeast coast of India. In: Ayyappan, S., Jena, J.K., Mohan, J.M. (Eds.), Proc. 5th Indian Fisheries Forum, AFSIB, Mangalore & AeA, Bhubaneswar, India, 245—248.

Senthilkumar, B., Purvaja, R., Ramesh, R., 2008. Seasonal and tidal dynamics of nutrients and chlorophyll *a* in a tropical mangrove estuary, southeast coast of India. Indian J. Mar. Sci. 37 (2), 132—140.

Shannon, C.E., Wiener, W., 1949. The Mathematical Theory of Communication. Univ. Illinois Press, Urbana, 125 pp.

Shashi Shekhar, T.R., Kiran, B.R., Puttaiah, E.T., Shivaraj, Y., Mahadevan, K.M., 2008. Phytoplankton as index of water quality with reference to industrial pollution. J. Environ. Biol. 29 (2), 233—236.

Sin, Y., Wetzel, L.R., Anderson, C.I., 1999. Spatial and temporal characteristic of nutrient and phytoplankton dynamics In the York

River Estuary, Virginia. Analysis of long-term data. Estuaries 22 (2), 260—275, http://dx.doi.org/10.2307/1352982.

Siva Sankar, R., Padmavathi, G., 2012. Species composition, abundance and distribution of phytoplankton in the harbour areas and coastal waters of Port Blair, South Andaman. Int. J. Oceanogr. Mar. Ecol. Syst. 1 (3), 76—83, http://dx.doi.org/10.3923/ijomes.2012.76.83.

Skejić, S., Bojanić, N., Matijević, S., Vidjak, O., Grbec, B., Ninčević-Gladan, Ž., Šestanović, S., Šantić, D., 2014. Analysis of the phytoplankton community in the vicinity of domestic sewage outflow during stratified conditions. Mediterr. Mar. Sci. 15 (3), 574—586, http://dx.doi.org/10.12681/mms.866.

Smayda, T.J., 1980. Phytoplankton species succession. In: Morris, I. (Ed.), Physiological Ecology of Phytoplankton. Univ. California Press, Berkeley, 493—570.

Smith, D.L., 1977. A Guide to Marine Coastal Plankton and Marine Invertebrate Larvae. Kendal/Hunt Publ. Co., Dubuque, 16 pp.

Soundarapandian, P., Preamkumar, T., Dinakaran, G.K., 2009. Studies on the phyisco- chemical characteristics and nutrients in the Uppanar estuary of Cuddalore, south east coast of India. Curr. Res. J. Biol. Sci. 1 (3), 102—105.

Spatharis, S., Danielidis, D.B., Tsirtsis, G., 2007. Recurrent *Pseudo-nitzschia calliantha* (Bacillariophyceae) and *Alexandrium insuetum* (Dinophyceae) winter blooms induced by agricultural runoff. Harmful Algae 6 (6), 811—822, http://dx.doi.org/10.1016/j.hal.2007.04.006.

Sridhar, R.T., Thangaradjou, S., Senthil Kumar, Kannan, L., 2006. Water quality and phytoplankton characteristics in the Palk Bay, Southeast coast of India. J. Environ. Biol. 27 (3), 561—566.

Steinhart, G.S., Likens, G.E., Soto, D., 2002. Physiological indicators of nutrient deficiency in phytoplankton in southern Chilean lakes. Hydrobiologia 489 (1—3), 21—27.

Strickland, J.D.H., Parsons, T.R., 1972. A Practical Hand Book of Seawater Analysis, 2nd ed. Fish. Res. Board Canada, Ottawa, 310 pp.

Su, J., Tian, T., Krasemann, H., Schartau, M., Wirtz, K., 2015. Response patterns of phytoplankton growth to variations in resuspension in the German Bight revealed by daily MERIS data in 2003 and 2004. Oceanologia 57 (4), 328—341, http://dx.doi.org/10.1016/j.oceano.2015.06.001.

Subramanian, B., Mahadevan, V., 1999. Seasonal and diurnal variations of hydro biological characters of coastal waters of Chennai (Madras) Bay of Bengal. Indian J. Mar. Sci. 28 (4), 429—433.

Subramanyan, R.A., 1946. Systematic account of marine plankton diatoms of Madras Coast. Proc. Indian Acad. Sci. 24 (4), 85—197, http://www.ias.ac.in/j_archive/procb/24/4/85-197/viewpage.html.

Sukumaran, M., Muthukumaravel, K., Sivakami, R., 2013. Seasonal variation in physico-chemical characteristics of Agniar Estuary, Southeast Coast of India. Asia Pac. J. Res. 2 (8), 108—120, http://apjor.com/files/1376844720.pdf.

Thangaradjou, T., Vijayanaskara, S.G., Raja, S., Poornimaa, D., Shanthia, R., Balasubramaniana, T., Babub, K.N., Shuklab, A. K., 2012. Influence of environmental variables on phytoplankton floristic pattern along the shallow coasts of southwest Bay of Bengal. Algal Res. 1 (2), 143—154, http://dx.doi.org/10.1016/j.algal.2012.07.005.

Thangaradjou, T., Sarangi, R.K., Shanthi, R., Poornima, D., Raja, K., Saravanakumar, A., 2013. Changes in nutrients ratio along the central Bay of Bengal coast and its influence on chlorophyll distribution. J. Environ. Biol. 35 (3), 467—477.

Thillai Rajsekar, K., Perumal, P., Santhanam, P., 2005. Phytoplankton diversity in the Coleroon estuary, southeast coast of India. J. Mar. Biol. Assoc. India 47 (2), 127—132.

Vengadesh Perumal, N., Rajkumar, M., Perumal, P., Thillai Rajasekar, K., 2009. Seasonal variations of plankton diversity in the Kaduviyar estuary, Nagapattinam, southeast coast of India. J. Environ. Biol. 30 (6), 1035—1046.

Venkataraman, G.A., 1939. Systematic account of some South Indian diatoms. Proc. Indian Acad. Sci. 10, 293—368.

Vinayachandran, P.N., Murty, V.S.N., Ramesh Babu, V., 2002. Observations of barrier layer formation in the Bay of Bengal. J. Geophys. Res. 107 (12), 1—14, http://drs.nio.org/drs/handle/2264/1362.

Wickham, H., 2009. ggplot2: Elegant Graphics for Data Analysis, Springer-Verlag, New York, 213 pp., http://dx.doi.org/10.1007/978-0-387-98141-3.

Oceanologia (2018) 60, 128—138

Available online at www.sciencedirect.com

ScienceDirect

journal homepage: www.journals.elsevier.com/oceanologia/

ORIGINAL RESEARCH ARTICLE

Composition and diel vertical distribution of euphausiid larvae (calyptopis stage) in the deep southern Adriatic

Barbara Gangai Zovko [a,*], Davor Lučić [a], Marijana Hure [a], Ivona Onofri [a], Branka Pestorić [b]

[a] *University of Dubrovnik, Institute for Marine and Coastal Research, Dubrovnik, Croatia*
[b] *Institute of Marine Biology in Kotor, Kotor, Montenegro*

Received 20 February 2017; accepted 14 September 2017
Available online 6 October 2017

KEYWORDS
Euphausiid larvae;
Mediterranean Sea;
Secondary production;
Vertical distribution;
Weighted mean depth

Summary Diel changes in the vertical distribution and abundance of calyptopes were studied in the deepest area of the southern Adriatic over four seasons (July 2003, February 2004, October 2004, April 2009). Temperature variations were limited to the upper 100 m and salinity variations were small. Of previously known adult euphausiid species — 12 for the Adriatic (Gangai et al., 2012) and 13 for the Mediterranean (Mavidis et al., 2005) — calyptopes of 11 species of euphausiids were recorded. Abundance of calyptopes of all species was the highest in spring. Species were characterized according to their mean depth: surface (0—50 m), sub-surface (50—200 m), mesopelagic (200—800 m), or bathypelagic (800—1200 m) and vertical dispersion (scattered or non-scattered). Four diel patterns emerged: (i) nocturnal ascent to upper layers (*Euphausia brevis*, *E. hemigibba*, *E. krohnii*, *Nematoscelis megalops*, *N. couchii*), (ii) migration to upper layers at middle of the day and at night, and descent during the morning and evening (*Stylocheiron maximum* — only winter), (iii) weakly-migrating or non-migrating (*S. longicorne*), (iv) irregular migration independent of the day/night cycle (*S. abbreviatum*, *S. maximum* — during spring, summer and autumn, *T. aequalis*).

* Corresponding author at: University of Dubrovnik, Institute for Marine and Coastal Research, Kneza Damjana Jude 12, Dubrovnik, Croatia. Tel.: +385 20324728; fax: +0038520 32 38 72.
E-mail address: barbara.gangai@unidu.hr (B. Gangai Zovko).
Peer review under the responsibility of Institute of Oceanology of the Polish Academy of Sciences.

ELSEVIER Production and hosting by Elsevier

http://dx.doi.org/10.1016/j.oceano.2017.09.001

1. Introduction

The Adriatic Sea consists of two contrasting ecosystems: the Northern Adriatic, eutrophic shelf area where nutrients are supplied by lateral terrestrial inputs; and the Southern Adriatic, semicircular oligotrophic basin with depths to about 1200 m, influenced by water masses from the Ionian Sea. The most prominent bathymetry feature in the Adriatic is the South Adriatic Pit (SAP), which is preserving cyclonic circulation around its perimeter (Gačić et al., 2002). The SAP interacts with the Eastern Mediterranean through the Strait of Otranto (~800 m depth). Advection of saline Levantine Intermediate Water (LIW) alternates with low-salinity Modified Atlantic Water (MAW) that originates in the Western Mediterranean (Gačić et al., 2010; Vilibić et al., 2012) on a roughly 10-year cycle termed the Adriatic-Ionian Bimodal Oscillation or BiOS (Gačić et al., 2010). The low primary production, low chlorophyll *a*, and high temperatures in many oligotrophic environments favor heterotrophic plankton communities (Duarte et al., 2013). One such region, the phosphate-limited Eastern Mediterranean Sea (Krom et al., 2010; Siokou-Frangou et al., 2010), is the predominant influence on the open waters of the South Adriatic (Malanotte-Rizzoli et al., 1997). Being a temperate area, the Adriatic Sea is characterized by a strong seasonal variability of the phytoplankton biomass reaching a maximum in spring (Antoine et al., 1995) followed by zooplankton annual peak in this period (Benović et al., 2005; Hure et al., 1980; Kršinić, 1998). Picophytoplankton dominates the South Adriatic and appears to be its main primary producers (Najdek et al., 2014). Microphytoplankton production is restricted to lower-salinity, nutrient-rich coastal waters, the deep chlorophyll maximum, and periods during or following winter convection (Batistić et al., 2012; Cerino et al., 2012; Gačić et al., 2002). The microzooplankton is dominated by tintinnids (Fonda Umani and Monti, 1993). Herbivorous copepods are dominant in mesozooplankton community throughout the year, while carnivorous species are also better represented (Fonda Umani, 1996). The community of this area shows high diversity and greater stability.

Euphausiids play an important role in pelagic food webs. This is expressed by their substantial contribution to ocean biomass (Casanova, 2003; Mauchline and Fisher, 1969) and their diel vertical migrations that rapidly transport organic matter from the productive epipelagic zone to deeper layers (Harvey et al., 2009; Longhurst and Harrison, 1989; Longhurst et al., 1989). These migrations are modulated principally by light and temperature. It is not unusual that distribution varies during larval development because different stages require different nutritional and predator-avoidance needs (Spiridonov and Casanova, 2010).

Investigating only larvae instead of adults is sensible as these occur in high numbers and can be sampled reliably with planktonic nets. Also, data on Mediterranean euphausiids is largely restricted to older papers (Casanova, 1970, 1974; Casanova-Soulier, 1963; Franqueville, 1971; Mauchline and Fisher, 1969; Mavidis et al., 2005; Ruud, 1936; Trégouboff and Rose, 1957; Wiebe and D'Abramo, 1972) and relatively little attention has been paid to their developmental stages (Andersen et al., 1998; Brancato et al., 2001; Casanova, 1970, 1974; Gangai et al., 2012; McGehee et al., 2004). This data fills a knowledge gap in the Mediterranean Sea of larval euphausiid.

Investigations of the Adriatic Sea euphausiids thus far have been restricted to the deep South Adriatic Pit (~1200 m) and a limited area of the Jabuka Pit in the mid-Adriatic (~275 m). The first records of Adriatic euphausiids were by Ruud (1936) who identified 12 species in the southern section. Hure (1955, 1961) and Šipoš (1977a) later confirmed these findings. Guglielmo (1979) provided records from the deep Southern Adriatic using an Isaacs-Kidds mid-water trawl. The first data for euphausiid developmental stages are those of Gangai et al. (2012) who noted their importance in the secondary production of the oligotrophic Southern Adriatic and related furciliae and calyptopes migrations to extrapolated mean-depth light intensity. Diel differences in calyptopes numbers within designated depth layers were interpreted as an indication of the extent of diel vertical migration. Gangai et al. (2012) found larvae of 11 euphausiid species with first record of *Thysanoessa gregaria* previously reported only from the western and central Mediterranean (Brinton et al., 2000; Casanova, 1974; Mauchline and Fisher, 1969; Mavidis et al., 2005).

With euphausiids and their developmental stages among the least known elements of the Mediterranean and Adriatic holoplankton, the objectives of this study were to: (1) determine the composition and abundance of Adriatic calyptopes; (2) compare these with data from earlier investigations; (3) describe and explain any changes in the composition of Adriatic calyptopes; (4) identify the pattern of calyptopes diel and seasonal distribution over the four seasons. A key assumption is that seasonal samples collected at short intervals and at different times of day provide data with sufficient resolution to accomplish all stated research objectives. Depending on temperature and feeding, each calyptopis stage lasts a few days before molting. Another assumption is that all species whose calyptopes have been found in our samples spawn in deep Adriatic and their distribution is limited by depth.

2. Material and methods

2.1. Study area

Zooplankton was sampled at a single station (41°44′N 17°52′E, ~1200 m depth, Fig. 1) in the southern Adriatic Sea during four seasons (10 and 11 February 2004; 24 April 2009; 22, 23, 24, 25, 27 and 28 July 2003; 18 October 2004). This is the deepest part of the Adriatic and therefore the most representative place to study distribution of euphausiid larvae. Thirty-five sample series were collected (Table 1) with a Nansen opening-closing net (200 μm mesh, 113 cm diameter) at the following depth intervals: 0–15 (above the summer thermocline), 15–50, 50–100, 100–200, 200–400, 400–600, 600–800, and 800–1200 m. Some tows overlapped sunrise or sunset with day or night periods (Table 1). Average hauling speed of all tows was 0.5 m s^{-1}. Samples were preserved in a 4% formalin-seawater solution buffered with $CaCO_3$. Species were identified with an Olympus SZX-9 stereomicroscope.

2.2. Data analysis

Euphausiids pass through six developmental stages: egg, nauplius, metanauplius, calyptopis, furcilia, and postlarvae.

Figure 1 Location of the sampling station (shaded circle) in the Southern Adriatic.

Table 1 Time and frequency of zooplankton sampling together with sunrise and sunset times.

Date	Sampling time [h]	Sunrise and sunset [h]
10 February 2004	13:20–17:15, 19:10–22:40, 22:50–23:30	↑ 06:52 ↓ 17:12
11 February 2004	6:45–11:00, 13:45–16:35, 17:00–21:20, 21:25–21:50	↑ 06:51 ↓ 17:13
24 April 2009	4:10–8:00, 8:05–11:15, 15:10–18:20, 22:40–1:30	↑ 05:52 ↓ 19:40
24 April 2009	17:26–21:15, 22:18–1:45, 4:30–8:15	↑ 05:52 ↓ 19:40
22 July 2003	19:25–22:50	↑ 05:29 ↓ 20:19
23 July 2003	01:42–02:45, 06:25–9:30, 12:20–14:30, 15:45–17:40, 20:05–22:05	↑ 05:30 ↓ 20:18
24 July 2003	00:25–04:00, 06:00–9:00, 14:40–15:00, 18:30–22:20	↑ 05:31 ↓ 20:17
25 July 2003	01:15–02:30, 06:05–08:15	↑ 05:32 ↓ 20:16
27 July 2003	23:50–03:25, 05:45–09:00, 13:45–16:05	↑ 05:34 ↓ 20:14
28 July 2003	00:15–03:10, 05:50–08:00, 13:30–16:15	↑ 05:35 ↓ 20:13
18 October 2004	23:30–1:00, 8:30–11:25, 19:20–22:30	↑ 07:04 ↓ 18:00

There are three calyptopis stages: Ca I has functional mouthparts, as well as the first thoracic leg (maxilliped); Ca II has the beginning of a segmented abdomen; Ca III has the beginning of uropods and telson separated from the 6th abdominal somite. Owing to the small number of individuals collected, all three calyptopis stages were combined to analyze composition and calculate densities.

Abundance was expressed as number of individuals 100^{-3} of all found calyptopes species (Table 2). Identification followed Brinton et al. (2000), Casanova (1974) and Mauchline and Fisher (1969). A SeaBird OC25 probe was used to measure hydrographic properties and chlorophyll *a* concentrations for the whole water column. The probe is accurate to 0.01°C temperature, 0.003 salinity, and 0.5 m depth. The weighted mean depth (WMD) of all representative species was calculated as:

$$\mathrm{WMD} = \frac{\Sigma(n_i\, z_i\, d_i)}{\Sigma(n_i\, z_i)},$$

where d_i is the midpoint of the depth interval of a sample i, z_i is the thickness of the stratum, n_i is the number of individuals within each depth layer (ind. 100 m^{-3}).

Table 2 List of calyptopes in the South Adriatic and their abundance (number of individuals 100 m^{-3}) during investigated seasons.

Calyptopes (number of individuals 100 m^{-3})	Winter	Spring	Summer	Autumn
Euphausia brevis	321	40	80	0
Euphausia hemigibba	18	212	8	0
Euphausia krohnii	399	234	232	0
Meganyctiphane snorvegica	0	16	0	0
Nematoscelis megalops	17	46	3	0
Nyctiphanes couchii	12	194	194	0
Stylocheiron abbreviatum	16	94	224	58
Stylocheiron longicorne	1	0	128	16
Stylocheiron maximum	7	8	15	2
Thysanoessa gregaria	24	0	0	0
Thysanopoda aequalis	2470	2953	194	23

3. Results

3.1. Hydrographical conditions

In winter and spring, mean temperature decreased from less than 16°C at the surface to 13°C at the bottom (Fig. 2). Temperature was higher in summer and autumn: 23.5°C at the surface and 15°C below 50 m.

Salinity was higher in winter (38.50 at the surface and 38.98 at 400 m) and spring (38.4–39.06 at 200 m, Fig. 3) with small variations in summer (38.6 at the surface to 38.5 at the bottom) and autumn (38.7–38.8).

Chlorophyll (0.85 mg m^{-3}) was higher in the surface layer in winter and between 50 and 100 m in summer (0.83 mg m^{-3}, Fig. 4).

3.2. Calyptopes composition and abundance

Calyptopes of 11 euphausiid species were recorded (Table 2). Based on the frequency of occurrence, calyptopes were labeled as very rare (0.03–0.99%), rare (1–20%), common (21–70%), or very common (70–100%). The present work focused on the most abundant species, those classified as "very common" or "common". *Thysanopoda aequalis* calyp-

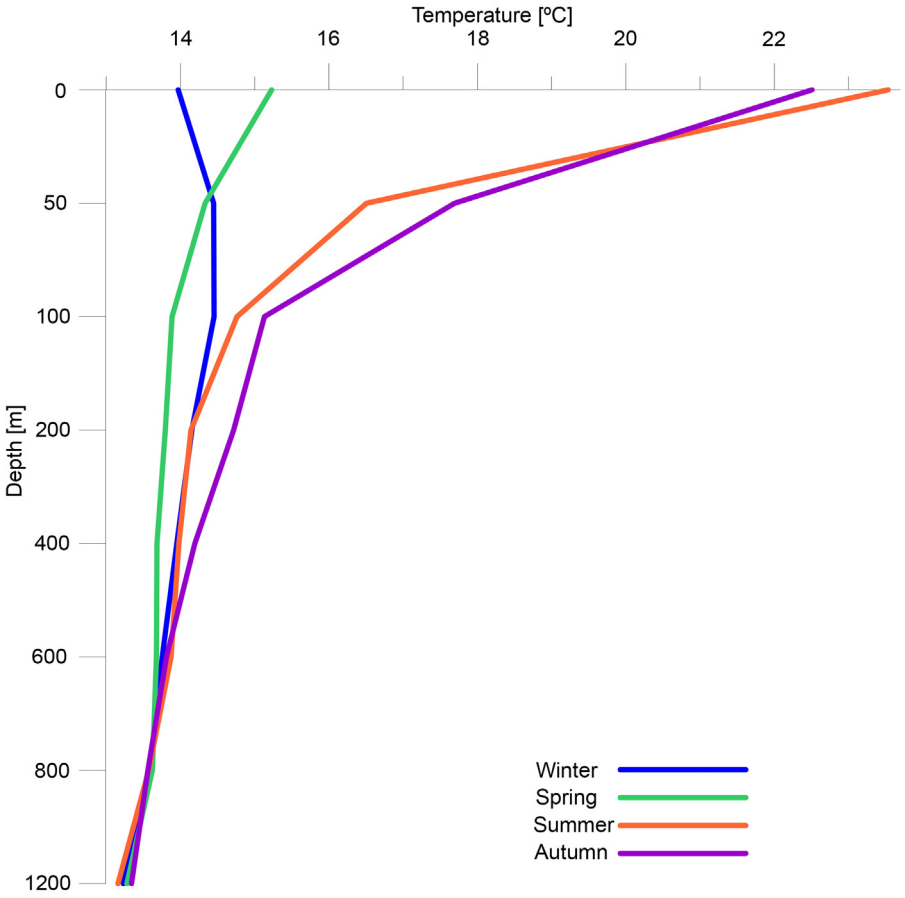

Figure 2 Vertical profile of seasonal temperature in the water column in the Southern Adriatic. Data represent average values.

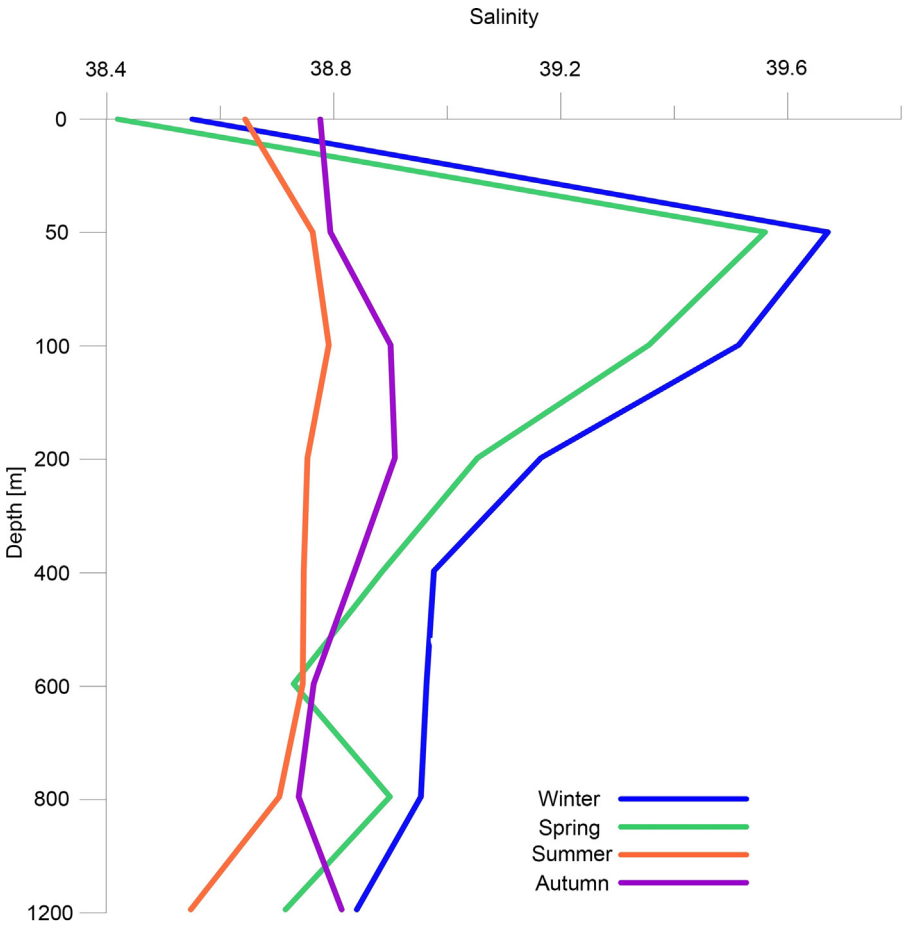

Figure 3 Vertical profile of seasonal salinity in the water column in the Southern Adriatic. Data represent average values.

topes were "very common": 80.54% in spring and 75.18% in winter. "Common" calyptopes included those of *Euphausia krohnii* (21.52%) and *Stylocheiron abbreviatum* (20.78%) in summer; and *S. abbreviatum* (58.58%) and *T. aequalis* (23.23%) in autumn. All other species were either "rare" or "very rare".

T. aequalis calyptopes were found in all seasons. They were dominant in spring (81%, 2954 ind. 100 m^{-3}), present at a high level in winter (75%, 2469 ind. 100 m^{-3}), and made smaller contributions in autumn (23%, 23 ind. 100 m^{-3}) and summer (18%, 194 ind. 100 m^{-3}). They were found at all times of the day throughout the water column in winter. No pronounced diel migration was observed. *T. aequalis* calyptopes were most numerous in evening and at night. Calyptopes were found in whole water column in the spring during night and morning, and below 100 m during the day. They were less numerous and scattered throughout the water column in summer and autumn (Fig. 5).

E. krohnii developmental stages were more numerous in winter (12%, 399 ind. 100 m^{-3}) and spring (5%, 208 ind. 100 m^{-3}). Their calyptopes inhabited the entire water column in winter, except between 400 and 600 m (Fig. 6). They were found between 50 and 400 m in the morning, remained there through the day, and were in the upper 200 m in the evening and at night. In spring, they were in upper 200 m of morning samples, descended to 100–400 m during the day, and rose to the surface at night (Fig. 6). Calyptopes were recorded in all layers except the deepest in summer. Higher relative abundances were found at the surface and in the 100–200 m layer.

Nyctiphanes couchii calyptopes were found in the winter, spring, and summer at 5.9%. In winter, calyptopes were found in the surface and bottom layers (Fig. 7) but were collected in all layers in spring. The aggregation was in the surface and sub-surface layers at night in spring. Most of the aggregation was between 50 and 200 m in the morning, although some remained in the bottom layer. During summer, calyptopes were found in the sub-surface in the evening and between 400 and 600 m at night.

S. abbreviatum calyptopes were present in all seasons (Fig. 8) but were more abundant in summer (21%, 224 ind. 100 m^{-3}). Two groups were distinguished in winter morning samples: one between 200 and 400 m and the other between 800 and 1200 m. Most migrated to the upper layer (50–100 m) during the day, but a small portion remained in each of the two aforementioned morning layers. There was some dispersion from 200 to 1200 m in the evening. The aggregation rose overnight but did not reach the upper 100 m. In spring, *S. abbreviatum* calyptopes were scattered in the morning, sank during the day, and migrated to 50–200 m at night. In summer during the day, most of the calyptopes aggregated in the 200–600 m layer; only a small

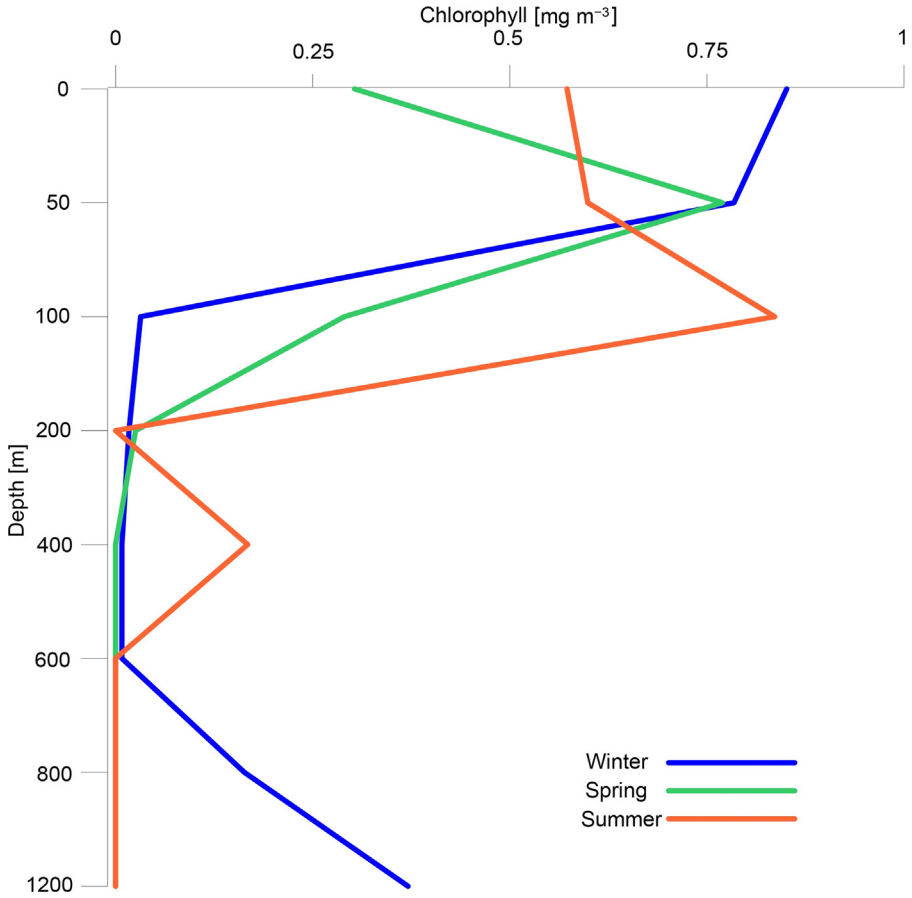

Figure 4 Vertical seasonal profile of chlorophyll *a* in the water column in the Southern Adriatic. Data represents average values.

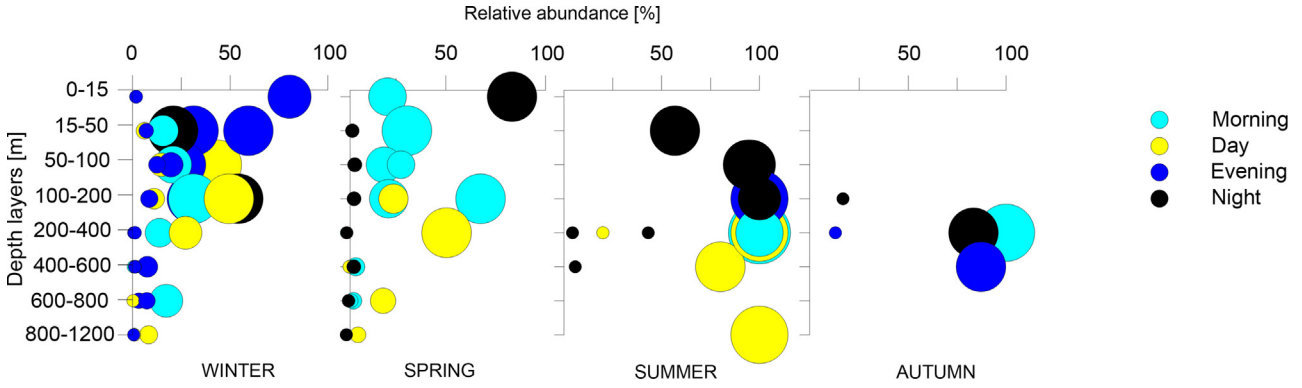

Figure 5 Vertical distribution of *Thysanopoda aequalis* calyptopes. Relative abundance on the upper axe represents percentage of calyptopes found in that layer. Bubble size indicates relative abundance of calyptopes during certain part of the day (from 1% till 100%) during one series of sampling in that layer.

fraction descended deeper. As in summer, in autumn calyptopes reached a maximum density between 200 and 600 m and exhibited only limited diel migrations.

The highest number of *Euphausia brevis* calyptopes was in winter (321 ind. 100 m^{-3}) when they undertook diel vertical migrations. Most of calyptopes inhabited the 50–400 m layer during the day (Fig. 9). At night, part of the calyptopes rose to the sub-surface layer and part descended to 200 m. During spring mornings they grouped at 100–200 m and migrated to the surface at night. In summer during the day they migrated from 100 to 600 m, with only a small part of the aggregation found at the surface.

3.3. Migration and depth distribution

Four calyptopes vertical migration patterns were identified in the Adriatic: (i) nocturnal ascent to upper layers (*E. brevis*, *E. hemigibba*, *E. krohnii*, *Nematoscelis megalops*, *Nyctiphanes couchii*); (ii) migration to upper layers in the middle

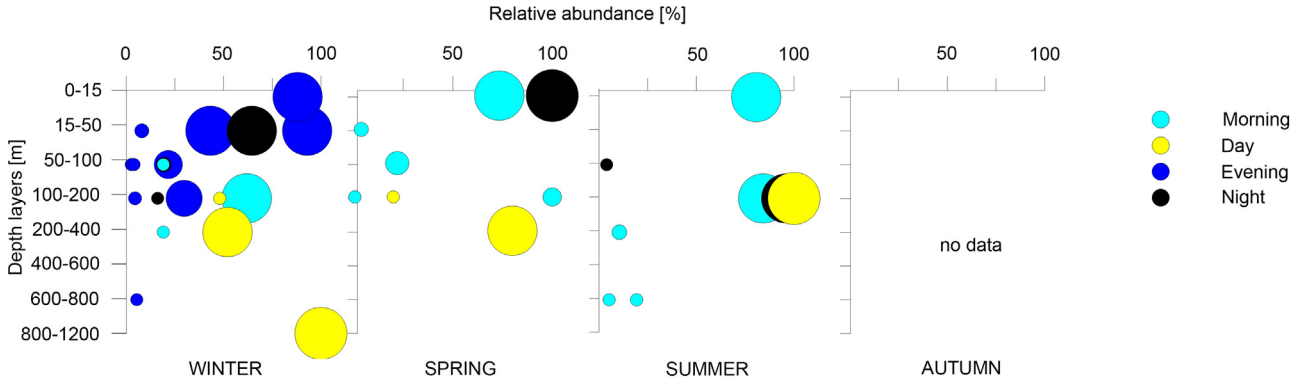

Figure 6 Vertical distribution of *Euphausia krohnii* calyptopes. Relative abundance on the upper axe represents percentage of calyptopes found in that layer. Bubble size indicates relative abundance of calyptopes during certain part of the day (from 4% till 100%) during one series of sampling in that layer.

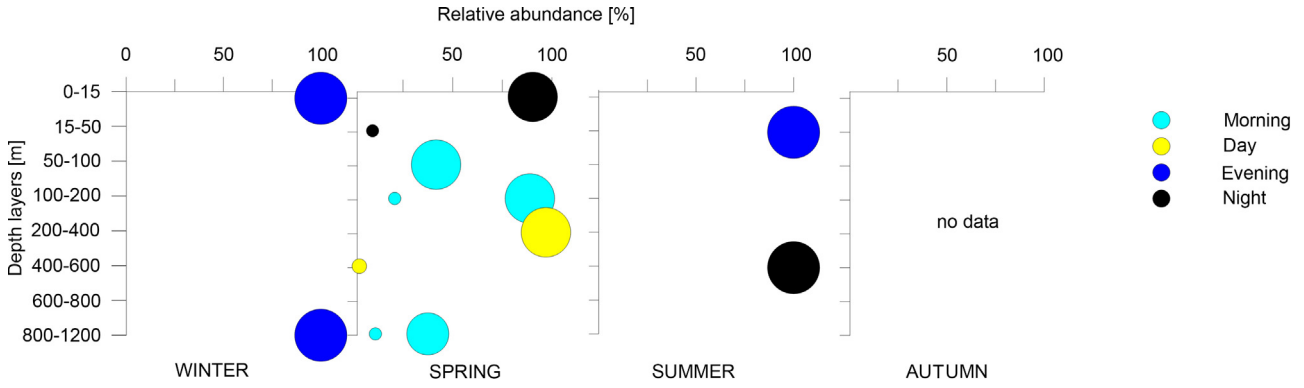

Figure 7 Vertical distribution of *Nyctiphanes couchii* calyptopes. Relative abundance on the upper axe represents percentage of calyptopes found in that layer. Bubble size indicates relative abundance of calyptopes during certain part of the day (from 3% till 100%) during one series of sampling in that layer.

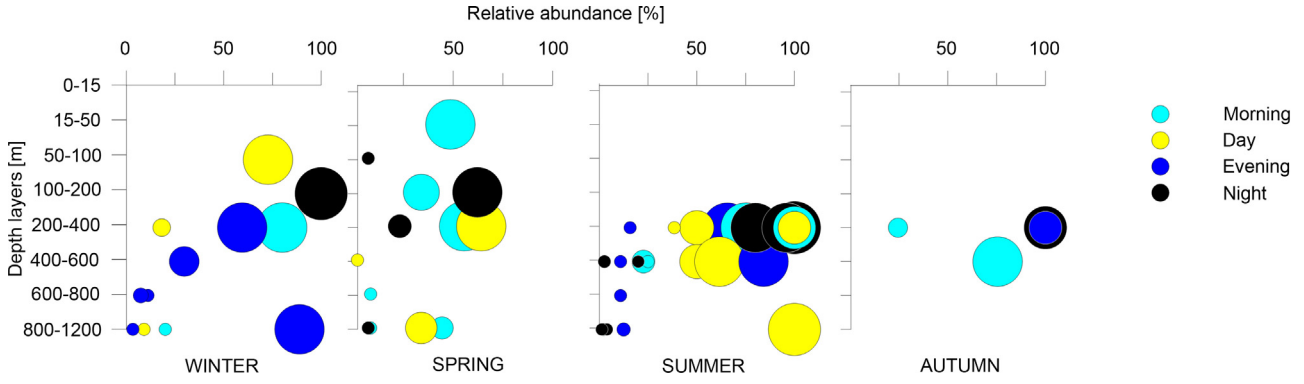

Figure 8 Vertical distribution of *Stylocheiron abbreviatum* calyptopes. Relative abundance on the upper axe represents percentage of calyptopes found in that layer. Bubble size indicates relative abundance of calyptopes during certain part of the day (from 1% till 100%) during one series of sampling in that layer.

of the day and at night, and descent during the morning and evening (*Stylocheiron maximum* in winter); (iii) weakly-migrating or non-migrating calyptopes (*Stylocheiron longicorne*); (iv) irregular migration (*S. abbreviatum*, *S. maximum* in spring, summer, and autumn; *T. aequalis*). The migratory pattern of *Meganyctiphanes norvegica* calyptopes has not been determined owing to limited data.

As determined by weighted mean depth (WMD) averaged over seasons, calyptopes typically were found in one of four layers labeled surface (0–50 m), sub-surface (50–200 m), mesopelagic (200–800 m), and bathypelagic (800–1200 m). In winter, *E. brevis*, *E. hemigibba*, *E. krohnii*, *N. megalops*, and *T. gregaria* were sub-surface species. Three species of Stylocheiron (*S. abbreviatum*, *S. longicorne*, *S. maximum*)

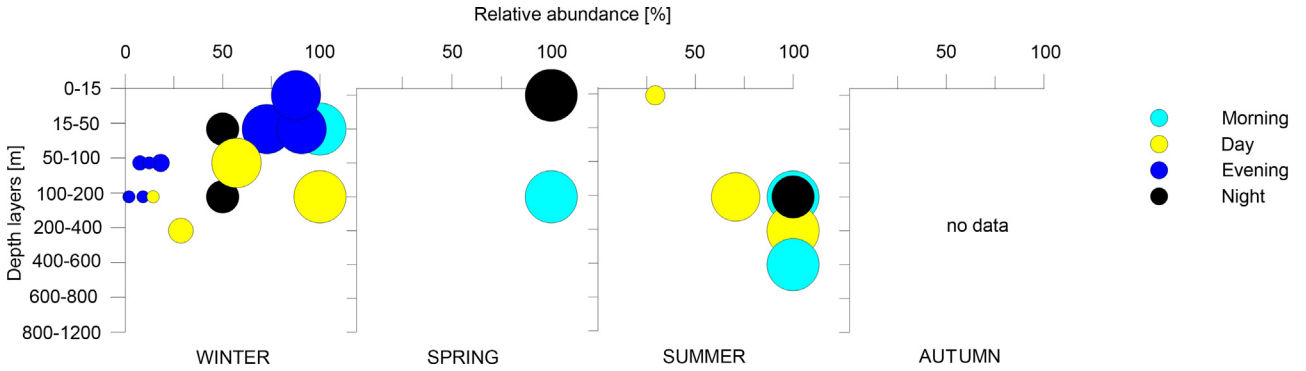

Figure 9 Vertical distribution of *Euphausia brevis* calyptopes. Relative abundance on the upper axe represents percentage of calyptopes found in that layer. Bubble size indicates relative abundance of calyptopes during certain part of the day (from 2% till 100%) during one series of sampling in that layer.

Table 3 Weighted mean depth (WMD) and range of depth distribution (RDD) (both in meters) of calyptopes during seasons.

Calyptopes/season	Winter		Spring		Summer		Autumn	
	WMD [m]	RDD [m]	WMD [m]	RDD [m]	WMD [m]	RDD [m]	WMD [m]	RDD [m]
Euphausia brevis	98	0–600	103	0–400	217	0–800	–	–
Euphausia hemigibba	150	100–200	–	–	–	–	–	–
Euphausia krohnii	183	0–1200	156	0–400	45	0–800	–	–
Meganyctiphanes norvegica	–	–	300	200–400	–	–	–	–
Nyctiphanes couchii	924	0–1200	403	0–1200	39	15–600	–	–
Nematoscelis megalops	150	100–200	–	–	300	200–400	–	–
Stylocheiron abbreviatum	681	50–1200	489	15–1200	361	200–1200	428	200–600
Stylocheiron longicorne	300	200–400	–	–	203	100–600	336	100–600
Stylocheiron maximum	727	50–1200	545	100–1200	330	100–600	150	100–200
Thysanoessa gregaria	137	0–200	–	–	–	–	–	–
Thysanopoda aequalis	279	0–1200	274	0–1200	274	15–1200	420	100–800

and *T. aequalis* were mesopelagic, and *N. couchii* was bathypelagic (Table 3). *E. brevis* and *E. krohnii* calyptopes had sub-surface WMDs in spring when all others were mesopelagic. In summer, *E. krohnii* and *N. couchii* were in the surface layer and others were mesopelagic (Table 3). During autumn, *S. maximum* calyptopes were in the sub-surface layer and *S. abbreviatum*, *S. longicorne*, and *T. aequalis* were mesopelagic.

The range of depth distribution (RDD) was used to characterize calyptopes as either scattered or non-scattered. Accordingly, *N. couchii*, *S. abbreviatum*, and *T. aequalis* calyptopes were "scattered". Those of *S. abbreviatum* and *S. maximum* had high RDDs that fit the broad depth-range over which they were collected. The bathypelagic calyptopes of *N. couchii* extended from the surface to the bottom (Table 3), but in winter they were exclusively in the deepest layer.

4. Discussion

Annual variation of environmental factors in the upper 100 m of the deep Southern Adriatic (Figs. 2–4) are generally consistent with findings from earlier studies, although summer and autumn temperatures (23.5°C surface, 15°C below 50 m) were noticeably higher than in researches of Hure et al. (1980) and Kršinić (1998). The latter may be a consequence of the recent warming trend documented in the Mediterranean and Adriatic (Batistić et al., 2014). Some of the changes in zooplankton composition can be related to regional climate fluctuations (Berline et al., 2011) and the influence of deep-convection in the South Adriatic (Gačić et al., 2002).

Among 12 species of adults (Guglielmo, 1979; Šipoš, 1977a,b) and 11 calyptopes of the same species (Gangai et al., 2012), this investigation confirmed 11 species of calyptopes previously found in Adriatic. Calyptopes of *Stylocheiron suhmii* and *Nematoscelis atlantica* were not found although these species were formerly listed as residents of the Adriatic (Guglielmo, 1979; Ruud, 1936; Šipoš, 1977a,b). In this study sampling method suitable for evaluating euphausiid larval stages was used, but no confident estimates could be done for postlarval stages or adults, as these are able to avoid the plankton net. This study focused on the most abundant species: *T. aequalis*, *E. krohnii*, *N. couchii*, *S. abbreviatum*, and *E. brevis*. The vertical distribution of calyptopis abundance of these species varied daily and seasonally.

The lack of data for calyptopes in the wider Mediterranean precludes direct comparison with the present study. Comparisons thus must be restricted to available data on the total number of all euphausiid larval stages. Casanova (1970) identified larval stages of 13 species in the Mediterranean. In the western basin, those of *E. krohnii* and *N. megalops*

dominated; in the central, *T. aequalis* larvae were dominant; and in the eastern Casanova (1974) found those of *T. aequalis*, *E. hemigibba*, and *M. norvegica*. *N. megalops* and *E. krohnii* were most abundant in the Strait of Messina (Brancato et al., 2001). Comparing the results of Brancato et al. (2001) and Casanova (1970) with those of this study suggests that the composition of Southern Adriatic euphausiids is influenced by both eastern and western Mediterranean populations. This is inconsistent with the findings of Šipoš (1977b) who identified predominantly western Mediterranean species in the Adriatic. This discrepancy might be explained by the expansion of tropical species arriving *via* the Strait of Gibraltar and the Suez Canal (Raitsos et al., 2010) in response to basin-scale climate change (Shaltout and Omstedt, 2014; Ulbrich et al., 2013). Changes in the circulation of major water masses that enter the Adriatic from the Ionian Sea (Gačić et al., 2010) also influence the composition of Adriatic planktonic fauna (Pečarević et al., 2013).

The highest number of all calyptopes was in spring (3797 ind. 100 m^{-3}). Generally, Southern Adriatic zooplankton reaches their annual peak in this period (Benović et al., 2005; Hure et al., 1980; Kršinić, 1998) following the phytoplankton bloom (Antoine et al., 1995). The lowest number was in the fall (99 ind.100 m^{-3}). The abundance of calyptopis found by the present work was higher than previously reported in the Mediterranean.

Diel vertical migration of calyptopes varies between (Andersen et al., 2001) and within species (Andersen and Sardou, 1992; Mauchline and Fisher, 1969; Taki et al., 2009). Triggers are both physico-chemical (light, gravity, oxygen) and biological (predation). Gangai et al. (2012) studied the effect of light intensity and hydrographic conditions on larval migratory patterns and found difference in calyptopes abundance between morning, day, sunset, and night showing clearly that some species migrated vertically. That confirms that behavioral mechanisms together with hydrographic conditions are important in forming aggregations, acting to maintain species in favorable areas limiting their energy use (Mauchline and Fisher, 1969; Spiridonov and Casanova, 2010). Calyptopes and furciliae stages typically had different ranges and vertical distributions, both of which suggest different migratory behavior. Calyptopes had a smaller range of migration than furciliae or adults. They also inhabited a wider depth range. Those of some species notably exhibited an irregular migration pattern in which part of the group lagged – or did not even join – the diel rise of the main aggregation. Moreover, calyptopes frequently were found in the near-bottom layer. There is no evidence to suggest that calyptopes living at 600 m ever rose to the surface layer (Mauchline and Fisher, 1969) this explains the presence of two separate groups of calyptopes of the same species: one living in the upper layers and the other near the bottom. Depending on temperature and feeding, each calyptopis stage lasts a few days before molting. Therefore our assumption is that all species whose calyptopes have been found in our samples spawn in the Adriatic. The timing of their appearance and abundance thus are determined by the reproductive characteristics of the parent group. *T. gregaria* has a short mating season (one season), while others – *E. krohnii*, *E. brevis*, *E. hemigibba*, *N. couchii*, *T. aequalis*, *N. megalops*, and all three representatives of *Stylocheiron* extend reproduction over two or more seasons.

Weighted mean depth data indicate the preferred vertical zones of Southern Adriatic calyptopes. Calyptopes of the epipelagic species *E. brevis*, *E. krohnii*, and *E. hemigibba* are found in the upper 100 m and subsurface layer (100–200 m) where the influence of surface currents, freshwater inflow, and seasonal temperature and light variations are most evident. The mezopelagic zone (200–800 m) is inhabited by *N. megalops, S. abbreviatum, S. longicorne*, *S. maximum*, and *T. aequalis*. *N. couchii* larvae frequently were collected in the bottom layer, in contrast to the neritic habitat of adult *N. couchii* in the Mediterranean and Adriatic described by D'Amato et al. (2008) and Šipoš (1977b).

Scattered and non-scattered aggregations, classified according to the range of their depth distribution, illustrate that calyptopes have different vertical distributions over the course of the year. Likely these are associated, at least in part, with the different depths at which their ecological preferences are found as the area's physical environment undergoes seasonal changes. Vertical migration seems to provide the best chances of utilizing resources from the environment they inhabit. Thus, behavioral mechanisms are important in maintaining aggregations and interact with hydrographic conditions to maintain species in a favorable area.

In the absence of a continuous observational presence in the area, through either monthly ship-based sampling or autonomous platforms, their ecology and behavior will remain insufficiently studied. However, our results indicate the possibility of considerable variations in production, bathymetric distribution and diel vertical migrations in oligotrophic open waters of temperate regions, driven by an overall complexity of processes in the entire water column.

5. Conclusion

The present work reports data for larval euphausiids stages in the open-water station in the oligotrophic South Adriatic Sea sampled at morning, midday, evening and night. Among the 11 species identified in the present study, the most abundant calyptopis was *T. aequalis*. Four diel patterns vertical migrations were emerged: (i) nocturnal ascent to upper layers (*E. brevis*, *E. hemigibba*, *E. krohnii*, *N. megalops*, *N. couchii*), (ii) migration to upper layers at middle of the day and at night, and descent during the morning and evening (*S. maximum* – winter), (iii) weakly-migrating or non-migrating (*S. longicorne*), (iv) irregular migration independent of the day/night cycle (*S. abbreviatum*, *S. maximum* – spring, summer and autumn, *T. aequalis*).

The overall conclusion is that euphausiids developmental stages during the year have different scatter distributions and different ecological preferences. Though not homogenous, all species are interrelated by preference of bathymetric distribution and specific daily vertical migration. Therefore it can be assumed that distribution is conditioned by environmental and production particularities of certain area and is caused by the different migration rhythm of the same species depending on geographic location, which has not yet been sufficiently studied in the Mediterranean Sea. Thus, results of our findings contribute additional and important understanding on the calyptopes composition, abundance and behavior in the oligotrophic waters of Southern Adriatic and eastern Mediterranean Sea.

Acknowledgements

We acknowledge the generous support of the Ministry of Science, Education, and Sport of the Republic of Croatia and of the University of Dubrovnik.

References

Andersen, V., Frederique, F., Sardou, J., Picheral, M., Scotto, M., Nival, P., 1998. Vertical distributions of macroplankton and micronekton in the Ligurnian and Thyrrhenian Seas (northwestern Mediterranean). Oceanol. Acta 21 (5), 655—676, http://dx.doi.org/10.1016/S0399-1784(98)90007-X.

Andersen, V., Nival, P., Caparroy, P., Gubanova, A., 2001. Zooplankton community during the transition from spring bloom to oligotrophy in the open NW Mediterranean and effects of wind events. 1. Abundance and specific composition. J. Plankton Res. 23 (3), 227—242, http://dx.doi.org/10.1093/plankt/23.3.227.

Andersen, V., Sardou, J., 1992. The diel migrations and vertical distributions of zooplankton and micronekton in the Northwestern Mediterranean Sea. 1. Euphausiids, mysids, decapods and fishes. J. Plankton Res. 14 (8), 1129—1154, http://dx.doi.org/10.1093/plankt/14.8.1129.

Antoine, D., Morel, A., Andre, J.M., 1995. Algal pigment distribution and primary production in the eastern Mediterranean as derived from coastal zone color scanner observations. J. Geophys. Res. 100 (C8), 16193—16209, http://dx.doi.org/10.1029/95JC00466.

Batistić, M., Garić, R., Molinero, J.C., 2014. Interannual variations in Adriatic Sea zooplankton mirror shifts in circulation regimes in the Ionian Sea. Climate Res. 61, 231—240, http://dx.doi.org/10.3354/cr01248.

Batistić, M., Jasprica, N., Carić, M., Čalić, M., Kovačević, V., Garić, R., Njire, J., Mikuš, J., Bobanović-Ćolić, S., 2012. Biological evidence of a winter convection event in the South Adriatic: a phytoplankton maximum in the aphotic zone. Cont. Shelf Res. 44, 57—71, http://dx.doi.org/10.1016/j.csr.2011.01.004.

Benović, A., Lučić, D., Onofri, V., Batistić, M., Njire, J., 2005. Bathymetric distribution of medusae in the open waters of the middle and south Adriatic Sea during spring 2002. J. Plankton Res. 27 (1), 79—89, http://dx.doi.org/10.1093/plankt/fbh153.

Berline, L., Siokou-Frangou, I., Marasović, I., Vidjak, O., Fernández de Puelles, M.L., Mazzocchi, M.G., Assimakopoulou, G., Zervoudaki, S., Fonda Umani, S., Conversi, A., Garcia-Comas, C., Ibanez, F., Gasparini, S., Stemmann, L., Gorsky, G., 2011. Intercomparison of six Mediterranean zooplankton time series. Prog. Oceanogr. 97—100, 76—91, http://dx.doi.org/10.1016/j.pocean.2011.11.011.

Brancato, G., Minutoli, R., Granata, A., Sidoti, O., Guglielmo, L., 2001. Diversity and vertical migration of euphausiids across the Straits of Messina area. In: Faranda, F.M., Guglielmo, L., Spezie, G. (Eds.), Mediterranean Ecosystems: Structures and Processes. Springer-Verlag Italia, Milan, 503 pp., http://dx.doi.org/10.1007/978-88-470-2105-1_18.

Brinton, E., Ohman, M.D., Townsend, A.W., Knight, M.D., Breidgeman, A.L., 2000. Euphausiids of the world ocean. World Biodiversity Database CD-ROM Series. Springer-Verlag, Berlin.

Casanova, B., 1970. Répartition bathymétriqué des euphausiacés dans le bassin occidental de la méditerranée. Revue des Travaux de l'Institut des Pêches Maritimes 34 (2), 205—219.

Casanova, B., 1974. Les euphausiacés de Méditerranée (Systématique et développement larvaire. Biogéographie et Biologie). (Ph.D. thesis). Université de Provence, Aix-Marseille, 380 pp.

Casanova, B., 2003. The order Euphausiacea Dana, 1852. Crustaceana 76 (9), 1083—1121.

Casanova-Soulier, B., 1963. Les euphausiacés de la Méditerranée. Commission internationale pour l'Exploration scientifique de la Mer Méditerranée. Comité du Plancton, Monaco.

Cerino, F., Bernardi-Aubry, F., Coppola, J., La Ferla, B., Maimone, G., Socal, G., Totti, C., 2012. Spatial and temporal variability of pico-, nano- and microphytoplankton in the Southern Adriatic Sea (Mediterranean Sea). Cont. Shelf Res. 44, 94—105, http://dx.doi.org/10.1016/j.csr.2011.06.006.

D'Amato, M.E., Harkins, G.W., de Oliveira, T., Teske, P.R., Gibbons, M.J., 2008. Molecular dating and biogeography of the neritic krill Nyctiphanes. Mar. Biol. 155 (2), 243—247, http://dx.doi.org/10.1007/s00227-008-1005-0.

Duarte, C.M., Regaudie-de-Gioux, A., Arrieta, J.M., Delgado-Huertes, A., Augusti, S., 2013. The oligotrophic ocean is heterotrophic. Annu. Rev. Mar. Sci. 5, 551—569, http://dx.doi.org/10.1146/annurev-marine-121211-172337.

Fonda Umani, S., 1996. Pelagic production and biomass in the Adriatic Sea. Scientia Marina 60 (Suppl. 2), 65—77.

Fonda Umani, S., Monti, M., 1993. Distribuzione dei popolamenti microzooplanctonici nell'Arcipelago Toscano. In: Nuccio, C. (Ed.), Progetto Mare. Ricerca sullo stato biologico efisico dell'Alto Tirreno Toscano. Univ. Firenze, 157—260.

Franqueville, C., 1971. Macroplancton profond (invertébrés) de la Méditerranée nord-occidentale. Tethys 3, 11—56.

Gačić, M., Borzelli, G.L.E., Civitarese, G., Cardin, V., Yari, S., 2010. Can internal processes sustain reversals of the ocean upper circulation? The Ionian Sea example. J. Geophys. Res. 37 (9), L09608, http://dx.doi.org/10.1029/2010GL043216.

Gačić, M., Civitarese, G., Miserocchi, S., Cardin, V., Crise, A., Mauri, E., 2002. The open-ocean convection in the southern Adriatic: a controlling mechanism of the spring phytoplankton bloom. Cont. Shelf Res. 22 (14), 1897—1908, http://dx.doi.org/10.1016/S0278-4343(02)00050-X.

Gangai, B., Lučić, D., Morović, M., Brautović, I., Miloslavić, M., 2012. Population structure and diel vertical migration of euphausiid larvae in the open southern Adriatic Sea (July 2003). Crustaceana 85 (6), 659—684, http://dx.doi.org/10.1163/156854012X643942.

Guglielmo, L., 1979. Osservazioni sulla ripartizione verticale degli Euphausiacei in aque profonde del sud Adriatico (luglio, 1974). Mem. Biol. Mar. Oceanogr. 9 (1—2), 25—33.

Harvey, M., Galbriaith, P.S., Descroix, A., 2009. Vertical distribution and diel vertical migration in the St Lawrance marine systems (Canada) in relation with the cold intermediate layer thermal properties. Prog. Oceanogr. 80 (1—2), 1—21, http://dx.doi.org/10.1016/j.pocean.2008.09.001.

Hure, J., 1955. Distribution annuelle verticale du zooplancton sur une station de L'Adriatique méridionale. Acta Adriat. 7 (7), 1—72.

Hure, J., 1961. Diurnal migration and seasonal vertical distribution of zooplankton in the deepest sea. Acta Adriat. 9 (6), 1—59.

Hure, J., Ianora, A., Scotto di Carlo, B., 1980. Spatial and temporal distribution of copepod communities in the Adriatic Sea. J. Plankton Res. 2 (4), 295—316, http://dx.doi.org/10.1093/plankt/2.4.295.

Krom, M.D., Emeis, K.C., Van Cappellen, P., 2010. Why is the Eastern Mediterranean phosphorus limited? Prog. Oceanogr. 85, 236—244, http://dx.doi.org/10.1016/j.pocean.2010.03.003.

Kršinić, F., 1998. Vertical distribution of protozoan and microcopepod communities in the South Adriatic Pit. J. Plankton Res. 20 (6), 1033—1060, http://dx.doi.org/10.1093/plankt/20.6.1033.

Longhurst, A.R., Bedo, A., Harrison, W.G., Head, E.J.H., Horne, E.P., Irwin, B., Morales, C., 1989. NFLUX: a test of vertical nitrogen flux by diel vertical migrant biota. Deep Sea Res. Pt. A 36 (11), 1705—1719, http://dx.doi.org/10.1016/0198-0149(89)90067-8.

Longhurst, A.R., Harrison, W.G., 1989. The biological pump: profiles of plankton production and consumption in the upper ocean. Prog. Oceanogr. 22 (1), 47—123, http://dx.doi.org/10.1016/0079-6611(89)90010-4.

Malanotte-Rizzoli, P., Manca, B.B., Ribera d'Alcala, M., Theocaris, A., Bergamasco, A., Bregant, D., Budillon, G., Civitarese, G., Georgopoulos, D., Michelato, A., 1997. A synthesis of the Ionian Sea hydrography, circulation and water mass pathways during

POEM — phase I. Prog. Oceanogr. 39, 153—204, http://dx.doi.org/10.1016/S0079-6611(97)00013-X.

Mauchline, J., Fisher, L.R., 1969. The biology of euphausiids. Advances in Marine Biology. Acad. Press, London, UK, 454 pp.

Mavidis, M., Aplikioti, M., Kirmitzoglou, I., Koukouras, A., 2005. The euphausiacean fauna (Malacostraca) of the Aegean Sea, and comparison with those of the neighboring seas. Crustaceana 78 (1), 19—27, http://dx.doi.org/10.1163/1568540054024538.

McGehee, D.E., Demer, D.A., Warren, J.D., 2004. Zooplankton in Ligurnian Sea: Part I. Characterization of their dispersion, relative abundance and environment during summer 1999. J. Plankton Res. 26 (12), 1409—1418, http://dx.doi.org/10.1093/plankt/fbh132.

Najdek, M., Paliaga, P., Šilović, T., Batistić, M., Garić, R., Supić, N., Ivančić, I., Ljubimir, S., Korlević, M., Jasprica, N., 2014. Picoplankton community structure before, during and after convection event in the offshore waters of the Southern Adriatic Sea. Biogeosciences 11, 2645—2659, http://dx.doi.org/10.5194/bg-11-2645-2014.

Pečarević, M., Mikuš, J., BratošCetinić, A., Dulčić, J., Čalić, M., 2013. Introduced marine species in Croatian waters (Eastern Adriatic Sea). Mediterr. Mar. Sci. 14 (1), 224—237, http://dx.doi.org/10.12681/mms.383.

Raitsos, D.E., Beaugrand, G., Georgopoulos, D., Zenetos, A., Pancucci-Papadopoulou, M., Theocharis, A., Papathanassiou, E., 2010. Global climate change amplifies the entry of tropical species into the Eastern Mediterranean Sea. Limnol. Oceanogr. 55 (4), 1478—1484, http://dx.doi.org/10.4319/lo.2010.55.4.1478.

Ruud, T.J., 1936. Euphausiacea. Rep. Dan. Oceanogr. Exped. Mediterr. 2, 1—86.

Shaltout, M., Omstedt, A., 2014. Recent sea surface temperature trends and future scenarios for the Mediterranean Sea. Oceanologia 56 (3), 411—443, http://dx.doi.org/10.5697/oc.56-3.411.

Siokou-Frangou, I., Christaki, U., Mazzocchi, M.G., Montresor, M., Ribera d'Alcalá, M., Vaqué, D., Zingone, A., 2010. Plankton in the open Mediterranean Sea: a review. Biogeosciences 7, 1543—1586, http://dx.doi.org/10.5194/bg-7-1543-2010.

Spiridonov, V., Casanova, B., 2010. Order Euphausiacea Dana, 1852. In: Schram, F.R., Vaupel Klein, J.C. von (Eds.), Treatise on Zoology — Anatomy, Taxonomy, Biology; The Crustacea; Complementary to the Volumes Translated from the French of the Traité de Zoologie Vol. 9, Part A Eucarida: Euphausiacea, Amphionidacea, and Decapoda (partim), 1—82.

Šipoš, V., 1977a. Distribution of Euphausiids in the Adriatic Sea in autumn 1974 and spring 1975. Rap. Commission Internatnl. Mer Mediterranee 24 (10), 123—124.

Šipoš, V., 1977b. Eufauzidi Jadranskog mora, Magistarski rad, Sveučilište u Zagrebu, Zagreb.

Taki, K., Yabuki, T., Noiri, Y., Hayashi, T., Naganobu, M., 2009. Larval development and spawning ecology of euphausiids in the Ross Sea and its adjacent waters in 2004/05. Plankton Benthos Res. 4 (4), 135—146, http://dx.doi.org/10.3800/pbr.4.135.

Trégouboff, G., Rose, M., 1957. Manuel de planctologie Méditerranéenne. Centre Nat. Recher. Sci., Paris, 587 pp.

Vilibić, I., Matijević, S., Šepić, J., Kušpilić, G., 2012. Changes in the Adriatic oceanographic properties induced by Eastern Mediterranean Transient. Biogeosciences 9, 2085—2097.

Ulbrich, U., Xoplaki, E., Dobricic, S., García-Herrera, R., Lionello, P., Adani, M., Baldi, M., Barriopedro, D., Coccimiglio, P., Dalu, G., Efthymiadis, D., Gaetani, M., Galati, M.B., Gimeno, L., Goodess, C.M., 2013. Past and current climate changes in the mediterranean region, chapter regional assessment of climate change in the mediterranean. Adv. Glob. Change Res. 50, 9—51, http://dx.doi.org/10.1007/978-94-007-5781-3_2.

Wiebe, P.H., D'Abramo, L., 1972. Distribution of euphausiid assemblages in the Mediterranean Sea. Mar. Biol. 15 (2), 139—149, http://dx.doi.org/10.1007/BF00353642.

Oceanologia (2018) 60, 139—152

Available online at www.sciencedirect.com

ScienceDirect

journal homepage: www.journals.elsevier.com/oceanologia/

ORIGINAL RESEARCH ARTICLE

Microbial plankton communities in the coastal southeastern Black Sea: biomass, composition and trophic interactions

Ulgen Aytan [a,*], Ali Muzaffer Feyzioglu [b], Andre Valente [c], Ertugrul Agirbas [a], Elaine S. Fileman [d]

[a] *Faculty of Fisheries, Recep Tayyip Erdogan University, Rize, Turkey*
[b] *Faculty of Marine Sciences, Karadeniz Technical University, Trabzon, Turkey*
[c] *Marine and Environmental Sciences Centre, Faculty of Sciences, University of Lisbon, Lisbon, Portugal*
[d] *Plymouth Marine Laboratory, Plymouth, United Kingdom*

Received 13 February 2017; accepted 28 September 2017
Available online 24 October 2017

KEYWORDS
Phytoplankton;
Microzooplankton;
Carbon biomass;
Microbial food web;
Grazing;
Black Sea

Summary We investigated biomass and composition of the pico-, nano- and microplankton communities in a coastal station of the southeastern Black Sea during 2011. We also examined trophic interactions within these communities from size-fractionated dilution experiments in February, June and December. Autotrophic and heterotrophic biomasses showed similar seasonal trends, with a peak in June, but heterotrophs dominated throughout the year. Autotrophic biomass was mainly comprised by nanoflagellates and diatoms in the first half of the year, and by dinoflagellates and *Synechococcus* spp. in the second half. Heterotrophic biomass was mostly dominated by heterotrophic bacteria, followed by nanoflagellates and microzooplankton. Dilution experiments suggest that nano- and microzooplankton were significant consumers of autotrophs and heterotrophic bacteria. More than 100% of bacterial production was consumed by grazers in all experiments, while 46%, 21% and 30% of daily primary production were consumed in February, June and December, respectively. In February, autotrophs were the main carbon source, but in December, it was heterotrophic bacteria. An intermediate situation was observed in June, with similar carbon flows from autotrophs and heterotrophic bacteria. Size-fraction

* Corresponding author at: Faculty of Fisheries, Recep Tayyip Erdogan University, 53100, Rize, Turkey. Tel.: +90 505 4775150.
E-mail address: ulgen.kopuz@erdogan.edu.tr (U. Aytan).

Peer review under the responsibility of Institute of Oceanology of the Polish Academy of Sciences.

Production and hosting by Elsevier

http://dx.doi.org/10.1016/j.oceano.2017.09.002

dilution experiments suggested that heterotrophic nanoflagellates are an important link between the high heterotrophic bacterial biomass and microzooplankton. In summary, these results indicate that nano- and microzooplankton were responsible for comprising a significant fraction of total microbial plankton biomass, standing stocks, growth and grazing processes. This suggests that in 2011, the microbial food web was an important compartment of the planktonic food web in the coastal southeastern Black Sea.

1. Introduction

Biogenic carbon transfers from autotrophic to heterotrophic organisms through two main pathways: the classical herbivorous food web and the microbial food web (Azam et al., 1983; Legendre and Rassaulzadegan, 1995; Sherr et al., 1986; Sommaruga, 1995). In the classical herbivorous food web, energy is channelled directly from large diatoms to metazoans (Pomeroy, 1974). In the microbial food web energy is channelled to higher trophic levels from bacteria and small phytoplankton (<20 μm) to nano-microzooplankton (Azam et al., 1983; Calbet and Landry, 2004). Therefore, through the microbial food web, heterotrophic nanoflagellates (HNF) and microzooplankton (<200 μm, especially ciliates and heterotrophic dinoflagellates) play significant roles in structuring plankton communities (Calbet, 2008) and in nutrient regeneration (Calbet and Saiz, 2005). They control lower level production and dynamics (Calbet and Landry, 2004) and are a favourite prey for mesozooplankton in a range of aquatic environments, from the poles to upwelling regions to oligotrophic ocean gyres (Atkinson, 1996; Calbet and Saiz, 2005; Stoecker and Capuzzo, 1990). The microbial food web is less efficient due to energy losses in each trophic step and dominant in oligotrophic waters. However, many productive systems have multivorous food webs where both the classical and microbial food webs play important roles in carbon cycling (Legendre and Rassaulzadegan, 1995). Thus, information on the different trophic compartments and their interactions is important for understanding the functioning of the planktonic food web and its representation in ecological models.

The Black Sea ecosystem has significant potential in terms of fishing among the world oceans, but drastic changes in biogeochemical properties occurred during the last four decades (Besiktepe et al., 1999; Daskalov, 2002; Kideys, 2002; Oguz and Gilbert, 2007; Oguz et al., 2012a). Pollution, eutrophication, over-fishing, climatic cooling/warming and introduction of non-native species altered the Black Sea ecosystem in the 1990s (Oguz and Gilbert, 2007). Nutrient concentrations decreased in the 2000s compared with the eutrophication period, which has been regarded as an improvement of the Black Sea ecosystem state (Pakhomova et al., 2014). However, the ecosystem seems not to have recovered to the classical herbivorous food web of the pre-eutrophication period prior to 1970 and is now characterized by a food web dominated by dinoflagellates and other nano-size phytoplankton species with respect to diatoms, and relatively low levels of phytoplankton (Oguz and Velikova, 2010). Despite improvements, the Black Sea is still under serious environmental threats as a result of uncontrolled coastal pollution and high river discharge of several industrialized countries into this semi-enclosed basin. Climatic changes may have also played a role in shifts towards domination of dinoflagellates and nanoflagellates, reduced frequency and magnitude of phytoplankton blooms, and declines in phytoplankton biomass (Daskalov, 2002; Kideys, 2002; Nesterova et al., 2008; Oguz and Gilbert, 2007; Oguz et al., 2012a). Long-term changes of in situ phytoplankton biomass in the interior basin indicate distinct decadal changes that followed closely temperature variations, with higher (lower) biomass occurred during cold (warm) years (Nesterova et al., 2008; Oguz et al., 2006). It has been speculated that warming over the next decades (Collins et al., 2013) might significantly increase carbon flow through the microbial food web (Caron and Hutchins, 2012). However, there is little information on the importance of the microbial food web in the Black Sea, since previous studies mainly analysed the dynamics of classical food web contributors such as diatoms, dinoflagellates and their mesozooplankton predators, in particular, copepods (BSC, 2008). A number of studies have investigated components of the microbial food web (heterotrophic bacteria, pico-autotrophs, small flagellates and microzooplankton), but these have mostly focused on specific compartments or taxonomic subsets during limited periods and in specific regions (e.g. Becquevort et al., 2002; Feyzioglu et al., 2004; Kopuz et al., 2012; Sorokin et al., 1995; Uysal, 2001). To the best of our knowledge, a simultaneous assessment of the whole microbial community has not been done for the Black Sea. A few studies indicate the importance of nano- and microzooplankton as grazers. Bouvier et al. (1998) measured feeding activity of nano- and micrograzers on heterotrophic bacteria and nanoplankton during summer 1995 in the NW Black Sea based on the uptake of fluorescently labelled-prey, and Stelmakh and Georgieva (2014) reported microzooplankton grazing on phytoplankton based on dilution experiments conducted in the Western Black Sea.

The SE Black Sea is an important part of the Black Sea in terms of fishing. A milder climate provides more favourable spawning and overwintering grounds for the anchovy, and the region currently sustains 80% of the total fish catch in the Black Sea (Oguz et al., 2012b). As such lower trophic levels dynamics should be understood as much as possible. However, there are no studies on trophic interactions within a

microbial food web and on complete community assessments. The present study simultaneously addresses the dynamics of autotrophic and heterotrophic plankton <200 μm during a seasonal progression and discusses the balance between prey and predator in the SE Black Sea. To test the hypothesis that the microbial food web is an important pathway of carbon, the population dynamics of the various planktonic groups are described and the carbon flow within the microbial food web is determined.

2. Material and methods

2.1. Study site and sampling

Sampling was carried out at a coastal monitoring station (40°57′03″N; 40°11′22″E) in the southeastern Black Sea during eight cruises from February to December 2011 on board r/v *KTU Denar I*. This station has been monitored since 2001 (e.g. Agirbas et al., 2014, 2015). The sampling station has a depth of 50 m and is situated 0.5 nautical miles off from the coast (Fig. 1). The region is characterized by a narrow continental shelf compared to the northwestern Black Sea and is influenced by the meandering rim current, the permanent circulation feature that encirculates the Black Sea in a counterclockwise direction, as well by local river discharges. In summer, waters are thermally stratified and in winter, vertical mixing can go as deep as the water column depth. Within the euphotic depth (~30 m), reported concentrations of nutrients are highly variable (Agirbas et al., 2014, 2015). Nitrite + nitrates have been found to vary between 0.2–5 μM. Phosphate is usually very low (~0.01 μM), sometimes not detectable, and silicates around 5 μM. The spring bloom is mainly dominated by diatoms, followed by increases of dinoflagellates and cocolitophores in summer, and autumn blooms of these two groups have also been found (Agirbas et al., 2015). Changes in trophic status based on chlorophyll-*a* have been reported for the last decade in the region (Agirbas et al., 2015).

Profiles of water column structure were collected with Idronaut Ocean Seven 316 Plus CTD profiler and fluorescence was recorded with Satlantic hyperspectral radio spectrophotometer in order to obtain subsurface chlorophyll maximum (SCM) and euphotic depths. Samples for nutrients ($NO_2 + NO_3$, PO_4, and SiO_2) were taken with 5 m intervals within euphotic zone and analysed using a SEAL AutoAnalyzer. Ammonium was not measured because it is scarce in a surface layer. Samples were collected for pico-, nano-, microplankton from the SCM using 5 l Niskin bottles mounted on a SBE32 Carousel water sampler.

2.2. Abundance and biomass

2.2.1. Pico- and nanoplankton

Pico- and nanoplankton sub-samples (50 ml) were fixed with 1% glutaraldehyde. Samples (10 ml) were drawn under low vacuum (<5 mm Hg) onto 0.2 μm and 0.8 μm black Nuclepore filters, with cellulose nitrate backing filters (1.2 μm) to enhance even cell distribution for pico- and nanoplankton, respectively. Acridine orange (200 μl) solution was added during filtration to stain heterotrophic bacteria and nanoflagellates (Hobbie et al., 1977). Counts for *Synechococcus* spp. were made on unstained preparations due to their autofluorescence property. Filters were mounted on glass slides with a drop of immersion oil between the filter and glass coverslip. They were either processed immediately or frozen for subsequent analysis within 2 weeks. Cell counts were performed under a Nikon E 600 epifluorescence microscope with a filter combination of B-2A (blue excitation, dichroic mirror DM 505, excitation filter EX 450–490, barrier filter BA 520) and G-1A (green excitation, dichroic mirror DM 575, excitation filter EX 546/10, barrier filter BA 580). Bacterial cells were counted in at least 30 microscopic fields. Mean cell volumes were estimated using image analysis system composed of a digital camera, computer and the image analysis software. Heterotrophic nanoflagellates (HNF) were distinguished from autotrophic nanoflagellates (ANF) by the

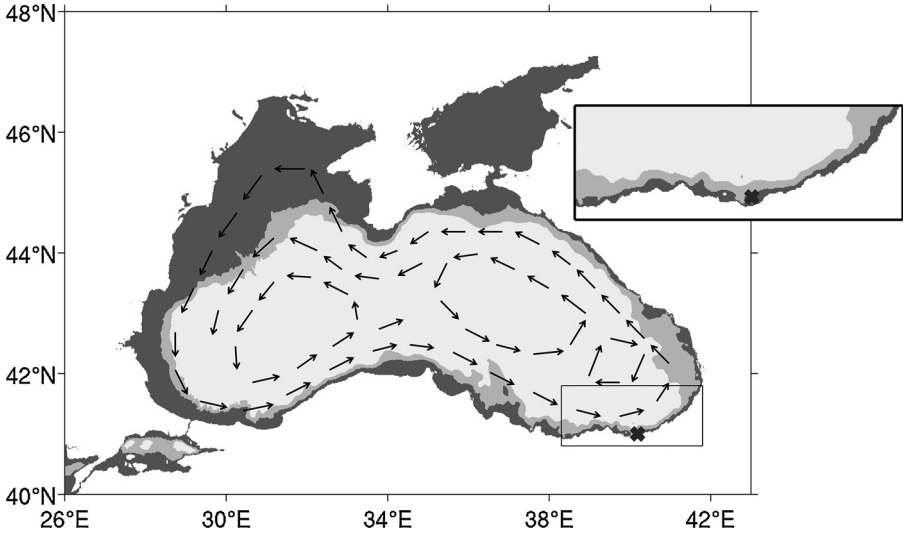

Figure 1 Map showing study area, sampling station, bathymetry and a schematic representation of the general circulation in the Black Sea. The three grey colours represent bathymetric contours of <200 m, 200–1000 m, and >1000 m.

absence of fluorescence. To calculate carbon content of heterotrophic bacteria, *Synechococcus* spp. and nanoflagellates, 77 (Carlson et al., 1999), 123 (Waterbury et al., 1986) and 220 (Børsheim and Bratbak, 1987) fg C per cubic micron were used, respectively.

2.2.2. Microplankton

Microplankton sub-samples (50 or 200 ml depending upon microplankton abundance) were preserved with glutaraldehyde at a final concentration of 1% and stored in the dark (Stoecker et al., 1994). The samples were concentrated by settling for 1 week and siphoning off the supernatant (Karlson et al., 2010). One millilitre of the concentrated samples was placed in a Sedgwick rafter counting chamber and observed using Nikon E 600 epifluorescence microscope at 100–400× magnification. A minimum of 50–100 microplankton observed within 10–20 fields of view were enumerated and grouped into major taxa (diatoms, autotrophic and heterotrophic dinoflagellates, ciliates). In addition, glutaraldehyde fixed samples (0.5% f.c.) were concentrated onto black polycarbonate filters and examined under fluorescence microscopy to estimate the proportion of chlorophyll *a*nd non-chlorophyll containing cells under blue (450–480 nm) light (considered autotroph and heterotroph, respectively) (Karlson et al., 2010). The biomass of each group was estimated by assigning standard geometric shapes or combinations of shapes to specific organisms and measuring the dimensions (Edler, 1979; Hillebrand et al., 1999). Measurements were taken for at least 50 individuals for the abundant taxa and all present individuals for the rare taxa using Image ProPlus 6.2 software (Media Cybernetics, Bethesda, MD). These volume (μm^3) measurements were converted to estimates of carbon content by using the following conversion factors, pg C $cell^{-1}$ = 0.288 × $volume^{0.811}$ or diatoms; pg C $cell^{-1}$ = 0.760 × $volume^{0.819}$ for dinoflagellates (Menden-Deuer and Lessard, 2000); pg C $cell^{-1}$ = (volume × 0.053) + 444.5 for tintinnids (Verity and Langdon, 1984); pg C $cell^{-1}$ = volume × 0.19 for other ciliates (Putt and Stoecker, 1989).

2.3. Size-fractionated dilution experiments

Size-fractioned grazing experiments were performed during February, June and December 2011 to assess the grazing impact of the <200 μm (Landry and Hassett, 1982) and of the <20 μm grazers on autotrophic and heterotrophic plankton. Dilution experiments were planned to cover three distinct periods of the year representing distinct frames of the ecosystem functioning. February would represent the well-mixed period of water column, June a period of thermal stratification characterized by increases in dinoflagellates and cocolitophores following the diatoms spring bloom (e.g. Agirbas et al., 2014; Eker-Develi and Kideys, 2003), and December a period of erosion of the seasonal thermocline. Seawater for each experiment was collected in 5 l Niskin bottles from the subsurface chlorophyll maximum (SCM) based on in situ fluorescence profiles, transferred gently into two 20 l carboys, and then transported immediately to the laboratory where the dilution experiments were conducted. All experimental bottles, silicone tubing, and other materials were acid-washed (10% HCl) and rinsed with Milli-Q water prior to each experiment. Filtered seawater (FSW) for experiments was generated by gentle gravity filtration of the incubation water using cartridge filters (0.2 μm pore size). Depending on the concentration of plankton abundance, the filtration process took approximately 2–4 h. The remaining seawater (initial seawater, ISW) was gently prescreened by syphoning through a submerged 20 μm and 200 μm mesh to remove microzooplankton + mesozoopankton and mesozooplankton, respectively. In parallel treatments, whole seawater (unscreened), containing assemblages of natural plankton was used to assess the impact of screening on microzooplankton and grazing by mesozooplankton. The ISW was diluted by FSW to four target dilutions of 20, 45, 70, and 100% (ISW: ISW plus FSW) in transparent polycarbonate bottles. The incubation volume was 3.2 l and treatments were carried out in duplicate. Some studies add low concentration of nutrients to prevent that phytoplankton growth rates are altered in a result of dilution process (e.g. Calbet et al., 2008; Dupuy et al., 2011). However, nutrient addition might have negative effects on growth coefficients of phytoplankton (Landry and Hassett, 1982; Worden and Binder, 2003) and feeding behaviour of microzooplankton (Worden and Binder, 2003). Therefore, nutrients were not added to the bottles to keep plankton communities close to in situ conditions. The experimental bottles were placed in deck incubators for 24-h period. Incubator was cooled to ambient temperatures with running seawater and screened to ambient light intensity using appropriate light screens. Experimental bottles were gently rotated to avoid sedimentation for 4–6 times during incubation.

Initial and final samples of incubation were collected to enumerate Chl-*a* concentration and carbon biomass of *Synechococcus* spp., HB and HNF as described in Section 2.2.1. Chl-*a* was determined by filtering 250–500 ml of water (depending on season and dilution level) through Whatman glass fibre filters (GF/F, 25 mm diameter). After filtration, the filters were stored frozen at −80°C until fluorometric analysis of acetone extracts (Parsons et al., 1984) using a Turner Designs Fluorometer.

Growth rates of autotrophs, *Synechococcus* spp., HB, HNF and grazing rates of heterotrophic protists were calculated using the exponential model of Landry and Hassett (1982):

$$P_t = P_0 e^{(k-g)t},$$

where P_0 and P_t are the initial and final concentrations of Chl-*a* and prey carbon biomass, and t is the incubation time. The instantaneous coefficients of prey growth (μ) and grazing mortality (g) were estimated by linear regression of apparent growth rate against fraction of unfiltered seawater. The apparent growth rate (k) for each dilution was calculated according to the following equation:

$$k = \frac{1}{t}\ln\left(\frac{P_t}{P_0}\right).$$

Non-significant grazing rates were not excluded following recommendations of Latasa (2014) and Landry (2014). Daily prey production (P) and grazing losses (G) (μg C l^{-1} d^{-1}) (for both significant and non-significant grazing rates) were calculated according to Landry et al. (2000):

$$P = \mu\left(\frac{P_0[e^{(\mu-g)t}-1]}{[\mu-g]t}\right),$$

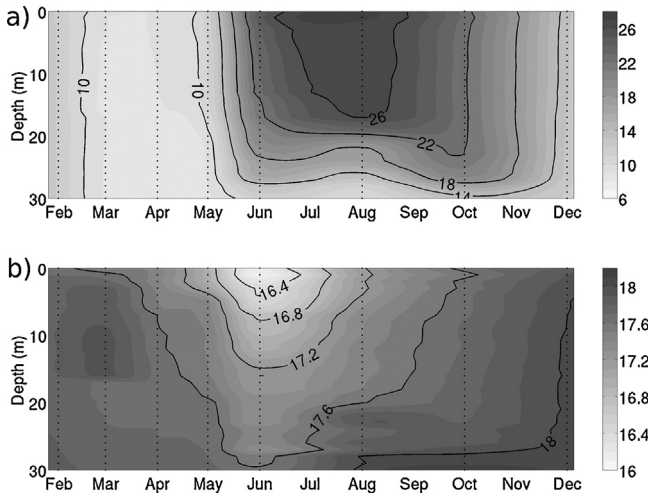

Figure 2 Temperature (°C) (a) and salinity (b) profiles of sampling station between February and December 2011.

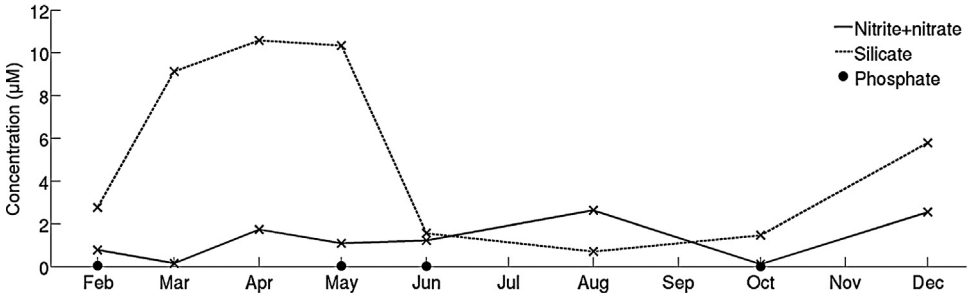

Figure 3 Average nutrient concentrations within euphotic zone between February and December 2011. PO_4 concentrations were below detection limit except for February, May, June and October (<0.04 μM).

$$G = g\left(\frac{P_0[e^{(\mu-g)t}-1]}{[\mu-g]t}\right).$$

Nano- and microzooplankton grazing pressure on initial prey standing stock (P_i, %) was calculated according to the following equations:

$$P_i = \frac{G}{P_0}\times 100.$$

3. Results

3.1. Water column structure

The study area exhibited typical hydrographic conditions of the Black Sea (Oguz et al., 2006). Overall, a well-mixed water column was found from February through April, whereas marked stratification was detected in the summer months, with a thermocline located at ~20 m depth and up to 15°C temperature difference between the surface and deeper waters (Fig. 2a). The highest (27.3°C) and lowest (8.1°C) surface temperatures were detected in August and February, respectively. The presence of low salinity at the surface was occasionally observed, especially in summer (Fig. 2b). The surface salinity was lowest (16.2) in June and highest in February (Fig. 2b). Euphotic depth varied between 21–31 m, being shallower in winter and deeper in summer. Euphotic zone averages of SiO_2 showed a clear seasonal cycle, with concentrations ranging from 0.70 (August) to 10.6 μM (April). Seasonal variations of NO_{2+3} were less clear, varying from 0.11 (October and March) to 2.62 μM (August). PO_4 concentrations were below detection limit except for February, May, June and October (<0.04 μM) (Fig. 3). N P^{-1} ratios in the euphotic zone were 20, 34, 42 and 18 for February, May, June and October, respectively. Averaged SCM concentration ranged between 0.47–2.18 μg l^{-1} reaching maxima in late spring (May) (Fig. 4).

3.2. Autotrophic and heterotrophic carbon biomass and composition

The total plankton carbon biomass was highest (155 μg C l^{-1}) in June, and lowest (~40 μg C l^{-1}) in February, October and December (Fig. 4). The autotrophic carbon (Auto-C) and heterotrophic carbon (Hetero-C) biomasses showed similar trends during the study period, ranging from 8 to 62 μg C l^{-1} and 27 to 93 μg C l^{-1}, respectively (Fig. 5). For all samples, the Auto-C and Hetero-C biomasses averaged (±SD) 20 ± 17 μg C l^{-1} and 49 ± 25 μg C l^{-1}, respectively. In all samples, Hetero-C always comprised more than 60% of total plankton carbon biomass (Fig. 4). As an indicator of the trophic characteristic of a system, the median of Hetero-C to Auto-C ratios was 2.3.

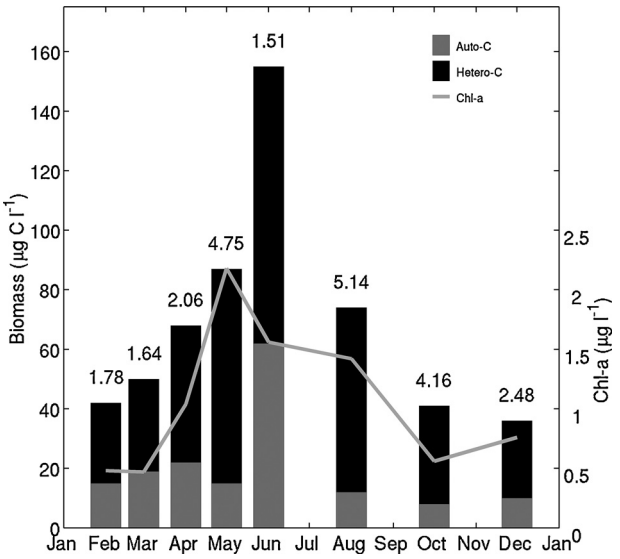

Figure 4 Total carbon biomass of autotrophic (Auto-C) and heterotrophic (Hetero-C) plankton, Chl-*a*, and heterotroph/autotroph ratio (numbers on top of bars) from February to December 2011 at the sampling station.

The Auto-C biomass was comprised by *Synechococcus* spp. (Syn), autotrophic nanoflagellates (ANF), prymnesiophytes (Prym), autotrophic dinoflagellates (A-Dino) and diatoms (Fig. 5). The relative contributions of these groups to Auto-C biomass is shown in Fig. 6a. Autotrophic picoplankton (A-Pico) consisted entirely of *Synechococcus* spp, with biomass ranging from 0.4 to 6.1 μg C l^{-1}. The contribution of A-Pico to the Auto-C biomass increased in May during stratification and remained relatively high until December. The biomass of autotrophic nanoplankton (A-Nano) varied from 0.7 to 18 μg C l^{-1}. A-Nano (mostly ANF) significantly contributed to the Auto-C biomass from February to May, with an average (±SD) of 42 ± 12%. This contribution was particularly high (>50%) in February and March. In June a major bloom of prymnesiophytes, *Emiliania huxleyi*, was observed. After June, the biomass of A-Nano and its contribution to Auto-C biomass was lower. Autotrophic microplankton (A-Micro) biomass ranged from 4.9 to 38 μg C l^{-1}, and its contribution to Auto-C was on average (±SD) 58 ± 11%. The A-Micro biomass was relatively stable throughout the year, with the exception of a pronounced maximum in June during high A-Dino biomass. A-Micro biomass was dominated by A-Dino from June to October (>75%) and diatoms during the rest of

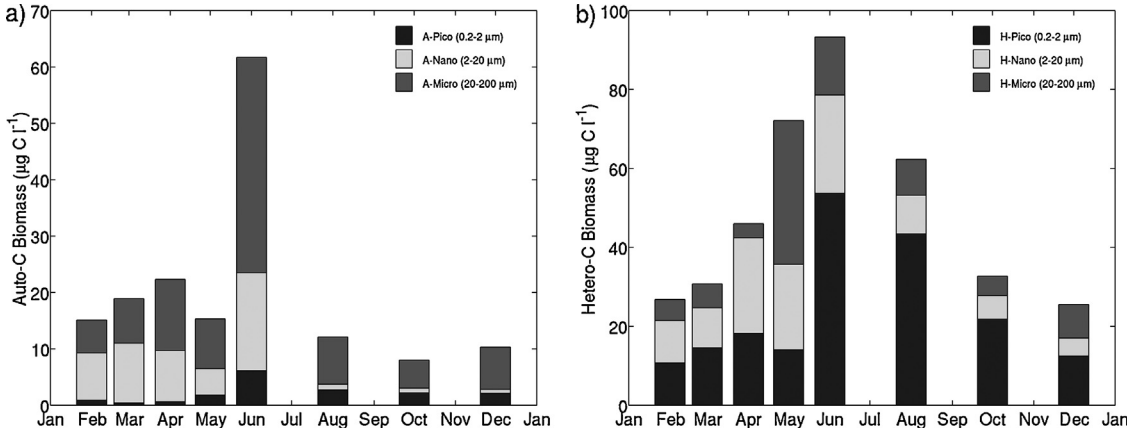

Figure 5 Contribution of size classes to autotrophic (a) and heterotrophic (b) carbon biomass from February to December 2011 at the sampling station.

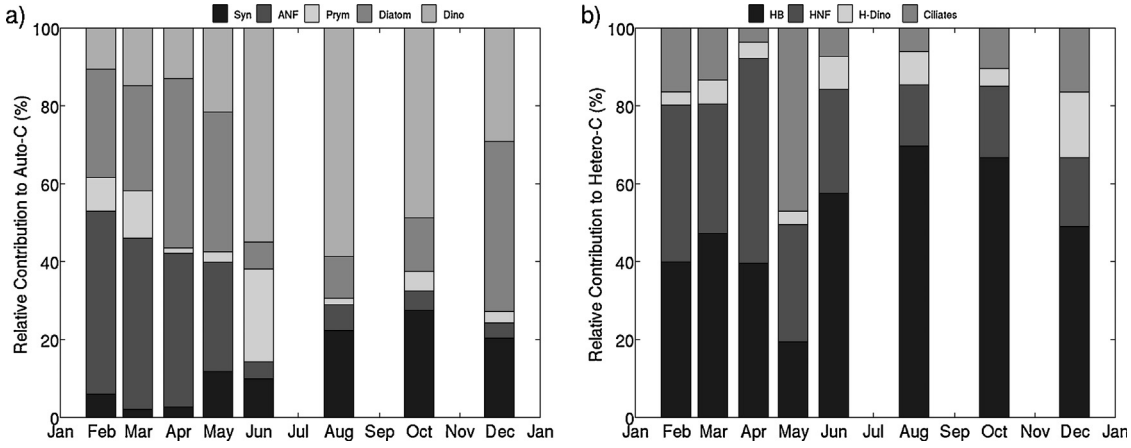

Figure 6 Relative contribution to total Auto-C (a) and Hetero-C (b) biomass <200 μm by groups from February to December 2011 at the sampling station. Auto-C: *Synechococcus* spp. (Syn), autotrophic nanoflagellates (ANF), prymnesiophytes (Prym), autotrophic dinoflagellates (A-Dino) and diatom. Hetero-C: heterotrophic bacteria (HB), heterotrophic nanoflagellates (HNF), heterotrophic dinoflagellates (H-Dino) and ciliates.

the year (>60%). Diatom biomass varied between 1.1–9.7 μg C l^{-1} with maxima in April dominated by the genera *Chaetoceros* and *Rhizosolenia*. A-Dino biomass varied from 1.6 to 34 μg C l^{-1} with maxima in June and main genera were *Gonyaulax*, *Ceratium* and *Prorocentrum*. The C:Chl-*a* ratio was calculated using Auto-C biomass and Chl-*a*, and ranged between 7 and 40 (median of 18). To summarize, we observed one peak of Auto-C biomass in the June sampling, due to a bloom of *E. huxleyi* and A-Dino. In the remaining samplings, the A-Micro biomass was relatively stable (average ± SD of 15 ± 5 μg C l^{-1}) changing from diatoms in winter to dinoflagellates in summer, and the A-Nano and A-Pico biomass showed opposite seasonal patterns. The A-Nano biomass was higher in the first half of the year and the A-Pico biomass was higher in the second half. There was no correlation between Auto-C biomass with temperature, Chl-*a* concentrations, or nutrients ($p > 0.05$). However, Auto-C biomass significantly correlated with salinity ($r^2 = -0.72$, $p < 0.05$).

The Hetero-C biomass was comprised of heterotrophic bacteria (HB), heterotrophic nanoflagellates (HNF), heterotrophic dinoflagellates (H-Dino) and ciliates (Fig. 5). The relative contribution of these groups to Hetero-C biomass is shown in Fig. 6b. Micrometazoans <200 μm were only present at low abundance (<1 ind. l^{-1}) so their contributions to Hetero-C < 200 μm were not considered. Heterotrophic picoplankton (H-Pico), composed entirely of heterotrophic bacteria, was the most substantial component of the Hetero-C biomass, with contributions ranging between 19% and 70%. H-Pico biomass ranged from 11 to 54 μg C l^{-1} with highest concentrations in June. The biomass of heterotrophic nanoplankton (H-Nano) composed entirely of HNF, ranging between 4.5–25 μg C l^{-1} and was the second most important contributor to Hetero-C biomass in majority of samples. Heterotrophic microplankton (H-Micro) was represented by H-Dino and ciliates, and their combined biomass ranged from 6 to 61 μg C l^{-1}. In the majority of samples, ciliates were the most substantial component of H-Micro biomass (62% contribution to H-Micro, for all samples). Ciliates were dominated by the genera *Laboea* and *Strombidium*, while H-Dino was dominated by *Protoperidium* and *Gyrodinium*. No significant correlation between Hetero-C biomass and temperature, Chl-*a* concentration or nutrients ($p > 0.05$) were found. However, Hetero-C biomass significantly correlated with salinity ($r^2 = -0.86$, $p < 0.05$).

There was no significant correlation between Hetero-C and Auto-C biomass ($p > 0.05$). The carbon biomass of total grazers (HNF + microzooplankton) correlated significantly with Chl-*a* ($r^2 = 0.79$, $p < 0.05$) but significant correlation was absent for Auto-C biomass ($p > 0.05$). Among the grazers, only H-Dino was significantly correlated with HB ($r^2 = 0.74$, $p < 0.05$), *Synechococcus* spp. ($r^2 = 0.80$, $p < 0.05$) and A-Dino ($r^2 = 0.73$, $p < 0.05$) (Table 1).

3.3. Trophic interactions

The dilution experiments exhibited distinct results during 2011 (Table 2). Growth and grazing rates for the whole phytoplankton community and group-specific (*Synechococcus* spp., HB and HNF) were calculated based on the measured net changes in total Chl-*a* and taxon-specific carbon biomass, respectively. Production and grazing losses were computed based on the estimated growth and grazing rates (including both significant and non-significant data), and carbon biomass.

In the <200 μm fraction, initial Chl-*a* concentration ranged between 0.47–1.52 μg l^{-1}, with highest concentrations in June (Table 3). The phytoplankton growth rates were particularly high in February (1.67 d^{-1}) and June (2.43 d^{-1}), but low in December (0.23 d^{-1}). Grazing rates were moderate in February (0.77 d^{-1}) and June (0.53 d^{-1}), and also low in December (0.07 d^{-1}). Growth rates always exceed grazing rates. Estimates of mean daily PP followed the growth rates, being 43.1 μg C l^{-1}, 289.7 μg C l^{-1} and 3 μg C l^{-1} in February, June and December, respectively. Mean daily removal of primary production (PP) by nano-microzooplankton ranged between 21–46% with the highest value in February. Overall, the unscreened and <200 μm fraction experiments yielded similar results (Table 2). The <20 μm fraction represented 77%, 32% and 39% of the <200 μm Chl-*a* in February, June and December, respectively. Estimated growth rates were similar to the <200 μm fraction, and also always exceed grazing rates. Mean daily PP (<20 μm) were 19.9 μg C l^{-1}, 50.0 μg C l^{-1} and 1.2 μg C l^{-1} in February, June and December, respectively. Mean daily removal of PP (<20 μm) by nanozooplankton ranged between 7–144%, with the highest value in December and the lowest in June (Table 2).

As a result of a low fluorescence of *Synechococcus* spp., the June experiment was not considered. Initial abundance of *Synechococcus* spp. in experimental bottles was 3.37×10^7 cells l^{-1} in February and 2.62×10^7 cells l^{-1} in December. In the <200 μm fraction, estimated growth rates

Table 1 Correlation coefficients between heterotrophic protists and potential preys. Hb, heterotrophic bacteria; Syn, *Synechococcus* spp.; Anf, autotrophic nanoflagellate; Prym, prymnesiophyte; A-Dino, autotrophic dinoflagellates; Auto-C, autotrophic carbon biomass; Hnf, heterotrophic nanoflagellates; H-Dino, heterotrophic dinoflagellates; Cil, ciliate; Hetero-C, heterotrophic carbon biomass; Total grazers (HNF + H-Dino + Cil).

	Hb	Syn	Anf	Prym	A-Dino	Diatom	Auto-C	Chl-*a*
Hnf	0.11	0.09	0.17	0.26	0.26	0.39	0.47	0.33
H-Dino	**0.74***	**0.80***	−0.25	0.55	**0.73***	−0.05	0.50	0.13
Cil	−0.02	−0.01	−0.01	−0.03	−0.02	0.01	−0.01	**0.70***
Hetero-C	0.59	0.57	−0.03	0.46	0.60	0.01	0.53	0.46
Total grazer	0.03	0.09	0.02	0.11	0.12	0.12	0.19	**0.79***

* $p < 0.05$.

Table 2 Mean growth and grazing mortality rates of phytoplankton (Chl-*a*), *Synechococcus* spp., heterotrophic bacteria (HB) and heterotrophic nanoflagellate (HNF) calculated from the size-fractioned dilution experiments. μ, growth rate; g, grazing mortality rate; r^2, the correlation coefficient of the linear regression of apparent growth rate against fraction of unfiltered seawater; P, prey production; G, grazing losses; P_i, percentage of prey standing stock daily removed by grazing.

Experiment	Date	Size fraction	μ (d^{-1})	g (d^{-1})	g:μ	r^2	P (μg C l^{-1} d^{-1})	G (μg C l^{-1} d^{-1})	P_i [%]
Chlorophyll *a*	February 2011	Unscreened	1.72	0.90	0.52	0.76*	43.6	22.8	139.4
		<200 μm	1.67	0.77	0.46	0.67*	43.1	20.0	124.7
		<20 μm	1.14	0.47	0.41	0.82**	19.9	8.2	67.2
	June 2011	Unscreened	2.21	0.74	0.33	0.67*	200.8	67.2	168.6
		<200 μm	2.43	0.53	0.21	0.79*,a	289.7	63.2	158.6
		<20 μm	1.68	0.11	0.07	0.18	50.0	3.3	26.7
	December 2011	Unscreened	0.10	0.02	0.20	0.03a	1.3	0.3	2.1
		<200 μm	0.23	0.07	0.30	0.08	3.0	0.9	7.6
		<20 μm	0.28	0.39	1.44	0.63*,a	1.2	1.7	36.9
Synechococcus	February 2011	Unscreened	0.37	0.48	1.29	0.95**	0.4	0.6	45.5
		<200 μm	0.35	0.68	1.94	0.90**	0.4	0.8	57.8
		<20 μm	0.11	0.72	6.54	0.89**	0.1	0.8	53.7
	December 2011	Unscreened	0.80	0.55	0.68	0.84**	1.0	1.5	70.3
		<200 μm	0.46	0.19	0.41	0.43	1.1	0.4	21.9
		<20 μm	1.27	0.51	0.40	0.56*	3.7	1.5	76.5
HB	February 2011	Unscreened	0.47	0.70	1.50	0.72*	4.6	6.9	62.3
		<200 μm	0.57	0.66	1.16	0.79*,a	6.1	7.1	63.1
		<20 μm	0.15	0.38	2.53	0.62*	1.2	3.1	33.9
	June 2011	Unscreened	0.82	1.08	1.32	0.98**	42.1	55.5	94.7
		<200 μm	0.80	1.20	1.50	0.90**	37.6	56.5	98.8
		<20 μm	0.77	1.22	1.58	0.95**	35.5	56.4	98.6
	December 2011	Unscreened	0.66	0.90	1.36	0.92**	12.6	17.0	79.9
		<200 μm	0.63	0.76	1.20	0.96**	11.1	13.4	71.5
		<20 μm	0.79	0.49	0.62	0.53	18.6	11.6	57.0
HNF	February 2011	Unscreened	0.46	0.36	0.78	0.18a	7.7	6.1	37.7
		<200 μm	0.50	0.39	0.78	0.70*,a	7.4	5.8	41.2
	June 2011	Unscreened	0.93	0.17	0.18	0.02	32.4	5.9	23.7
		<200 μm	0.99	0.42	0.42	0.14	33.0	14.0	56.0
	December 2011	Unscreened	0.21	0.26	1.23	0.30a	0.22	0.3	5.3
		<200 μm	0.25	0.77	3.08	0.67*,a	0.24	0.8	15.0

[a] One outlier removed (Gallegos, 1989).
[*] $p < 0.05$.
[**] $p < 0.01$.

Table 3 Initial concentration of Chl-*a* (μg l^{-1}) and contribution of different size groups and physico-chemical parameters from size fractioned dilution experiments.

Time	<20 μm Chl-*a*	20–200 μm Chl-*a*	<200 μm Chl-*a*	Temp. (°C)	NO_{2+3} (μM)	PO_4 (μM)	SiO_4 (μM)	N P^{-1}
February 2011	0.36	0.11	0.47	8.9	0.78	0.04	2.76	20
June 2011	0.48	1.04	1.52	23.7	1.22	0.03	1.57	41
December 2011	0.29	0.45	0.74	12.3	1.94	nd	5.79	2

nd, non-detectable.

of *Synechococcus* spp. were 0.35–0.46 d^{-1}, and grazing rates were 0.19–0.68 d^{-1}. Estimated daily *Synechococcus* spp. production was lower in February (0.4 μg C l^{-1}) than in December (1 μg C l^{-1}). Mean daily removal of *Synechococcus* spp. production by nano-microzooplankton was much higher in February (194%) than in December (41%). Despite differences between the unscreened and <200 μm fraction, estimated mean daily PP by *Synechococcus* spp. was nearly identical due to low initial biomass (Table 2). Comparing the <20 μm fraction with the <200 μm, the grazing rates increased in both June and December, but growth rates decreased in February and increased in December. Daily removal of production by nano-grazers drastically increased to 654% in February, while remained the same in December (40%) (Table 2).

Initial abundance of HB in experimental bottles was 2.67×10^9 cells l^{-1} in February, 5.71×10^9 cells l^{-1} in June and 1.27×10^9 cells l^{-1} in December. HB growth rates were 0.57–0.80 d^{-1} and grazing rates were 0.66–1.20 d^{-1}, in the <200 μm fraction. Both growth and grazing rates were higher in June. Estimates of mean daily BP (bacterial production) ranged between 6.1–37.6 μg C l^{-1} with lowest in February and highest in June. Nano-microzooplankton exerted substantial grazing pressure on bacteria, always removing >100% of daily BP. Overall, the unscreened and <200 μm fraction experiments yielded similar results (Table 2). In the <20 μm fraction, grazing rates were also higher than growth rates, except in December. Mean daily removal of BP ranged between 62–253%, with highest in February and lowest in December (Table 2).

Initial abundance of HNF in experimental bottles was 5.36×10^3 cells l^{-1} in February, 1.98×10^7 cells l^{-1} in June and 1.32×10^3 cells l^{-1} in December. In the <200 μm fraction, growth rates of HNF were 0.25–0.99 d^{-1}, with maxima in June. Grazing rates were 0.39–0.77 d^{-1}, with maxima in December. Mean daily HNF production changed from 7.4 μg C l^{-1} in February to 33 μg C l^{-1} in June to 0.24 μg C l^{-1} in December. Mean daily removal of HNF production ranged between 42% in June to 308% in December. A significant increase of grazing rates in June and December occurred from the unscreened to <200 μm treatments (Table 2).

4. Discussion

4.1. Community structure of autotrophic and heterotrophic plankton

The present study focuses on a monitoring station which could be taken as being representative of the coastal SE Black Sea, a critical fishing area for the Black Sea (Oguz et al., 2012a) and where the regional ecosystem health is considered to be a relatively less degraded ecosystem than the northern shelfs (Oguz et al., 2012b). The hydrography followed an expected pattern, with mixed waters in winter and thermally stratified waters in summer. Lower surface salinity was observed from spring to summer in agreement with seasonality of river discharges (Kara et al., 2008). The nutrients, in particular nitrate, were low, but in agreement with other reports for the southern Black Sea (Eker-Develi and Kideys, 2003).

The autotrophic communities showed clear changes throughout the year. From February to May, diatoms and ANF comprised the majority of Auto-C biomass (combined average ± SD contribution of 73 ± 7%), with similar contributions from both communities. In June, when the water column fully stratified, a major increase in dinoflagellates and coccolithophores (mostly *E. huxleyi*) biomass was observed. Summer blooms of these groups are common in the Black Sea (e.g. Agirbas et al., 2014; Eker-Develi and Kideys, 2003; Oguz and Merico, 2006). A prominent increase in *Synechococcus* spp. carbon biomass was also observed in June, as is the case in nutrient-depleted stratified waters (e.g. Agawin et al., 1998; Feyzioglu et al., 2004; Uysal, 2001). In the following months, the total Auto-C rapidly decreased and it became dominated primarily by A-Dino and secondarily by *Synechococcus* spp. In December, when the thermocline weakened, a return of diatoms was observed. Overall, an unexpected result was the low diatom biomass during the first half of the year when compared to those reported in previous years in the Black Sea (Agirbas et al., 2014; Eker et al., 1999; Eker-Develi and Kideys, 2003). One explanation is that our discrete sampling did not coincide with any bloom. An additional explanation was the warm winter of 2010/2011 in the SE Black Sea, which had the highest sea surface temperature winter-average of the preceding eight winters (Agirbas et al., 2015). The warm winter may have provided favourable conditions for both nutrient limitation and an earlier top-down control on A-Micro (e.g. Caron and Hutchins, 2012). In such conditions, the spring seasonal bloom is expected to either be weakened or absent (e.g. Oguz et al., 2006). Nevertheless, as discussed further on, estimated high growth rates of autotrophs during the February dilution experiment suggest no nutrient limitation, which in turn would point to high-turnover rates as an explanation for the low diatom biomass. The prominence of ANF until May as a contributor to Auto-C may be connected with the low diatom biomass or, perhaps, it is a common winter-period situation outside sporadic diatom blooms. Significant contributions of A-Nano to total Auto-C have been found in other regions during winter and outside seasonal blooms (e.g. Teixeira et al., 2011; Verity et al., 2002). Whether this is a typical feature of the regional lower trophic levels or the result of an anomalous winter, remains unclear and prompts for more studies in the area. In this study, no distinction was made between mixotrophs and strict heterotrophs, therefore the presence of mixotrophic dinoflagellates may have led to an overestimate in autotrophic biomass. However, summer biomass of mixotrophs is reported to be 4% of the total carbon biomass of the phagotrophic organisms in the NW Black Sea (Bouvier et al., 1998).

Heterotrophic bacteria contributed on average half of the Hetero-C biomass reaching the highest values in the summer months. Similar high (>50%) contributions of HB to Hetero-C have been found in other coastal regions (e.g. Dupuy et al., 2011; Linacre et al., 2012). Our HB carbon biomass fall within the range of previous studies in the Black Sea, though these were only focused on the spring and summer periods (Bouvier et al., 1998; Kopuz et al., 2012; Sorokin et al., 1995). Among the grazers, both HNF and H-Micro presented a seasonal succession with highest biomass in the spring-summer period. Generally, HNF carbon biomass was higher, with a notable exception in May during a ciliate bloom. These results are in agreement with other studies that report higher contributions of small heterotrophic flagellates outside productive

seasons (e.g. Calbet et al., 2008; Teixeira et al., 2011). The ciliate bloom on May might have been triggered by the onset of thermal stratification as previously reported (e.g. Becquevort et al., 2002; Dupuy et al., 2011). Between May and June, the reduction in H-Micro biomass, in particular, ciliate may reflect a top-down control by mesozooplankton, since ciliates can sometimes be a favoured food items for copepods (e.g. Atkinson, 1996; Calbet and Saiz, 2005).

Overall, the seasonal trajectories of <200 μm carbon biomass of autotrophic and heterotrophic plankton were similar. Significant correlations were found between ciliates and chlorophyll-*a* (Table 1), but no significant correlation is found between ciliates and the autotrophic groups exposing the weaknesses and difficulty of interpreting these correlations. An interesting finding for this coastal system was the high ratio of heterotrophic to autotrophic carbon. Instances where the biomass of heterotrophs exceeds that of autotrophs (e.g. Cho and Azam, 1990; Fuhrman et al., 1989; Gasol et al., 1997; Simon et al., 1992; Sorokin, 1977) are typical of the oligotrophic ocean and have been explained by high turnover rate of the autotrophic pool (Odum, 1971) or low nutrient input (Duarte et al., 2000). In this highly dynamic coastal region, the year of 2011 might have been an unusual year with low primary production and high recycling, a situation which can occur naturally because of climate variations. The excess of heterotrophic biomass, in particular HB, might also have occurred due to the high dissolved organic carbon concentrations in the Black Sea (~2 times higher than the open ocean; Ducklow et al., 2007).

4.2. Food web interactions

Our dilution experiments present valuable data on the growth and grazing dynamics within the microbial food web in the coastal SE Black Sea. This supplements the few such studies so far in the Black Sea (Bouvier et al., 1998; Stelmakh, 2013; Stelmakh et al., 2009; Stelmakh and Georgieva, 2014). Our experiments lack temporal coverage to resolve a complete seasonal cycle, but they do represent three contrasting scenarios of the microbial food web structure in 2011. Initial concentrations in the dilution experiments of the autotrophic and heterotrophic communities are shown in Fig. 5. In February, there was a high contribution (~50%) of ANF to total Auto-C biomass, thus representative of a mid-winter, non-bloom situation. The June experiment was performed during the most productive sampling, coincident with a bloom of prymnesiophytes and dinoflagellates, thus representative of the typical early-summer blooms in the SE Black Sea (e.g. Agirbas et al., 2014; Eker-Develi and Kideys, 2003; Oguz and Merico, 2006). Finally, the December experiment was characterized by a relatively low Auto-C biomass. A common situation to all experiments was the high ratio of HB to Auto-C biomass (0.7, 0.9 and 1.2 for February, June and December, respectively).

Nano- and microzooplankton play an important role in the carbon transfer to higher trophic levels and have been estimated to consume ~60% of daily PP in coastal waters (Calbet, 2008). In the Black Sea, annual removal of PP was reported as 65% (Stelmakh and Georgieva, 2014). In this study, considering the whole autotrophic community (<200 μm fraction experiment) the percentage of PP consumed by nano-microzooplankton was 46%, 21% and 30% in February, June and December, respectively. While the February estimate was within reported ranges, the June and December estimates were relatively lower than those in the literature. A possible reason for low grazing in June might be related to the concurrent bloom of *E. huxleyi*. Our size-fraction dilution experiments indicate that almost no production of <20 μm was consumed by nano-grazers. Low grazing rates concomitantly with a high biomass of *E. huxleyi* was also reported in the Northern Black Sea (Stelmakh, 2013; Stelmakh and Georgieva, 2014) and other regions (e.g. Fileman et al., 2002; Fredrickson and Strom, 2009; Strom et al., 2003). Nevertheless, we note that despite low grazing (21%), still a large portion of carbon (63 μg C l^{-1} d^{-1}) was being channelled to the grazers, indicating an active microbial food web. During December, the low community grazing might have been related to the very low growth rate, which in turn may indicate low nutritional quality of the autotrophic prey. Overall, for the three experiments, the grazing rates were always lower than growth rates, allowing the standing stock to grow. Estimated growth rates in February and June were high, which suggests autotrophs were not nutrient-limited although nutrients were scarce. Low nutrients do not necessarily imply that phytoplankton growth is under strong nutrient control since the nutrient reservoirs could be quickly renewed through remineralization by heterotrophs, especially during the high abundance of autotrophs in June. In December, although nitrate and silicate were higher than February and June, the phosphate was undetectable, which may have been the cause of the lowest growth recorded. Dilution experiments are not free of problems (Schmoker et al., 2013) and the high growth rates of February and June may have resulted from artefacts such as an increase in the nutrient pool (and remineralization) due to broken cells during filtration. Nevertheless, the experiments were meticulously done, filtration was slow (by gravity) and we have no reason to suspect this was the case. Also, the question remains of whether or not phytoplankton growth rates were affected during incubations as a result of no nutrient amendments. Another uncertainty in our data is related to mixotrophy. In the northwest Black Sea, based on uptake of fluorescently labelled prey, Bouvier et al. (1998) reported an absence of mixotrophic nanoflagellates and the occurrence of mixotrophic dinoflagellates in only one station, with grazing activity mainly on heterotrophic bacteria and nanoplankton. Since mixotrophs can be either grazers or prey they can confound our results. Some known mixotrophic ciliates (e.g. *Laboea* and *Strombidium* spp.) were found during microscopic examination (<15%), but no chloroplasts were observed.

In other regions, picophytoplankton have been shown to be an important contributor to the microbial food web (e.g. Azam et al., 1983). In the Black Sea, the biomass of *Synechococcus* spp. can be an important contributor to Auto-C (e.g. Kopuz et al., 2012), but the consumption by nano-micrograzers has not yet been reported. In this work, although they were significantly grazed (194% of daily *Synechococcus* PP was removed by nano-micro grazers in February), because of the low biomass and growth rates, carbon flow to grazers was lower than other groups. However, the importance of *Synechococcus* spp. to grazers might increase deeper in the water column since maximal biomass has been reported at the euphotic depth (~30 m) in the Black Sea

especially during thermal stratification (Kopuz et al., 2012; Uysal, 2001).

The importance of HB production and its consumption by microbial grazers has been documented for other coastal regions in the world (e.g. Linacre et al., 2012; Teixeira et al., 2011) but it is still poorly documented in the Black Sea (Bouvier et al., 1998). A clear pattern from our dilution experiments was that HB were always heavily grazed by nano-microzooplankton (daily removal of >100% BP) thus top-down control appear to play an important role in regulating HB biomass. Despite heavy predation, we observe relatively high HB biomass throughout the year, which may be maintained by the high dissolved organic carbon concentrations in the Black Sea (Ducklow et al., 2007). HB biomass may be controlled by several sources other than local phytoplankton production such as river-transported materials, terrestrial runoff, anthropogenic discharges, benthic fluxes, cycles of sediment resuspension and seasonal re-emergences of subsurface coloured dissolved organic matter (CDOM) accumulations (Lee et al., 2001). Non-planktonic sources may explain the imbalance observed in the experiment of December when there was not enough primary production to be converted to HB (considering 25% growth efficiency).

Our experimental data (<200 μm) revealed that autotrophic prey were more important than HB as a carbon source for grazers in February, but the reverse was observed in December when the grazing on autotrophs was not significant (for <200 μm), and the vast majority of total carbon comprised HB (~95% of total) (Fig. 7). However, carbon flow from autotrophs in particular from *Synechococcus* spp. was observed in <20 μm size fractioned. The preference of HB in December appears related as a strategy for available food resources since the total daily production (>200 μm autotrophs + HB = 14.3 μg C l^{-1} d^{-1}) was dominated by HB production (79%). In June, an intermediate situation was observed, with similar contributions of autotrophs and HB to total biomass. Both growth rates of autotrophs and HB were high, and a possible explanation for the bacterivorous pattern is that heterotrophic protists, in particular <20 μm, preferred to prey on the metabolically active bacteria (e.g. Gonzalez et al., 1990) rather than *E. huxleyi*, which might deter grazing. In February, low growth rates of HB and high growth rates of autotrophs, in particular ANF as indicated by the <20 μm size fraction experiment, appear sufficient to explain the preference of grazers towards autotrophs. There are no studies in the Black Sea comparing the carbon flow from autotrophs and heterotrophs to grazers, but our results indicate that nano- and micro-grazers seem to be sustained by more than one pattern of autotrophic and heterotrophic preys.

Our <20 μm size fraction experiment indicates that HNF seems to be an important grazer within the microbial food web. HNF grazed heavily on pico-sized prey in particular HB, which confirms the role of HNF as an important consumer in the Black Sea as reported in other regions (e.g. Andersen and Fenchel, 1985; Calbet et al., 2008; Dupuy et al., 2011; Fenchel, 1982). Comparing the experiments with and without grazers >20 μm, the small differences in HB grazing losses indicate that HB was mostly grazed by HNF. This is most notable in June and December when HB grazing losses where higher, HNF seem to be an important link of transferring HB carbon within the microbial food web. The importance of HNF as a consumer of small autotrophs was only evident in February when grazing losses of the <20 μm fraction were half of the <200 μm fraction, suggesting that a significant amount of carbon was transferred to grazers by small autotrophs. In June, these experiments suggest that grazers mainly preyed on >20 μm autotrophs, and in December, as previously described, the main carbon source was from heterotrophs. Given the high bacterial biomass of the region and high consumption of HNF production, then HNF would be a key organism to transfer this energy to microzooplankton which in turn are favourite prey for mesozooplankton (e.g. Atkinson, 1996; Calbet and Saiz, 2005; Stoecker and Capuzzo, 1990).

5. Conclusions

Heavily exploited fisheries and multiple ecosystem regime shifts in the Black Sea during the last half-century call for an understanding of the structure and functioning of regional microbial plankton communities. This is a first attempt to

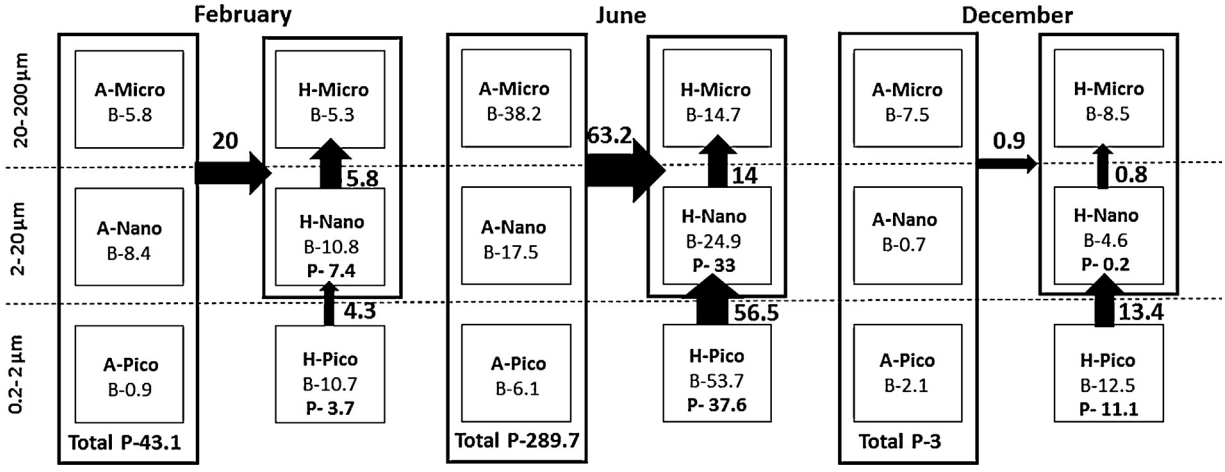

Figure 7 Schematic representation of carbon flow within microbial food web in the SE Black Sea during 2011. Arrows show daily grazing losses (μg C l^{-1} d^{-1}) according to estimation of <200 μm experiments. The thickness of arrows corresponds to amount of carbon flow from autotrophs, H-Pico and H-Nano. B, biomass (μg C l^{-1}); P, daily production (μg C l^{-1} d^{-1}).

investigate the relative importance of pico-, nano- and microplankton communities in the Black Sea and the major trophic interactions between them. Small autotrophs and heterotrophic bacteria comprised an important compartment of plankton biomass and were important carbon sources for nano- and microzooplankton. Since nano- and microzooplankton are available for direct mesozooplankton ingestion, they might be considered as an important link between lower level production and higher trophic levels in the SE Black Sea, in particular in the years of low autotrophic production. The distinct carbon pathways found in the three experiments indicate that the system is complex and that it varies throughout the year, and possibly between years. There is a need to continuously monitor microbial plankton communities and understand their contribution to mesozooplankton diet, in particular copepods, which in turn support planktivorous fish stocks in the region. Dedicated experiments with continued long-term monitoring at fixed times and locations, with standardized techniques and additional measurements of CDOM pool are necessary. This study emphasizes that for realistic approaches to carbon cycling in the Black Sea, it is essential to consider trophic interactions between the full spectrum of prey and predator.

Acknowledgements

This study was funded by Research Fund of Karadeniz Technical University (Grant No: 2009.117.001.6). We are extremely grateful to Dr. Angus Atkinson for his constructive comments and Prof. Dr. Hasan Baha Buyukisik for technical advice on experimental design and valuable discussions in the course of this study. We are grateful to the captains and crew of r/v *Denar* for their cooperation at sea. We also thank the anonymous reviewers for their constructive comments.

References

Agawin, N.S.R., Duarte, C.M., Agustí, S., 1998. Growth and abundance of *Synechococcus* sp. in a Mediterranean Bay: seasonality and relationship with temperature. Mar. Ecol. Prog. Ser. 170, 45—53, http://dx.doi.org/10.3354/meps170045.

Agirbas, E., Feyzıoglu, A.M., Aytan, U., Valente, A., Kurt Yıldız, I., 2015. Are trends in SST, surface Chlorophyll-*a*, primary production and wind stress similar or different over the decadal scale in the south-eastern Black Sea? Cah. Biol. Mar. 56 (4), 329—336.

Agirbas, E., Feyzioglu, A.M., Kopuz, U., Llywellyn, C.A., 2014. Phytoplankton community composition in the south-eastern Black Sea determined with pigments measured by HPLC-CHEMTAX analyses and microscopy cell counts. J. Mar. Biol. Assoc. U.K. 1—18, http://dx.doi.org/10.1017/S0025315414001040.

Andersen, P., Fenchel, T., 1985. Bacterivory by microheterotrophic flagellates in seawater samples. Limnol. Oceanogr. 30, 198—202, http://dx.doi.org/10.4319/lo.1985.30.1.0198.

Atkinson, A., 1996. Subantarctic copepods in an oceanic, low chlorophyll environment: ciliate predation, food selectivity and impact on prey populations. Mar. Ecol. Prog. Ser. 130, 85—96, http://dx.doi.org/10.3354/meps130085.

Azam, F., Fenchel, T., Field, J.G., Gray, J.S., Meyer-Reil, L.A., Thingstad, F., 1983. The ecological role of water column microbes in the sea. Mar. Ecol. Prog. Ser. 10, 257—263.

Becquevort, S., Bouvier, T., Lancelot, C., Cauwet, G., Deliat, G., Egorov, V.N., Popovichev, V.N., 2002. The seasonal modulation of organic matter utilization by bacteria in the Danube—Black Sea mixing zone. Estuar. Coast. Shelf Sci. 54, 337—354, http://dx.doi.org/10.1006/ecss.2000.0651.

Besiktepe, S.T., Unluata, U., Bologa, A.S., 1999. Environmental Degradation of the Black Sea: Challenges and Remedies. NATO Science Series, 2/56. Kluwer Acad. Publishers, Dordrecht, The Netherlands, 393 pp., http://dx.doi.org/10.1007/978-94-011-4568-8.

Børsheim, K.Y., Bratbak, G., 1987. Cell volume to cell carbon conversion factors for a bacterivorous *Monas* sp. enriched from seawater. Mar. Ecol. Prog. Ser. 36, 171—175.

Bouvier, T., Becquevort, S., Lancelot, C., 1998. Biomass and feeding activity of phagotrophic mixotrophs in the northwestern Black Sea during the summer 1995. Hydrobiologia 363, 289—301, http://dx.doi.org/10.1023/A:1003196932229.

BSC, 2008. State of the Environment of the Black Sea (2001—2006/7). In: Oguz, T. (Ed.), Publications of the Commission on the Protection of the Black Sea Against Pollution (BSC) 2008-3, Istanbul, Turkey. 448 pp.

Calbet, A., 2008. The trophic role of microzooplankton in marine systems. ICES J. Mar. Sci. 65, 325—331, http://dx.doi.org/10.1093/icesjms/fsn013.

Calbet, A., Landry, M.R., 2004. Phytoplankton growth, microzooplankton grazing, and carbon cycling in marine systems. Limnol. Oceanogr. 49, 51—57, http://dx.doi.org/10.4319/lo.2004.49.1.0051.

Calbet, A., Saiz, E., 2005. The ciliate-copepod link in marine food ecosystems. Aquat. Microb. Ecol. 38, 157—167, http://dx.doi.org/10.3354/ame038157.

Calbet, A., Trepat, I., Almeda, R., Salo, V., Saiz, E., Movilla, J.I., Alcaraz, M., Yebra, L., Simo, R., 2008. Impacts of micro- and nanograzers on phytoplankton assessed by standard and size fractionated dilutions. Aquat. Microb. Ecol. 50, 154—156, http://dx.doi.org/10.3354/ame01171.

Carlson, C.A., Bates, N.R., Ducklow, H.W., Hansell, D.A., 1999. Estimation of bacterial respiration and growth efficiency in the Ross Sea, Antarctica. Aquat. Microb. Ecol. 19, 229—244, http://dx.doi.org/10.3354/ame019229.

Caron, D.A., Hutchins, D.A., 2012. The effects of changing climate on microzooplankton grazing and community structure: drivers, predictions and knowledge gaps. J. Plankton Res. 35 (2), 1—18, http://dx.doi.org/10.1093/plankt/fbs091.

Cho, B.C., Azam, F., 1990. Biogeochemical significance of bacterial biomass in the ocean's euphotic zone. Mar. Ecol. Prog. Ser. 63, 253—259.

Collins, M., Knutti, R., Arblaster, J., Dufresne, J.-L., Fichefet, T., Friedlingstein, P., Gao, X., Gutowski, T., Johns, W.J., Krinner, G., Shongwe, M., Tebaldi, C., Weaver, A.J., Wehner, M., 2013. Long-term climate change: projections, commitments and irreversibility. In: Stocker, T.F., Qin, D., Plattner, G.-K., Tignor, M., Allen, S. K., Doschung, J., Nauels, A., Xia, Y., Bex, V., Midgley, P.M. (Eds.), Climate Change 2013: The Physical Science Basis. Contribution of Working Group I to the Fifth Assessment Report of the Intergovernmental Panel on Climate Change. Cambridge University Press, 1029—1136, http://dx.doi.org/10.1017/CBO9781107415324.024.

Daskalov, G.M., 2002. Overfishing drives a trophic cascade in the Black Sea. Mar. Ecol. Prog. Ser. 225, 53—63, http://dx.doi.org/10.3354/meps225053.

Duarte, C.M., Agustí, S., Gasol, J.M., Vaqué, D., Vazquez-Dominguez, E., 2000. Effect of nutrient supply on the biomass structure of planktonic communities: an experimental test on a Mediterranean coastal community. Mar. Ecol. Prog. Ser. 206, 87—95, http://dx.doi.org/10.3354/meps206087.

Ducklow, H.W., Hansell, D.A., Morgan, J.A., 2007. Dissolved organic carbon and nitrogen in the Western Black Sea. Mar. Chem. 105, 140—150, http://dx.doi.org/10.1016/j.marchem.2007.01.015.

Dupuy, C., Talarmin, A., Hartmann, H.J., Delmas, D., Courties, C., Marquis, E., 2011. Community structure and grazing of the nano-microzooplankton on the continental shelf of the Bay of Biscay.

Estuar. Coast. Shelf Sci. 95, 1–13, http://dx.doi.org/10.1016/j.ecss.2011.05.002.

Edler, L. (Ed.), 1979. Phytoplankton and Chlorophyll: Recommendations on Methods for Marine Biological Studies in the Baltic Sea. Baltic Marine Biologists Publ. No. 5.

Eker, E., Georgieva, L., Senichkina, L., Kideys, A.E., 1999. Phytoplankton distribution in the western and eastern Black Sea in spring and autumn 1995. ICES J. Mar. Sci. 56, 15–22, http://dx.doi.org/10.1006/jmsc.1999.0604.

Eker-Develi, E., Kideys, A.E., 2003. Distribution of phytoplankton in the southern Black Sea in summer 1996, spring and autumn 1998. J. Marine Syst. 39, 203–211, http://dx.doi.org/10.1016/S0924-7963(03)00031-9.

Fenchel, T., 1982. Ecology of heterotrophic microflagellates. IV. Quantitative occurrence and importance as consumers of bacteria. Mar. Ecol. Prog. Ser. 9, 35–62.

Feyzioglu, A.M., Kurt, I., Boran, M., Sivri, N., 2004. Abundance and distribution of cyanobacteria *Synechococcus* spp. in the Southeastern Black Sea during 2001 summer. Indian J. Mar. Sci. 33 (4), 365–368.

Fileman, E.S., Cummings, D.G., Llewellyn, C.A., 2002. Microplankton community structure and the impact of microzooplankton grazing during an *Emiliania huxleyi* bloom, off the Devon coast. J. Mar. Biol. Assoc. U.K. 82 (3), 359–368, http://dx.doi.org/10.1017/S0025315402005593.

Fredrickson, K.A., Strom, S.L., 2009. The algal osmolyte DMSP as a microzooplankton grazing deterrent in laboratory and field studies. J. Plankton Res. 31 (2), 135–152, http://dx.doi.org/10.1093/plankt/fbn112.

Fuhrman, J.A., Sleeter, T.D., Carlson, C.A., Proctor, L.M., 1989. Dominance of bacterial biomass in the Sargasso Sea and its ecological implications. Mar. Ecol. Prog. Ser. 57, 207–217.

Gallegos, C.L., 1989. Microzooplankton grazing on phytoplankton in the Rhode River, Maryland: nonlinear feeding kinetics. Mar. Ecol. Prog. Ser. 57, 23–33.

Gasol, J.M., del Giorgio, P.A., Duarte, C.M., 1997. Biomass distribution in marine planktonic communities. Limnol. Oceanogr. 42 (6), 1353–1363, http://dx.doi.org/10.4319/lo.1997.42.6.1353.

Gonzalez, J.M., Sherr, E.B., Sherr, B.F., 1990. Size-selective grazing on bacteria by natural assemblages of estuarine flagellates and ciliates. Appl. Environ. Microb. 56, 583–589.

Hillebrand, H., Dürselen, C.D., Kirschtel, D., Pollingher, D., Zohary, T., 1999. Biovolume calculation for pelagic and benthic microalgae. J. Phycol. 35, 403–424.

Hobbie, J.E., Daley, R.J., Jasper, S., 1977. Use of nucleopore filters for counting bacteria by fluorescence microscopy. Appl. Environ. Microb. 33, 1225–1228, http://dx.doi.org/10.1046/j.1529-8817.1999.3520403.x.

Kara, B., Wallcraft, A.J., Hurlburt, H.R., Stanev, E.V., 2008. Air-fluxes and river discharges in the Black Sea with a focus on Danube and Bosphorus. J. Marine Syst. 74, 74–95, http://dx.doi.org/10.1016/j.jmarsys.2007.11.010.

Karlson, B., Godhe, A., Cusack, C., Bresnan, E., 2010. Introduction to methods for quantitative phytoplankton analysis. In: Karlson, B., Cusack, C., Bresnan, E. (Eds.), Microscopic and Molecular Methods for Quantitative Phytoplankton Analysis. IOC Manuals and Guides, No. 55, IOC/2010/MG/55. UNESCO, Paris, 110 pp.

Kideys, A.E., 2002. Fall and rise of the Black Sea ecosystem. Science 297, 1482–1484, http://dx.doi.org/10.1126/science.1073002.

Kopuz, U., Feyzioglu, A.M., Agirbas, E., 2012. Picoplankton dynamics during late spring 2010 in the South-Eastern Black Sea. Turk. J. Fish. Aquat. Sci. 12, 397–405, http://dx.doi.org/10.4194/1303-2712-v12_2_28.

Landry, M.R., 2014. On database biases and hypothesis testing with dilution experiments: response to comment by Latasa. Limnol. Oceanogr. 59 (3), 1095–1096, http://dx.doi.org/10.4319/lo.2014.59.3.1095.

Landry, M.R., Constantinou, J., Latasa, M., Brown, S.L., Bidigare, R. R., Ondrusek, M.E., 2000. Biological response to iron fertilization in the eastern equatorial Pacific (IronEx II). III. Dynamics of phytoplankton growth and microzooplankton grazing. Mar. Ecol. Prog. Ser. 201, 57–72, http://dx.doi.org/10.3354/meps201057.

Landry, M.R., Hassett, R.P., 1982. Estimating the grazing impact of marine micro-zooplankton. Mar. Biol. 67, 283–288, http://dx.doi.org/10.1007/BF00397668.

Latasa, M., 2014. Comment: A potential bias in the databases of phytoplankton growth and microzooplankton grazing rates because of the improper formulation of the null hypothesis in dilution experiments. Limnol. Oceanogr. 59 (3), 1092–1094, http://dx.doi.org/10.4319/lo.2014.59.3.1092.

Lee, H., Kudo, I., Yanada, M., Maita, Y., 2001. Bacterial abundance and production and heterotrophic nanoflagellate abundance in subartic coastal waters (Western North Pacific Ocean). Aquat. Microb. Ecol. 23, 263–271.

Legendre, L., Rassaulzadegan, F., 1995. Plankton and nutrient dynamics in marine water. Ophelia 42, 153–172, http://dx.doi.org/10.1080/00785236.1995.10422042.

Linacre, L., Landry, M.R., Cajal-Medrano, R., Lara-Lara, J.R., Hernández-Ayón, J.M., Mouriño-Pérez, R.R., García-Mendoza, E., Bazán-Guzmán, C., 2012. Temporal dynamics of carbon flow through the microbial plankton community in a coastal upwelling system off northern Baja California, Mexico. Mar. Ecol. Prog. Ser. 461, 31–46, http://dx.doi.org/10.3354/meps09782.

Menden-Deuer, S., Lessard, E.J., 2000. Carbon to volume relationships for dinoflagellates, diatoms, and other protist plankton. Limnol. Oceanogr. 45, 569–579, http://dx.doi.org/10.4319/lo.2000.45.3.0569.

Nesterova, D., Moncheva, S., Mikaelyan, A., Vershinin, A., Akatov, V., Boicenco, L., Aktan, Y., Sahin, F., Gvarishvili, T., 2008. The state of phytoplankton. In: State of the Environment of the Black Sea (2001–2006/7). The Commission on the Protection of the Black Sea Against Pollution Publication. 112–147.

Odum, E.P., 1971. Fundamentals of Ecology, 3rd ed. W.B. Saunders, Philadelphia, 574 pp.

Oguz, T., Akoglu, E., Salihoglu, B., 2012b. Current state of overfishing and its regional differences in the Black Sea. Ocean Coast. Manage. 58, 47–56.

Oguz, T., Dippner, J.W., Kaymaz, Z., 2006. Climatic regulation of the Black Sea hydro-meteorological and ecological properties at interannual-to-decadal time scales. J. Marine Syst. 60, 3–4, http://dx.doi.org/10.1016/j.jmarsys.2005.11.011.

Oguz, T., Gilbert, D., 2007. Abrupt transitions of the top-down controlled Black Sea pelagic ecosystem during 1960–2000: evidence for regime-shifts under strong fishery exploitation and nutrient enrichment modulated by climate-induced variations. Deep-Sea Res. Pt. I 54, 220–242, http://dx.doi.org/10.1016/j.dsr.2006.09.010.

Oguz, T., Merico, A., 2006. Factors controlling the summer *Emiliania huxleyi* bloom in the Black Sea: a modeling study. J. Marine Syst. 59, 173–188, http://dx.doi.org/10.1016/j.jmarsys.2005.08.002.

Oguz, T., Salihoglu, B., Moncheva, S., Abaza, V., 2012a. Regional peculiarities of community-wide trophic cascades in strongly degraded Black Sea food web. J. Plankton Res. 34, 338–343, http://dx.doi.org/10.1093/plankt/fbs002.

Oguz, T., Velikova, V., 2010. Abrupt transition of the northwestern Black Sea shelf ecosystem from a eutrophic to an alternative pristine state. Mar. Ecol. Prog. Ser. 405, 231–242, http://dx.doi.org/10.3354/meps08538.

Pakhomova, S., Vinogradova, E., Yakushev, E., Zatsepin, A., Shtereva, G., Chasovnikov, V., Podymov, O., 2014. Interannual variability of the Black Sea Proper oxygen and nutrients regime: the role of climatic and anthropogenic forcing. Estuar. Coast. Shelf Sci. 140, 134–145, http://dx.doi.org/10.1016/j.ecss.2013.10.006.

Parsons, T.R., Maita, Y., Lalli, C., 1984. Manual of Chemical and Biological Methods for Sea Water Analysis. Pergamon Press, Great Britain, 173 pp.

Pomeroy, L.R., 1974. The ocean's food web, a changing paradigm. BioScience 24, 499—504, http://dx.doi.org/10.2307/1296885.

Putt, M., Stoecker, D.K., 1989. An experimentally determined carbon:volume ratio for marine 'oligotrichous' ciliates from estuarine and coastal waters. Limnol. Oceanogr. 34, 1097—1103.

Schmoker, C., Hernandez-Leon, S., Calbet, A., 2013. Microzooplankton grazing in the oceans: impacts, data variability, knowledge gaps and future directions. J. Plankton Res. 35, 691—706, http://dx.doi.org/10.1093/plankt/fbt023.

Sherr, B.F., Sherr, E.B., Andrew, T.L., Fallon, R.D., Newell, S.Y., 1986. Trophic interactions between heterotrophic protozoa and bacterioplankton in estuarine water analysed with selective metabolic inhibitors. Mar. Ecol. Prog. Ser. 32, 169—179.

Simon, M., Cho, B.C., Azam, F.A., 1992. Significance of bacterial biomass in lakes and the ocean: comparison to phytoplankton biomass and biogeochemical implications. Mar. Ecol. Prog. Ser. 86, 103—110.

Sommaruga, R., 1995. Microbial and classical food webs: a visit to a hypertrophic lake. FEMS Microbiol. Ecol. 17, 257—270, http://dx.doi.org/10.1111/j.1574-6941.1995.tb00150.x.

Sorokin, Y.I., 1977. The heterotrophic phase of plankton succession in the Japan Sea. Mar. Biol. 41, 107—117, http://dx.doi.org/10.1007/BF00394018.

Sorokin, Y.I., Sorokin, P.Y., Avdeev, V.A., Sorokin, D.Y., Ilchenko, S.V., 1995. Biomass, production and activity of bacteria in the Black Sea, with special reference to chemosynthesis and the sulfur cycle. Hydrobiologia 308, 61—76, http://dx.doi.org/10.1007/BF00037788.

Stelmakh, L., 2013. Microzooplankton grazing impact on phytoplankton blooms in the coastal seawater of the southern Crimea (Black Sea). Int. J. Mar. Sci. 3 (15), 121—127, http://dx.doi.org/10.5376/ijms.2013.03.0015.

Stelmakh, L.V., Babich, I.I., Tugrul, S., Moncheva, S., Stefanova, K., 2009. Phytoplankton growth rate and zooplankton grazing in the western part of the Black Sea in the autumn period. Oceanology 49, 83—92, http://dx.doi.org/10.1134/S000143700901010X.

Stelmakh, L., Georgieva, E., 2014. Microzooplankton: the trophic role and involvement in the phytoplankton loss and bloom-formation in the Black Sea. Turk. J. Fish. Aquat. Sci. 14, 955—964, http://dx.doi.org/10.4194/1303-2712-v14_4_15.

Stoecker, D.K., Capuzzo, J.M., 1990. Predation on protozoa: its importance to zooplankton. J. Plankton Res. 12 (5), 891—908, http://dx.doi.org/10.1093/plankt/12.5.891.

Stoecker, D.K., Gifford, D.J., Putt, M., 1994. Preservation of marine planktonic ciliates: losses and cell shrinkage during fixation. Mar. Ecol. Prog. Ser. 110, 293—299.

Strom, S.L., Wolfe, G.V., Holmes, J., Stecker, H., Shimeneck, C., Lambert, S., Moreno, E., 2003. Chemical defense in the microplankton I: feeding and growth rates of heterotrophic protists on the DMS-producing phytoplankter *Emiliania huxleyi*. Limnol. Oceanogr. 48 (1), 217—229, http://dx.doi.org/10.4319/lo.2003.48.1.0217.

Teixeira, I., Figueiras, F.G., Crespo, B.G., Predracoba, S., 2011. Microzooplankton feeding impact in a coastal upwelling system on the NW Iberian margin: the Ria de Vigo. Estuar. Coast. Shelf Sci. 91, 110—120, http://dx.doi.org/10.1016/j.ecss.2010.10.012.

Uysal, Z., 2001. Chroococcoid cyanobacteria *Synechococcus* spp. in the Black Sea: pigments, size, distribution, growth and diurnal variability. J. Plankton Res. 23 (2), 175—189, http://dx.doi.org/10.1093/plankt/23.2.175.

Verity, P.G., Langdon, C., 1984. Relationships between lorica volume, carbon, nitrogen, and ATP content of tintinnids in Narragansett Bay. J. Plankton Res. 6, 859—868, http://dx.doi.org/10.1093/plankt/6.5.859.

Verity, P.G., Wassmannb, P., Frischera, M.E., Howard-Jonesa, M.H., Alle, A.E., 2002. Grazing of phytoplankton by microzooplankton in the Barents Sea during early summer. J. Marine Syst. 38, 109—123, http://dx.doi.org/10.1016/S0924-7963(02)00172-0.

Waterbury, J.B., Valois, F.W., Franks, D.G., 1986. Biological and ecological characterization of the marine unicellular cyanobacterium *Synechococcus*. In: Platt, T., Li, W.K.W. (Eds.), Photosynthetic Picoplankton. Can. Bull. Fish. Aquat. Sci. 214, 71—120.

Worden, A.Z., Binder, B.J., 2003. Application of dilution experiments for measuring growth and mortality rates among *Prochlorococcus* and *Synechococcus* populations in oligotrophic environments. Aquat. Microb. Ecol. 30, 159—174.

Oceanologia (2018) 60, 153—168

Available online at www.sciencedirect.com

ScienceDirect

journal homepage: www.journals.elsevier.com/oceanologia/

ORIGINAL RESEARCH ARTICLE

A fuzzy KNN-based model for significant wave height prediction in large lakes

Mohammad Reza Nikoo [a,*], Reza Kerachian [b,1], Mohammad Reza Alizadeh [a,2]

[a] Department of Civil and Environmental Engineering, School of Engineering, Shiraz University, Shiraz, Iran
[b] School of Civil Engineering and Center of Excellence for Engineering and Management of Civil Infrastructures, College of Engineering, University of Tehran, Tehran, Iran

Received 20 May 2017; accepted 28 September 2017
Available online 1 November 2017

KEYWORDS
Significant wave height prediction;
Fuzzy *K*-nearest neighbor;
Bayesian networks;
Support vector regression;
Regression tree induction

Summary Some algorithms based on fuzzy set theory (FST) such as fuzzy inference system (FIS) and adaptive-network-based fuzzy inference system (ANFIS) have been successfully applied to significant wave height (SWH) prediction. In this paper, perhaps for the first time, the fuzzy *K*-nearest neighbor (FKNN) algorithm is utilized to develop a fuzzy wave height prediction model for large lakes, where the fetch length depends on the wind direction. As fetch length (or wind direction) can affect the wave height in lakes, this variable is also considered as one of the inputs of the prediction model.

The results of the FKNN model are compared with those of some soft computing techniques such as Bayesian networks (BNs), regression tree induction (named M5P), and support vector regression (SVR). The developed FKNN model is used for SWH prediction in the western part of Lake Superior in North America. The results show that the FKNN and M5P model can outperform the other soft computing techniques.

* Corresponding author at: Department of Civil and Environmental Engineering, School of Engineering, Shiraz University, Zand Street, Shiraz 7134851156, Iran. Tel.: +98 713 6133497; fax: +98 711 6473161.
E-mail addresses: nikoo@shirazu.ac.ir (M.R. Nikoo), kerachian@ut.ac.ir (R. Kerachian), alizadeh.mohamadreza@yahoo.com (M.R. Alizadeh).
[1] Tel.: +98 912 5339529.
[2] Tel.: +98 917 3061374.
Peer review under the responsibility of Institute of Oceanology of the Polish Academy of Sciences.

ELSEVIER Production and hosting by Elsevier

1. Introduction

Significant wave height (SWH) is an important hydrodynamic variable for design and operation of coastal and offshore structures. A successful prediction model should be able to accurately predict the wave parameters in different conditions. Review of related literature about wave parameters estimation models shows that the application of data mining and artificial intelligence models is a promising alternative to effort demanding and time consuming numerical or physical wave estimation tools (Balouchi et al., 2015; Etemad-Shahidi and Mahjoobi, 2009; Malekmohamadi et al., 2008; Nikoo et al., 2015; Özger, 2010).

In the past decade, in order to tackle the limitations of numerical and empirical models and eliminate the prior

https://doi.org/10.1016/j.oceano.2017.09.003

knowledge requirement about interactions among inputs, parameters, and outputs in SWH prediction problems, different soft computing techniques have successfully been applied. Artificial neural network (ANN), fuzzy inference systems (FIS), adaptive-network-based fuzzy inference system (ANFIS), Bayesian network (BN) and genetic programming (GP) are the most common methods, which have been used for SWH prediction. For example, FIS and ANFIS methods have been used by Özger and Şen (2007), Mahjoobi et al. (2008), Zanaganeh et al. (2009), Malekmohamadi et al. (2011), Patil et al. (2012), Karimi et al. (2013), Nikoo et al. (2014) and Kazemi Elaki et al. (2016) for estimating wave parameters. Altunkaynak and Wang (2012) developed a model based on Geno Kalman Filtering (GKF) for predicting SWH in the Lake Okeechobee, Florida. They compared the results of the GKF and an ANN and concluded that the GKF can provide better predictions. Nikoo and Kerachian (2017) developed an Artificial Immune Recognition System (AIRS) and five data mining techniques (i.e. ANN, SVR, BN and Rough Set Theory (RST)) for SWH predictions with different time lags. The AIRS model was applied for the SWH prediction in the Lake Superior in North America and its results were compared with those of other models. The results showed that AIRS and ANN models outperform other data-driven models in forecasting extreme SWHs. In a more recent study (i.e. Berbić et al., 2017), the real-time estimation of wave height within the successive 30 min up to 5.5 h time span was achieved using ANN and support vector machine (SVM) and later they used the least error-prone model and investigated the effect of taking into account the wind velocity on the accuracy of wave height prediction.

In this paper, fuzzy *K*-nearest neighbor (FKNN), which was initially introduced by Keller et al. (1985), is utilized for SWH prediction. The FKNN is a branch of supervised learning methods, which particularly account for the similarity between the training sample data and the test data. The main advantage of using the FKNN is that despite its deterministic form (KNN), the unbiased weighting of instances is considered in the decision rule regardless of its distance to the pattern to be classified, and thus the fuzzy form has a greater accuracy (Derrac et al., 2016). One disadvantage of the FKNN is that it is computationally expensive. Since this model should be run for all data set, it is time consuming and requires large memory size to store all training data.

Reviewing the literature shows that FKNN has been successfully applied in different studies. For example, Xiao and Wang (2010) utilized an FKNN-based machine learning approach to provide a prediction system for protein quaternary structural type. Chen et al. (2011) developed a bankruptcy prediction model based on an adaptive FKNN algorithm. They optimized the neighborhood size *K* and the fuzzy strength parameter *m* using a Particle Swarm Optimization (PSO) approach. Wang and Xiao (2011) used FKNN to predict and classify the risk types of Human Papillomavirus (HPV) based on the bioinformatics analysis. Somari et al. (2016) utilized KNN and FKNN in particle contamination detection. Fredj and Ouni (2017) applied the crisp and fuzzy KNN algorithm for Timit phoneme recognition and their results showed that FKNN could provide better recognition.

The developed FKNN model for predicting SWH are compared with three soft computing models (i.e. SVR, BN, and M5P), which have been widely used in this context. All models are utilized for SWH prediction in Lake Superior and their results are compared using a set of statistical error indices, namely root mean square relative error (RMSRE), root mean relative error (RMRE), correlation coefficient (CC), bias and scatter index (SI). The differences between the used soft computing models have been visually plotted to make a better comparison of the models' performances.

2. Methods

As details of M5P, SVR and BN models are presented in Etemad-Shahidi and Mahjoobi (2009), Malekmohamadi et al. (2011), Etemad-Shahidi and Ghaemi (2011) and Abed-Elmdoust and Kerachian (2012), in the following section, the main characteristics of the FKNN algorithm are presented.

Classification algorithms are mainly used for measuring the similarity of a set of objects based on some measures of distance. The *K*-nearest neighbor (KNN) algorithm is one the oldest pattern classifier methods with no preprocessing requirement (Cover and Hart, 1967). The decision rule of common classification algorithms such as M5P, SVR and BN assume equal weights for object membership utilities, neglecting different patterns of similarity. Taking the advantage of fuzzy set theory (Zadeh, 1965), the FKNN has been shown to not only have a lower error in classifying the objects but also it has a greater confidence measure of the classification (Keller et al., 1985). The FKNN provides a more realistic vector of membership for the objects and it also accounts for the degree of object membership to the classes of objects. In this algorithm, a class is assigned to the most common class considering its *K*-nearest neighbors. FKNN assigns fuzzy membership to the samples and helps decision makers for fuzzy decisions (Chen et al., 2011; Keller et al., 1985).

The purpose of FKNN algorithm is to divide (cluster) the sample vectors $X = \{x_1, x_2, \ldots, x_n\} \subset R^n$ into c $(1 < c < n)$ fuzzy subsets. For $i = 1, 2, \ldots, c$ and $j = 1, 2, \ldots, n$ the fuzzy membership matrix is shown by U, where U_{ij} is the fuzzy membership degree of x_j in class i. In a non-fuzzy version of the algorithm, the jth object is assigned to the ith class which has the greatest U_{ij} in comparison with the fuzzy membership degree of all the other classes. The matrix U has two constraints as follows (Keller et al., 1985):

$$\sum_{i=1}^{c} u_{ij} = 1, \quad "j, \tag{1}$$

$$u_{ij} \hat{I} [0,1], \quad 0 < \sum_{j=1}^{n} u_{ij} < n. \tag{2}$$

The first constraint (Eq. (1)), ensures that all the objects' membership degrees are obtained across all the classes ($i = 1, 2, \ldots, c$) and the summation of all the membership degrees equals to one. Eq. (2) indicates that the fuzzy membership degrees for all the objects lie in the interval of equal or greater than zero and equal or lower than one. The two constraints show that if an object belongs to a class with $U = 1$ then its membership degree to the other classes is definitely zero. In addition, the summation of all the fuzzy membership degrees for all the objects in one class is greater

than zero since otherwise, the class does not exist and utmost it is lower than the number of objects n. In FKNN algorithm, fuzzy membership's degree is assigned to each vector considering the vectors' distances from their KNNs membership as follows (Warren and Damin, 1997):

$$u_i(x) = \frac{\sum_{j=1}^{K}\left(\frac{u_{ij}}{||x-x_j||^{\frac{2}{(m-1)}}}\right)}{\sum_{j=1}^{K}\left(\frac{1}{||x-x_j||^{\frac{2}{(m-1)}}}\right)}, \quad (3)$$

where K is the predefined number of nearest neighbor and m is a constant parameter. Parameter m determines the weight of each nearest neighbor in the calculation of the fuzzy membership value. Eq. (3) is the key role in measuring the membership degree of an object to the ith class which is governed by the inversed distances of the object x from its K nearest neighbors and their class memberships. Unlike the non-fuzzy version classification algorithms, the reverse correlation between the membership degree and the distances plays the role of a weighting function to penalize/reward those with farther/closer distance from the other objects in the class. More clearly, if an object belongs to the class A with 0.95 membership degree while it only belongs to the class B with 0.05 membership degree then it would be logically true that the object belongs to A for sure. However, if the membership degrees for the object were 0.55 and 0.45 for classes A and B respectively, then there should be some hesitation prior to the object assignment to any of the classes A or B. Finally, the assignment, which generates a greater measure of similarity, will determine the membership of that object to either A or B. Eq. (3) reflects all these situations by considering a weighting function based on the inverse distances of the set of objects in a class.

Parameter m indicates the severity in penalizing/rewarding those objects with farther/closer distances from the other objects. m is always greater than one and the closer its value to one, the closer neighbors are given a more influential role in calculating the membership degree of the object being classified. On the other hand, by increasing this parameter, the neighbors are more evenly weighted, and their relative distances from the point being classified have fewer effects. Also, $||x - x_j||$ is the Euclidean distance between x and its jth KNN.

In artificial intelligence models when the number of input variables is smaller than the size of the training set, the likelihood of overfitting is quite too low (Nikoo et al., 2015; Tetko et al., 1995). The cross validation is often used to ensure a model accuracy in its estimation of the output variables without reliance on the data used in the training set. Cross validation can save predictive models from problems such as overfitting and it assesses the model's independence on its training data set. Overfitting happens when the prediction loses its true meaning during the course of training by memorizing the mapping function from input data to the output variable, which is a common problem when the number of data for dividing into training and test data set is not enough without imposing any damage to the data. In this study, although the number of data available is significantly greater than the number of input variables, the likelihood of overfitting is low though to get an insight on how the predictive models are trustworthy in practice, the Nash–Sutcliffe model efficiency coefficient (E_{NS}) can be used. The Nash–Sutcliffe coefficient is defined as below (Nash and Sutcliffe, 1970):

$$E_{NS} = 1 - \frac{\sum_{i=1}^{n}(h_i^* - h_i)^2}{\sum_{i=1}^{n}(h_i^* - H)^2} \quad (4)$$

The Nash–Sutcliffe coefficient varies from $-\infty$ to 1, where a value close to one indicates a better accuracy and a value of exactly zero shows that the predictive model is a good as the mean of the observed data and any negative value shows that the predictive model result is less accurate even than the mean of the observed data. The Nash–Sutcliffe coefficient has been widely used in the literature as a measure of how efficient a predictive model can be as found in (Li, 2016; Parajka et al., 2015; Tiwari and Chatterjee, 2010).

A flowchart of the FKNN algorithm is presented in Fig. 1. The FKNN algorithm starts with given the input sample x and the K number of nearest neighbors. Next, the algorithm proceeds with initializing the first class, $i = 1$, and it then computes the distances between x and x_i. Further, if the number of classes, i, is equal or lower than K, $U_i(x)$ is included into the set of K nearest neighbors otherwise the algorithm searches for a x_i closer to x than any previous nearest neighbor. If the second condition holds true, the farthest of the K nearest neighbors is removed from the set and it is replaced with x_i. Following, i is incremented by one and if the K nearest neighbors to x are not determined the procedure is repeated until all the K-nearest neighbors to x are identified. Later, Eq. (3) is used to compute the fuzzy membership values for all the classes (Keller et al., 1985).

To draw on a fair judgment, a combination of performance metrics including root mean square relative error (RMSRE), root mean relative error (RMRE), correlation coefficient (CC), bias and scatter index (SI), has been used. Error measures also play a vital role in calibrating/refining forecasting models mostly by minimizing single/set of errors. In order to avoid a biased judgment, the use of different indices is necessary when comparing the efficiency of the models (Chai and Draxler, 2014). The relative error indicates the efficacy of the model relative to the magnitude of the measured object whereas the absolute error is not sensitive to the size of the object being measured. RMRE is the squared sum of the relative residuals of the predicted values versus the observed values. Since RMRE is scale-dependent, it is considered as a prominent measure of model accuracy (Monghasemi et al., 2015). The CC is Pearson correlation coefficient, a measure that determines model's statistical relationship of how much a resemblance exists between the model's estimations versus the real values. The CC always lies in the interval of -1 to 1, where 1 is a total positive linear correlation, 0 is no linear correlation, and -1 is a total negative linear correlation (Monghasemi et al., 2017). Bias represents the average residuals between the estimated and the observed values, which shows how close the estimated values are to the true observed values in statistics. A lower value of Bias indicates a closer fitness of the observed values. SI is defined as the standard deviation of the model's estimations and observed values from the average of each one normalized by the mean of the observed values, which is ideally as small as possible.

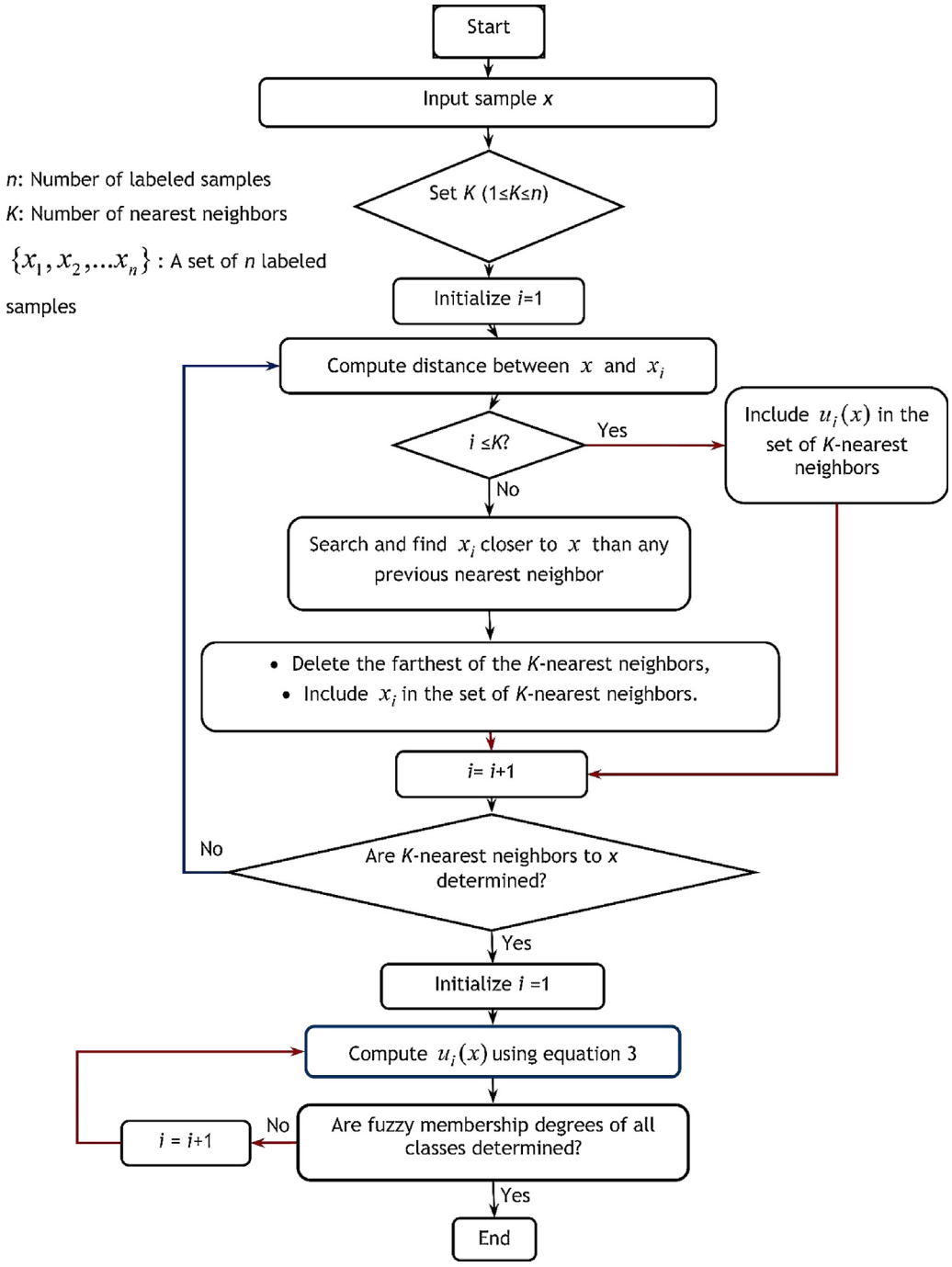

Figure 1 A flowchart of the Fuzzy *K*-Nearest Neighbor (FKNN) algorithm.

In order to evaluate the efficacy of the proposed FKNN-based SWH prediction model and also compare its results with those of the other soft computing models (i.e. BN, SVR and M5P), five different statistical measures, namely RMSRE, RMRE, CC, Bias and SI are used in the validation stage process of the models. These statistical measures are defined as below:

$$RMSRE = \sqrt{\frac{1}{n}\sum_{i=1}^{n}\left(\frac{h_i - h_i^*}{h_i^*}\right)^2}, \quad (5)$$

$$RMRE = \sqrt{\frac{1}{n}\sum_{i=1}^{n}\left|\frac{h_i - h_i^*}{h_i^*}\right|}, \quad (6)$$

$$CC = \frac{\sum_{i=1}^{n} h_i h_i^*}{\left(\sum_{i=1}^{n} h_i^2 \sum_{i=1}^{n} h_i^{*2}\right)^{1/2}}, \quad (7)$$

$$Bias = \frac{1}{n}\sum_{i=1}^{n}(h_i - h_i^*), \quad (8)$$

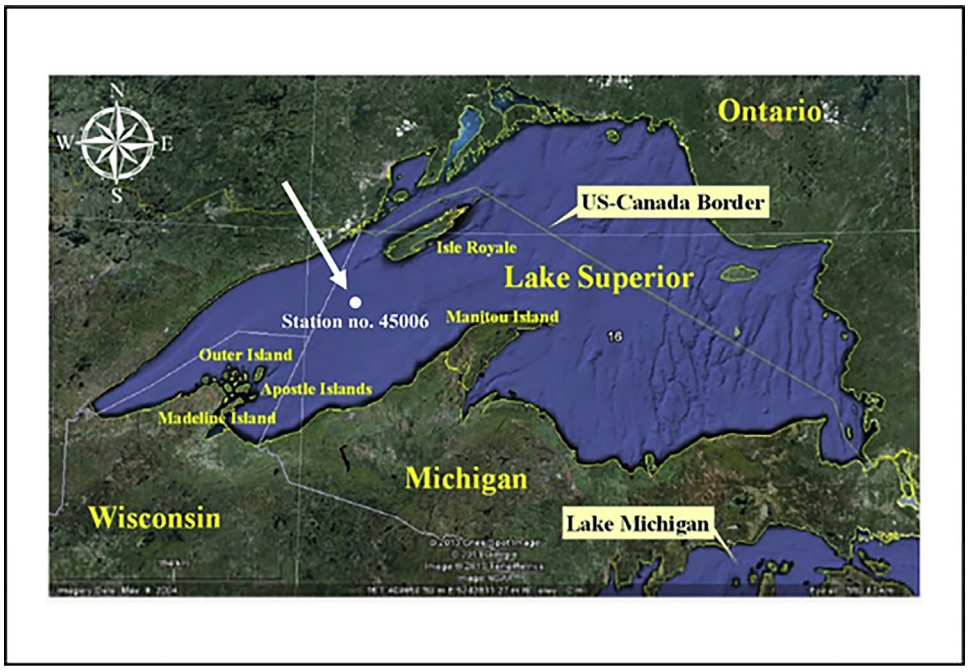

Figure 2 A GIS Map of the Lake Superior and the location of the station no. 45006.

Table 1 Basic characteristics of the Lake Superior.

Parameter	Area [km^2]	Surface elevation from the sea level [m]	Volume [km^3]	Maximum fetch length [km]	Mean depth [m]
Value	82,100	180	12,100	320	147

$$SI = \frac{\sqrt{1/n\sum_{i=1}^{n}((h_i^*-H^*)-(h_i-H))^2}}{H}, \quad (9)$$

where h_i and h_i^* are ith observed and predicted SWH, respectively and n is the number of data in the validation data set. Also, H and H^* denote the average observed and predicted SWHs in the validation data set, respectively.

3. Study area

In this study, the available wind speed, wind direction, and wave height data, which have been recorded at the station no. 45006 in the western part of Lake Superior in North America (Fig. 2) are used to evaluate the efficacy of the soft computing techniques in SWH prediction. The Lake Superior is the greatest lake in the region of North America by its fresh water storage volume and it is the third one of its type in the world. Lake Superior is shared by the states of Wisconsin and Michigan in the south and it reaches the Minnesota State on its west side and the province of Ontario, Canada is located on its north (see Fig. 2). It has a surface of greater than 82 thousands of square meters with the depth of 147 m on average, which is fed by over two hundreds rivers. The Lake Superiors' water level is not constant during a year. Its normal high water mark stands at 0.36 m above the datum level of 183.2 m, whereas the normal low water mark is 0.1 m below the datum. Accordingly, there is a 0.46 m difference between the highest and lowest levels on average. Studies show that the annual storms in the lake often feature wave heights of greater than 6 m. The basic characteristics of Lake Superior including its area, surface elevation, volume, maximum fetch length and mean depth are presented in Table 1. More details about this Lake can be found in Malekmohamadi et al. (2011) and Abed-Elmdoust and Kerachian (2012). To evaluate the efficacy of the developed soft computing models, the time series of wave and wind data monitored at the station no. 45006 from March 2005 to December 2006 with 1 h time interval are used. These data have been gathered and disseminated by the National Data Buoy Center (NDBC).

4. Results and discussion

Using historical hourly time series of observed wind and wave data from March 2005 to December 2006, 730 different input-output patterns were extracted in a way that they include both cold and warm months. 85 and 15 percent of these data (584 and 146 data sets, respectively) were used for training and testing (validating) the soft computing models, respectively. In order to divide available data to train and test sets, different common percentages such as 75:25, 80:20 and 85:15 were applied and the performances of models in training and validation stages were analyzed. Although one division percentage was not definitively superior to the others, the performances of models were slightly better using 85:15 percentages. The shuffled sampling strategy was used to split the data set to train and test data sets.

By random sampling, an independence and smooth generation of samples without any bias was achieved. The data set was checked to verify that the range of train set encompasses the range of test data set. Obviously, the performance of soft computing models may slightly vary due to changes in the separation percentage of available data. However, considering the long-term available data in the current work, the performances and the time complexities of the models are not sensitive to the percentages of the train and test data sets.

Based on the wind speeds-SWH data obtained from the station no. 45006, the variations of correlation coefficients between wind speed in different lag times and SWH are shown in Fig. 3. Also, Fig. 4 presents the correlation coefficients between average wind speed in different lag times and the significant wave height. The wind speeds during time steps $t-1$, $t-2$ and $t-3$ are significantly correlated with SWH as the CC for those are 0.7, 0.6, and 0.4, respectively. However, the CC of lower than 0.4 dictates less correlated data and the decreasing trends shows that as the time lags increases from $t-4$ to $t-10$ the CC drops from 0.35 to its lowest value of 0.1. Therefore, it is anticipated that including the first three lag times, namely, $t-1$, $t-2$, and $t-3$, for the wind speeds in the training data set of the soft computing approaches will improve their ability to predict the SWH.

The first three average wind speeds with more correlation with SWH are the average wind speed during time steps $t-1$ and $t-2$ (A_1) with CC of 0.7, the average wind speed during time steps $t-2$ and $t-3$ (A_2) and the average wind speed during time steps $t-2$, $t-3$ and $t-4$ (A_3) both of which has CC of 0.55, respectively. The average wind speed during time steps $t-12$, $t-13$, $t-14$, and $t-15$ has the least CC with almost 0.1. Consequently, six predictor variables, namely w_1, w_2, w_3 (i.e. wind speeds during time steps $t-1$, $t-2$ and $t-3$), A_1, A_2, and A_3, are used to train the developed soft computing models.

In this paper, the efficacy of the FKNN, BN, SVR and M5P models are evaluated for SWH prediction using the above mentioned six predictors. Moreover, in this study, to improve the accuracy of the models, in addition to the six mentioned predictors, WD is considered as a new predictor. The soft

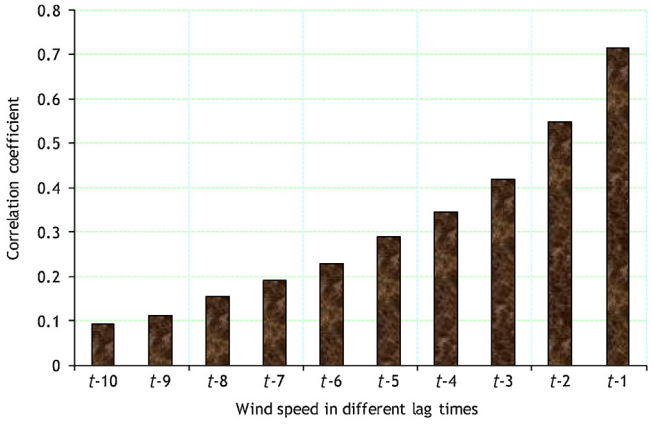

Figure 3 Correlation coefficients between the wind speed in different lag times and the significant wave height at the station no. 45006 in the Lake Superior.

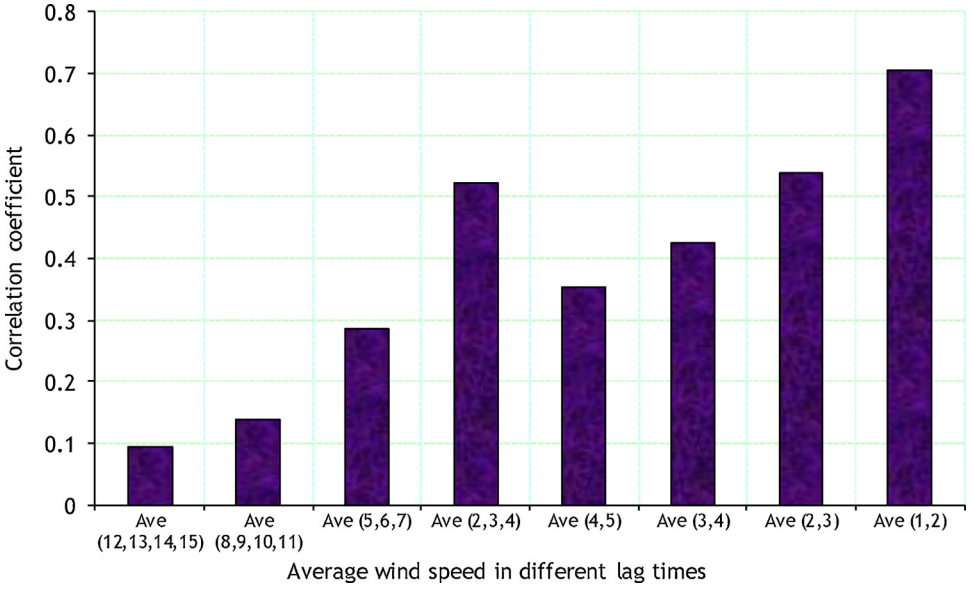

Figure 4 Correlation coefficients between average wind speed in different lag times and the significant wave height.

computing models which are trained using these seven predictors (A_1, A_2, A_3, w_1, w_2, w_3 and WD) are denoted by FKNN′, BN′, SVR′, and M5P′.

4.1. SWH predictions based on wind speed

The structures of the BN models are selected using the Hugin® software, which works based on Necessary Path Condition (NPC) algorithm. Also, Conditional Probabilities (CPTs) of the selected structures are determined using the Estimation–Maximization (EM) algorithm. The structure of the BN model with 6 predictors (Called BN) is shown in Fig. 5. Fig. 6 shows the structure of the second BN (BN′), which has 7 inputs (predictors).

To provide a fair comparison between the results of the two BN models (BN and BN′), the numbers of classes of input and output variables are considered to be the same (12 classes for input and output variables of both models).

In this paper, two SVR models called SVR and SVR′, which respectively have six and seven predictors (inputs), are trained and validated for SWH prediction. The SVR models have been trained using different types of Kernel functions. The results show that the Gaussian Kernel provides the best accuracy in SWH prediction. In both SVR models, in order to have the best prediction results, sensitivity analyses on the main parameters (coefficients) of the Gaussian Kernel function (i.e. C and γ) are done. In our case study, the best values for C and γ are obtained respectively 0.04 and 10 in the first model (SVR) and 0.001 and 0.1 in the second model (SVR′).

The developed rules for SWH prediction in the tree form are obtained by using the first developed M5P model (named M5P), are presented in Table 2. Rules of the M5P model are also derived based on the six predictors in a tree form (Fig. 7). Based on the results of the second developed M5P model (M5P′), nine rules are obtained for SWH prediction (Table 3 and Fig. 8).

According to the description of monitored data by NDBC, the directions of winds are considered from 0° to 360° in degrees clockwise from true North (http://www.ndbc.noaa.gov/). According to Table 3 and Fig. 8, the regression coefficients for wind direction (w_d) is zero for both rules 4 and 5 (two rules that depend on WD). In this case, to examine the sensitivity of the results of the M5P model to small changes in wind directions, different values of wind directions from both sides of the North direction (such as 1°:359°, 2°:358°, 3°:357°, ...) were analyzed using the derived rules. The results showed that there is maximum 5% discrepancy between the outputs of the rules, which indicates that the M5P model is not significantly sensitive to the changes of wind direction around the North. Obviously, based on the other rules derived from the M5P model, the results are not affected by WD changes (Table 3 and Fig. 8). In addition, the zero azimuth was selected to be in West and East and all wind angels have computed accordingly. The derived rules also revealed that the results of the M5P model are not considerably sensitive to the changes of WD because WD does not appear in the derived rules.

In this paper, as suggested by Keller et al. (1985), parameter m is considered to be equal to 2. Two FKNN model called FKNN and FKNN′ are proposed for SWH prediction with 6 and 7 predictors, respectively. The number of fuzzy class of SWH is considered to be 30. The best numbers of nearest neighbor (K) in both FKNN models (FKNN and FKNN′) are selected through a trial and error process. As an example, results of a sensitivity analysis for selecting the best value of the nearest neighbor (K) are presented in Fig. 9. The best values of K in the FKNN and FKNN′ models are selected as 3 and 4, respectively.

The Nash–Sutcliffe coefficient has been calculated for all the models to ensure that the overfitting problem has not occurred and the related results are presented in Table 4. The values of Nash–Sutcliffe coefficient are calculated for both

w_1, w_2 and w_3 are wind speed during time steps t-1, t-2 and t-3, respectively.
A_1= average wind speed during time steps t-1 and t-2.
A_2= average wind speed during time steps t-2 and t-3.
A_3= average wind speed during time steps t-2, t-3 and t-4.
H= Wave height.

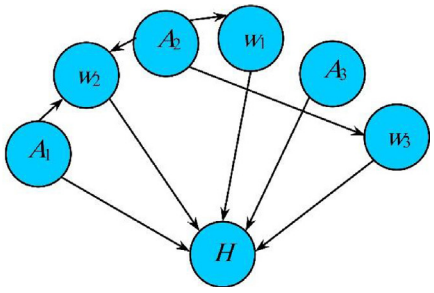

Figure 5 The structure of the first developed Bayesian network (BN) using six predictors for significant wave height prediction.

WD= wind direction.
w_1, w_2 and w_3 are wind speed during time steps t-1, t-2 and t-3, respectively.
A_1= average wind speed during time steps t-1 and t-2.
A_2= average wind speed during time steps t-2 and t-3.
A_3= average wind speed during time steps t-2, t-3 and t-4.
H= Wave height.

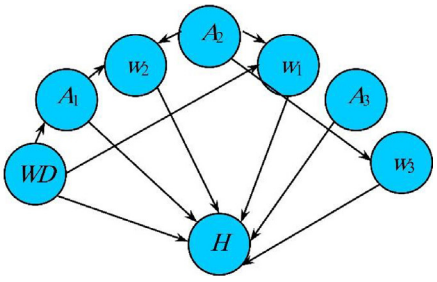

Figure 6 The structure of the second Bayesian network (BN′) using seven predictors for significant wave height prediction.

Table 2 The developed rules for SWH prediction using the M5P model.

Rules number	Regression model coefficients[a]						
	a_3	a_2	a_1	γ_3	γ_2	γ_1	c
1	0.0016	0.0193	0.0026	0	−0.0008	0.0012	0.243
2	0.0016	0.0034	0.0748	0.0218	0.0008	0.0019	−0.146
3	0.0555	0.0695	0.0064	−0.0575	−0.0093	0.0158	−0.0086
4	0.0051	0.038	0.0487	−0.0642	−0.0166	0.0067	0.4801
5	0.0053	0.103	0.0052	0	0.0008	0.0005	−0.149
6	0.0075	0.021	0.0052	0	0.0114	0.0005	0.356
7	0.0358	0.021	0.0052	−0.0241	−0.0618	0.0201	0.789
8	0.0245	0.021	0.0052	−0.0145	−0.0327	0.0123	0.610
9	0.0369	0.0465	0.0073	0	−0.0008	0.0654	−0.319
10	0.0467	0.0035	0.1049	0.0418	0.1121	0	−1.515

[a] Formulation of the regression model is $\gamma_1 w_1 + \gamma_2 w_2 + \gamma_3 w_3 + a_1 A_1 + a_2 A_2 + a_3 A_3 + c$.

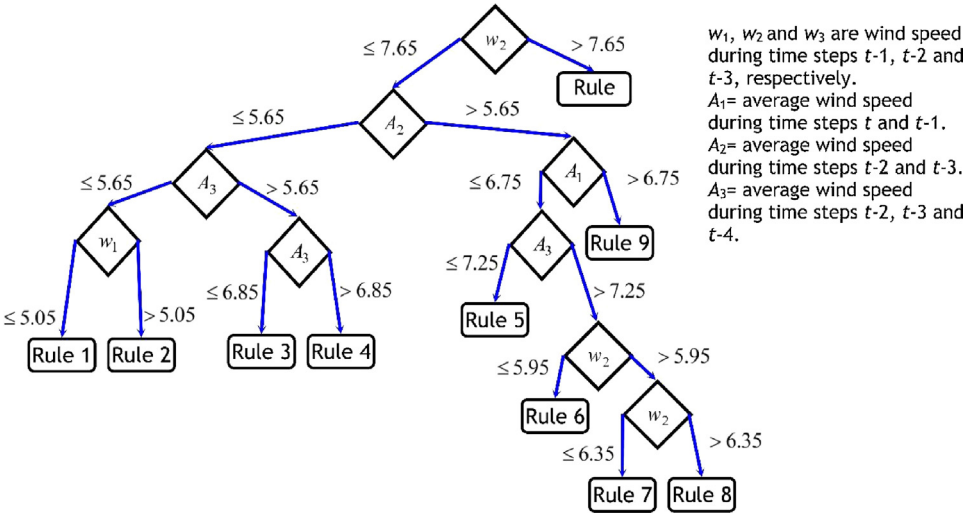

Figure 7 Decision tree rules for SWH prediction using the M5P model (with six predictors).

Table 3 Proposed rules for SWH prediction obtained using the M5P′ model.

Rules number	Regression model coefficients[a]							
	w_d	a_3	a_2	a_1	γ_3	γ_2	γ_1	c
1	0	0.0016	0.0193	0.0026	0	−0.0008	0.0012	0.244
2	0	0.0016	0.0034	0.0747	0.0218	−0.0008	0.0019	−0.144
3	0	0.0537	0.0855	0.0064	−0.0626	−0.0093	0.0043	0.0056
4	0	0.0052	0.038	0.0098	−0.022	−0.0482	0.035	0.497
5	0	0.0289	0.038	0.0098	−0.022	−0.0482	0.035	0.332
6	0	0.0052	0.038	0.0098	−0.022	−0.0331	0.0215	0.453
7	−0.0002	0.0292	0.0724	0.0467	0	−0.0008	0.0005	−0.248
8	−0.0008	0.0443	0.0003	0.084	0.0461	0.0692	0.0029	−0.836
9	−0.0018	0.0713	−0.0017	0.0119	0.0071	0.0717	0.1743	−1.483

[a] Formulation of the regression model is $w_d WD + \gamma_1 w_1 + \gamma_2 w_2 + \gamma_3 w_3 + a_1 A_1 + a_2 A_2 + a_3 A_3 + c$.

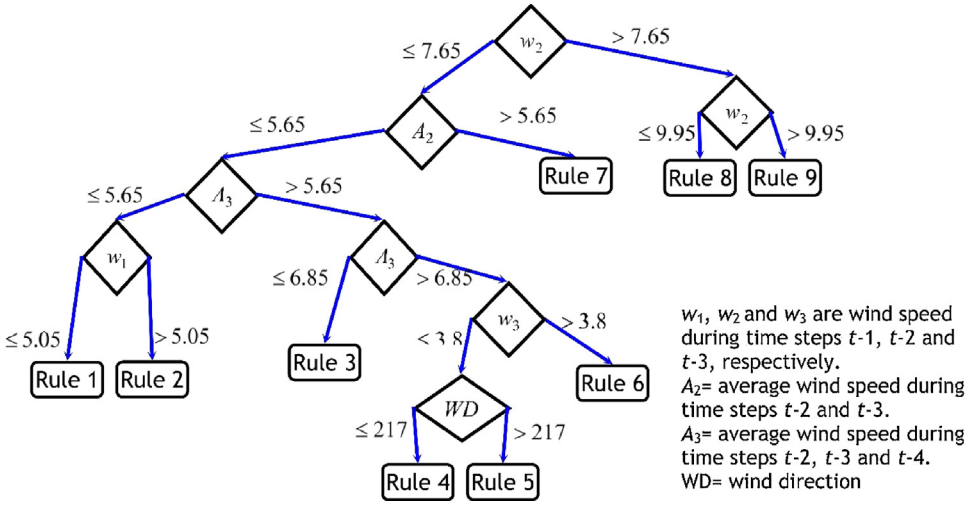

Figure 8 Decision tree rules for SWH prediction using the M5P′ model (with seven predictors).

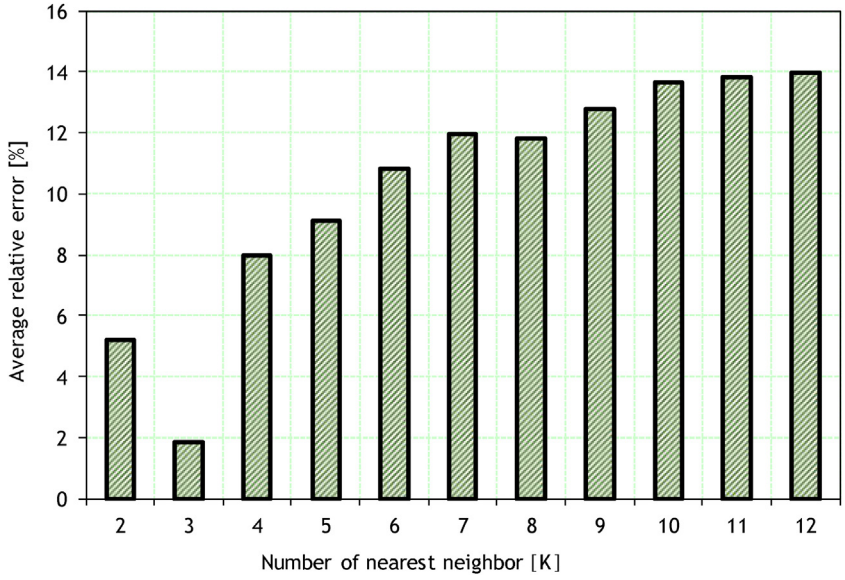

Figure 9 Variation of the average relative error in the validation process of the FKNN model considering different values for the nearest neighbor.

the two classes of 6 and 7 input variables. The closer the Nash–Sutcliffe coefficient to one, the better the accuracy of the developed predictive models.

According to Table 4, for the BNs and SVR models with six predictors, the least Nash–Sutcliffe coefficient is 0.406 and 0.712, respectively. The greatest Nash–Sutcliffe coefficient belongs to M5P model for the both two classes of 6 and 7 input variables (i.e. 0.968 and 0.981, respectively). The FKNN model with Nash–Sutcliffe coefficients of 0.966 and 0.973 indicates that the FKNN is accurate enough for SWH prediction in large lakes.

The values of statistical measures calculated for the FKNN, BN, SVR and M5P models (models with the six predictors) are presented in Table 5. The statistical error indices are listed for three different classes of wave height. In addition, in the row below the obtained statistical errors, the ranks are presented, where the lowest rank belongs to the one with the best performance and vice versa. To this regard, when the wave height class belongs to $0 < WH < 1$ then the Bias scores for SVR, BN, M5P and FKNN models are obtained as −0.051, −0.308, −0.009 and −0.31 where the closest one to zero is M5P model while the farthest

Table 4 Nash–Sutcliffe coefficient for FKNN, BN, SVR and M5P models in SWH prediction.

Model's type	Machine learning methods			
	SVR	BNs	M5P	FKNN
6 predictors	0.712	0.406	0.968	0.966
7 predictors	0.880	0.915	0.981	0.973

Table 5 Performance comparison of the FKNN, BN, SVR and M5P models in SWH prediction using the validation data set.

Statistical measure	Wave height class		Soft computing model			
			SVR	BN	M5P	FKNN
Bias [m]	$0 < WH < 1$	Value	−0.051	−0.308	−0.009	−0.031
		Rank	3	4	1	2
	$1 < WH < 2$	Value	0.559	−0.243	−0.247	−0.225
		Rank	4	2	3	1
	$WH > 2$	Value	1.613	0.405	−0.043	−0.038
		Rank	4	3	2	1
	Total[a]	Value	0.270	−0.270	−0.060	−0.070
		Rank	3	3	1	2
SI[b]	$0 < WH < 1$	Value	0.273	0.819	0.273	0.231
		Rank	3	4	2	1
	$1 < WH < 2$	Value	0.165	0.404	0.164	0.207
		Rank	2	4	1	3
	$WH > 2$	Value	0.187	0.405	0.110	0.118
		Rank	3	4	1	2
	Total	Value	1.039	0.644	0.506	0.266
		Rank	4	3	2	1
RMSRE[b]	$0 < WH < 1$	Value	0.282	0.279	0.266	0.244
		Rank	4	3	2	1
	$1 < WH < 2$	Value	0.697	0.565	0.226	0.208
		Rank	4	3	2	1
	$WH > 2$	Value	1.628	0.208	0.119	0.119
		Rank	3	2	1	1
	Total[a]	Value	0.682	0.430	0.265	0.260
		Rank	4	3	2	1
RMRE[b]	$0 < WH < 1$	Value	0.486	0.476	0.458	0.446
		Rank	4	3	2	1
	$1 < WH < 2$	Value	0.820	0.588	0.435	0.394
		Rank	4	3	2	1
	$WH > 2$	Value	1.257	0.418	0.310	0.307
		Rank	4	3	2	1
	Total[a]	Value	0.684	0.584	0.440	0.423
		Rank	4	3	2	1
CC[b]	$0 < WH < 1$	Value	0.966	0.969	0.971	0.979
		Rank	4	3	2	1
	$1 < WH < 2$	Value	0.990	0.948	0.990	0.984
		Rank	1	3	1	2
	$WH > 2$	Value	0.989	0.995	0.994	0.990
		Rank	4	1	2	3
	Total[a]	Value	0.904	0.918	0.987	0.986
		Rank	4	3	1	2
Summation of rankings	$0 < WH < 1$		18	17	9	6
	$1 < WH < 2$		15	15	9	8
	$WH > 2$		18	13	8	8
	Total[a]		19	15	8	7

[a] All data in the validation data set are used.
[b] These indices are dimensionless.

one is BN model, and thus they are ranked as 1st and 4th, respectively and similarity the ranks for SVR and FKNN models are computed. However, these rankings do not remain consistent as the wave height class varies. The comparison of the statistical error indices in the class of total makes the judgments to be made on each model's performance easier. To this regard, one can say that in terms of the Bias error the M5P model is better than FKNN where the former is scored −0.06 while the latter one could achieve −0.07; also this can be concluded that both SVR

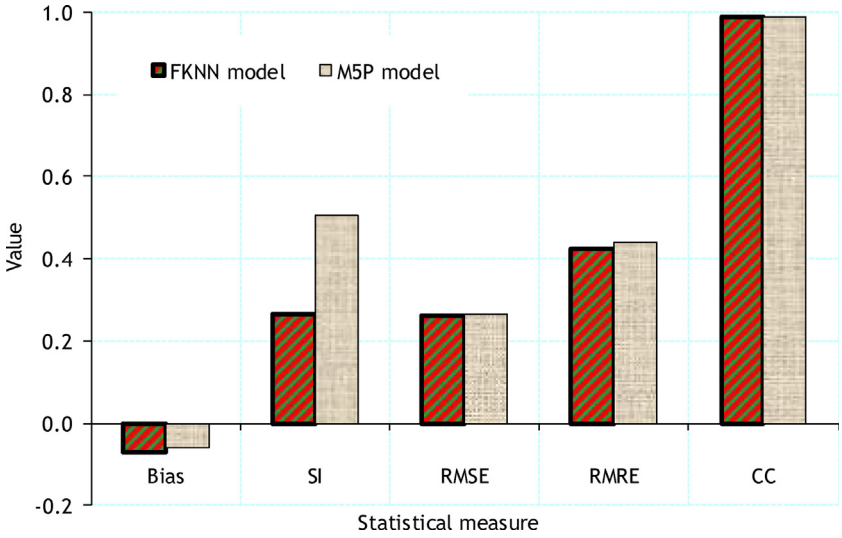

Figure 10 Comparing the results of the FKNN and M5P models using the validation set.

and BN models regardless of their variations in different classes, seemed to have similar performance in their prediction. To draw on a fair judgment, other statistical error indices should be analyzed as well. Regarding the SI, RMSRE, and RMRE error indices the FKNN method outperforms the M5P model except for the CC parameter where the latter one has scored 0.987 which is quite slightly greater than that of the FKNN value with 0.986. For all the statistical error indices, the SVR has an inferior performance than BN and the other two estimation models where it is ranked 4 except for the Bias parameter. To make a general assessment, the ranks are summed for each category of wave height as well as the total class where the lower the rank, the better performance for the model is expected. In general, the FKNN model with a total score of 7 is better than the M5P model although the two has equal ranks with respect to the wave heights greater than 2 m. The SVR model is definitely the worst estimation model since it has the greatest summation of the ranks, 18, for all the wave height classes, so it is the poorest model with the total rank of 19. Therefore, in general, the performance of the FKNN and M5P models are better than the other soft computing models. It should be noted that the FKNN model has more precision in the prediction of SWH in all classes of SWHs. Better performance of the developed FKNN model in the prediction of extreme wave heights (SWH $>$ 2) is remarkable because these waves usually have more adverse impacts. To make this comparison more visually detectable, Fig. 10 uses bar charts to mark the performance of the M5P and FKNN soft computing models with respect to the analyzed statistical errors. The differences in the heights of the bars clearly show that the FKNN model outperforms the M5P model.

4.2. SWH predictions based on wind speed and wind direction

In order to show the effect of including WD as a new predictor, the statistical error indices for all the soft computing models are listed in Table 6 similar to what presented in Table 5. This time, the FKNN′ model scores better in terms of Bias when compared to the M5P′ model with the Bias scores of −0.01 and −0.018 respectively. In general, it seems that the accuracy of FKNN model is still better than all the other three soft computations models. To compare the FKNN with FKNN′ model Fig. 11 shows four bar charts where each one represents a statistical error index including SI, RMSRE, Bias, and RMRE. Fig. 11a compares the SI error for both the FKNN and FKNN′ models in all the wave height categories and the heights of bars are lower than that for the FKNN′ model in all classes when compared to the FKNN model, and thus the former has a greater accuracy in its estimation of SWH. Fig. 11b and c also clearly shows that the FKNN′ model is better than that of FKNN model in terms of RMSRE and Bias respectively. Fig. 11d indicates that although the heights of bars stand lower for the FKNN′ model when compared to the ones for FKNN model, not a quite difference between the two models' performances can be expected. In summary, the accuracy of SWH predictions of the FKNN′ model is greater than FKNN when all the error indices are taken into account.

To draw a comparison between the accuracy of the developed, i.e., trained and tested, soft computing models of M5P′, FKNN′, and BN′, the estimated values of the three models versus the observed values have been plotted for all the test data set in Fig. 12. To make this comparison more clear, the test data set is divided into two sets (Fig. 12a and b). The *y*-axis in Fig. 12 shows the predicted SWH for each soft computing model as well as the observed values. In addition, as it was expected, Fig. 12 indicates that the BN′ model has the poorest accuracy comparing to M5P′ and FKNN′ models. However, the differences between the estimated values obtained from the M5P′ and FKNN′ models and the observed values are approximately low and it cannot be possibly judged that which one is more close to the observed values visually. Fig. 13 depicts the estimated values of SWH versus the observed ones for all the M5P′, FKNN′, and BN′ models. The equality line of $y = x$ has also been plotted to illustrate

Table 6 Performance comparison of the FKNN′, BN′, SVR′ and M5P′ models in SWH prediction using the validation data set.

Statistical measure	Wave height class		Soft computing model			
			SVR′	BN′	M5P′	FKNN′
Bias [m]	$0 < WH < 1$	Value	−0.017	0.112	0.003	−0.013
		Rank	3	4	1	2
	$1 < WH < 2$	Value	0.224	0.140	−0.109	−0.061
		Rank	4	3	2	1
	$WH > 2$	Value	1.044	0.479	0.015	0.028
		Rank	4	3	1	2
	Total[a]	Value	0.156	0.016	−0.018	−0.010
		Rank	4	2	3	1
SI[b]	$0 < WH < 1$	Value	0.245	0.283	0.228	0.228
		Rank	3	4	1	1
	$1 < WH < 2$	Value	0.132	0.195	0.129	0.173
		Rank	2	4	1	3
	$WH > 2$	Value	0.157	0.218	0.105	0.109
		Rank	3	4	1	2
	Total[a]	Value	0.566	0.449	0.358	0.217
		Rank	4	3	2	1
RMSRE[b]	$0 < WH < 1$	Value	0.589	0.481	0.262	0.240
		Rank	4	3	2	1
	$1 < WH < 2$	Value	0.246	0.239	0.144	0.198
		Rank	4	3	1	2
	$WH > 2$	Value	0.688	0.666	0.114	0.118
		Rank	4	3	1	2
	Total	Value	0.553	0.301	0.259	0.250
		Rank	4	3	2	1
RMRE[b]	$0 < WH < 1$	Value	0.548	0.414	0.446	0.440
		Rank	4	3	2	1
	$1 < WH < 2$	Value	0.457	0.453	0.391	0.385
		Rank	4	3	2	1
	$WH > 2$	Value	0.808	0.607	0.308	0.303
		Rank	4	3	2	1
	Total[a]	Value	0.565	0.479	0.432	0.420
		Rank	4	3	2	1
CC[b]	$0 < WH < 1$	Value	0.973	0.976	0.978	0.978
		Rank	3	2	1	1
	$1 < WH < 2$	Value	0.980	0.978	0.970	0.997
		Rank	3	2	4	1
	$WH > 2$	Value	0.982	0.992	0.968	0.996
		Rank	3	2	4	1
	Total[a]	Value	0.963	0.963	0.991	0.987
		Rank	3	3	1	2
Summation of rankings	$0 < WH < 1$		17	16	7	6
	$1 < WH < 2$		17	15	10	8
	$WH > 2$		18	15	9	8
	Total[a]		19	14	10	6

[a] All data in the validation data set are used.
[b] These indices are dimensionless.

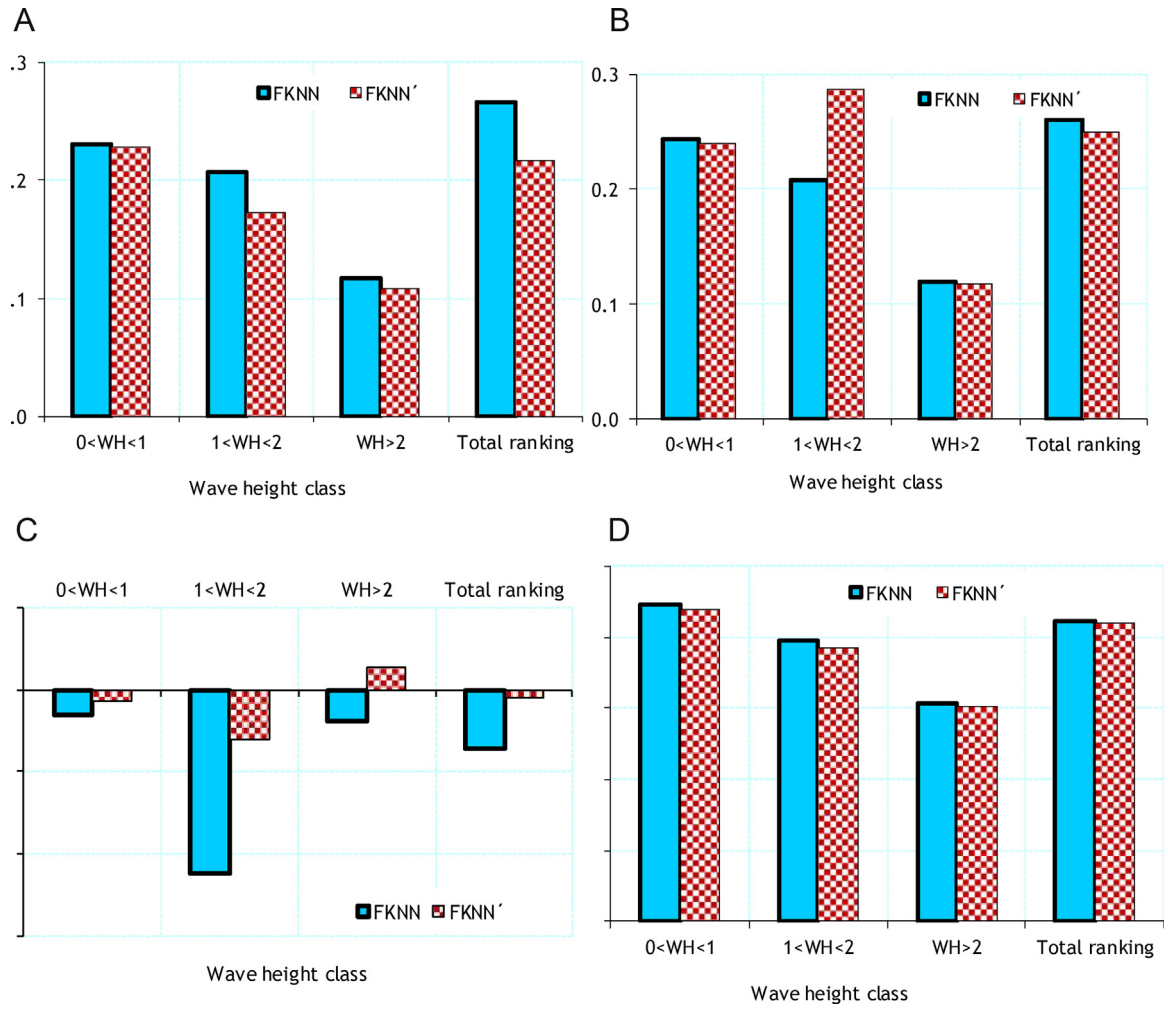

Figure 11 Comparing the efficacy of the FKNN and FKNN′ models in SWH prediction using the validation data set.

the scattered points on different sides of this line. The more close the points lie on this line the greater accuracy is achieved. According to Fig. 13, results of the BN′ model are more scattered on the lower side of the equality line ($y = x$) and there are some instances that the distances of the points from the line are large. While the predicted SWH by the M5P′ and FKNN′ models are more in agreement with observed data, the points denoted with pink square boxes, which belong to the BN′ model, are more aligned with the lower region of the equality line. In fact, the higher number of points below the equality line shows that the predicted values obtained from the BN′ model tend to be lower than the observed values. It can be concluded that the BN′ model underestimates SWH in comparison with other soft computations models. Therefore, a greater safety risk factor should be considered when the BN′ model is used.

The obtained results show that performance of the FKNN′ and M5P′ models in predicting SWH are better than other soft computing models.

5. Conclusion

Significant Wave Height (SWH) is an important hydrodynamic variable for design and operation of coastal and offshore infrastructures. In recent years, soft computing models are receiving more attention in the prediction of wave parameters in coastal engineering because of their precision and convenience usage.

In this paper, a fuzzy *K*-nearest neighbor (FKNN) model was utilized for SWH prediction in large lakes where the fetch length varies by changing the wind direction. In order to evaluate the results of the FKNN model, they were compared with the results of some well-known soft computing approaches, namely, Bayesian networks (BNs), regression tree induction (named M5P), and support vector regression (SVR). The soft computing techniques were utilized for SWH prediction in Lake Superior and their results were compared using some statistical measures. The results show that the

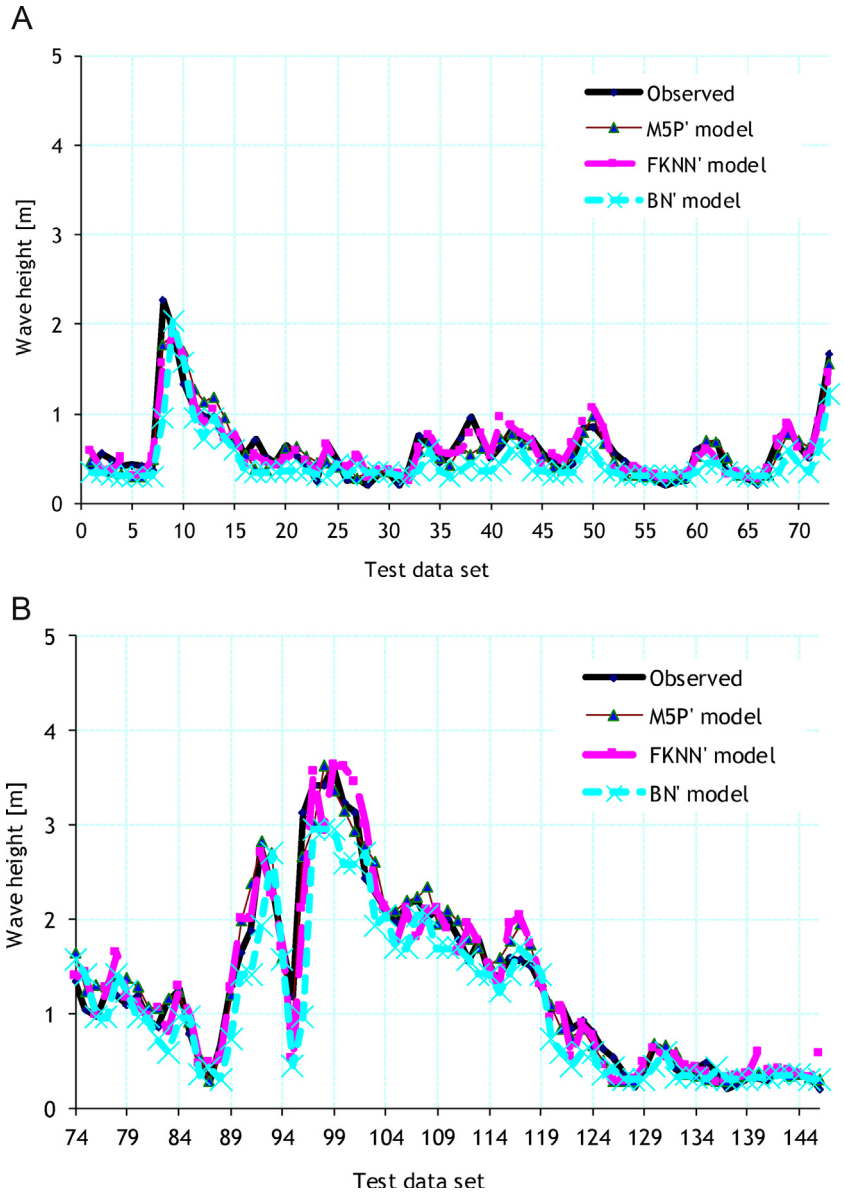

Figure 12 A comparison between the predicted and observed SWHs using the trained FKNN′, M5P′ and BN′ in the validation stage.

FKNN and M5P model can outperform the other soft computing techniques. Comparing values of the statistical error indices shows that the FKNN is better than M5P model in general. Particularly, in comparison with lower wave heights, the FKNN outperformed the M5P model in predicting the heights of waves with values greater than 2 m, which are waves of greater importance. Also, in order to examine the effect of considering Wind Direction (WD) as a new predictor, the same error indices were used. The results show that incorporating the WD predictor improves the accuracy of the soft computing models especially the FKNN model.

The FKNN model presented in this paper predicts the SWH at a fixed point. Development of a spatial SWH prediction model to consider recorded data of multiple buoys would have more general applications in coastal engineering, especially for estimating SWH in areas without wave data records. This paper examined the efficiency of the FKNN model for SWH in an enclosed body of water. In future works, the

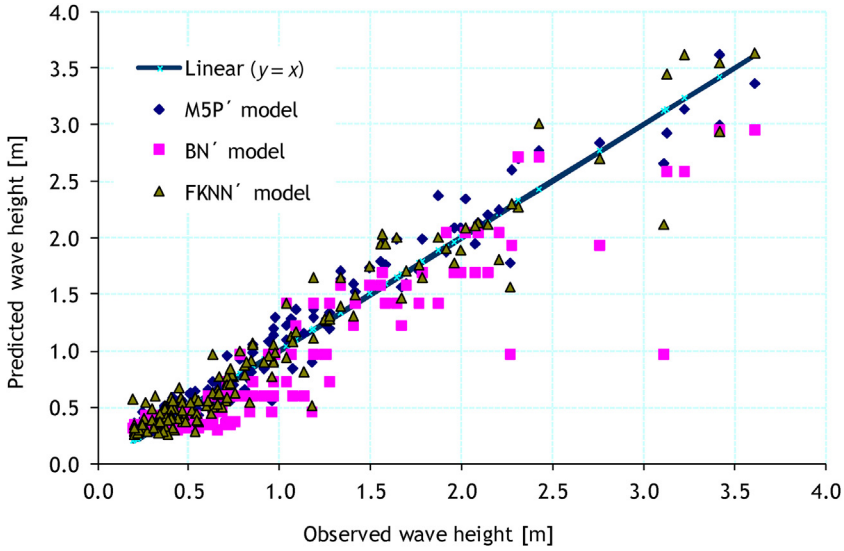

Figure 13 Comparing the performances of FKNN′, M5P′ and BN′ models in significant wave height prediction in the validation stage.

efficiency of the proposed model could be investigated in large seas and ocean.

References

Abed-Elmdoust, A., Kerachian, R., 2012. Wave height prediction using the rough set theory. Ocean Eng. 54, 244—250, http://dx.doi.org/10.1016/j.oceaneng.2012.07.020.

Altunkaynak, A., Wang, K.H., 2012. Estimation of significant wave height in shallow lakes using the expert system techniques. Expert Syst. Appl. 39 (3), 2549—2559, http://dx.doi.org/10.1016/j.eswa.2011.08.106.

Balouchi, B., Nikoo, M.R., Adamowski, J., 2015. Development of expert systems for the prediction of scour depth under live-bed conditions at river confluences: application of different types of ANNs and the M5P model tree. Appl. Soft Comput. 34, 51—59, http://dx.doi.org/10.1016/j.asoc.2015.04.040.

Berbić, J., Ocvirk, E., Carević, D., Lončar, G., 2017. Application of neural networks and support vector machine for significant wave height prediction. Oceanologia 59 (3), 331—349, http://dx.doi.org/10.1016/j.oceano.2017.03.007.

Chai, T., Draxler, R., 2014. Root mean square error (RMSE) or mean absolute error (MAE)? Geosci. Model Dev. 7 (1), 1525—1534.

Chen, H.L., Yang, B., Wang, G., Liu, J., Xu, X., Wang, S.J., Liu, D.Y., 2011. A novel bankruptcy prediction model based on an adaptive fuzzy *k*-nearest neighbor method. Knowl. - Based Syst. 24 (8), 1348—1359, http://dx.doi.org/10.1016/j.knosys.2011.06.008.

Cover, T., Hart, P., 1967. Nearest neighbor pattern classification. IEEE Trans. Inform. Theory 13 (1), 21—27, http://dx.doi.org/10.1109/TIT.1967.1053964.

Derrac, J., Chiclana, F., Garcia, S., Herrera, F., 2016. Evolutionary fuzzy *k*-nearest neighbors algorithm using interval-valued fuzzy sets. Inform. Sci. 329, 144—163, http://dx.doi.org/10.1016/j.ins.2015.09.007.

Etemad-Shahidi, A., Ghaemi, N., 2011. Model tree approach for prediction of pile groups scour due to waves. Ocean Eng. 38 (13), 1522—1527, http://dx.doi.org/10.1016/j.oceaneng.2011.07.012.

Etemad-Shahidi, A., Mahjoobi, J., 2009. Comparison between M5′ model tree and neural networks for prediction of significant wave height in Lake Superior. Ocean Eng. 36 (15—16), 1175—1181, http://dx.doi.org/10.1016/j.oceaneng.2009.08.008.

Fredj, I.B., Ouni, K., 2017. Comparison of crisp and fuzzy kNN in phoneme recognition. In: 2017 International Conference on Advanced Systems and Electric Technologies (IC_ASET), 14—17 January 2017, Hammamet, Tunisia, IEEE, 118—122, http://dx.doi.org/10.1109/ASET.2017.7983676.

Karimi, S., Kisi, O., Shiri, J., Makarynskyy, O., 2013. Neuro-fuzzy and neural network techniques for forecasting sea level in Darwin Harbor, Australia. Comput. Geosci. 52, 50—59, http://dx.doi.org/10.1016/j.cageo.2012.09.015.

Kazemi Elaki, N., Shabakhty, N., Abbasi Kia, M., Sanayee Moghaddam, S., 2016. Structural reliability: an assessment using a new and efficient two-phase method based on artificial neural network and a harmony search algorithm. Civil Eng. Infrastr. J. 49 (1), 1—20, http://dx.doi.org/10.7508/ceij.2016.01.001.

Keller, J.M., Gray, M.R., Givens, J.A., 1985. A fuzzy *k*-nearest neighbor algorithm. IEEE Trans. Syst. Man Cyb. SMC(4) 580—585, http://dx.doi.org/10.1109/TSMC.1985.6313426.

Li, J., 2016. Assessing spatial predictive models in the environmental sciences: accuracy measures, data variation and variance explained. Environ. Modell. Softw. 80, 1—8, http://dx.doi.org/10.1016/j.envsoft.2016.02.004.

Mahjoobi, J., Etemad-Shahidi, A., Kazeminezhad, M.H., 2008. Hindcasting of wave parameters using different soft computing methods. Appl. Ocean Res. 30 (1), 28—36, http://dx.doi.org/10.1016/j.apor.2008.03.002.

Malekmohamadi, I., Bazargan-Lari, M.R., Kerachian, R., Nikoo, M.R., Fallahnia, M., 2011. Evaluating the efficacy of SVMs, BNs, ANNs and ANFIS in wave height prediction. Ocean Eng. 38 (2), 487—497, http://dx.doi.org/10.1016/j.oceaneng.2010.11.020.

Malekmohamadi, I., Ghiassi, R., Yazdanpanah, M.J., 2008. Wave hindcasting by coupling numerical model and artificial neural networks. Ocean Eng. 35 (3), 417—425, http://dx.doi.org/10.1016/j.oceaneng.2007.09.003.

Monghasemi, S., Nikoo, M.R., Fasaee, M.A.K., Adamowski, J., 2015. A novel multi criteria decision making model for optimizing time-cost-quality trade-off problems in construction projects. Expert Syst. Appl. 42 (6), 3089—3104, http://dx.doi.org/10.1016/j.eswa.2014.11.032.

Monghasemi, S., Nikoo, M.R., Fasaee, M.A.K., Adamowski, J., 2017. A hybrid of genetic algorithm and evidential reasoning for optimal design of project scheduling: a systematic negotiation framework for multiple decision-makers. Int. J. Inf. Tech. Decis. 16 (2), 389—420, http://dx.doi.org/10.1142/S0219622017500079.

Nash, J.E., Sutcliffe, J.V., 1970. River flow forecasting through conceptual models part I - a discussion of principles. J. Hydrol. 10 (3), 282—290, http://dx.doi.org/10.1016/0022-1694(70)90255-6.

Nikoo, M.R., Kerachian, R., 2017. Wave height prediction using artificial immune recognition systems (AIRS) and some other data mining techniques. IJST-Trans. Civil Eng. 41 (3), 329—344, http://dx.doi.org/10.1007/s40996-017-0067-y.

Nikoo, M.R., Khorramshokouh, N., Monghasemi, S., 2015. Optimal design of detention rockfill dams using a simulation-based optimization approach with mixed sediment in the flow. Water Resour. Manag. 29 (15), 5469—5488, http://dx.doi.org/10.1007/s11269-015-1129-1.

Nikoo, M.R., Varjavand, I., Kerachian, R., Pirooz, M.D., Karimi, A., 2014. Multi-objective optimum design of double-layer perforated-wall breakwaters: application of NSGA-II and bargaining models. Appl. Ocean Res. 47, 47—52, http://dx.doi.org/10.1016/j.apor.2013.12.001.

Özger, M., 2010. Significant wave height forecasting using wavelet fuzzy logic approach. Ocean Eng. 37 (16), 1443—1451, http://dx.doi.org/10.1016/j.oceaneng.2010.07.009.

Özger, M., Şen, Z., 2007. Prediction of wave parameters by using fuzzy logic approach. Ocean Eng. 34 (3), 460—469, http://dx.doi.org/10.1016/j.oceaneng.2006.03.003.

Parajka, J., Merz, R., Skøien, J.O., Viglione, A., 2015. The role of station density for predicting daily runoff by top-kriging interpolation in Austria. J. Hydrol. Hydromech. 63 (3), 228—234, http://dx.doi.org/10.1515/johh-2015-0024.

Patil, S.G., Mandal, S., Hegde, A.V., 2012. Genetic algorithm based support vector machine regression in predicting wave transmission of horizontally interlaced multi-layer moored floating pipe breakwater. Adv. Eng. Softw. 45 (1), 203—212, http://dx.doi.org/10.1016/j.advengsoft.2011.09.026.

Somari, N.M., Abdullah, M.F., Osman, M.K., Nazelan, A.M.I., Ahmad, K.A., Appanan, S.P.R.S., Hooi, L.K., 2016. Particles contaminations detection during plasma etching process by using *k*-nearest neighbors and Fuzzy *k*-nearest neighbors. In: Computing and Engineering (ICCSCE), November 2016, 6th IEEE International Conference on Control System, IEEE. 512—516, http://dx.doi.org/10.1109/ICCSCE.2016.7893630.

Tetko, I.V., Livingstone, D.J., Luik, A.I., 1995. Neural network studies. 1. Comparison of overfitting and overtraining. J. Chem. Inf. Comp. Sci. 35 (5), 826—833.

Tiwari, M.K., Chatterjee, C., 2010. Development of an accurate and reliable hourly flood forecasting model using wavelet-bootstrap-ANN (WBANN) hybrid approach. J. Hydrol. 394 (3), 458—470, http://dx.doi.org/10.1016/j.jhydrol.2010.10.001.

Wang, P., Xiao, X., 2011. Predicting the risk type of human papillomaviruses based on sequence-derived features. In: iCBBE 5th International Conference on Bioinformatics and Biomedical Engineering, 10—12 May 2011, Wuhan, China, IEEE, 1—4, http://dx.doi.org/10.1109/icbbe.2011.5779985.

Warren, L.T., Damin, L., 1997. Two manufacturing applications of the fuzzy *K*-NN algorithm. Fuzzy Set Syst. 92 (3), 289—303, http://dx.doi.org/10.1016/S0165-0114(96)00176-5.

Xiao, X., Wang, P., 2010. Application of function domain and pseudo amino acid composition to predict hetero-oligomer protein structural types. In: iCBBE 4th International Conference on Bioinformatics and Biomedical Engineering, 18—20 June 2010, Chengdu, China, IEEE, 1—4, http://dx.doi.org/10.1109/ICBBE.2010.5515624.

Zadeh, L.A., 1965. Fuzzy sets. Inform. Comput. 8 (3), 338—353.

Zanaganeh, M., Mousavi, S.J., Shahidi, A.F.E., 2009. A hybrid genetic algorithm-adaptive network-based fuzzy inference system in prediction of wave parameters. Eng. Appl. Artif. Intel. 22 (8), 1194—1202, http://dx.doi.org/10.1016/j.engappai.2009.04.009.

Oceanologia (2018) 60, 169—186

Available online at www.sciencedirect.com

ScienceDirect

journal homepage: www.journals.elsevier.com/oceanologia/

ORIGINAL RESEARCH ARTICLE

Investigating the role of air-sea forcing on the variability of hydrography, circulation, and mixed layer depth in the Arabian Sea and Bay of Bengal

Atul Srivastava, Suneet Dwivedi *, Alok Kumar Mishra

K Banerjee Centre of Atmospheric and Ocean Studies and M N Saha Centre of Space Studies, University of Allahabad, Allahabad, UP 211002, India

Received 11 April 2017; accepted 2 October 2017
Available online 21 October 2017

KEYWORDS
Arabian Sea and Bay of Bengal;
Air-sea forcing;
Ocean general circulation model;
Hydrography and circulation;
Vertical stability

Summary An effort is made to understand and quantify the influence of near surface zonal and meridional winds, incoming shortwave radiation, and freshwater flux air-sea forcings on the seasonal variability of the hydrography, circulation, and mixed layer depth of the Arabian Sea (AS) and Bay of Bengal (BoB). Sensitivity experiments using an ocean general circulation model are carried out for this purpose in the Indian ocean around 65°—95°E, 5°—22°N during 1998—2014 (17 years). In the absence of near surface wind forcing, the sea surface temperature of the region greatly increases in all the seasons, whereas, in the absence of incoming shortwave radiation forcing, exactly opposite is the case. The sea surface salinity of the AS and BoB decreases in the absence of wind and shortwave radiation forcings, whereas, in the northern BoB it increases in the absence of freshwater flux forcing. The sub-surface changes in the stratification of temperature and salinity are also investigated. The influence of the air-sea forcings on the mixed layer depth of the region is found to be highly seasonally dependent. The effect of air-sea forcings on the seasonal variability of the upper ocean vertical stability is studied using the vertical shear of the horizontal velocity, buoyancy frequency, and energy required for mixing as quantifiers. The near surface wind forcing has highest contribution in changing the surface circulation of the region.

* Corresponding author at: K Banerjee Centre of Atmospheric and Ocean Studies and M N Saha Centre of Space Studies, University of Allahabad, Allahabad, UP 211002, India.
E-mail address: suneetdwivedi@gmail.com (S. Dwivedi).
Peer review under the responsibility of Institute of Oceanology of the Polish Academy of Sciences.

Production and hosting by Elsevier

https://doi.org/10.1016/j.oceano.2017.10.001

1. Introduction

The near surface air-sea forcings greatly influence the ocean variables. For example, the near surface winds transfer parts of its momentum to upper layers of the ocean and force the ocean water to be in motion resulting into ocean circulation. Similarly, the heating of the ocean near the surface occurs mainly due to the incoming shortwave radiation. The heat transfer (downward diffusion) from the surface of the ocean to the deeper layers and its advection is responsible for the ocean mixing to a large extent. Likewise the changes in the freshwater flux also affect the hydrography and circulation of the ocean.

Similar to other parts of the world oceans, the hydrography, circulation, and mixed layer depth of the Arabian Sea (AS) and Bay of Bengal (BoB) regions of the Indian ocean also depend heavily on the air-sea fluxes. The AS and BoB circulation is primarily considered as wind and buoyancy driven (Liu and Alexander, 2007; Schott and McCreary, 2001; Schott et al., 2002). Several observational and modelling studies have been carried out to study the effect of atmosphere-ocean interaction on the variability of the sea surface temperature (SST), sea surface salinity (SSS), mixed layer depth (MLD) and circulation of the AS and BoB. Gopalkrishna et al. (1988) studied the influence of winds on the variability of the mixed layer in the northern Indian Ocean during different phases of the summer monsoon. They found that the wind stress affects the MLD variability over the AS more as compared to BoB. Han et al. (2001) studied influence of precipitation minus evaporation and BoB river runoff on dynamics, thermodynamics, and mixed layer physics in the upper Indian Ocean. Han and Webster (2002) used a nonlinear 4½-layer reduced-gravity ocean model with active thermodynamics and mixed layer physics to investigate the causes of sea level interannual variability in the Bay of Bengal. It was found that the sea level changes in the bay result largely from the wind variability. Their analysis also revealed that the sea level anomalies in the equatorial ocean may serve as a potential index for prediction of floods and cholera in the Bangladesh. Shenoi et al. (2002) analyzed the heat budget of the near surface AS and BoB and studied its effect on the Indian summer monsoon. They showed that both in AS and BoB, there is a cycle with positive feedback, but the cycles in both the basins work in opposite directions (due to stronger and weak winds, respectively). This locks monsoon convective activity primarily over the bay and less rainfall over the AS. Wajsowicz (2002) performed an ocean modelling sensitivity study using two different wind-stress climatologies for investigating the effect of the Indonesian throughflow on the upper thermocline circulation and surface heat flux over the Indian Ocean. Weller et al. (2002) examined the role of surface forcing (particularly during the northeast (NE) and southwest (SW) monsoon season) in the semi-annual evolution of the upper-ocean temperature, salinity, and velocity fields in the AS using the moorings deployed from October 1994 to October 1995. The NE (SW) monsoon was found to be characterized by moderate (strong) winds, clear (cloudy) skies, and dry (moist) air resulting into an average loss (gain) of 19.7 (89.5) W m^{-2} of ocean energy and MLD deepening to 100 m (80 m). Gordon et al. (2003) found that the surface freshwater flux can change the upper ocean velocity field by creating dynamic height gradients. The change in the salinity stratification as a result of surface freshwater flux makes a corresponding change in the mixed layer depth which influences the velocity shear and entrainment rates (Han et al., 2001; Howden and Murtugudde, 2001; Sengupta et al., 2006). Perigaud et al. (2003) studied the impact of interannual rainfall anomalies on the temperature and salinity variability of the Indian ocean using 4½-layer nonlinear reduced gravity model. It was found that the precipitation anomalies significantly affect the model's SST and SSS in the Indian Ocean. Using a one-dimensional turbulent closure model, Prasad (2004) investigated the physical mechanisms governing the seasonal evolution of MLD and SST along meridional sections of the AS and BoB. He concluded that it is differences in surface wind stress and buoyancy forcing rather than differences in the vertical salinity stratification which is mainly responsible for the differences in MLD and SST of the AS and BoB. De Boyer Montégut et al. (2007) showed that the wind variability plays a strong role in driving the AS and BoB circulation by impacting latent heat fluxes. Agarwal et al. (2007) examined the response of an ocean general circulation model (OGCM) forced with wind products from the NCEP/NCAR reanalysis and QuikSCAT scatterometer. They found that the overall performance of OGCM forced with scatterometer winds is much better than the OGCM forced with NCEP/NCAR winds. Sharma et al. (2007) analyzed the impact of satellite derived forcings of winds and precipitation on the Indian Ocean model simulations. They also examined processes responsible for salinity variations in the Indian Ocean during dipole years 1994 and 1997. They found that the ocean model simulations forced with scatterometer winds describe the interannual variability of sea surface temperature (SST) more realistically than the model simulations forced with NCEP/NCAR winds. Anitha et al. (2008) used Argo temperature and salinity profiles for the years 2003 and 2004 to study the seasonal variations in the surface buoyancy flux in the BoB and AS. Their study brought out quantitative influence of winds to surface buoyancy and the applicability of scaling mixed layer using Monin-Obukhov length in the BoB and AS. Sreenivas et al. (2008) suggested that the wind stress and/or net heat gain variability are mainly responsible for influencing the mixed layer depths over the AS. Duncan and Han (2009) investigated intraseasonal sea surface temperature (SST) variability in the Indian Ocean during boreal summer with a series of experiments using the Hybrid Coordinate Ocean Model (HYCOM). They found that wind plays a much larger role in altering SSTs than either shortwave fluxes or precipitation. Seo et al. (2009) investigated the effects of freshwater forcing from river discharge into the Indian Ocean on oceanic vertical structure and the Indian monsoons using a fully coupled, high-resolution, regional climate model. Their results suggested that freshwater forcing plays an important role during the boreal winter by affecting SST and the coupled ocean-atmosphere interaction, with potential impacts on the broadscale regional climate. Jaswal et al. (2012) found the relationship between SST and surface air temperature over the AS and BoB and observed that the SST and air temperature are highly correlated over the AS as compared to the BoB. Using HYCOM, Zhang and Du (2012) analyzed seasonal variability of the salinity budget in the southeastern AS and the southern part of the BoB in the context of freshwater flux changes. The results showed that fresh water flux could not

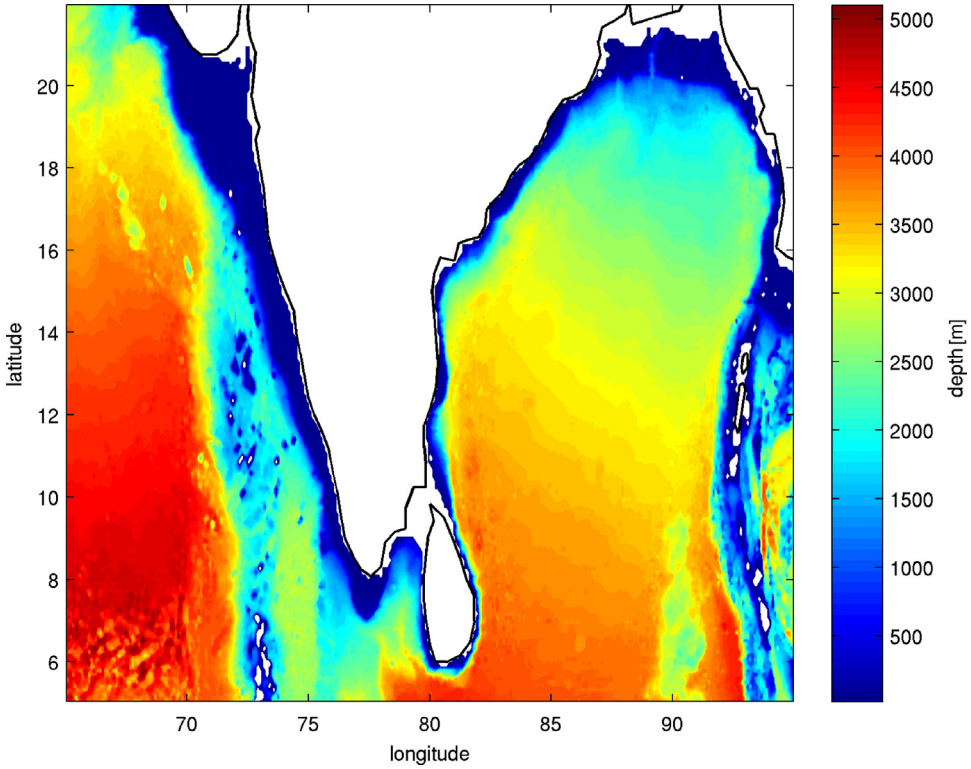

Figure 1 Bathymetry of region of interest (65°—95°E, 5°—22°N).

explain salinity changes in salinity budget of both the regions. Li et al. (2013) examined effects of diurnal cycle in solar radiation on the tropical Indian Ocean mixed layer variability during wintertime Madden-Julian Oscillations using HYbrid Coordinate Ocean Model (HYCOM). Akhil et al. (2014) performed a detailed modelling study over the BoB to understand strong seasonal cycle of the SSS in response to the Indian monsoon freshwater forcing. Their results confirmed that the strong freshening in the northern Bay during the monsoon results from the Ganges-Brahmaputra river discharge and from precipitation over the ocean. They also argued that it is the vertical processes and not the northward horizontal advection which drive that the erosion of the freshwater tongue along the east coast of India. Callaghan et al. (2014) have investigated the influence of surface forcing on near-surface and mixing layer turbulence in the tropical Indian Ocean. Da-Allada et al. (2015) suggested that the seasonal cycle of mixed layer salinity in the tropical Indian ocean is mainly influenced by the meridional advection driven by the monsoonal winds. Jana et al. (2015) examined the impact of seasonal river input on the BoB circulation features using ROMS ocean model. They also showed that the wind stress forcing plays a significant role during the summer monsoon season in changing the MLD and SST of the region, whereas, the buoyancy flux plays a significant role during the winter monsoon. Vinayachandran et al. (2015) investigated the impact of river runoff into the ocean on the Indian summer monsoon rainfall (ISMR). By carrying out 100 years long simulation experiments, they found that in the absence of river discharge, the global average SST rose by about 0.5°C and the ISMR increased by about 10% of the seasonal total with large increase in the eastern BoB and along the west coast of India.

There have not been many studies, however, where contribution of the near surface winds, incoming shortwave radiation, and freshwater flux in changing the circulation and variability of the region has been estimated separately using long-term high-resolution model output. The principal aim of the present manuscript is to attempt to do this with the help of realistic ocean model simulations. We use state-of-the-art regional ocean circulation model for this purpose and carry out several sensitivity experiments using it in an effort to decipher the relative roles of air-sea forcings in influencing the surface and sub-surface temperature and salinity, MLD, and circulation of the AS and BoB. A particular emphasis is given in estimating the seasonal variability of the SST, SSS, MLD, and surface currents in this context. The effect of air-sea forcings on the vertical stability of the ocean is also estimated using vertical shear of the horizontal velocity, buoyancy frequency, and energy required for mixing as quantifiers.

The configuration of the ocean circulation model, its setup along with brief details about different sensitivity experiments is given in Section 2. The results and discussion are described in Section 3. Conclusions are in Section 4.

2. Methodology

The ocean general circulation model, which we use for our study, is the MITgcm (Marshall et al., 1997). We make a regional configuration of the MITgcm in a limited area around the region 65°—95°E, 5°—22°N in the northern Indian Ocean. The model domain covers both the Arabian Sea as well as Bay of Bengal. The MITgcm is a z-coordinate model and solves the incompressible Navier—Stokes equation. We

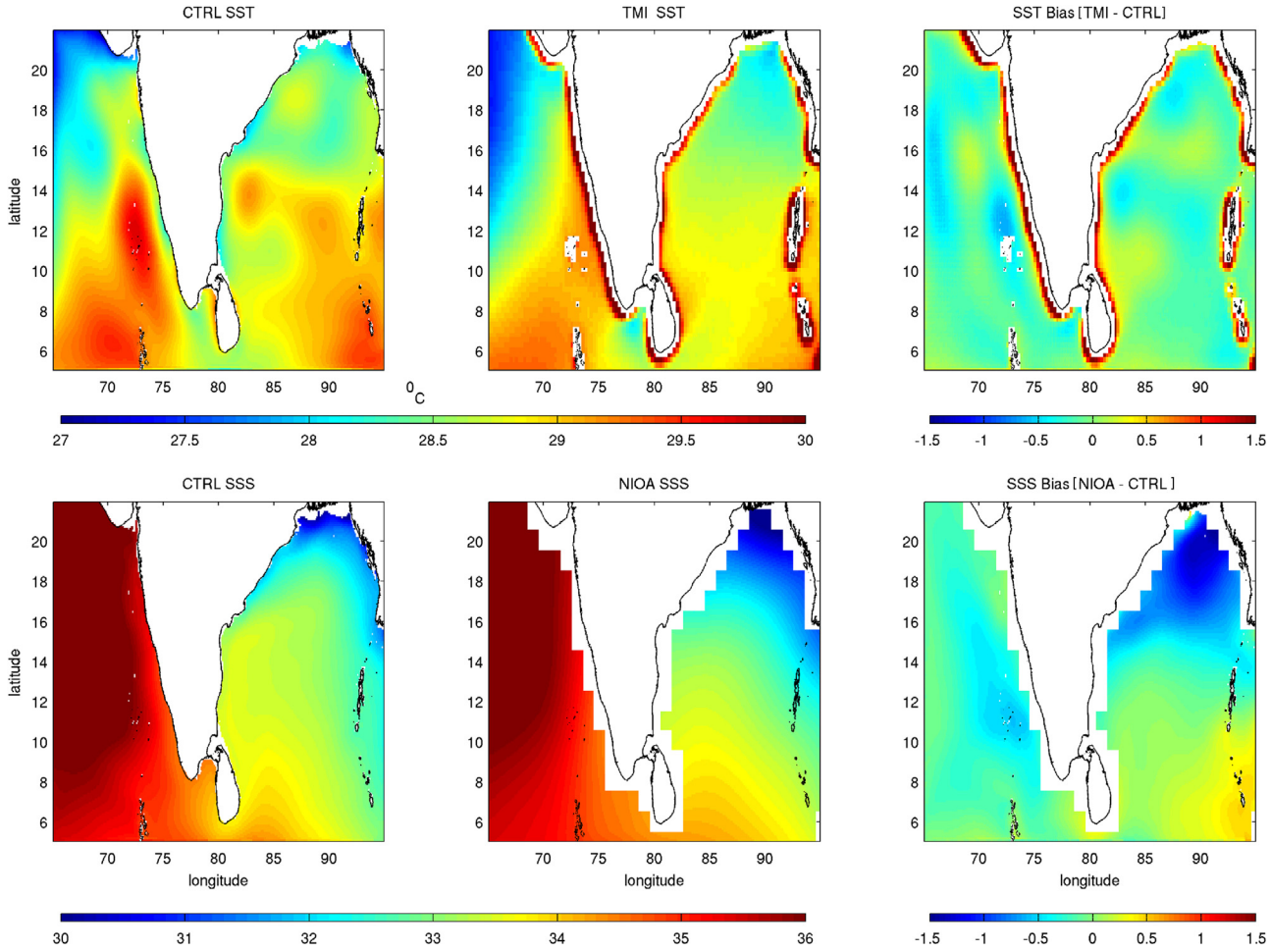

Figure 2 Comparison of the climatological SST between CTRL run and TMI dataset during 1998—2014 (left upper panel); SST bias between CTRL and TMI SST (right upper panel); comparison of the climatological SSS between CTRL and NIOA dataset during 1998—2014 (left lower panel); SSS bias between CTRL and NIOA SSS (right lower panel).

use the Boussinesq and hydrostatic approximations in our model setup. The model space is discretized using staggered Arakawa C grid. The horizontal resolution of the model is taken as 10 km. We use 28 levels in the vertical with the highest resolution of 5 m near the surface. The vertical resolution gradually decreases as we move towards ocean floor. The K-profile parameterization (KPP) scheme (Large et al., 1994) is used to represent the sub-grid scale mixing in vertical. We use 1′ topography data of Smith and Sandwell (1997) to derive the bathymetry of the model (Fig. 1). The model uses no-slip condition on sides as well as bottom. The eddy (harmonic) viscosity and diffusivity satisfying the CFL stability criteria are chosen in horizontal and vertical. The bottom frictional drag coefficient is taken as 0.001. A third order direct space-time advection scheme is employed for temperature and salinity. The nonlinear equation of state is used following the Jackett and McDougall (1995). Our model setup uses the open boundary conditions on all the sides. In other words, we allow inflow and outflow to and from the north, south, east and west boundaries. The boundary condition in the north is required only in a small portion in the Arabian Sea between 65° and 69°E since other grid points are land points (Fig. 1). Similarly, the eastern boundary condition is given along the grid points lying on 5°—15.5°N in the open ocean. We implemented open boundary conditions in the MITgcm following the method given in Zhang and Marotzke (1999). The Ocean Reanalysis System 4 (ORAS4) (Balmaseda et al., 2013) values of temperature, salinity, zonal and meridional velocity are used to prescribe these variables at each boundary. We interpolate the ORAS4 values at each boundary to the model grid for this purpose. The model computes net flow across the boundaries and adjusts all normal velocities on boundaries to obtain zero net inflow. We update the boundary values at an interval of 30 days. The imperfect model parameterizations and inaccuracies in the heat and freshwater flux forcing data generally result into systematic model bias. In order to prevent systematic drift in ocean variables (for example, temperature and salinity) caused by these inaccuracies, we introduce the surface temperature and salinity restoring in the ocean models. The model's surface temperature and salinity are relaxed towards ORAS4 monthly climatology with a time scale of 30 days. The model is spun-up for five years (from 1 Jan 1993 to 31 Dec 1997) with the initial temperature and salinity values derived from the World Ocean Atlas 2013 (WOA13). The production run is carried out by integrating the model for 17 years during 1 Jan 1998 to 31 Dec 2014. In an effort to demonstrate the effect of air-sea forcing variables on the

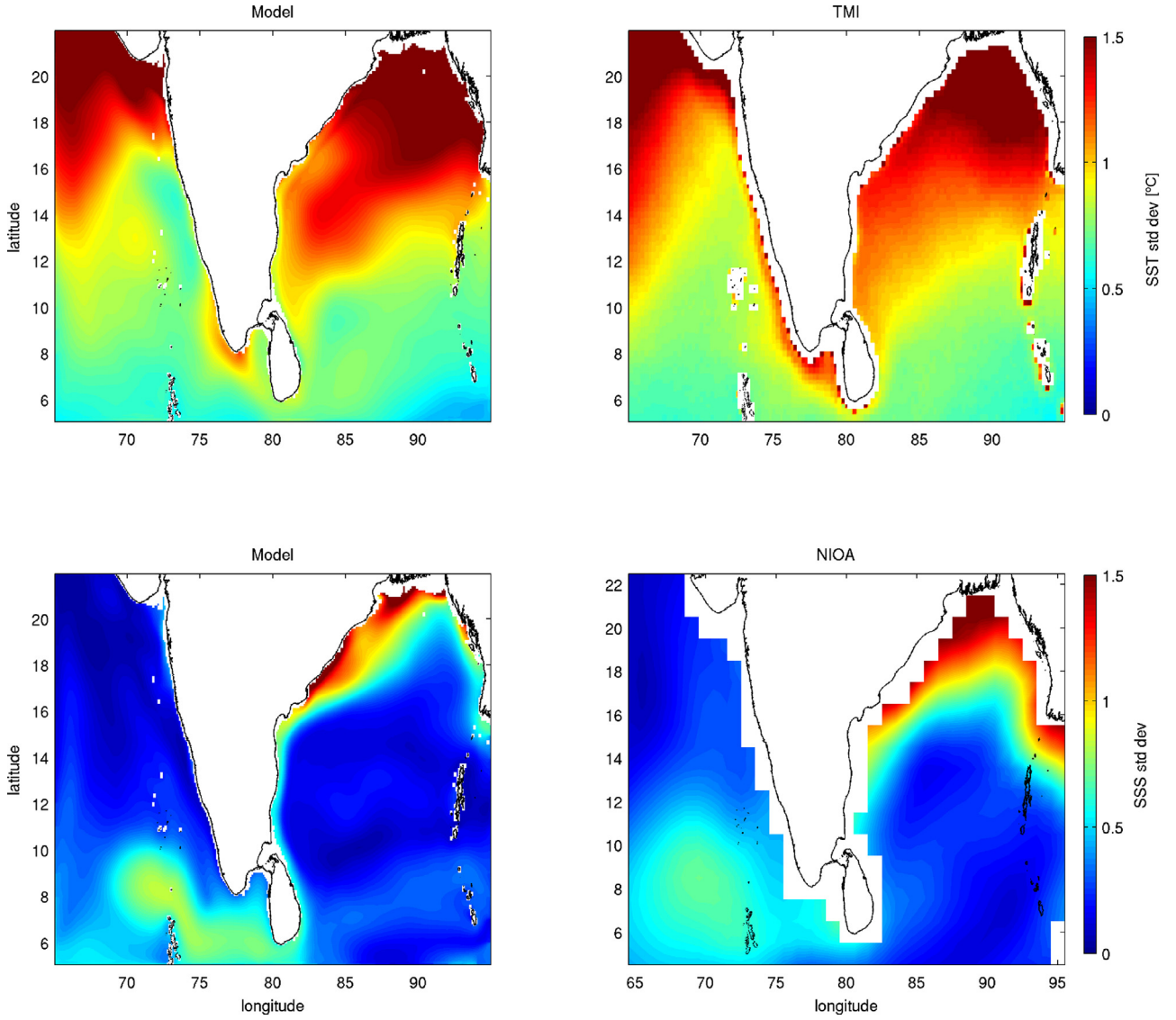

Figure 3 Standard deviation of the SST from CTRL run and TMI dataset (upper panel); standard deviation of the SSS from CTRL run and NIOA dataset (lower panel).

seasonal variability of hydrography, circulation and mixed layer depth, we perform four sensitivity (intercomparison) experiments. In the first experiment, hereinafter referred to as CTRL run, we force the model using the 6-hourly NCEP/NCAR reanalysis (Kalnay et al., 1996) air temperature, relative humidity, downward long-wave and short-wave radiation, precipitation, runoff, zonal and meridional wind data. The model calculates the air-sea fluxes, namely, ocean surface wind stress, heat, and freshwater flux (precipitation plus runoff minus evaporation) from these prescribed atmospheric states using the bulk formulae of Large and Pond (1982) (details are in Appendix A). In the second experiment, hereinafter referred to as WWINDS, we do not use the zonal and meridional winds to force the model. In other words, the zonal and meridional winds are set to zero. All the other air-sea forcings remaining the same as before (i.e. similar to CTRL run). Similarly, in the third and fourth experiment, hereinafter referred to as WSWAVE and WFWF, we do not use (i.e. we set zero) shortwave radiation and freshwater flux, respectively, to force the model while keeping all the other air-sea forcings same as in the CTRL run.

3. Results and discussion

We perform the CTRL, WWINDS, WSWAVE and WFWF sensitivity experiments using the method described in section 2 to understand the effect of winds, shortwave radiation and freshwater flux in influencing the circulation and variability of the AS and BoB. Before discussing the sensitivity experiment simulations, it would be useful to present model (CTRL) run's validation against the known observations. For this purpose, we show in Fig. 2 (upper panel) the mean sea surface temperature (SST) from CTRL run and compare it with SST values from the TRMM Microwave Imager (TMI) (Wentz, 2015). It may be clearly seen from the figure that the model very well captures the mean state of the SST. The correlation between TMI and CTRL run SST is 0.9 which is

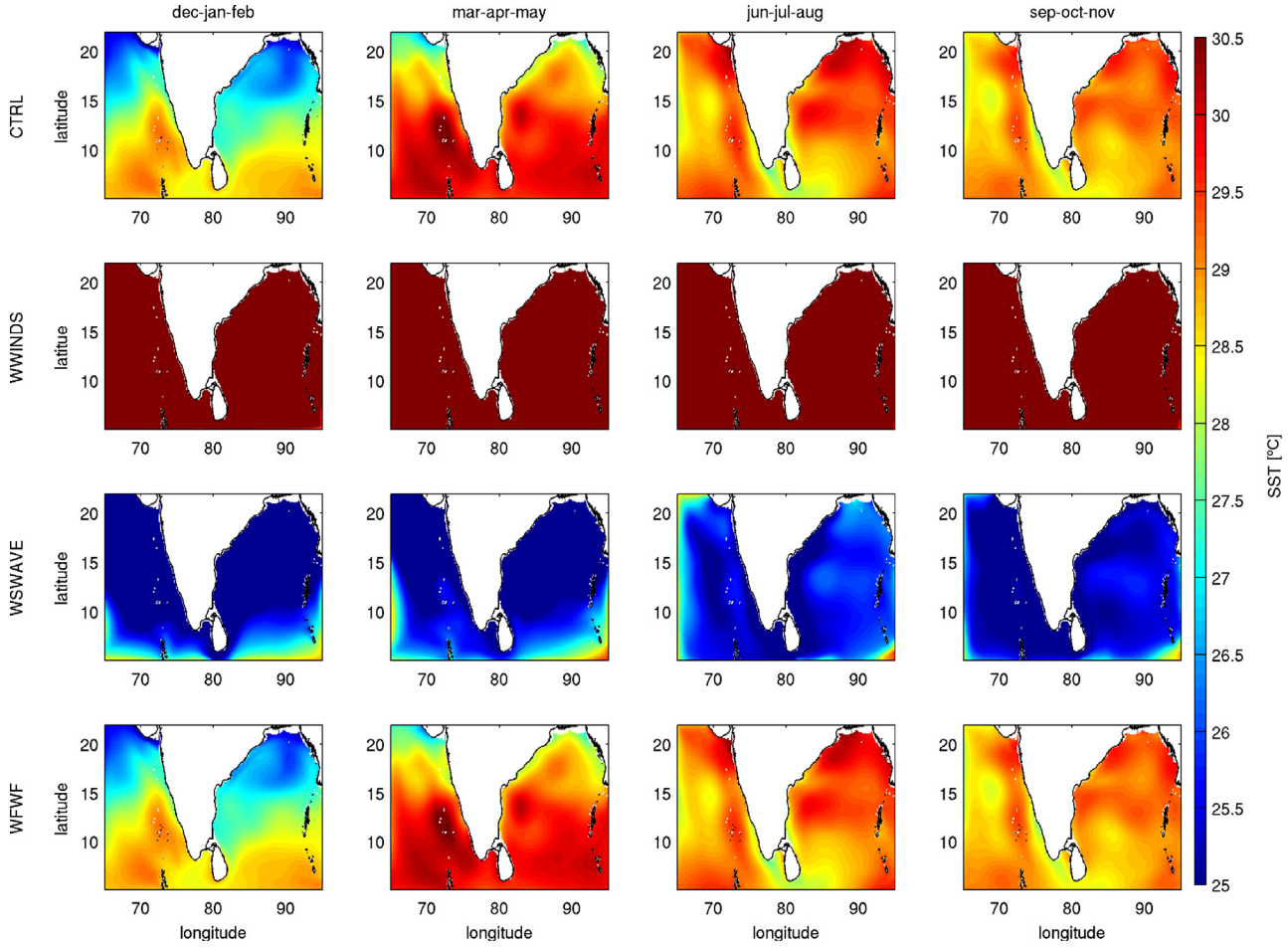

Figure 4 Seasonal variability of the SST of the region during DJF, MAM, JJA, and SON months over the period 1998—2014. 1st row shows SST from CTRL run, 2nd row shows SST from WWINDS experiment, while the 3rd and 4th row shows SST from WSWAVE and WFWF experiments, respectively.

significant at 99.9% level. The SST bias (TMI—CTRL) map suggests that the bias is very small in most parts of the domain, except along eastern Arabian sea and some parts of the central and northern Bay of Bengal. The bias seen along the coasts, however, may be ignored since TMI has known problems along the coasts (Wang et al., 2011). The root mean square error (RMSE) between the CTRL run and TMI SST is found to be 0.5°C, whereas the standard deviation of TMI SST is 1.2°C, thus confirming the quality of model output. We shown in Fig. 2 (lower panel) the model mean sea surface salinity (SSS) and compare it with corresponding values from the NIO Climatological Atlas (NIOA) (Chatterjee et al., 2012). We found that the CTRL run realistically simulates high (low) SSS in the AS (BoB) regions. The correlation coefficient between the CTRL SSS and the NIOA SSS is 0.91 (at 99.9% significance level). The (NIOA-CTRL) SSS bias is small in nearly all the regions, except in the northern BoB. The RMSE between the CTRL and NIOA SSS is 0.45 which is much smaller than the standard deviation of 1.74 of the NIOA SSS.

The spatio-temporal variability of the CTRL run's SST and SSS is presented in Fig. 3 for validation against the observations. We see that barring a few places, the SST and SSS variability over the AS and BoB is reasonably captured in the CTRL run. The SST in the BoB region is more variable as compared to the AS. The SST variability monotonically decreases from north to south of the domain. The northern BoB and AS show higher SST variability compared to the southern portion. The SSS variability on the other hand, is higher in the southern AS as compared to northern AS. In the BoB region, however, the northern region shows higher SSS variability.

One may argue that the open boundary conditions of our limited area regional ocean model setup may become a source of uncertainty. For example, westerly winds in northern spring and fall along the equator excite equatorial Kelvin waves, which accompanies deep thermocline. These waves hit the eastern boundary and propagate anti-clockwise along the coast of the Bay of Bengal. The resulting deep thermocline and variability in subsurface stratification affect the mixed layer depth in the bay (Rao and Sivakumar, 2003). A comparison of the depth of the 20°C isothermal surface (D20) from the CTRL run and ARGO data (not shown) clearly indicates the model's ability in correct simulation of the intrusion of these waves into the domain. We also show below (in Fig. 9, for example) the southward extension of high salinity water at 50—100 m depths. This clearly reveals that the model reproduces the North Arabian Sea High Salinity water (Kumar and Prasad, 1999) and/or the Persian Gulf

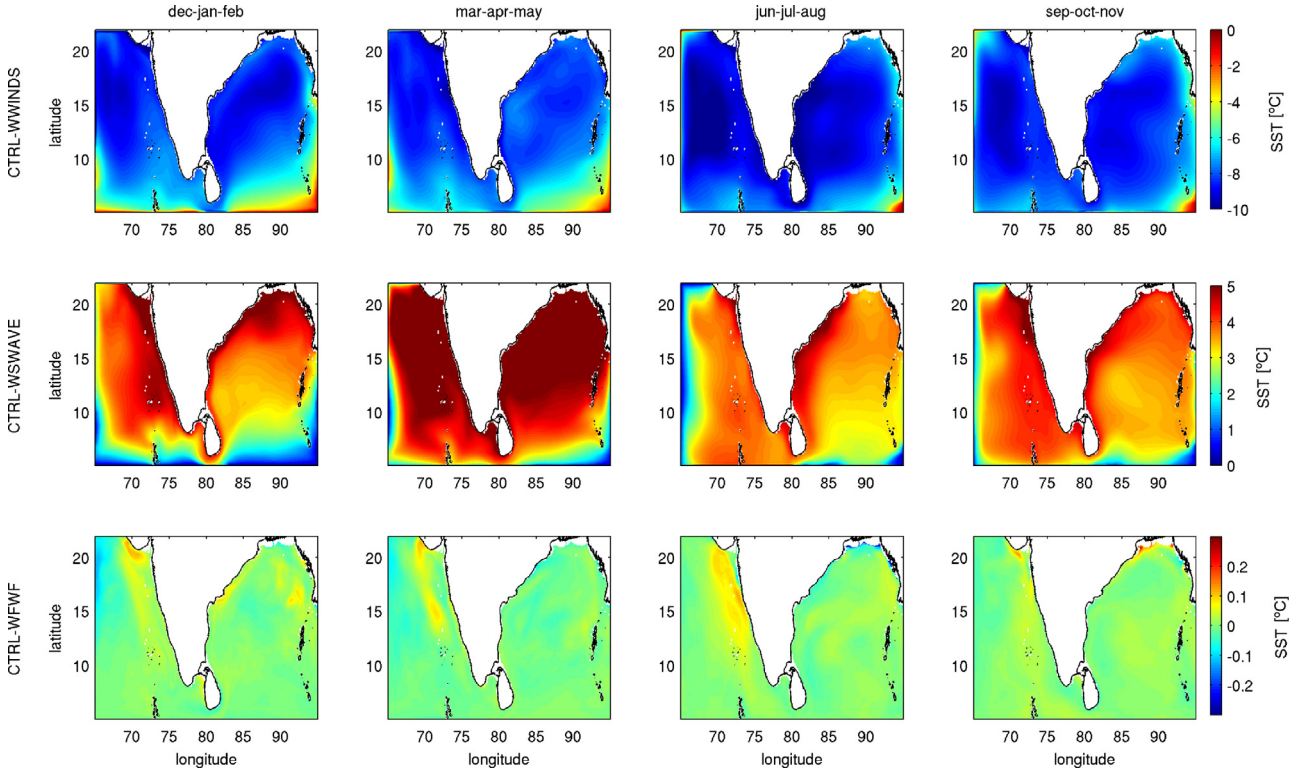

Figure 5 Seasonal SST difference map between CTRL run and sensitivity experiments. The 1st row shows SST difference between the CTRL and WWINDS experiment, 2nd row shows SST difference between CTRL and WSWAVE experiment, and 3rd row shows SST difference map between CTRL and WFWF experiment.

water (Prasad et al., 2001) although the model domain does not include the generation regions of these water masses. Thus, the boundary conditions at the domain end are very appropriate and strongly favour the use of bespoke high-resolution regional model setup for process studies.

We now discuss the seasonal variability of sea surface temperature (SST) from control run and sensitivity experiments to understand effect of winds, shortwave radiation and freshwater flux in influencing it over the AS and BoB. We show in Fig. 4 the spatial map of SST from CTRL run (1st row), WWINDS (2nd row), WSWAVE (3rd row), and WFWF (4th row) experiments. The seasons for this purpose are defined as winter (dec-jan-feb; DJF), pre-monsoon (mar-apr-may; MAM), monsoon (jun-jul-aug; JJA), and post-monsoon (sept-oct-nov; SON). It may be clearly seen from Fig. 4 (2nd row) that in the absence of near surface wind forcings, the SST increases to very high values as compared to CTRL run in all the seasons. On the other hand, in the absence of downward (incoming) shortwave radiation (Fig. 4, 3rd row), the SST decreases abruptly as compared to CTRL run. However, we also notice from Fig. 4 (4th row) that the effect of freshwater flux in influencing the SST of the region is rather very small. To further investigate the influence of near surface forcings on the SST of the region of study, we show in Fig. 5 the difference map of the sensitivity experiments with the CTRL run. We notice from the 1st row of the figure that the differences between CTRL and WWINDS experiment are significantly negative in all the seasons. However, the differences are highest in the JJA and SON seasons. We also notice from the figure that the southern BoB has smaller SST differences as compared to the southern AS. Further, the SST differences in the southern part of the domain are much smaller compared to the northern part. The large negative bias between CTRL and WWINDS experiments clearly establishes the role of near surface winds in influencing the SST of the region. The advection, mixing, and upwelling of waters become insignificant in the absence of winds and as a result surface waters of AS and BoB tend to become warmer. Almost opposite conditions though with smaller magnitudes are seen in the absence of incoming shortwave radiation (2nd row). Here the differences between the CTRL and WSWAVE experiments are positive in all the seasons meaning thereby that the absence of incoming shortwave radiation decreases the SST of the region. It is also interesting to note that maximum influence of the shortwave radiation is observed in the MAM (summer) season thus confirming the reliability of the model output. The absence of the incoming solar radiation also has a direct influence on the mixed layer depth of the region (explained later in the manuscript). In Fig. 5, 3rd row we show the SST difference map of the CTRL experiment with WFWF experiment. We notice from the figure that the SST differences, if any, are negligible as compared to the WWINDS and WSWAVE experiments. Thus, the effect of freshwater flux in changing the SST of the region is very small in all the seasons.

The sea surface salinity (SSS) of the AS and BoB is a highly seasonally varying quantity. The changes in the SSS of the region sometimes lead to cyclogenesis. Thus, it will be worthwhile to understand the factors responsible for the SSS variability over the model domain. For this purpose, we show in Fig. 6 the spatial map of the seasonally varying SSS from the CTRL run (1st row), WWINDS (2nd row), WSWAVE (3rd row), and WFWF (4th row) experiments. It may be

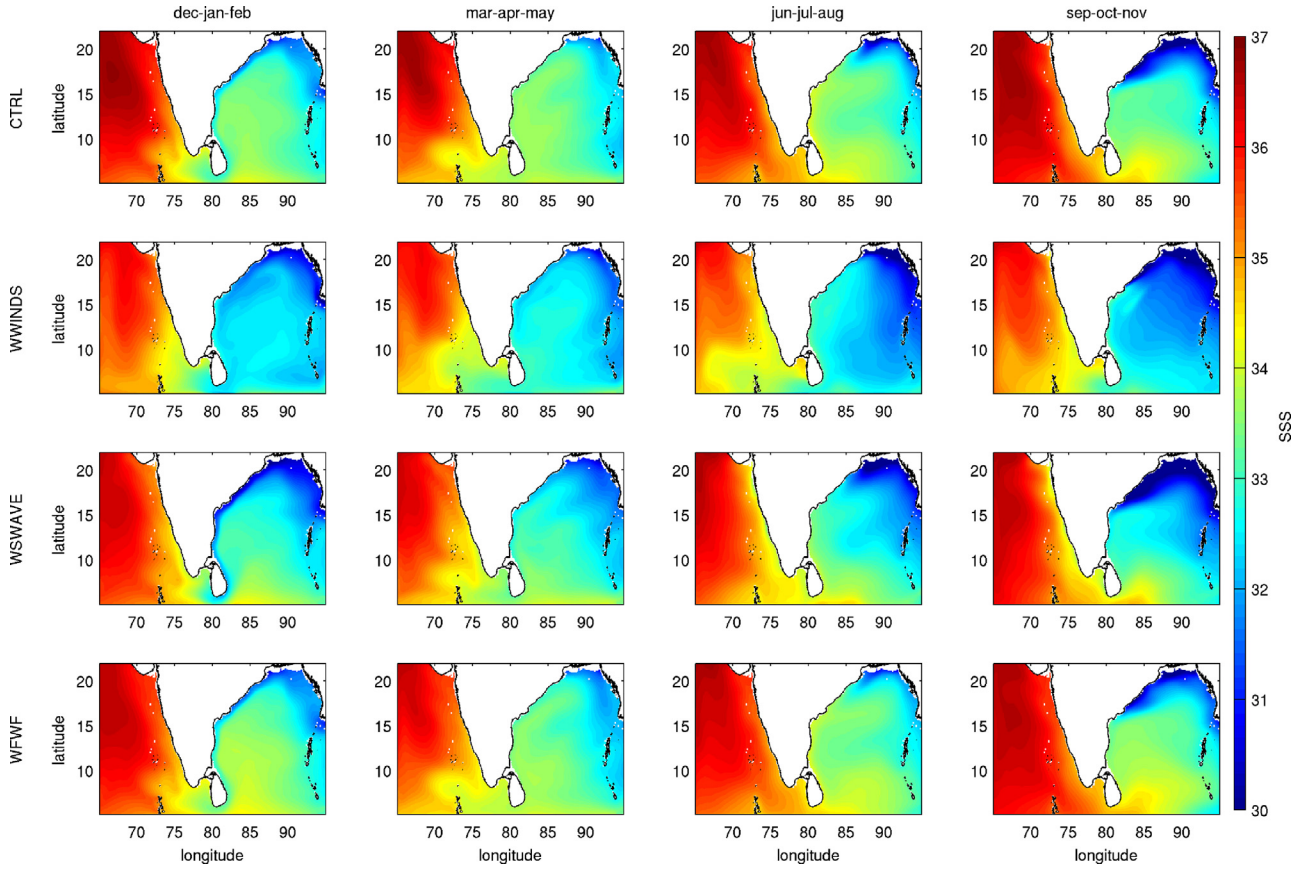

Figure 6 Seasonal variability of the SSS of the region during DJF, MAM, JJA, and SON months over the period 1998—2014. The SSS from CTRL run, WWINDS experiment, WSWAVE experiment, and WFWF experiment is shown in 1st row, 2nd row, 3rd row, and 4th row, respectively.

clearly seen from Fig. 6 (2nd row) that in the absence of near surface wind forcings, the SSS of the AS and BoB regions decreases as compared to the CTRL run in all the seasons. Similarly, in the absence of downward shortwave radiation (Fig. 6, 3rd row), the SSS of the region decreases. However, Fig. 6 (4th row) shows that the effect of freshwater flux in influencing the SSS of the region is different in different seasons. For example, at some spatial locations in the AS and BoB during DJF and MAM seasons, the SSS of the region decreases while in other regions it increases. On the other hand, the SSS of the northern BoB increases in the case of WFWF experiment.

To further diagnose and separate out the influence of near surface forcings on the SSS of the region, the difference map of different experiments with that of CTRL run is shown in Fig. 7. We find that the differences between CTRL and WWINDS experiment (Fig. 7, 1st row) are significantly positive in all the seasons except in the northwestern coast of BoB during monsoon (JJA) and post-monsoon (SON) seasons where it is negative. The highest SSS differences are found in the JJA and SON seasons and minimum in summer (MAM) season. It is also noticed that the SSS differences in the BoB are higher than AS in all the seasons. The significantly positive difference between CTRL and WWINDS experiments suggests that in the absence of near surface winds the surface salinity of the region decreases (due to decreased evaporation, for example), meaning thereby that wind forcing increases and maintains the SSS of the region through mixing and upwelling of waters. In the absence of wind forcing, the contribution of advection-diffusion processes become negligibly small and as a result the effect of river runoff and precipitation in the northwestern coast of BoB remains nearly absent during JJA and SON seasons. Thus, we observe negative SSS differences in these regions in the JJA and SON seasons. We see from Fig. 7, 2nd row that the SSS differences between CTRL and WSWAVE experiments are also either nearly zero or significantly positive in all the seasons. The magnitude of differences is smaller as compared to the WWINDS experiment. In this case also the maximum effect of shortwave radiation on the SSS of the region is observed in JJA and SON seasons in the BoB. The fact that the SSS differences between CTRL and WSWAVE experiments are positive in most of the regions suggests that the shortwave radiation forcing increases and maintains the surface salinity of the region. The SSS difference map of the CTRL experiment with WFWF experiment is shown in Fig. 7, 3rd row. We notice from the figure that there is a lot of seasonal variability in the SSS differences in this case unlike the difference maps shown in 1st (CTRL-WWINDS) and 2nd (CTRL-WSWAVE) rows. In the DJF season, the significant negative and positive differences in the SSS are observed in southern BoB and northern AS, respectively. Thus the effect of the river runoff is to decrease the SSS in the southern BoB and increase it in northern AS. The river runoff (freshwater flux) as a result of increased

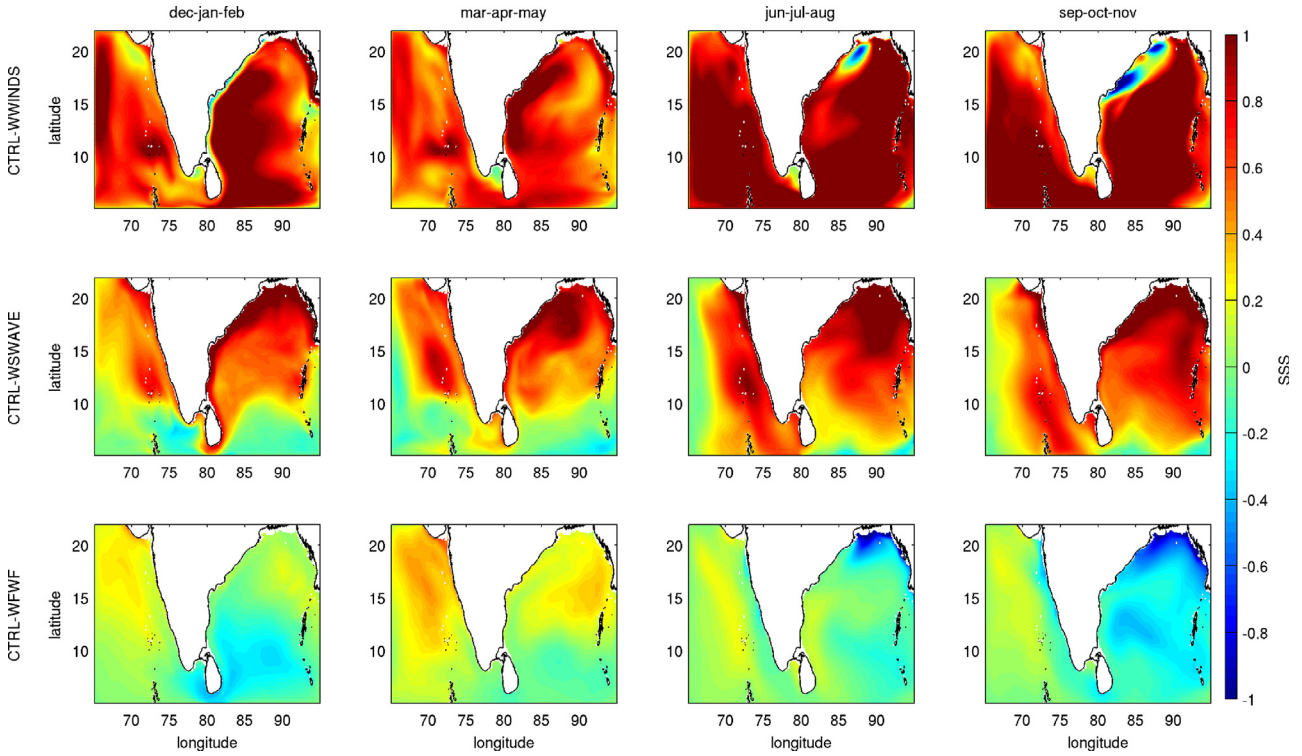

Figure 7 Seasonal SSS difference map between CTRL run and sensitivity experiments. The 1st row shows SSS difference between the CTRL and WWINDS experiment, 2nd row shows SSS difference between CTRL and WSWAVE experiment, and 3rd row shows SSS difference map between CTRL and WFWF experiment.

precipitation during monsoon (JJA) months starts to flow from north to south of the BoB during the post-monsoon (SON) months. This water mass reaches southern BoB in the winter (DJF) season and as a result the SSS of the region gets lowered. The negative SSS differences in the southern BoB during DJF clearly suggest that in the absence of the freshwater flux (WFWF experiment), the SSS lowering does not occur (SSS remains higher than normal values). On the other hand, the positive SSS differences are observed in the northern AS indicating that in the absence of freshwater flux, the SSS of the region decreases. In the summer (MAM) months, the SSS differences in central and northern AS and northeastern BoB are positive meaning thereby that in the absence of freshwater flux the SSS of these regions decreases. This effect, however, is more in the AS as compared to BoB. During monsoon (JJA) and post-monsoon (SON) seasons, the SSS differences in the AS are negligibly small. However, we notice large negative differences in the northern BoB during JJA. This is clearly due to increased river runoff as a result of monsoon rainfall in that season which is absent in the WFWF experiment. In the SON season, the large negative differences are observed in the northern and central BoB. The increased river runoff during JJA starts to flow southwards during SON with the help of east Indian coastal currents (EICC). This results in SSS lowering in the CTRL experiment. In the WFWF experiment no such SSS reduction is there and, therefore, the differences are negative. Thus the pronounced effect of the freshwater flux is realized in terms of SSS reduction in the BoB.

To put the results into perspective, it is also important to know how the sub-surface structure of temperature and salinity in the AS and BoB changes in the absence of winds, shortwave radiation and freshwater flux forcings. For this purpose, we show in Fig. 8 the latitude-depth map of temperature in the AS and BoB. Fig. 8 (upper panel) shows the latitude-depth map of temperature at 70°E in the AS. The output of sensitivity experiments is shown from left to right. We notice from Fig. 8 (upper panel) that the entire upper ocean vertical structure of the temperature gets changed in the absence of wind forcing (WWINDS) and incoming shortwave radiation forcing (WSWAVE). The strong changes in the upper ocean stratification are clearly visible in the WWINDS and WSWAVE experiments. The thermocline titling in the AS is not observed in the WWINDS experiment. Due to absence of advection, upwelling, entrainment, and mixing in the WWINDS experiment, the upper 50—100 m of the ocean becomes unrealistically warm. However, it is also observed that deeper than 150 m, the ocean becomes colder than usual. In the WSWAVE experiment, we notice that the ocean becomes unrealistically cold up to approximately top 100 m. We observe marked changes in the mixed layer depth structure and it becomes highly latitudinally dependent. The upper ocean stratification almost vanishes in this experiment. In contrast to the WWINDS and WSWAVE experiments, any distinct change in the latitude-depth map of the temperature is not seen in the WFWF experiment. Thus the upper ocean temperature stratification largely depends on the wind and shortwave radiation forcing. Fig. 8 (lower panel) shows the latitude-depth map of temperature at 90°E in the BoB. We notice that in the BoB also the upper ocean vertical structure of the temperature changes significantly in the WWINDS and WSWAVE experiments. The upper ocean stratification in the WWINDS experiment is entirely different from CTRL experiment. The upper ocean remains unusually warm

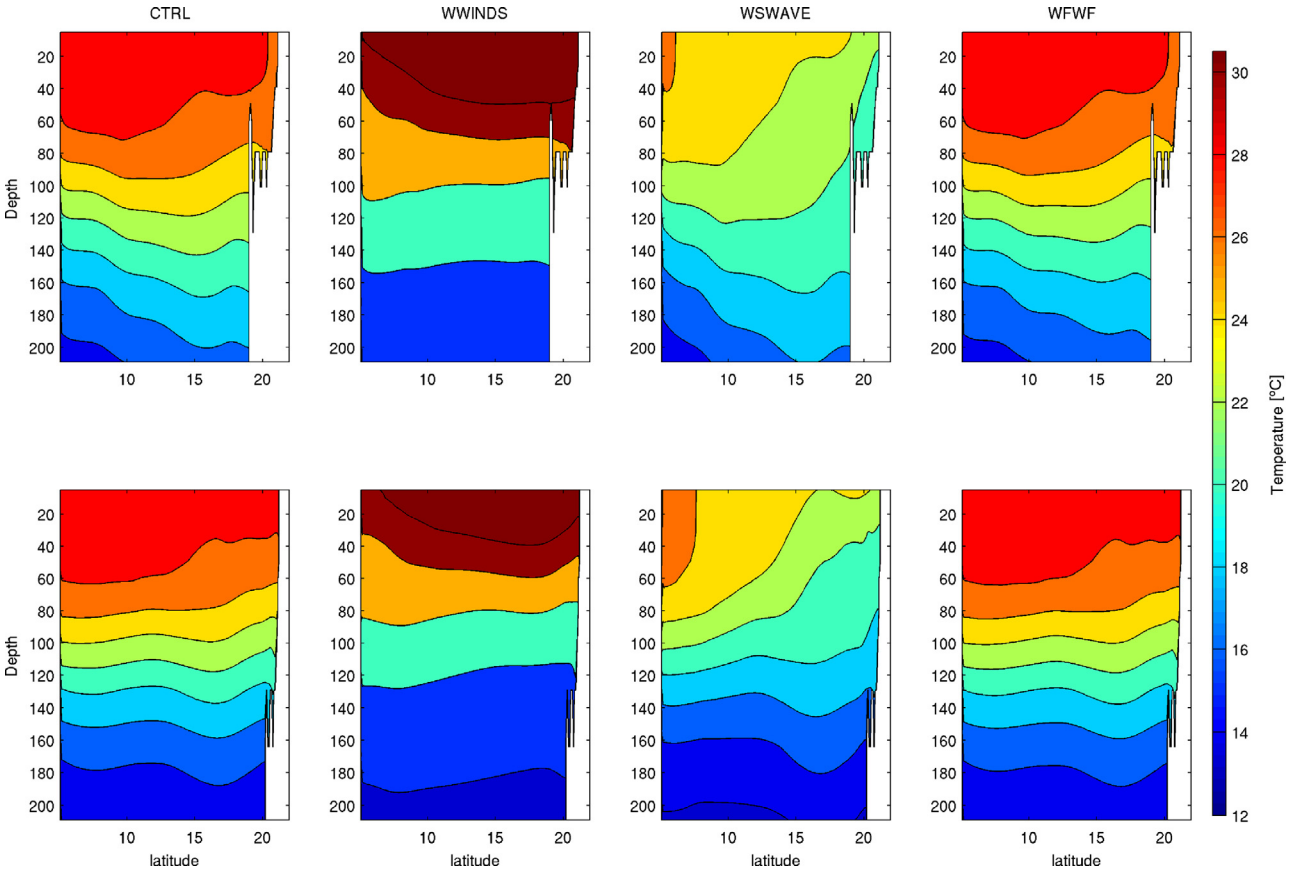

Figure 8 Latitude-depth map of (1st row) temperature at 70°E, (2nd row) temperature at 90°E from CTRL run and sensitivity experiments.

up to 100 m and unusually cold below this depth. The northern BoB (15°—20°N) upper ocean temperature remains warms up to greater depth as compared to the southern BoB (5°—8°N) in the WWINDS experiment. In the WSWAVE experiment we observe highly latitudinally dependent changes in the temperature stratification. The maximum changes are observed in the top 100 m. The upper ocean becomes unusually cold in the absence of incoming shortwave radiation. Upper latitude BoB is much colder than the lower latitudes. An increase in the mixed layer depth is seen as we move from higher to lower latitudes in the BoB. We do not observe any phenomenal change in the latitude-depth structure of the temperature in the WFWF experiment and the upper ocean stratification (temperature at different depths) remains more or less same as in the CTRL experiment.

The depth dependent structure of salinity in the AS (upper panel) and BoB (lower panel) is shown in Fig. 9. Fig. 9 (upper panel) shows the latitude-depth map of salinity at 70°E in the AS. We observe that the upper ocean salinity in the AS becomes unrealistically highly stratified in the absence of wind forcing (WWINDS). The near surface AS in the WWINDS experiment becomes very less saline as compared to CTRL experiment. At higher latitudes (20°—22°N), we also notice that deeper ocean (50—100 m) is more saline than upper ocean. On the other hand, the effect of incoming shortwave radiation forcing (WSWAVE) is recognized more in the higher latitudes (15°—22°N) as compared to lower latitudes. In the absence of incoming shortwave radiation forcing, the AS salinity at these latitudes becomes less saline on one hand and acquires almost uniform structure up to (>) 150 m depth on the other. Similarly, the effect of freshwater forcing (WFWF) is seen mostly in the higher latitudes of AS (15°—22°N) as compared to lower latitudes. In the absence of freshwater flux, the salinity at these latitudes becomes more uniform up to greater depths. Fig. 9 (lower panel) shows the latitude-depth map of salinity at 90°E in the BoB. We notice that BoB salinity is much lower as compared to AS. The depth dependent salinity structure of the BoB changes significantly in the absence of near surface wind forcing (WWINDS experiment). In the WWINDS experiment, similar to AS, the BoB salinity also becomes highly stratified and unrealistic (very low at lower depths at all latitudes, high at higher depths, and very high in southern and middle BoB between (5°—15°N)). This happens due to improper mixing as a result of absence of advection and upwelling of waters in the WWINDS experiment. In the WSAVE experiment also, the upper BoB salinity becomes low at higher latitudes (12°—22°N). In the absence of shortwave radiation forcing, low salinity values are noticed up to higher depths as compared to CTRL run. In the WFWF experiment, only small changes in the salinity of BoB are seen near the surface (due to lack of entrainment of freshwater coming from adjoining rivers) and the salinity structure at higher depths remains nearly the same as in the case of CTRL run.

The correct estimation of mixed layer depth (MLD) of the AS and BoB is very important. The MLD of the region is known to highly depend on the air-sea forcings. It is, therefore,

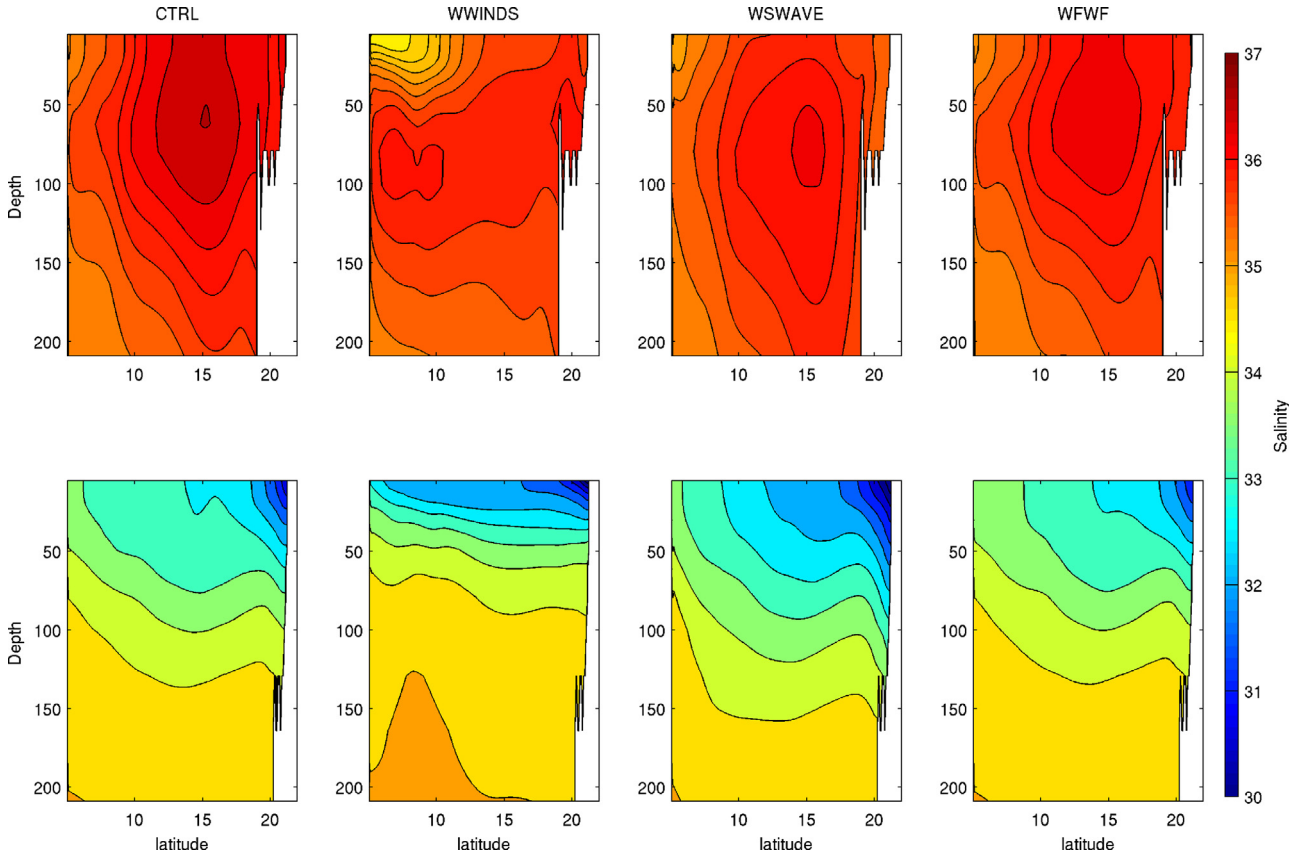

Figure 9 Latitude-depth map of (1st row) salinity at 70°E, (2nd row) salinity at 90°E from CTRL run and sensitivity experiments.

desirable to understand how near surface winds, incoming shortwave radiation and freshwater flux influence the MLD of the region. For this purpose, we show in Fig. 10 the difference map of the seasonally varying MLD of the AS and BoB from the CTRL run with that of WWINDS (1st row), WSWAVE (2nd row), and WFWF (3rd row) sensitivity experiments. The MLD of the region is computed using the criterion of Lorbacher et al. (2006). We notice from Fig. 10 (1st row) that the MLD difference (CTRL-WWINDS) becomes highly positive during winter season (DJF). Thus, in the absence of near surface wind forcing, the MLD of the region drastically decreases during DJF due to lack of momentum transfer, vertical mixing, and associated physical processes. On the other hand, during summer months of MAM, the northern (12°—22°N) AS and BoB shows increase in MLD (difference is negative), whereas, in the southern part of domain, the MLD decreases (positive MLD difference). During summer, the ocean already remains very warm (as a result of greater incoming solar radiation) and in the absence of near surface wind forcing warmer waters will percolate to higher depths causing nearly uniform temperature, salinity (and density) structure up to greater depths, thus resulting into an increase in the MLD. During summer monsoon months of JJA, the MLD of AS and BoB in the absence of wind forcing greatly decreases at nearly all locations (except along coastal BoB). This happens due to greater upper ocean stratification, increased freshwater flux, and lack of vertical mixing and advection of waters. Similarly, in the post-monsoon season of SON also, we observe decrease in the MLD (differences are positive) of the domain, except along coastal regions of AS and BoB. Although the MLD differences in the SON season are not as high as in the JJA. From Fig. 10 (2nd row) we see that the MLD difference (CTRL-SWAVE) during DJF is negative in the AS in most of the locations (except coastal regions between (10°—15°N)), whereas, it is positive in the BoB (except in the southernmost BoB). Thus, in the absence of incoming shortwave radiation, the MLD of the AS and southern BoB increases during DJF. On the other hand, the corresponding MLD of the BoB and coastal AS between 10° and 15°N decreases. During MAM, we notice higher magnitude of the negative MLD differences in the AS. The central (except along coasts) and southern BoB also exhibit high negative MLD differences during MAM. In contrast to this, the northern and coastal BoB as well as coastal AS between 10° and 15°N show positive MLD differences. In the absence of shortwave radiation during MAM, the SST decreases drastically. Moreover, the effect of wind forcing is very small due to very weak easterlies in than season. As a result uniform temperature (and density) is obtained up to greater depths thus causing an increase in MLD. During monsoon months of JJA, we notice positive MLD differences over the entire domain. The differences are much higher in the central and northern AS and BoB as compared to southern portion. It means that in the absence of incoming shortwave radiation, the MLD becomes shallower during JJA. The MLD shallowing during JJA occurs due to very low SST values in the absence of incoming solar radiation associated with strong winds leading to (Ekman) upwelling of deeper waters. During post-monsoon season of SON, we observe large negative MLD

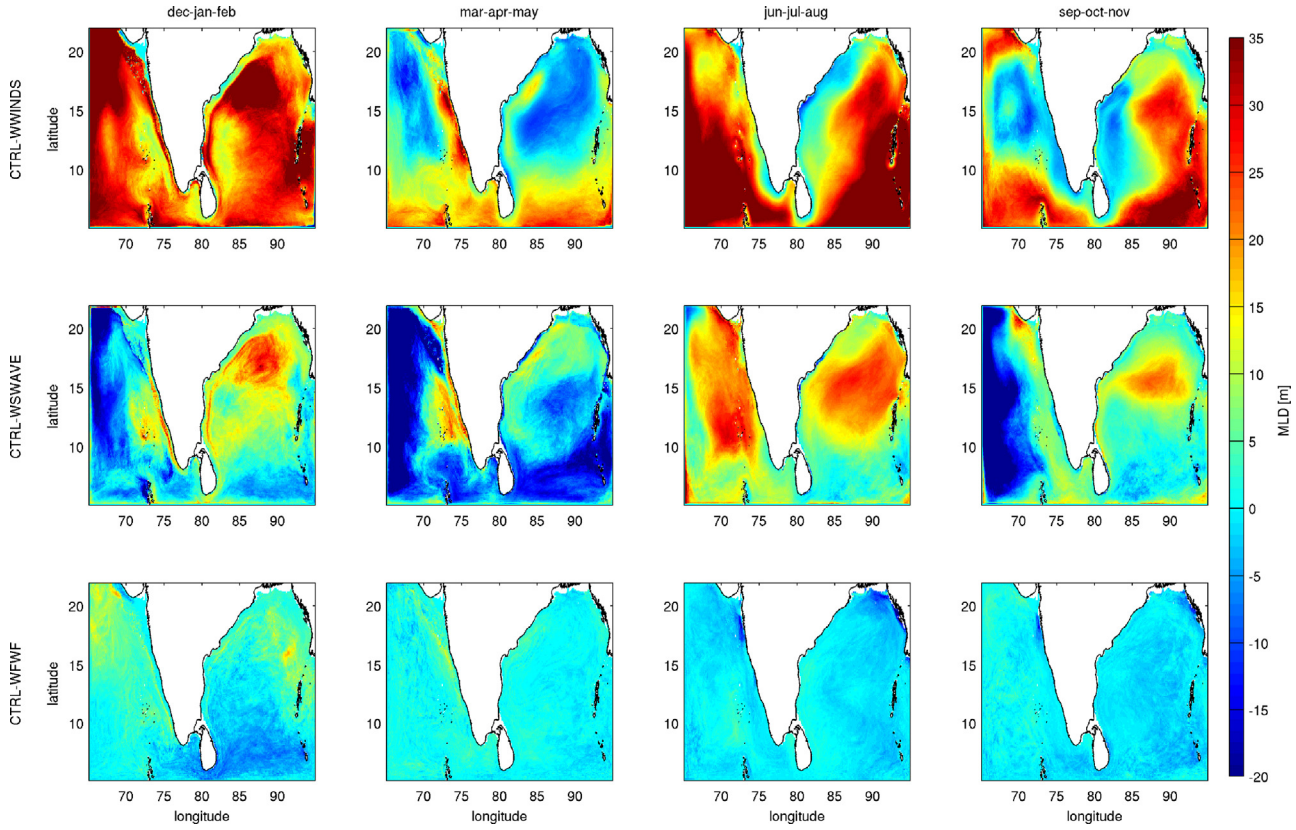

Figure 10 Maps of MLD difference between CTRL run and different sensitivity experiments. The 1st row shows MLD difference between the CTRL and WWINDS experiment, 2nd row shows MLD difference between CTRL and WSWAVE experiment, and 3rd row shows MLD difference map between CTRL and WFWF experiment.

differences along western AS and significantly positive MLD difference in the northern bay between 15° and 17°N. The positive MLD difference in the northern bay suggests that in the absence of incoming solar radiation, the MLD during SON decreases as a result of low SST and low SSS (due to increased freshwater flux). On the other hand, in the absence of incoming solar radiation the SST in the western AS decreases whereas SSS remains nearly unchanged (Fig. 6). The wind forcing and freshwater flux play insignificant role in upwelling and mixing of deeper waters in the western AS during SON and as result temperature remains uniform up to greater depths thus causing MLD deepening. From Fig. 10 (3rd row), we notice that the absence of freshwater flux forcing (WFWF) results into an increase in the MLD of the AS and BoB in all the seasons except during DJF season in which we observe MLD decrease in the northmost AS and northern BoB.

It will also be worthwhile to examine the role of air-sea fluxes in changing the vertical stability of the Arabian Sea and Bay of Bengal. The ocean vertical stability may be studied in terms of balancing effect of vertical shear of the horizontal currents and gravity (buoyancy frequency). The squared magnitude of vertical shear of the horizontal current is defined as:

$$S^2 = \left(\frac{\partial U}{\partial z}\right)^2 + \left(\frac{\partial V}{\partial z}\right)^2, \quad (1)$$

where U and V are zonal and meridional components of horizontal current, respectively.

Countering the shear is the stabilizing effect of gravity, quantified by the squared buoyancy frequency (also known as Brunt Vaisala frequency) defined as:

$$N^2 = -\left(\frac{g}{\rho}\right)\frac{\partial \rho}{\partial z}, \quad (2)$$

where ρ is density and g is gravitational acceleration (Smyth and Moum, 2013).

For $S^2 > N^2$, the instability and turbulence are likely, since shear is sufficient to do the work against gravity needed to initiate vertical motions (Smyth and Moum, 2013). On the other hand, when $N^2 > S^2$, the ocean will be vertically stable. In other words, an increase in the value of N^2 (S^2) will result into increased stability (instability) of the ocean and vice versa. We show in Fig. 11, the seasonal evolution of N^2 in the Bay of Bengal (averaged over 80°–95°E, 5°–22°N) and Arabian Sea (averaged over 65°–80°E, 5°–22°N) for different experiments. We notice that the N^2 values of CTRL and WFWF experiments are very close to each other, except for small decrease in N^2 values in the WFWF experiment during JJA (monsoon) and SON (post-monsoon) months in the BoB. However, high increase in the N^2 values (and hence vertical stability) as compared to the CTRL run is clearly evident in WWINDS experiment in the upper ocean (approx. up to thermocline depths). The increased stability in the absence of near surface wind forcing (WWINDS experiment) is due to increase in the vertical density gradients ($-\partial\rho/\partial z$) (Eq. (2)) i.e. as a result of rapid decrease in density with depth. Thus,

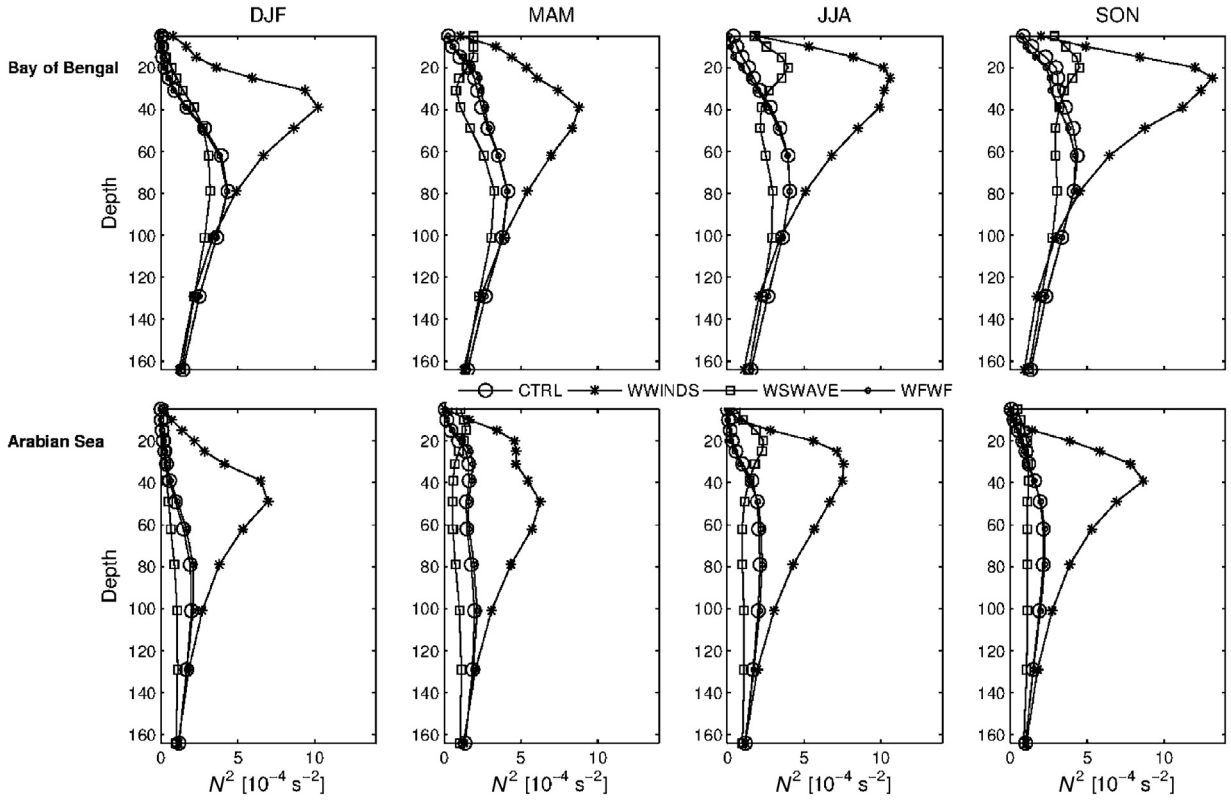

Figure 11 Squared buoyancy frequency (N^2) in the Bay of Bengal during different seasons (upper row). The results from the CTRL, WWINDS, WSWAVE, and WFWF experiments are represented by the circle, asterisk, square, and dot, respectively; (lower row) same as in the upper row but for the Arabian Sea.

the near surface winds play a dominant role in maintaining density stratification in the upper AS and BoB. The increase in the N^2 for WWINDS experiment is evident in all the seasons in the BoB as well as AS. The relatively higher increase in N^2, however, is observed in the BoB as compared to AS. The post monsoon months of SON in the BoB show highest N^2 values in the absence of near surface wind forcings since density change with depth (density gradient given in Eq. (2)) further increases as a result of increased freshwater flux in these months. In the WSWAVE experiment, we notice interesting changes in N^2 in the upper ocean. In the absence of shortwave radiation forcing, the N^2 values of WSWAVE experiment are higher than corresponding values from CTRL experiment approximately up to mixed layer depth. However, below this depth the N^2 values from WSWAVE experiment become lower than N^2 values from CTRL experiment approximately up to thermocline depth. This suggests an increase (decrease) in upper ocean vertical stability in the absence of shortwave radiation up to mixed layer depth (between mixed layer depth and thermocline depth). This feature is evident in all the seasons in the AS as well as BoB. Thus the heating of the upper ocean by the shortwave radiation tends to lower (enhance) the vertical stability of the ocean up to mixed layer depth (between mixed layer depth and thermocline depth).

Similarly, in Fig. 12 the seasonal profile of S^2 is shown for different experiments. We notice that except in the months of JJA, S^2 values are very small (~O(2) smaller) as compared to N^2. It is also seen from the figure that values in the Bay of Bengal are higher as compared to the Arabian Sea. To highlight the differences in the value of S^2 of different experiments, we also show zoomed portion of S^2 profiles for the upper 40 m in Fig. 12. The fact that the CTRL and WFWF experiments have nearly the same values for all seasons, except during SON, suggest that the effect of freshwater flux forcing on the vertical stability of the ocean is very small except during post-monsoon season. We also notice from the figure that values of S^2 decrease for WWINDS experiment, whereas they increase for WSWAVE experiment. In the absence of near surface winds, the zonal and meridional velocities will reduce drastically which will result into a sharp reduction in wind shear (Eq. (1)). On the other hand, in the absence of shortwave radiation, the upper ocean vertical velocity gradients increase due to increased velocity variability with depth. The highest values of vertical wind shear are obtained during the monsoon (JJA) season due to strongest currents in that season. Figure also shows that that the vertical wind shear in the BoB is higher as compared to AS in all the seasons, which may be due to stronger surface currents and higher vertical velocity gradients in the BoB as compared to the AS.

Another useful proxy for studying the upper-ocean stratification is the energy required for mixing (ERM). The ERM [J m^{-2}] is a metric of the potential energy of the upper water column (Shenoi et al., 2002). The ERM is computed as (Chowdary et al., 2016):

$$ERM = \frac{1}{8} * (\rho_b - \rho_s) * g * h^2, \quad (3)$$

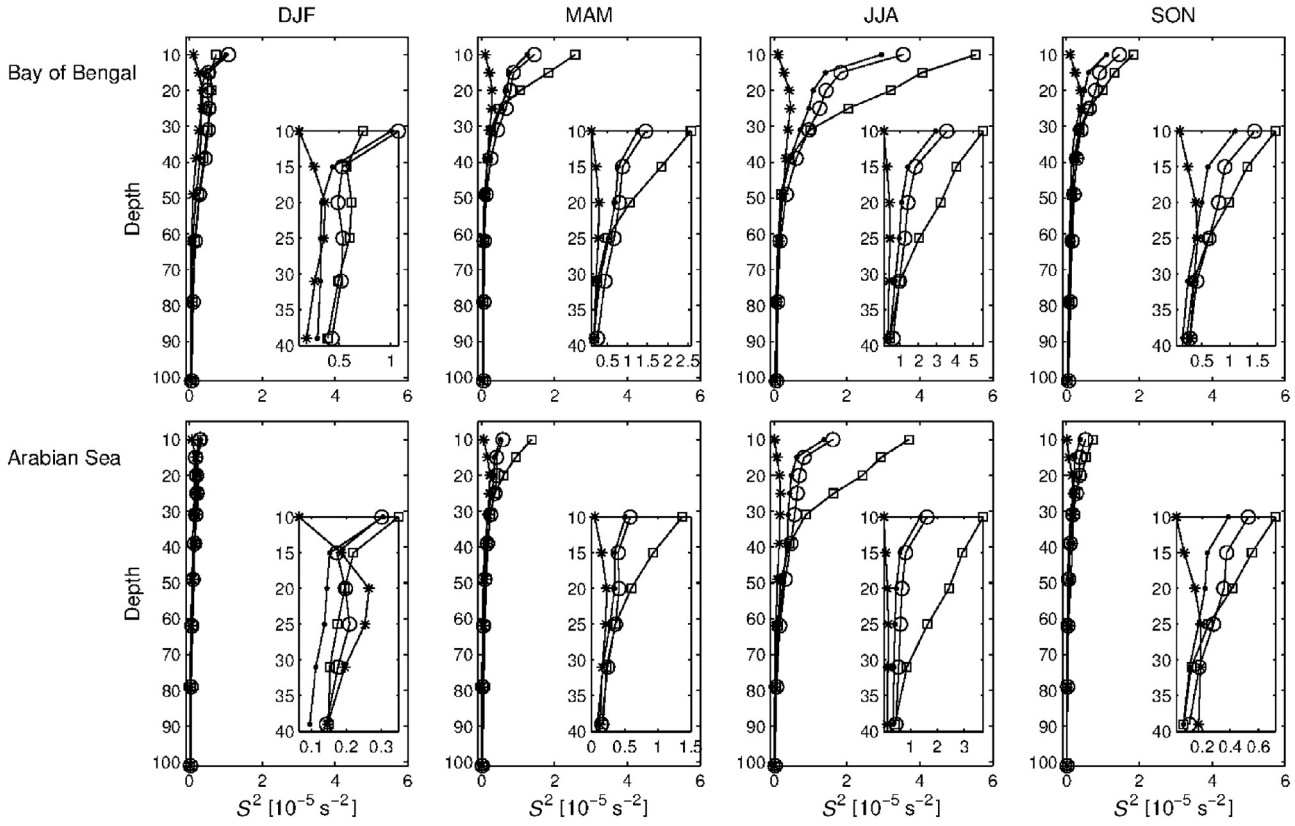

Figure 12 Squared vertical shear of the horizontal current (S^2) in the Bay of Bengal during different seasons (upper row). The results from the CTRL, WWINDS, WSWAVE, and WFWF experiments are represented by the circle, asterisk, square, and dot, respectively; (lower row) same as in the upper row but for the Arabian Sea.

where g is acceleration due to gravity, ρ_s is surface layer density of ocean and ρ_b is density at the base of mixed layer depth (h). The energy required for mixing the water column to base of the mixed layer is the difference between the potential energy of a stratified column at the base of mixed layer and that of the same column when it is unstratified (or mixed vertically). The spatial map of the seasonal variability of the ERM over the model domain is shown in Fig. 13 for CTRL run and WWINDS, WSWAVE, and WFWF experiments. Due to low salinity of the surface waters in the BoB, the mean ERM in the BoB is generally greater than that in the AS, except during summer season (MAM). The ERM in the BoB during MAM months and in the northern BoB during JJA months is less than AS since weaker winds during these seasons are incapable of mixing highly stratified surface water. The WWINDS experiment presents this scenario in a more pronounced way. In the absence of wind forcing, the ERM decreases (as compared to CTRL run) as a result of decreased MLD (Eq. (3)) and insufficient mixing of near surface stratified water. We, however, notice an increase in ERM in the AS during SON season for WWINDS experiment. This may be due to very low advection-diffusion (no winds in the WWINDS experiment) and low air-sea forcings during SON in the AS (for example, no winds, very low shortwave radiation and very low freshwater flux in the AS). Thus, the vertical entrainment appears to be the only process contributing to the increase in ERM in the AS during SON. In the WSWAVE experiment, the ERM of the BoB (except during MAM months) decreases as compared to CTRL run. This happens due to decrease in the BoB MLD in the absence of shortwave radiation. On the other hand, barring the JJA season, the ERM over most parts of the AS (except coastal AS during SON) increases in the absence of incoming shortwave radiation forcing due to increase in the MLD. The absence of freshwater flux forcing (WFWF experiment) has a very low effect on ERM, except during post-monsoon months of SON in the BoB during which ERM decreases in the head bay.

It is important to understand the influence of air-sea fluxes on the circulation of the region. In Fig. 14, we compare the surface currents of the CTRL run with the sensitivity experiments. From Fig. 14 (2nd row) it is clear that in the absence of near surface wind forcing, the AS and BoB surface currents weaken to a great extent (eddies, cyclonic, and anticyclonic features are absent) and the circulation pattern also becomes very different. For example, during JJA and SON, the direction of flow in the WWINDS experiment in the southern BoB is totally different (almost opposite) from the CTRL run. From Fig. 14 (3rd row) we see that the maximum effect of the incoming shortwave radiation is seen during summer month (MAM). Compared to CTRL run, the surface currents become very strong in the absence of shortwave radiation during MAM. The changes in the circulation pattern due to absence of incoming solar radiation are rather small during other seasons. Similarly, from Fig. 14 (4th row) it is

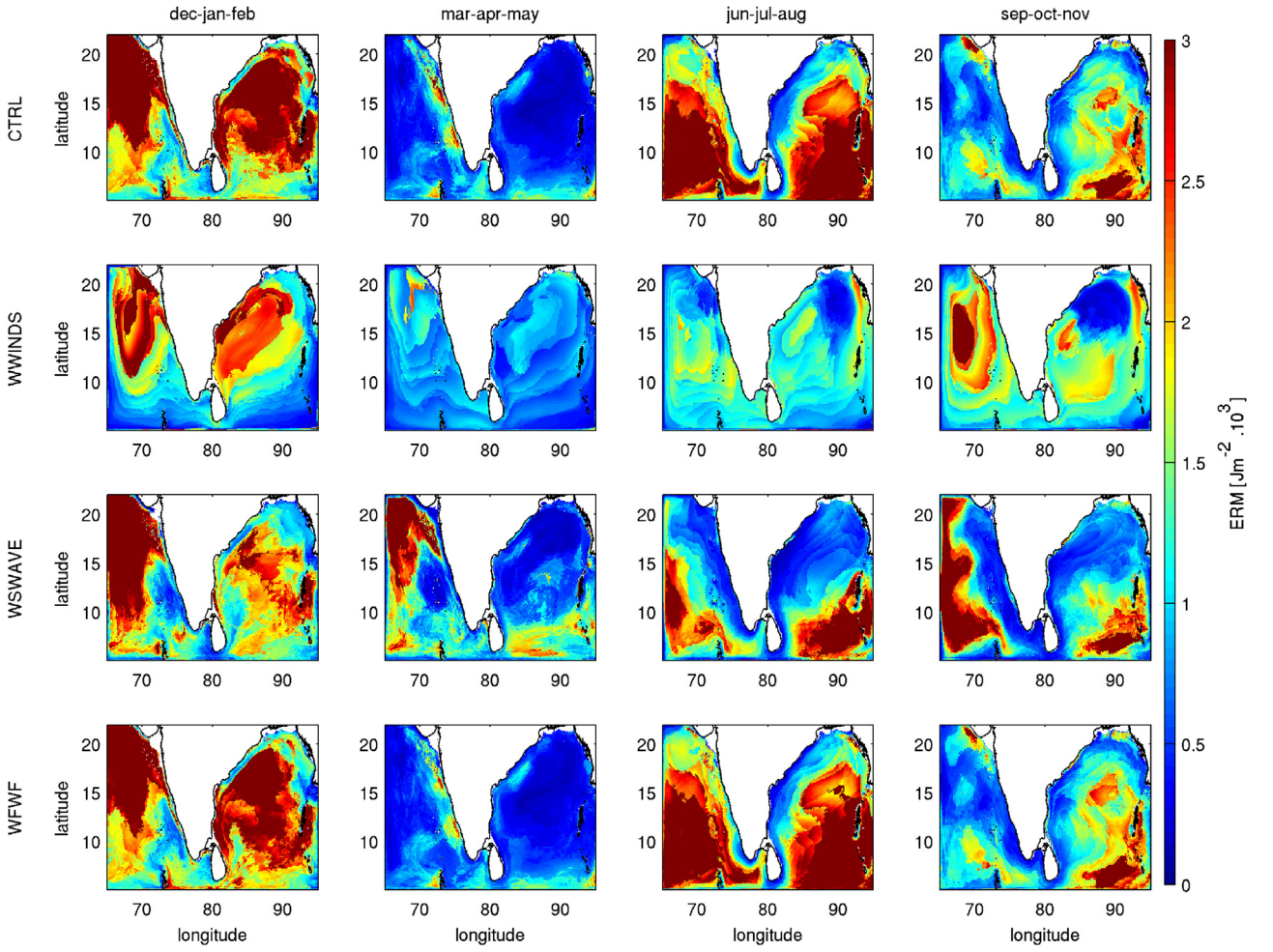

Figure 13 Energy Required for Mixing (ERM) in different seasons of the year. The ERM from CTRL run, WWINDS experiment, WSWAVE experiment, and WFWF experiment is shown in 1st row, 2nd row, 3rd row, and 4th row, respectively.

evident that the absence of freshwater flux forcing (WFWF experiment) has a little effect on the circulation of the region in all seasons of the year.

4. Conclusions

We configure and run a limited area high-resolution (∼10 km in horizontal) ocean circulation model (MITgcm) in the Indian ocean region around 65°—95°E, 5°—22°N covering the Arabian sea and Bay of Bengal for a period of 17 years during 1998—2014. Several sensitivity experiments are carried out to understand and quantify the influence of near surface zonal and meridional winds, incoming shortwave radiation, and freshwater flux air-sea forcings on the surface and sub-surface hydrography, circulation, and mixed layer depth of the Arabian Sea and Bay of Bengal. We examined the influence of air-sea forcings on the seasonal variability of the SST, SSS, MLD and surface currents. We found that in the absence of near surface wind forcing, the SST of the region greatly increases in all the seasons, whereas, in the absence of incoming shortwave radiation forcing, we get exactly opposite results. It is found that the effect of the freshwater flux forcing on the SST of the region is very small. It is also found that the SSS of the Arabian sea and Bay of Bengal decreases in the absence of near surface wind forcing and incoming shortwave radiation, whereas, in the northern Bay of Bengal it increases in the absence of freshwater flux forcing. We also analyzed sub-surface temperature and salinity variability in different sensitivity experiments. We find that the air-sea forcings greatly influence the seasonal variability of mixed layer depth of the region. We further investigated the effect of near surface winds, shortwave radiation and freshwater flux forcings on the seasonal variability of vertical stability of upper ocean by using buoyancy frequency, vertical shear of the horizontal velocity, and energy required for mixing as quantifiers. It is found that the near surface winds play a dominant role in maintaining density stratification and hence controlling the buoyancy frequency in the upper AS and BoB. The heating of upper ocean by the shortwave radiation tends to lower the buoyancy frequency of the ocean up to mixed layer depth, whereas it enhances the buoyancy frequency of the ocean between mixed layer depth and thermocline depth. We also found that in the absence of wind forcing, the vertical shear of the horizontal velocity (S^2) decreases. On the other hand, in the absence of incoming shortwave radiation, the value of S^2 increases. The spatio-temporal variability of the energy required for mixing (ERM) point towards dominant role of winds in controlling upper ocean

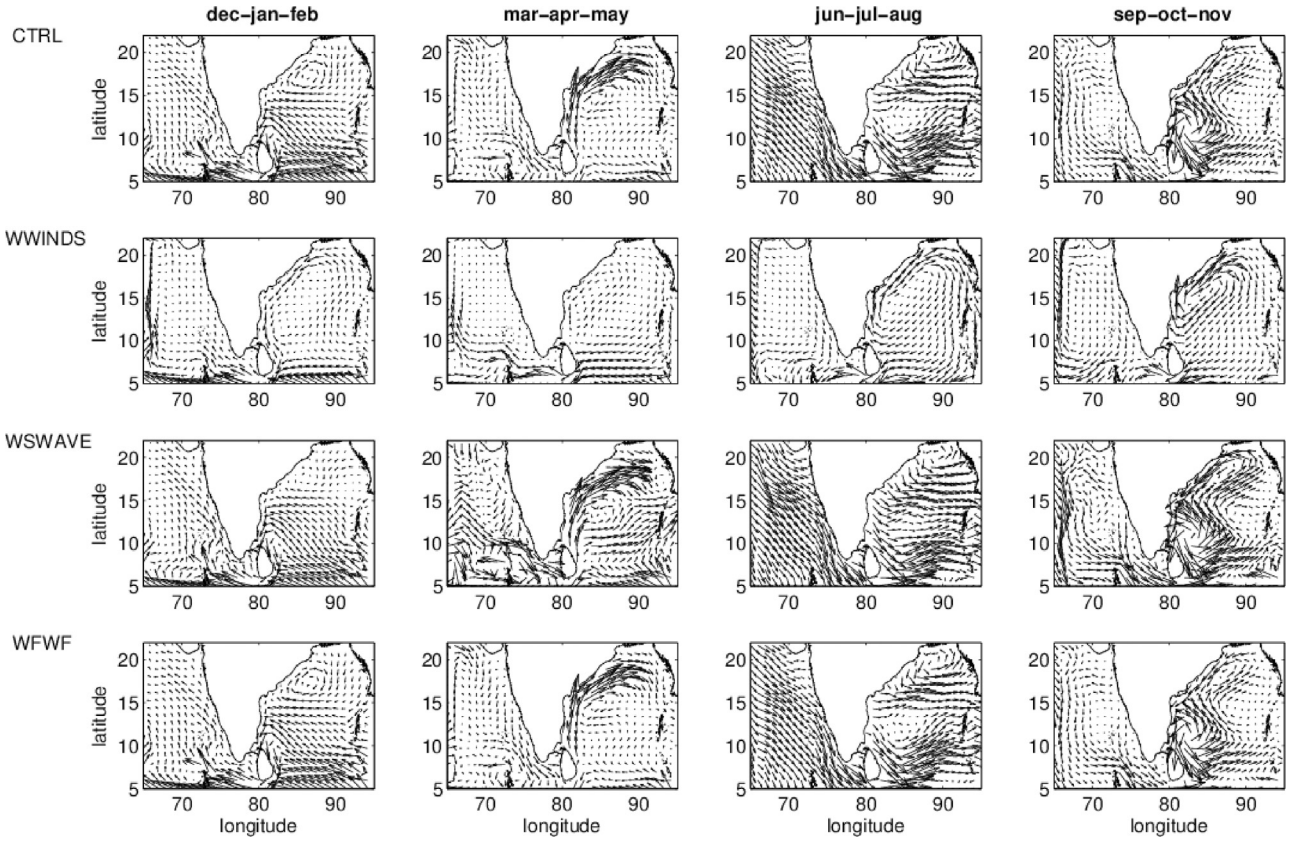

Figure 14 Seasonal variability of the surface currents of the region during DJF, MAM, JJA, and SON months over the period 1998–2014. 1st row shows surface currents from CTRL run, while the 2nd, 3rd, and 4th row shows currents from WWINDS, WSWAVE and WFWF experiments, respectively.

mixing properties. We have also been able to convincingly demonstrate that the near surface wind has highest influence in changing the circulation of the region.

It may be argued that our model domain does not include the Andaman Sea in the east, from where the coastal Kelvin waves enter the Bay and parts of the Arabian Sea in the west and also wave propagation from the equatorial region, however, it is to be emphasized that by using open boundary conditions along the boundaries in our high-resolution regional model setup we have taken into account all these circulations features. Moreover, quality of our model solutions (surface as well as sub-surface) also suggests that all important circulation patterns are clearly captured with correct magnitudes. With a modest computational facility, the trade-off is always involved in choosing between low-resolution global models vs. high-resolution (limited area) regional models for process studies. However, the experience with the current prototype model setup suggests that if appropriate boundary conditions at the domain end are available then the use of latter is strongly favoured for process studies.

Acknowledgments

Authors thank two anonymous reviewers for their useful suggestions on an earlier version of the manuscript. SD thanks ISRO, MoES, and DST for providing financial support in the form of research projects. AKM thanks MoES for providing research fellowship. Thanks are also due to NCEP/NCAR, ECCO-JPL and APDRC Data Centers for providing reanalysis and observational datasets freely available for research purpose.

Appendix A

The following bulk formulae is used to calculate the surface wind stress and surface heat flux from the prescribed air-sea forcing fields.

A.1. Wind stress

The zonal and meridional wind stress are computed using the zonal and meridional winds as:

$$\tau_u = \rho_a * C_d * W_s * u_{10}, \quad \text{(A1)}$$

$$\tau_v = \rho_a * C_d * W_s * v_{10}, \quad \text{(A2)}$$

where ρ_a (=1.2 kg m^{-3}) is the density of air at the surface, C_d is the drag coefficient, u_{10} and v_{10} are the zonal and meridional winds at 10 m, respectively, and W_s $\left(=\sqrt{u_{10}^2+v_{10}^2}\right)$ is the wind speed at 10 m. The neutral drag coefficient (C_d) at 10 m is taken as 1.2×10^{-3} for wind speeds between 4–11 m s^{-1} and as $(0.49 + 0.065\ Ws) \times 10^{-3}$ for wind speeds between 11–25 m s^{-1}.

A.2. Surface heat flux

The model computes net surface heat flux using the external (air-sea) forcings as:

$$Q_{HFLUX} = -Q_{HS} - Q_{HL} + Q_{LWF} + Q_{SWF}, \quad \text{(A3)}$$

where Q_{HS} and Q_{HL} are the sensible heat flux [W m^{-2}] and latent heat flux [W m^{-2}] into the ocean, Q_{LWF} and Q_{SWF} are the net longwave radiation flux [W m^{-2}] and net shortwave radiation flux [W m^{-2}] to the atmosphere, respectively.

The sensible heat flux (Q_{HS}) is parametrized as:

$$Q_{HS} = \rho_a * C_h * C_{pa} * W_s * \Delta t. \quad \text{(A4)}$$

Similarly, the latent heat flux (Q_{HL}) is computed as:

$$Q_{HL} = \rho_a * C_e * L_{vap} * W_s * \Delta q, \quad \text{(A5)}$$

where ρ_a (=1.2 kg m^{-3}) is the density of air at the surface, C_h is the Stanton number, C_e is the Dalton number, C_{pa} (=1005 J kg^{-1} K^{-1}) is the specific heat of air at constant pressure, L_{vap} (=2.5 $\times$ 10^6 J kg^{-1}) is latent heat of vaporization, W_s is the wind speed at 10 m, Δt is the difference of air temperature at 2 m and surface temperature, and Δq is the difference of specific humidity at 2 m and at surface. The Stanton number C_h is taken as 0.0327 $\times$ $\sqrt{C_d}$ for unstable flow and 0.0180 $\times$ $\sqrt{C_d}$ for stable flow. Similarly, the neutral Dalton number C_e is taken as = 0.0346 $\times$ $\sqrt{C_d}$.

The net longwave radiation flux Q_{LWF} is given as:

$$Q_{LWF} = \varepsilon s T^4 - Q_{DLW}, \quad \text{(A6)}$$

where ε (=0.98) is the ocean emissivity, σ is Stefan Boltzmann constant (5.670 $\times$ 10^{-8} J K^{-4} m^{-2} s^{-1}), T is surface temperature and Q_{DLW} is the downward longwave radiation.

Similarly, we also compute net shortwave radiation flux Q_{SWF} as:

$$Q_{SWF} = -Q_{DSW}(1.0-\alpha), \quad \text{(A7)}$$

where Q_{DSW} is downward short wave radiation and α is albedo (0.1).

A.3. WWINDS and WSWAVE sensitivity experiments

In the absence of winds, wind stress will be zero from Eqs. (A1) and (A2). In addition to this, the sensible heat flux and latent heat flux will also be zero (using Eqs. (A4) and (A5)) and the contribution in the net heat flux shall be only from shortwave and longwave radiation flux.

Similarly, in the absence of shortwave radiation, the surface heat flux and mechanical energy transfer between atmosphere and ocean will change (Eqs. (A3) and (A7)). It influences the stability of atmospheric boundary layer. The cooling of the atmospheric boundary layer in the absence of solar radiation will reduce the turbulent transport and hence may result into reduction in the wind speed also.

References

Agarwal, N., Sharma, R., Basu, S.K., Sarkar, A., Agarwal, V.K., 2007. Evaluation of relative performance of QuikSCAT and NCEP reanalysis winds through simulations by an OGCM. Deep-Sea Res. Pt. I Oceanogr. Res. Pap. 54 (8), 1311–1328.

Akhil, V.P., Durand, F., Lengaigne, M., Vialard, J., Keerthi, M.G., Gopalakrishna, V.V., Deltel, C., Papa, F., de Boyer Montégut, C., 2014. A modeling study of the processes of surface salinity seasonal cycle in the Bay of Bengal. J. Geophys. Res. Oceans 119 (6), 3926–3947.

Anitha, G., Ravichandran, M., Sayanna, R., 2008. Surface buoyancy flux in Bay of Bengal and Arabian Sea. Ann. Geophys. 26 (3), 395–400.

Balmaseda, M.A., Mogensen, K., Weaver, A.T., 2013. Evaluation of the ECMWF ocean reanalysis system ORAS4. Q. J. R. Meteorol. Soc. 139 (674), 1132–1161.

Callaghan, A.H., Ward, B., Vialard, J., 2014. Influence of surface forcing on near-surface and mixing layer turbulence in the Tropical Indian Ocean. Deep-Sea Res. Pt. I Oceanogr. Res. Pap. 94, 107–123.

Chatterjee, A., Shankar, D., Shenoi, S.S.C., Reddy, G.V., Michael, G. S., Ravichandran, M., Sanjeevan, V.N., 2012. A new atlas of temperature and salinity for the North Indian Ocean. J. Earth Syst. Sci. 121 (3), 559–593.

Chowdary, J.S., Parekh, A., Ojha, S., Gnanaseelan, C., Kakatkar, R., 2016. Impact of upper ocean processes and air-sea fluxes on seasonal SST biases over the tropical Indian Ocean in the NCEP Climate Forecasting System. Int. J. Climatol. 36 (1), 188–207.

Da-Allada, C.Y., Gaillard, F., Kolodziejczyk, N., 2015. Mixed-layer salinity budget in the tropical Indian Ocean: seasonal cycle based only on observations. Ocean Dyn. 65 (6), 845–857.

De Boyer Montégut, C., Mignot, J., Lazar, A., Cravatte, S., 2007. Control of salinity on the mixed layer depth in the world ocean: 1. General description. J. Geophys. Res. - Oceans 112, C06011, http://dx.doi.org/10.1029/2006JC003953.

Duncan, B., Han, W., 2009. Indian Ocean intraseasonal sea surface temperature variability during boreal summer: Madden-Julian Oscillation versus submonthly forcing and processes. J. Geophys. Res. - Oceans 114, C05002, http://dx.doi.org/10.1029/2008JC004958.

Gopalkrishna, V.V., Sadhuram, Y., Babu, V.R., 1988. Variability of mixed layer depth in the northern Indian Ocean during 1977 and 1979 summer monsoon seasons. Indian J. Mar. Sci. 17 (4), 258–264.

Gordon, A.L., Susanto, R.D., Vranes, K., 2003. Cool Indonesian throughflow as a consequence of restricted surface layer flow. Nature 425 (6960), 824–828.

Han, W., Webster, P.J., 2002. Forcing mechanisms of sea level interannual variability in the Bay of Bengal. J. Phys. Oceanogr. 32 (1), 216–239.

Han, W., McCreary, J.P., Kohler, K.E., 2001. Influence of precipitation minus evaporation and Bay of Bengal rivers on dynamics, thermodynamics, and mixed layer physics in the upper Indian Ocean. J. Geophys. Res. -Oceans 106 (C4), 6895–6916.

Howden, S.D., Murtugudde, R., 2001. Effects of river inputs into the Bay of Bengal. J. Geophys. Res. - Oceans 106 (C9), 19825–19843.

Jackett, D.R., McDougall, T.J., 1995. Minimal adjustment of hydrographic profiles to achieve static stability. J. Atmos. Oceanic Tech. 12, 381–389.

Jana, S., Gangopadhyay, A., Chakraborty, A., 2015. Impact of seasonal river input on the Bay of Bengal simulation. Cont. Shelf Res. 104, 45–62.

Jaswal, A.K., Singh, V., Bhambak, S.R., 2012. Relationship between sea surface temperature and surface air temperature over Arabian Sea, Bay of Bengal and Indian Ocean. J. Ind. Geophys. Union 16 (2), 41–53.

Kalnay, E., Kanamitsu, M., Kistler, R., Collins, W., Deaven, D., Gandin, L., Iredell, M., Saha, S., White, G., Woollen, J., Zhu, Y., Leetmaa, A., Reynolds, R., Chelliah, M., Ebisuzaki, W., Higgins, W., Janowiak, J., Mo, K.C., Ropelewski, C., Wang, J., Jenne, R., Joseph, D., 1996. The NCEP/NCAR 40-year reanalysis project. Bull. Am. Meteorol. Soc. 77, 437–470.

Kumar, S.P., Prasad, T.G., 1999. Formation and spreading of Arabian Sea high-salinity water mass. J. Geophys. Res. - Oceans 104 (C1), 1455—1464.

Large, W.G., Pond, S., 1982. Sensible and latent heat flux measurements over the ocean. J. Phys. Oceanogr. 12 (5), 464—482.

Large, W.G., McWilliams, J.C., Doney, S.C., 1994. Oceanic vertical mixing: a review and a model with a nonlocal boundary layer parameterization. Rev. Geophys. 32 (4), 363—403.

Li, Y., Han, W., Shinoda, T., Wang, C., Lien, R.C., Moum, J.N., Wang, J.W., 2013. Effects of the diurnal cycle in solar radiation on the tropical Indian Ocean mixed layer variability during wintertime Madden-Julian Oscillations. J. Geophys. Res. - Oceans 118 (10), 4945—4964.

Liu, Z., Alexander, M., 2007. Atmospheric bridge, oceanic tunnel, and global climatic teleconnections. Rev. Geophys. 45 (2), RG2005, http://dx.doi.org/10.1029/2005RG000172.

Lorbacher, K., Dommenget, D., Niiler, P.P., Köhl, A., 2006. Ocean mixed layer depth: a subsurface proxy of ocean-atmosphere variability. J. Geophys. Res. - Oceans 111 (C7), http://dx.doi.org/10.1029/2003JC002157.

Marshall, J., Adcroft, A., Hill, C., Perelman, L., Heisey, C., 1997. A finite-volume, incompressible Navier Stokes model for studies of the ocean on parallel computers. J. Geophys. Res. - Oceans 102 (C3), 5753—5766.

Perigaud, C., McCreary, J.P., Zhang, K.Q., 2003. Impact of interannual rainfall anomalies on Indian Ocean salinity and temperature variability. J. Geophys. Res. - Oceans 108 (C10), http://dx.doi.org/10.1029/2002JC001699.

Prasad, T.G., 2004. A comparison of mixed-layer dynamics between the Arabian Sea and Bay of Bengal: one-dimensional model results. J. Geophys. Res.- Oceans 109 (C3), http://dx.doi.org/10.1029/2003JC002000.

Prasad, T.G., Ikeda, M., Kumar, S.P., 2001. Seasonal spreading of the Persian Gulf Water mass in the Arabian Sea. J. Geophys. Res. -Oceans 106 (C8), 17059—17071.

Rao, R.R., Sivakumar, R., 2003. Seasonal variability of sea surface salinity and salt budget of the mixed layer of the north Indian Ocean. J. Geophys. Res.- Oceans 108 (C1), 3009, http://dx.doi.org/10.1029/2003JC002157.

Schott, F.A., McCreary, J.P., 2001. The monsoon circulation of the Indian Ocean. Prog. Oceanogr. 51 (1), 1—123.

Schott, F.A., Dengler, M., Schoenefeldt, R., 2002. The shallow overturning circulation of the Indian Ocean. Prog. Oceanogr. 53 (1), 57—103.

Sengupta, D., Bharath Raj, G.N., Shenoi, S.S.C., 2006. Surface freshwater from Bay of Bengal runoff and Indonesian throughflow in the tropical Indian Ocean. Geophys. Res. Lett. 33 (22), L22609, http://dx.doi.org/10.1029/2006GL027573.

Seo, H., Xie, S.P., Murtugudde, R., Jochum, M., Miller, A.J., 2009. Seasonal effects of Indian Ocean freshwater forcing in a regional coupled model. J. Clim. 22 (24), 6577—6596.

Sharma, R., Agarwal, N., Basu, S., Agarwal, V.K., 2007. Impact of satellite-derived forcings on numerical ocean model simulations and study of sea surface salinity variations in the Indian Ocean. J. Climate 20 (5), 871—890.

Shenoi, S.S.C., Shankar, D., Shetye, S.R., 2002. Differences in heat budgets of the near-surface Arabian Sea and Bay of Bengal: implications for the summer monsoon. J. Geophys. Res. - Oceans 107 (C6), http://dx.doi.org/10.1029/2000JC000679.

Smith, W.H.F., Sandwell, D.T., 1997. Global seafloor topography from satellite altimetry and ship depth soundings. Science 277, 1957—1962.

Smyth, W.D., Moum, J.N., 2013. Marginal instability and deep cycle turbulence in the eastern equatorial Pacific Ocean. Geophys. Res. Lett. 40 (23), 6181—6185.

Sreenivas, P., Patnaik, K.V.K.R.K., Prasad, K.V.S.R., 2008. Monthly variability of mixed layer over Arabian Sea using ARGO data. Mar. Geod. 31 (1), 17—38.

Vinayachandran, P.N., Jahfer, S., Nanjundiah, R.S., 2015. Impact of river runoff into the ocean on Indian summer monsoon. Environ. Res. Lett. 10 (5), 054008.

Wajsowicz, R., 2002. Air-sea interaction over the Indian Ocean due to variations in the Indonesian Throughflow. Clim. Dyn. 18 (5), 437—453.

Wang, Y., Liu, P., Li, T., Fu, Y., 2011. Climatologic comparison of HadISST1 and TMI sea surface temperature datasets. China Earth Sci. 54 (8), 1238—1247.

Weller, R.A., Fischer, A.S., Rudnick, D.L., Eriksen, C.C., Dickey, T.D., Marra, J., Leben, R., 2002. Moored observations of upper-ocean response to the monsoons in the Arabian Sea during 1994—1995. Deep-Sea Res. Pt. II 49 (12), 2195—2230.

Wentz, F.J., 2015. A 17-yr climate record of environmental parameters derived from the Tropical Rainfall Measuring Mission (TRMM) Microwave Imager. J. Clim. 28, 6882—6902.

Zhang, K.Q., Marotzke, J., 1999. The importance of open-boundary estimation for an Indian Ocean GCM-data synthesis. J. Mar. Res. 57, 305—334.

Zhang, Y., Du, Y., 2012. Seasonal variability of salinity budget and water exchange in the northern Indian Ocean from HYCOM assimilation. Chin. J. Oceanol. Limnol. 30 (6), 1082—1092.

Oceanologia (2018) 60, 187—192

Available online at www.sciencedirect.com

ScienceDirect

journal homepage: www.journals.elsevier.com/oceanologia/

ORIGINAL RESEARCH ARTICLE

Some probabilistic properties of deep water wave steepness

Dag Myrhaug *

Norwegian University of Science and Technology (NTNU), Trondheim, Norway

Received 2 June 2017; accepted 12 October 2017
Available online 2 November 2017

KEYWORDS
Wave steepness;
Spectral steepness parameter;
Phillips spectrum;
JONSWAP spectrum;
Joint frequency tables;
Wave statistics

Summary This paper provides some probabilistic properties of the deep water wave steepness and the spectral wave steepness by using distributions based on data from the Norwegian continental shelf. Here the average statistical properties represented by the mean value and the standard deviation of the two steepness parameters are considered. Examples of results for the wave steepness are given for a Phillips spectrum and a family of JONSWAP spectra for wind sea, and for sea states described by a joint frequency table of significant wave height and mean zero-crossing wave period for combined wind sea and swell. The results for the spectral wave steepness are obtained by using a joint distribution of significant wave height and spectral wave steepness, and the average statistical features are given for joint frequency tables of significant wave height and mean zero-crossing wave period from three locations on the Norwegian continental shelf.

1. Introduction

The wave steepness for individual waves as well as the spectral wave steepness for a sea state are parameters which are frequently used to represent the random wave characteristics at sea, relevant e.g. for a design of offshore and coastal structures. The wave steepness for individual waves is defined in terms of the wave height H and the wave period T, while the spectral wave steepness is defined in terms of the significant wave height H_s and the mean zero-crossing wave period T_z (or the spectral peak period T_p). Various aspects of wave steepness statistics, also jointly with the wave height, have been discussed by Myrhaug and Kjeldsen (1984), Myrhaug and Kvålsvold (1995). Further details of the relevance and the literature on wave steepness statistics are given in e.g. Myrhaug and Fouques (2007). The spectral wave steepness is also a random variable and has been addressed in e.g. Guedes Soares et al. (2001), Bitner-Gregersen and Guedes Soares (2007), Myrhaug and Fouques (2008). Guedes Soares

* Department of Marine Technology, Otto Nielsens vei 10, NO-7491 Trondheim, Norway. Tel.: +47 73 59 55 27; fax: +47 73 59 55 28.
E-mail address: dag.myrhaug@ntnu.no.
Peer review under the responsibility of Institute of Oceanology of the Polish Academy of Sciences.

ELSEVIER Production and hosting by Elsevier

https://doi.org/10.1016/j.oceano.2017.10.003

et al. (2001) analyzed the statistics of total ship losses in the North Atlantic and found that areas with high mean wave steepness coincided with areas with many accidents. Bitner-Gregersen and Guedes Soares (2007) used five databases from the North Atlantic to investigate the uncertainty of predicting the characteristic wave steepness from joint distributions of H_s and T_z, in addition to give a review of the literature. Myrhaug and Fouques (2008) provided a joint distribution of H_s and spectral wave steepness defined in terms of H_s and T_p based on data from the northern North Sea.

In the present paper, some average probabilistic properties of the deep water wave steepness and the spectral wave steepness are considered. The average statistical properties are given in terms of the mean value and the standard deviation. The Myrhaug and Fouques (2007) wave steepness distribution is used to estimate the statistical values of the wave steepness for individual waves within a sea state; i.e. for a given value of the spectral wave steepness for a sea state. Examples of results are given for a Phillips spectrum, for a family of JONSWAP spectra, and for sea states described by a joint frequency table of H_s and T_z. The statistical properties of the spectral wave steepness defined in terms of H_s and T_z are provided by using a joint distribution of significant wave height and spectral wave steepness, obtained by transforming the Mathisen and Bitner-Gregersen (1990) joint distribution of H_s and T_z.

The paper is organized as follows. The introduction is followed by Section 2 giving the background by presenting the Myrhaug and Fouques (2007) wave steepness distribution (Section 2.1) and the joint distribution of significant wave height and spectral wave steepness (Section 2.2). Section 3 presents examples of estimates of wave steepness (Section 3.1) and spectral wave steepness (Section 3.2). Summary and conclusions are given in Section 4.

2. Background

2.1. Myrhaug and Fouques (2007) *pdf* of wave steepness

According to Myrhaug and Fouques (2007) the probability density function (*pdf*) of the normalized deep water wave steepness $s = S S_{rms}^{-1}$ (where $S = H/((g/2\pi)T^2)$ is the wave steepness) is given by the following combined lognormal and Weibull *pdfs*

$$p(s) = \begin{cases} p_1(s) = \dfrac{1}{\sqrt{2\pi}\sigma s}\exp\left[-\dfrac{1}{2}\left(\dfrac{\ln s-\mu}{\sigma}\right)^2\right]; & s \le s_1 = 1.2 \\ p_2(s) = \theta\dfrac{s^{\theta-1}}{\zeta^\theta}\exp\left[-\left(\dfrac{s}{\zeta}\right)^\theta\right]; & s > s_1 = 1.2 \end{cases} \tag{1}$$

Here $\mu = -0.257$, $\sigma = 0.523$ are the mean value and the standard deviation, respectively, of ln*s*, and $\zeta = 0.84$, $\theta = 1.40$ are the Weibull parameters. Furthermore, $S_{rms} = 0.7\, s_m$ where $s_m = H_s/((g/2\pi)T_z^2)$ is the spectral wave steepness, $H_s = 4\sqrt{m_0}$ is the significant wave height, $T_z = 2\pi\sqrt{m_0/m_2}$ is the mean zero-crossing wave period, $m_n = \int_0^\infty \omega^n S(\omega)d\omega$; $n = 0, 1, 2, \ldots$ are the spectral moments, $S(\omega)$ is the single-sided wave spectrum, $\omega = 2\pi/T$ is the wave frequency, and $g = 9.81\ \mathrm{ms}^{-2}$ is the acceleration of gravity. Thus, the *pdf* of *s* is strictly a conditional distribution of *S* for a given sea state, i.e. for given values of H_s and T_z. Consequently, statistical values of the wave steepness can be obtained for a given sea state. The data upon which Eq. (1) is based, were taken from a larger database measured with the Waverider buoys located at Utsira, Halten and Tromsøflaket during the period 1974–1978: see Myrhaug and Fouques (2007) and the references therein for more details.

In the following the expected (mean) value, $E[S]$, and the variance, $Var[S] = E[S^2] - (E[S])^2$ of the wave steepness will be considered. Thus, this requires the calculation of $E[s^n]$ for $n = 1$ and $n = 2$, i.e.

$$E[s^n] = \int_0^\infty s^n p(s)ds = \int_0^{s_1} s^n p_1(s)ds + \int_{s_1}^\infty s^n p_2(s)ds. \tag{2}$$

Here (Bury, 1975)

$$\int_0^{s_1} s^n p_1(s)ds = e^{n\mu+\frac{1}{2}n^2\sigma^2}\Phi\left[\frac{\ln s_1-(\mu+n\sigma^2)}{\sigma}\right], \tag{3}$$

where Φ is the standard Gaussian cumulative distribution function (*cdf*)

$$\Phi(v) = \frac{1}{\sqrt{2\pi}}\int_{-\infty}^{v} e^{-t^2/2}dt. \tag{4}$$

Furthermore (Abramowitz and Stegun, 1972; Chs. 6.5 and 26.4)

$$\int_{s_1}^\infty s^n p_2(s)ds = \zeta^n\Gamma\left[1+\frac{n}{\theta}, \left(\frac{s_1}{\zeta}\right)^\theta\right], \tag{5}$$

where $\Gamma(r, t)$ is the incomplete gamma function; $\Gamma(r, 0) = \Gamma(r)$ where Γ is the gamma function, and $\Gamma(r, \infty) = 0$.

Then, by using Eqs. (1)–(5), the results are

$$E[s] = 0.873, \tag{6}$$

$$Var[s] = 0.238. \tag{7}$$

This gives the ratio between the standard deviation of the wave steepness and the mean value of the wave steepness, i.e. the coefficient of variation = $\sqrt{Var[s]}/E[s] = 0.559$. Now it follows that

$$E[S] = E[s]\cdot S_{rms} = E[s]\cdot 0.7\cdot\frac{2\pi}{g}\frac{H_s}{T_z^2} = 0.391\frac{H_s}{T_z^2} \tag{8}$$

with the standard deviation to the mean value ratio of *S* equal to 0.559.

2.2. Joint *pdf* of significant wave height and spectral wave steepness

Here the joint *pdf* of H_s and s_m is obtained from the joint *pdf* of H_s and T_z given by Mathisen and Bitner-Gregersen (1990) as summarized in Appendix B, representing wave data from the three locations Utsira, Halten and Tromsøflaket on the Norwegian continental shelf. The Utsira data are the same as those referred to in Section 3.

The joint *pdf* of H_s and s_m is obtained from Eq. (B1) by following the same procedure as in Myrhaug and Fouques (2008), i.e. by a change of variables from H_s, T_z to H_s, s_m which takes the form

$$p(H_s, s_m) = p(s_m|H_s)p(H_s), \tag{9}$$

where $p(H_s)$ is given in Eq. (B2). The change of variable only affects $p(T_z|H_s)$ since $T_z = [H_s/(g/2\pi)]^{1/2} s_m^{-1/2}$. By using the Jacobian $|dT_z/ds_m|$, this yields the lognormal *pdf* of s_m given H_s as

$$p(s_m|H_s) = \frac{1}{\sqrt{2\pi}\sigma_{s_m} s_m} \exp\left[-\frac{1}{2}\left(\frac{\ln s_m - \mu_{s_m}}{\sigma_{s_m}}\right)^2\right], \tag{10}$$

where μ_{s_m} and $\sigma^2_{s_m}$ are the mean value and the variance, respectively, of $\ln s_m$, given as

$$\mu_{s_m} = \ln\left(\frac{H_s}{g/2\pi}\right) - 2\mu, \tag{11}$$

$$\sigma^2_{s_m} = 4\sigma^2, \tag{12}$$

where $\mu = \mu_t$ and $\sigma = \sigma_t$ are given in Eqs. (B4) and (B5), respectively.

In Section 3 the results will be exemplified by considering the statistical quantities $E[H_s]$, $E[s_m|H_s]$ and the coefficient of variation $R = \sigma[s_m|H_s]/E[s_m|H_s]$, given by (Bury, 1975)

$$E[H_s] = \varepsilon_h + \rho_h \Gamma\left(1 + \frac{1}{\theta_h}\right), \tag{13}$$

$$E[s_m|H_s] = \exp\left(\mu_{s_m} + \frac{1}{2}\sigma^2_{s_m}\right), \tag{14}$$

$$R = \left(e^{\sigma^2_{s_m}} - 1\right)^{1/2}. \tag{15}$$

3. Examples of estimates of wave steepness and spectral wave steepness

3.1. Estimates of wave steepness

Estimates of the wave steepness will now be exemplified by using a Phillips spectrum, by a family of JONSWAP spectra, and by a joint frequency table of H_s and T_z.

First, the Phillips spectrum is given as (see e.g. Tucker and Pitt, 2001)

$$S(\omega) = \alpha \frac{g^2}{\omega^5}; \quad \omega \geq \omega_p, \tag{16}$$

$$S(\omega) = 0; \quad \omega < \omega_p, \tag{17}$$

where $\alpha = 0.0081$ is the Phillips constant, $\omega_p = 2\pi/T_p$ is the spectral peak frequency, and T_p is the spectral peak period. Then, according to the definition of the spectral moments m_n, $H_s/T_z^2 = m_2/(\pi^2\sqrt{m_0}) = g\sqrt{\alpha}/\pi^2 = 0.0895$, and thus from Eq. (8)

$$E[S] = 0.0350. \tag{18}$$

Then, in order to give an impression of the variation of the parameter, the mean value plus and minus (±) one standard deviation is provided; given by

Table 1 Conditional mean value plus and minus one standard deviation for given sea states at Utsira.

H_s(m)/T_z(s)	2.5	3.5	4.5	5.5	6.5	7.5	8.5	9.5	10.5
1	0.0626 ± 0.0350	0.0319 ± 0.0178	0.0193 ± 0.0108	0.0129 ± 0.0072	0.0093 ± 0.0052	0.0070 ± 0.0039	0.0054 ± 0.0030		
2	0.125 ± 0.0699	0.0638 ± 0.0357	0.0386 ± 0.0216	0.0259 ± 0.0145	0.0185 ± 0.0103	0.0139 ± 0.0078	0.0108 ± 0.0060	0.0087 ± 0.0049	
3			0.0579 ± 0.0324	0.0388 ± 0.0217	0.0278 ± 0.0155	0.0209 ± 0.0117	0.0162 ± 0.0091	0.0130 ± 0.0073	0.0106 ± 0.0059
4			0.0772 ± 0.0432	0.0517 ± 0.0289	0.0370 ± 0.0207	0.0278 ± 0.0155	0.0216 ± 0.0121	0.0173 ± 0.0097	0.0142 ± 0.0079
5				0.0646 ± 0.0361	0.0463 ± 0.0259	0.0348 ± 0.0195	0.0271 ± 0.0151	0.0217 ± 0.0121	0.0177 ± 0.0099
6					0.0555 ± 0.0310	0.0417 ± 0.0233	0.0325 ± 0.0182	0.0260 ± 0.0145	0.0213 ± 0.0119
7						0.0487 ± 0.0272	0.0379 ± 0.0212	0.0303 ± 0.0169	0.0248 ± 0.0139
8							0.0433 ± 0.0242	0.0347 ± 0.0194	0.0284 ± 0.0159
9							0.0487 ± 0.0272	0.0390 ± 0.0218	0.0319 ± 0.0178
10								0.0433 ± 0.0242	0.0355 ± 0.0198
11								0.0477 ± 0.0266	0.0390 ± 0.0218
12									0.0426 ± 0.0238

mean value±one standard deviation

$$= (0.0154, 0.0546). \quad (19)$$

Second, by using a family of JONSWAP spectra the following results are obtained by using Eq. (8) and Eqs. (A5)–(A7) in Appendix A:

$$\gamma = 1: \quad E[S] = 0.0307, \quad (20)$$

mean value±one standard deviation

$$= (0.0135, 0.0479), \quad (21)$$

$$\gamma = 3: E[S] = 0.0407, \quad (22)$$

mean value±one standard deviation

$$= (0.0180, 0.0634), \quad (23)$$

$$\gamma = 5: E[S] = 0.0464, \quad (24)$$

mean value±one standard deviation

$$= (0.0205, 0.0725). \quad (25)$$

Here γ is the spectral peakedness parameter as given in Appendix A. It should be noted that $\gamma = 1$ corresponds to the Pierson-Moskowitz spectrum. It is also noticed that the wave steepness increases as γ increases. Furthermore, it appears that $E[S]$ is larger for the Phillips spectrum than for the Pierson-Moskowitz spectrum which is due to that the Phillips spectrum contains waves with higher frequencies than the Pierson-Moskowitz spectrum, i.e. overall these sea states contain steeper waves than those described by a Pierson-Moskowitz spectrum. However, $E[S]$ for $\gamma = 3$ and $\gamma = 5$ are larger than for the Phillips spectrum, reflecting that overall these sea states contain steeper waves than those described by a Phillips spectrum. One should also note that all these mean values are lower than the wave steepness values in the range 0.05–0.13 as given in Myrhaug and Kjeldsen (1986, Fig. 3), belonging to the same database upon which the wave steepness distribution in Eq. (1) is based. However, these latter values are associated with steep and high waves in the database (see Myrhaug and Kjeldsen (1986) for more details).

Till now wind sea has been considered. However, if swell and combined wind sea and swell are considered then other spectral formulations have to be used, e.g. the Torsethaugen spectrum (Torsethaugen, 1996), or to use a joint frequency table of H_s and T_z given in Mathisen and Bitner-Gregersen (1990), which represents data obtained by a Waverider buoy covering the period 1974–1986 at the Utsira location on the Norwegian continental shelf. Thus, these data and the data upon which the wave steepness distribution are based represent partly the same area and period. Now estimates of $E[S]$ according to Eq. (8) and the mean value plus and minus one standard deviation are given in Table 1 for the sea states H_s, T_z corresponding to those for which there are data in Mathisen and Bitner-Gregersen (1990). The results in Table 1 exhibit the following expected features: $E[S]$ decreases as T_z increases for a given value of H_s, i.e. as the spectral wave steepness decreases; $E[S]$ increases as H_s increases for a given value of T_z, i.e. as the spectral wave steepness increases. It is also noted that the values of the wave steepness cover the wide range 0.0054–0.125.

3.2. Estimates of spectral wave steepness

Here estimates of the spectral wave steepness are exemplified by using the joint frequency tables of H_s and T_z from the three locations Utsira, Halten and Tromsøflaket given by Mathisen and Bitner-Gregersen (1990). First, $E[H_s]$ is calculated according to Eq. (13) and the Weibull parameters in Table B1 for each class of H_s and T_z at the three locations. Second, $E[s_m|E[H_s]]$ and the coefficient of variation are calculated according to Eqs. (14) and (15), respectively. The results are given in Table 2, showing that there are small differences between the results obtained for the three locations; the values of $E[H_s]$ are in the range 2.11–2.34 m, and the mean value of $E[s_m|E[H_s]]$ is about 0.045 with the standard deviation to mean value ratio of about 0.32. Overall, one should note that this value of $E[s_m|E[H_s]]$ is lower than the spectral wave steepness values in the range 0.048–0.082, as given in Myrhaug and Kjeldsen (1984), which are based on data representing partly the same area and period as those from Mathisen and Bitner-Gregersen (1990). However, these latter values represent sea states which are selected based on that they contain at least one steep and high wave (see Myrhaug and Kjeldsen (1984) for more details).

Table 2 Statistical results for H_s and s_m at Utsira, Halten and Tromsøflaket based on the Mathisen and Bitner-Gregersen (1990) joint *pdf* of H_s and T_z.

Location	Utsira	Halten	Tromsøflaket
$E[H_s]$(m), Eq. (13)	2.11	2.30	2.34
$E[s_m\|E[H_s]]$, Eq. (14)	0.0464	0.0450	0.0454
R, Eq. (15)	0.313	0.316	0.315
Mean value plus and minus one standard deviation	(0.0319, 0.0609)	(0.0308, 0.0592)	(0.0311, 0.0597)

4. Conclusions

Some average probabilistic features of the wave steepness and the spectral wave steepness in terms of the mean values and the standard deviations are presented. The results are exemplified by using distributions representing deep water waves based on data from the Norwegian continental shelf.

Estimates of the wave steepness are obtained by using the Myrhaug and Fouques (2007) distribution together with a Phillips spectrum and a family of JONSWAP spectra for wind sea, and for combined wind sea and swell the sea states are described by a joint frequency table of H_s and T_z. For wind sea the mean values of the wave steepness are in the range 0.031–0.046; for combined wind sea and swell the mean values are in the wider range 0.0054–0.125. For both wind sea as well as wind sea and swell the standard deviation to mean value ratio is 0.56.

Estimates of the spectral wave steepness are obtained by using a joint distribution of significant wave height and spectral wave steepness. The results are exemplified for joint frequency tables of H_s and T_z from Utsira, Halten and Tromsøflaket on the Norwegian continental shelf. There are small differences between the results for the three locations; the mean value of the spectral wave steepness for given values of the mean significant wave height in the range 2.11–2.34 m is about 0.045, with the standard deviation to mean value ratio of about 0.32.

Appendix A. A family of JONSWAP spectra for wind sea

Here a brief summary of a family of JONSWAP spectra for wind sea as given in Myrhaug and Kjeldsen (1987) is provided. It should be noted that the spectrum in Myrhaug and Kjeldsen (1987) is given in terms of the frequency $f = \omega/2\pi$ in $Hz = s^{-1}$, and thus $S(\omega) = S(f)/2\pi$, giving the JONSWAP spectrum

$$S(\omega) = \alpha \frac{g^2}{\omega^5} \exp\left[-\frac{5}{4}\left(\frac{\omega_p}{\omega}\right)^4\right] \gamma^{\exp\left[-\frac{1}{2}\left(\frac{\omega-\omega_p}{\sigma_b\omega_p}\right)^2\right]}, \tag{A1}$$

where $\sigma_b = 0.08$ is the width of the spectral peak, α is an equilibrium range parameter determining the high frequency part of the spectrum, and γ is the spectral peakedness parameter. By considering wind sea this spectral formulation is valid in a subspace of the whole H_s, T_p (or H_s, T_z) space, i.e.

$$3.6\sqrt{H_s} \le T_p \le 5\sqrt{H_s}, \tag{A2}$$

where H_s and T_p are in meters and seconds, respectively; α is taken as

$$\alpha = 0.036 - 0.0056\frac{T_p}{\sqrt{H_s}} \tag{A3}$$

and γ is given by

$$\gamma = \exp\left[3.484\left(1 - 0.1975\alpha\frac{T_p^4}{H_s^2}\right)\right]. \tag{A4}$$

Then, for given values of H_s and T_p according to Eq. (A2), the corresponding values of α and γ can be determined and accordingly the wave spectrum in Eq. (A1). Furthermore, for a JONSWAP spectrum the ratio T_p/T_z depends on γ (see Fig. 11 in Myrhaug and Kjeldsen (1987)). In this article $\gamma = 1$, 3, 5 are considered, where $\gamma = 1$ corresponds to the Pierson-Moskowitz spectrum. Then, for:

$$\gamma = 1;\ \alpha = 0.0081,\ T_p = 5\sqrt{H_s},\ T_p = 1.40T_z \tag{A5}$$

$$\gamma = 3;\ \alpha = 0.0136,\ T_p = 4\sqrt{H_s},\ T_p = 1.29T_z \tag{A6}$$

$$\gamma = 5,\ \alpha = 0.016,\ T_p = 3.6\sqrt{H_s},\ T_p = 1.24T_z \tag{A7}$$

More details about this JONSWAP formulation are given in Myrhaug and Kjeldsen (1987).

Appendix B. Mathisen and Bitner-Gregersen (1990) joint *pdf* of H_s and T_z

The joint *pdf* of H_s and T_z used by Mathisen and Bitner-Gregersen (1990) is given as

$$p(H_s, T_z) = p(T_z|H_s)p(H_s), \tag{B1}$$

where $p(H_s)$ is the marginal *pdf* of H_s given by the following three-parameter Weibull *pdf*

$$p(H_s) = \frac{\theta_h}{\zeta_h}\left(\frac{H_s-\varepsilon_h}{\zeta_h}\right)^{\theta_h-1} \exp\left[-\left(\frac{H_s-\varepsilon_h}{\zeta_h}\right)^{\theta_h}\right];\quad H_s \ge \varepsilon_h, \tag{B2}$$

where θ_h, ζ_h, ε_h are the Weibull parameters. $p(T_z|H_s)$ is the conditional *pdf* of T_z given H_s, given by the following lognormal *pdf*

$$p(T_z|H_s) = \frac{1}{\sqrt{2\pi}\sigma_t T_z}\left[-\frac{1}{2}\left(\frac{\ln T_z - \mu_t}{\sigma_t}\right)^2\right], \tag{B3}$$

where μ_t and σ_t are the mean value and the standard deviation, respectively, of $\ln T_z$, given by

$$\mu_t = a_1 + a_2 H_s^{a_3}, \tag{B4}$$

$$\sigma_t = b_1 + b_2 e^{b_3 H_s}. \tag{B5}$$

Here the same values of the parameters as used by Mathisen and Bitner-Gregersen (1990) are adopted; see Table B1. These data represent wave conditions at three deep water locations on the Norwegian continental shelf. The data were obtained by Waverider buoys located at Utsira (1974–1986), Halten (1974–1984), Tromsøflaket (1977–1983) covering the years given in the parenthesis; see Mathisen and Bitner-Gregersen (1990) for more details. As mentioned in Section 3, these data and the data upon which the wave steepness distribution is based, are from the same locations and represent partly the same periods.

Table B1 Parameters in the Mathisen and Bitner-Gregersen (1990) joint *pdf* of H_s and T_z.

Location	Utsira	Halten	Tromsøflaket
Weibull parameters for H_s, Eq. (B2)			
ρ_h (*m*)	1.50	1.91	1.41
θ_h	1.15	1.27	1.12
ε_h (*m*)	0.679	0.532	0.987
Parameters for mean of $\ln T_z$, Eq. (B4)			
a_1	0.933	1.09	1.24
a_2	0.578	0.479	0.337
a_3	0.395	0.417	0.538
Parameters for standard deviation of $\ln T_z$, Eq. (B5)			
b_1	0.0550	0.0407	0.0728
b_2	0.336	0.221	0.383
b_3	−0.585	−0.289	−0.665

References

Abramowitz, M., Stegun, I.A., 1972. Handbook of Mathematical Functions, 10th ed. Dover Publ., Inc., New York, 1046 pp.

Bitner-Gregersen, E., Guedes Soares, C., 2007. Uncertainty of average wave steepness prediction from global wave databases. In: Proc. of MARSTRUCT, Glasgow, 3–10.

Bury, K.V., 1975. Statistical Models in Applied Science. John Wiley & Sons, New York, 646 pp.

Guedes Soares, C., Bitner-Gregersen, E., Antano, P., 2001. Analysis of the frequency of ship accidents under severe North Atlantic weather conditions. In: Proc. Conf. on Design and Operation for Abnormal Conditions II. RINA, London, 221–230.

Mathisen, J., Bitner-Gregersen, E., 1990. Joint distributions for significant wave height and wave zero-up-crossing period. Appl. Ocean Res. 12 (2), 93–103.

Myrhaug, D., Fouques, S., 2007. Discussion of "Distributions of wave steepness and surf parameter" by M. Aziz Tayfun. J. Waterway, Port, Coast. Ocean Eng. 133 (3), 242–243, http://dx.doi.org/10.1061/(ASCE)0733-950X(2007)133:3(242).

Myrhaug, D., Fouques, S., 2008. Bivariate distributions of significant wave height with characteristic wave steepness and characteristic surf parameter. In: Proc. 27th Int. Conf. on Offshore Mechanics and Arctic Eng., Paper No. OMAE2008-57728, Estoril, Portugal.

Myrhaug, D., Kjeldsen, S.P., 1984. Parametric modelling of joint probability density distributions for steepness and asymmetry in deep water. Appl. Ocean Res. 6 (4), 207–220.

Myrhaug, D., Kjeldsen, S.P., 1986. Steepness and asymmetry of extreme waves and the highest waves in deep water. Ocean Eng. 13 (6), 549–568.

Myrhaug, D., Kjeldsen, S.P., 1987. Prediction of occurrences of steep and high waves in deep water. J. Waterway, Port, Coast. Ocean Eng. 113 (2), 122–138, http://dx.doi.org/10.1061/(ASCE)0733-950X(1987)113:2(122).

Myrhaug, D., Kvålsvold, J., 1995. Comparative study of joint distributions of primary wave characteristics. J. Offshore Mech. Arctic Eng. 117 (2), 91–98, http://dx.doi.org/10.1115/1.2827069.

Torsethaugen, K., 1996. Model for doubly peaked wave spectra. Technical Report No. STF22 A96204, SINTEF Civ. & Env. Eng., Trondheim, Norway.

Tucker, M.J., Pitt, E.G. (Eds.), 2001. Waves in Ocean Engineering. 1st ed. Elsevier, Amsterdam, 548 pp.

Oceanologia (2018) 60, 193—206

Available online at www.sciencedirect.com

ScienceDirect

journal homepage: www.journals.elsevier.com/oceanologia/

ORIGINAL RESEARCH ARTICLE

Distribution of metals and extent of contamination in sediments from the south-eastern Baltic Sea (Lithuanian zone)

Nijolė Remeikaitė-Nikienė [a,b,*], Galina Garnaga-Budrė [a,d], Galina Lujanienė [b], Kęstutis Jokšas [c,e], Algirdas Stankevičius [a,d], Vitalijus Malejevas [a,b], Rūta Barisevičiūtė [b]

[a] *Environmental Protection Agency, Department of Marine Research, Klaipėda, Lithuania*
[b] *State Research Institute Center for Physical Sciences and Technology, Vilnius, Lithuania*
[c] *Nature Research Center, Institute of Geology and Geography, Vilnius, Lithuania*
[d] *Klaipėda University, Klaipėda, Lithuania*
[e] *Vilnius University, Vilnius, Lithuania*

Received 24 December 2016; accepted 15 November 2017
Available online 2 December 2017

KEYWORDS
Metals;
Enrichment factor;
Geoaccumulation index;
Contamination factor;
The Baltic Sea;
The Curonian Lagoon

Summary The distribution of metals (Pb, Cu, Cd, Ni, Cr, Zn) in surface sediments and the potential pollution sources in the south-eastern part (SE) of the Baltic Sea (Lithuanian zone) were investigated in relation to the environmental characteristics (amount of fine-grained particles, TOC content in sediments, origin of sedimentary organic matter, salinity, water depth) in 2011—2014. The higher metal concentrations were measured in sediments of the Curonian Lagoon and in the open waters. An approach using various environmental indices (enrichment factor EF, geoaccumulation index I_{geo} and contamination factor CF) was used to quantitatively assess a contamination degree. The principal component analysis (PCA) was applied in order to further scrutinize pollution from metal sources. The values of the contamination indices showed no/very low sediment contamination with Ni and Cr, minor—moderate contamination with Cu, Zn and Pb and moderate—considerable pollution with Cd. The strong relationships among metals suggested their similar distribution pattern and a combination of natural and anthropogenic sources. The higher metal concentrations coincided with an increasing amount of fine-grained fraction and organic carbon. In the territorial waters, the distribution of elements was related to the water

* Corresponding author. Environmental Protection Agency, Department of Marine Research, Taikos av. 26, LT-91222, Klaipėda, Lithuania. Tel.: +370 46 41 0450; fax. +370 46 41 0460.
E-mail addresses: n.remeikaite@gmail.com, n.remeikaite@aaa.am.lt (N. Remeikaitė-Nikienė).
Peer review under the responsibility of Institute of Oceanology of the Polish Academy of Sciences.

Production and hosting by Elsevier

https://doi.org/10.1016/j.oceano.2017.11.001

depth. In addition, the binding of metals with insoluble iron sulphides might explain their high concentrations at the most remote and deepest stations.

1. Introduction

The intense development of anthropogenic activities since the late 19th century has resulted in enhanced loads of pollutants (e.g., nutrients, metals) from a large densely populated catchment area to the Baltic Sea (HELCOM, 2010). For example, a nearly threefold increase in Cu and Zn accumulation rates was observed in the Gulf of Finland from the period of 1850—1900 to 1975—1998 (Vaalgamaa and Conley, 2008). Metals enter the Baltic Sea either adsorbed onto suspended particles or in dissolved forms mostly through the rivers discharge (Leivuori et al., 2000; Yurkovskis and Poikāne, 2008). The significant input of cadmium, lead and mercury via atmospheric deposition was also reported by HELCOM (2010). For instance, 47.5 tonnes of cadmium and 274.2 tonnes of lead entered the Baltic Sea as waterborne pollutants, while the atmospheric deposition accounted for 7.1 tonnes of cadmium and 234 tonnes of lead (HELCOM, 2010). In water systems metals tend to accumulate in sediments in association with organic matter, fine-grained sediments, sulphides and iron-manganese hydroxides and they may be released with changing conditions in sediments, such as changes in pH, dissolved oxygen or temperature (Dang et al., 2015; Leivuori et al., 2000). Several elements, such as Zn and Cu, are known to be essential elements for life, while others, such as Pb and Cd, do not play any physiological role and are highly toxic to all organisms even at low concentration (Jakimska et al., 2011). Therefore, among the metals, particular attention is paid to mercury, cadmium, lead and nickel which are identified as priority and priority hazardous substances by European Commision (Directive 2013/39/EU). To maintain marine ecosystems, management plans considering the human-induced contamination have to be established, where pollutant distribution and transport pattern, sources of contamination and behaviour in ecosystems need to be identified. Since metals originating from natural (e.g., erosion) and anthropogenic sources accumulate together in sediments, it is important (while not an easy task) to determine the ratio between the natural and artificial constituents of sediments (García et al., 2008; Ho et al., 2012).

A common approach to estimate an anthropogenic impact on sediments is to calculate the contamination factors for metal concentrations above uncontaminated background levels. For this purpose, many different enrichment calculation methods (e.g., enrichment factor, geoaccumulation index and contamination factor) have been used in various studies (e.g., Bonnail et al., 2016; Costa et al., 2015; Zalewska et al., 2015). In spite of many geochemical studies (e.g., Emelyanov et al., 2001, 2014, 2015; Mažeika et al., 2004; Pustelnikovas et al., 2007) in the SE Baltic Sea area, the results which concern the extent of the sediment pollution with heavy metals are lacking. The reported bulk metal concentrations may show the natural geochemical peculiarities in the region, however, they do not reflect the ratio between the natural and human-induced pollution of sediments. Moreover, due to the different methodologies (in particular, leaching methods) used by the scientists, it is difficult to compare and estimate the degree of the sediment pollution with heavy metals.

The main tasks of the present study were: (i) to evaluate the distribution of metals in bottom sediments of the SE Baltic Sea (Lithuanian zone) and to define the most polluted sites; (ii) to clarify the influence of the environmental factors (mineral and organic constituents of sediments, origin of organic matter, water depth and salinity) on the accumulation of metals; (iii) to identify the possible sources of contamination and the main driving factors in the Curonian Lagoon, Klaipeda Strait, coastal waters and offshore area. In order to assess a degree of contamination of the SE Baltic Sea, the enrichment factor (EF), the geoaccumulation index (I_{geo}) and the contamination factor (CF) were calculated. Results might be used in preparing the management plans and strategies for the initial assessment of the human-induced contamination in the SE Baltic Sea.

2. Methods

2.1. Study area

The area of this study includes the Lithuanian part of the Curonian Lagoon and the Baltic Sea (the SE Baltic Sea) (Fig. 1).

The Curonian Lagoon is a shallow semi-enclosed transitory brackish-to-fresh water body separated from the SE Baltic Sea by a narrow Curonian Spit (Fig. 1). The southern and central parts of the lagoon are freshwater (<0.5‰), while the northern part is oligohaline with irregular salinity (from 0 to 8‰) fluctuations (Remeikaitė-Nikienė et al., 2012). The mean depth of the lagoon is 3.8 m. The lithological composition of the bottom sediments in the Curonian Lagoon is heterogeneous of the main 4 types — medium sand, fine sand, coarse silt and fine silty mud (Trimonis et al., 2003).

The lagoon is connected to the Baltic Sea through the narrow Klaipėda Strait where the Klaipėda town and the Klaipėda Port are located. This is the area where the intensive transfer and settling of sedimentary matter, provided by the Nemunas River and saline water, take place. The Nemunas River mostly supplies silty (0.01—0.1 mm) and clayey (<0.01 mm) particles into the lagoon, while saline water intrusions bring sandy (0.1—0.25 mm) marine sediments. High concentrations of metals are measured in harbour and they may be the source of internal pollution due to sediment dredging which reactivates the contaminants in the sediments (Pustelnikovas et al., 2007).

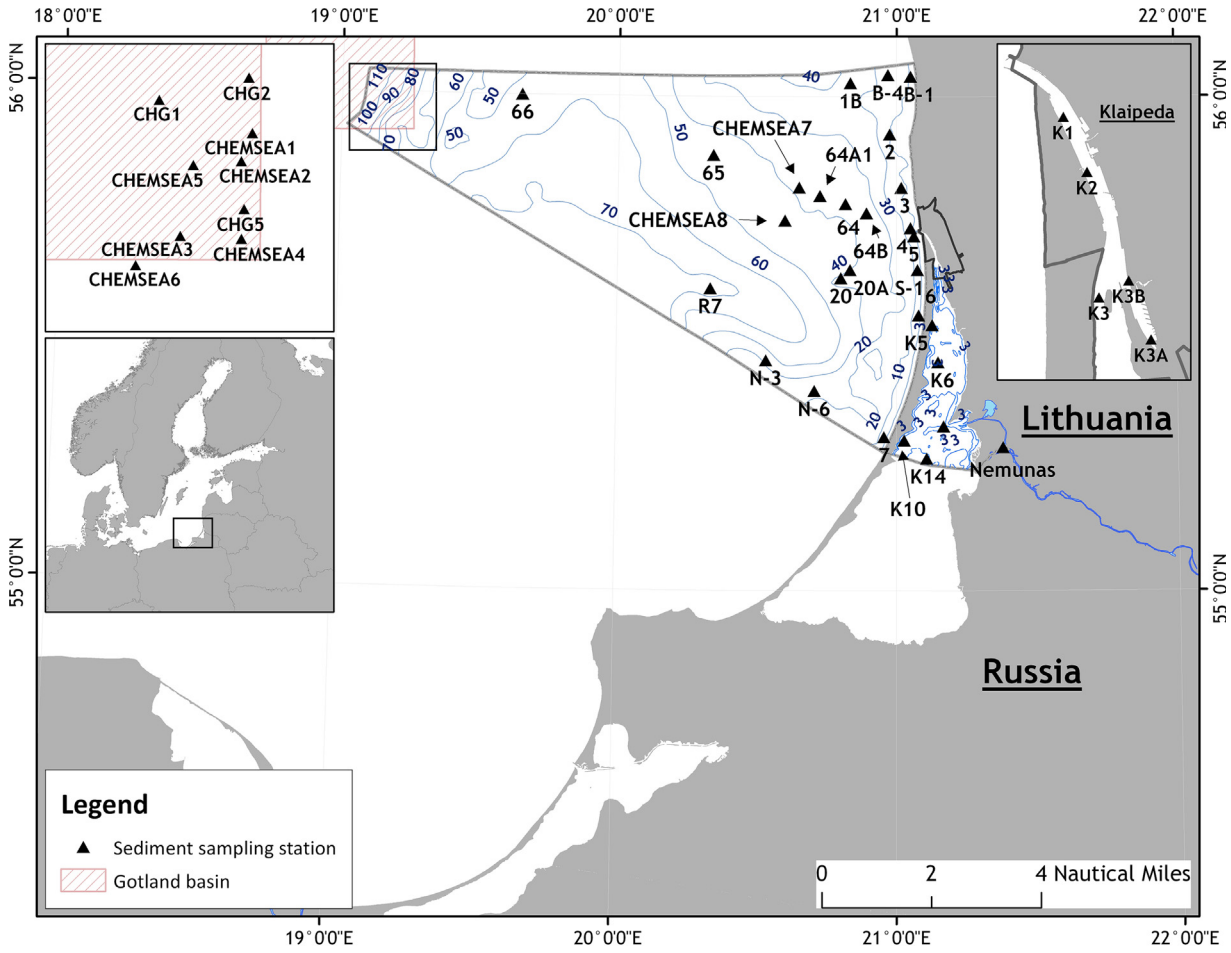

Figure 1 The map of the study area in the Lithuanian part of the Curonian Lagoon and the Baltic Sea.

The active hydrodynamics in the Lithuanian coastal waters prevents the lack of oxygen in the water column. However, hypoxic conditions and appearance of hydrogen sulfide (H_2S) were often recorded in the Gotland Deep (Emelyanov, 2014). The sand and gravel are the typical sediments in the shallow and exposed SE Baltic Sea coastal waters, while mud and silt accumulate in a deeper area (Bitinas et al., 2005; Emelyanov, 2001). The observed linear sedimentation rates mostly vary between 1.0 and 2.0 mm y^{-1} in the open Baltic Sea waters (Mažeika et al., 2004) and 2.5—3.6 mm y^{-1} or even 5—15 mm y^{-1} (Pustelnikovas, 2008 and references therein) in the Curonian Lagoon.

For the data analysis, the research stations were grouped according to the salinity zonation and taking into account the principal sedimentary environments: (1) the Curonian Lagoon; (2) the Klaipėda Strait; (3) territorial waters of the SE Baltic Sea and (4) open waters (Table 1). The stations were located in order to reflect the main anthropogenic pressures: (1) the impact of the Nemunas River (stations in the Curonian Lagoon, K12, K10, K14, K5); (2) the impact of the discharge from the Nemunas River and saline water intrusion (K1, K2, K3) as well as the industrial activities in the Klaipėda Port (in Malku Bay, st. K3A, K3B); (3) the impact of the plume of the Curonian Lagoon into the Baltic Sea (st. 3, 4, 5); (4) the impact of the activities in the Būtingė oil terminal (st. B-1, 1B, B-4); (5) the impact of the dumping of the dredged sediments from the Klaipėda Port (st. 20, 20A). The remaining sampling sites in the Lithuanian territorial waters and the Exclusive economic zone are situated in order to observe the common contamination trends.

2.2. Bottom sediments sampling and analysis

Bottom sediment samples were taken three times per year (in spring, summer, autumn) in the Baltic Sea and in the Curonian Lagoon during the period of 2011—2014. Sediments were collected from r/v *Vėjūnas* (Klaipėda) using a Van Veen grab sampler (sampling area of 0.1 m^2). Sediments from the uppermost layer (0—5 cm) were subsampled, stored in individual plastic containers and frozen on board (at −20°C) until further processing in the laboratory (Remeikaitė-Nikienė et al., 2016). The types of bottom sediments of the Curonian Lagoon were characterized on the basis of the decimal granulometric classification according to the dominant fraction and the median diameter (Md) according to EN ISO 14688-1: 2004 and EN ISO 14688-2: 2004. Implementing the WFD requirements, the sediment samples for the granulometric analysis were taken from the Curonian Lagoon and its outflow to the Baltic Sea area (transitional waters) in 2012. The suggested frequency of monitoring of the coastal

Table 1 The main morphometric and hydrological characteristics of the study area.

Research zones	Stations, No.	Variability of salinity	Water depth, m	Variability in sediment types
The Curonian Lagoon	K10, K12, K14, K6, K5	0.5 (st. K12)–7 (st. K5)	1.8–5.6	Fine sand, silt, with shell deposits
The Klaipėda Strait	K1, K2, K3, K3A, K3B	0.5–8	4–15	Fine sand, silt
Baltic Sea territorial – coastal waters	4, 3, 5, 2, 6, 7, 20, 20A, 1B, 64, 64A1, 64B, B-1, B-4, S-1, N-6	0.5 (st. 4)–8	12–46	Fine sand, sand, gravel, aleurite, glacial deposits
Baltic Sea open waters	65, 66, N-3, CHEMSEA1-8, CHG1, CHG2, CHG5, R7	7–12	40–117	Silt, aleurite, sand, gravel

waters is once per six years, thus, the sediment samples from the coastal and open sea area were not taken for the granulometric analysis in 2011–2014.

The analysis of metals was performed in two laboratories. For the national monitoring purposes sediment samples were analyzed at the laboratory of the Environment Research Department of the Environmental Protection Agency (EPA, accredited according to the ISO/IEC 17025) in 2011–2014. A 0.5 g of each dried sediment sample was leached with 6 ml of nitric acid (≥69%) in a microwave, diluted to 50 ml, and then analyzed by atomic absorption spectrometry with the graphite furnace (AAS) or/and the inductively coupled plasma optical emission spectrometer (ICP-OES). Concentrations of Cd were analyzed by AAS according to ISO 15586:2003. The ICP-OES method (ISO 11885:2007) was used for the analysis of Cr, Zn and Al. Both methods were used for the analysis of Pb, Cu and Ni depending on the concentrations of these metals in samples. The precision of the analytical procedures, expressed as the standard deviation, ranged within approximately from 5.2 to 14% for AAS and from 7.6 to 18% for ICP-OES methods. The certified reference materials CRM BCR-277R (IRM) and ICP Multielement standard solution (Merck) were used. The limit of determination for the AAS method ranged from 0.01 mg kg^{-1} for Cd to 0.10 mg kg^{-1} for Pb and Ni; for the ICP method – from 0.20 mg kg^{-1} for Cr to 4.5 mg kg^{-1} for Cu.

For the metal investigation the samples from several common stations (Nemunas, K3A, 4, 5, 6, 7, 20A, 65, 66, CHEMSEA2) and new stations (CHG1, R7) were analyzed at the Institute of Geology and Geography of the Nature Research Center (NRC) in 2011 and 2013. For metal (Pb, Cu, Cd, Ni, Cr, Zn, Fe and Al) analysis the total digestion method was used. A 0.25 g of each freeze-dried sediment sample was heated using a microwave in concentrated acids mixture (HNO3-HClO4-HF) to fuming and taken to dryness. The residue was dissolved in HCl (Loring and Rantala, 1992). The content of trace elements in the bottom sediments was analyzed with Perkin Elmer Optima 7000 DV ICP-OES. For quality control of the results the NIST Standard reference material 2702 (Inorganics in Marine Sediments) was used. The limit of detection for the ICP method ranged from 0.07 μg l^{-1} for Cd to 1.4 μg l^{-1} for Pb. The precision of the analytical procedures, expressed as the standard deviation, was approximately up to 15%.

The amount of TOC and the isotopic signatures were analyzed in samples taken during the period of 2012–2014. For the total nitrogen (%), organic carbon (%) and isotope ratio measurements ($\delta^{13}C$, $\delta^{15}N$) the sediment samples were acidified with 2 M HCl to remove carbonates, then dried at 60°C overnight and weighed (3÷90 mg depending on the organic matter content) into tin capsules. The measurements were made on a FlashEA1112 elemental analyzer connected to the isotope ratio mass spectrometer (Thermo Finnigan Delta Plus Advantage).

2.3. Estimation of EFs

The sediment pollution intensity indices (enrichment factor – EF, geoaccumulation index – I_{geo}, contamination factor – CF) were calculated in the study. Since no background data of metals in uncontaminated marine sediments in the study area are available, therefore, the global Earth's shale values for metals reported by Turekian and Wedepohl (1961) were used as background values for metals (Pb = 20; Cu = 45; Cd = 0.3; Ni = 68; Cr = 90; Zn = 95 mg kg^{-1} dry weight).

The EFs are widely used to calculate the ratio between uncontaminated background levels and contaminated sediment layers (e.g., Costa et al., 2015; Selvaraj et al., 2010; Zalewska et al., 2015). In the calculations of EFs, the normalization against Al is widely applied, mainly because it has a minor anthropogenic input and it is not significantly influenced by changes in the redox potential as compared with Fe (Ho et al., 2012 and references therein; Selvaraj et al., 2010).

The EFs were calculated as follows (Zalewska et al., 2015):

$$EF = \frac{C_{sample}/N_{sample}}{C_{shale}/N_{shale}}, \quad (1)$$

where *C* and *N* refer to the concentrations of the elements (e.g. Cu) and normalizers (e.g. Al) in the sample of surface sediments (*sample*) and the Earth's shale (*shale*), respectively.

For the evaluation of EF data, the following classification (Costa et al., 2015; Zalewska et al., 2015) was used: EF <1 – indicates no enrichment, EF <3 – minor enrichment, EF between 3 and 5 – moderate enrichment, EF between 5 and 10 – moderately severe enrichment, EF between 10 and 25 – severe enrichment, EF between 25 and 50 – very severe enrichment, EF > 50 – extremely severe enrichment. The EF values lower than 1.5 (García et al., 2008) or <2

Table 2 The average (±standard deviation) metal concentrations after partial and total leaching in the common stations (Nemunas, 4, 5, 6, 7, 20A, 65, 66 and CHEMSEA2) (t = t-test, *$p < 0.05$).

Method	Pb	Cu	Cd	Ni	Cr	Zn	Al, %
Partial leaching[a]	3.81 ± 1.4	1.4 ± 0.9	0.04 ± 0.02	2.8 ± 1.1	8.4 ± 3.6	12.1 ± 3.4	0.19 ± 0.07
Total leaching[a]	7.52 ± 1.3	2.4 ± 0.9	0.11 ± 0.05	2.3 ± 0.9	16.6 ± 11.1	14.2 ± 3.9	1.54 ± 0.15
Statistics	$t = -5.18$*	$t = -1.88$	$t = -3.29$*	$t = 0.79$	$t = -1.89$	$t = -0.99$	$t = -21.48$*
Partial leaching[b]	16.6 ± 13.1	8.4 ± 4.5	0.33 ± 0.30	10.4 ± 6.5	20.3 ± 5.3	42.3 ± 29.1	0.79 ± 0.50
Total leaching[b]	13.9 ± 10.1	11.2 ± 4.9	0.38 ± 0.11	20.9 ± 14.4	31.5 ± 13.4	39.5 ± 17.7	3.20 ± 0.70
Statistics	$t = 0.21$	$t = -0.31$	$t = -0.18$	$t = -0.63$	$t = -1.10$	$t = 0.11$	$t = -3.94$*

The stations with similar type of sediments were grouped.
[a] Nemunas, 4, 5, 6, 7, 20A, 66 (fine sand, sand).
[b] 65, CHEMSEA2 (aleurites).

(Abreu et al., 2016) indicate that the metal is entirely from crustal materials or natural processes, whereas EF values higher than 1.5 or 2 suggest an increasing portion of the anthropogenic sources (Abreu et al., 2016; García et al., 2008). The enrichment factors (EFs) were calculated based only on the total metal concentrations since the significant differences between Al content after partial an total extraction methods were observed (Table 2).

The geoaccumulation index (I_{geo}) is also quite widely applied in assessments of the sediment pollution with metals (García et al., 2008; Müller, 1979; Zalewska et al., 2015):

$$I_{geo} = \mathrm{Log}_2\left(\frac{C_n}{1.5B_n}\right), \quad (2)$$

where C_n is the concentration of the element in the enriched samples, and the B_n is the background or pristine value of the element. Factor 1.5 is introduced to minimize the effect of possible variations in the background values which may be attributed to lithologic variations in the sediments. The method assesses the degree of metal pollution in terms of seven enrichment classes based on the increasing numerical values of the index: $I_{geo} < 0$, uncontaminated; $0 \le I_{geo} < 1$, uncontaminated to moderately contaminated; $1 \le I_{geo} < 2$, moderately contaminated; $2 \le I_{geo} < 3$, moderately to heavily contaminated; $3 \le I_{geo} < 4$, heavily contaminated; $4 \le I_{geo} < 5$, heavily to extremely contaminated; $5 \ge I_{geo}$, extremely contaminated (García et al., 2008; Müller, 1979; Zalewska et al., 2015).

The method of the contamination factor (CF) evaluates the enrichment in metals in relation to the background concentrations of each metal in sediments. CF is the ratio obtained by dividing the concentration of each metal in the sediments by the background value (Bonnail et al., 2016):

$$CF = \frac{C_s}{C_{ref}}, \quad (3)$$

where C_s and C_{ref} are concentrations of the element in the sediment sample and the background or pristine value of the element, respectively. The method of the CF calculation is identical to the EF calculation, except the fact that the CFs do not normalize concentrations against the normalizing element. In order to evaluate the degree of contamination in sediments, the following gradations are proposed: $CF < 1$, no/low contamination; $1 \le CF < 3$, moderate; $3 \le CF < 6$, considerable; $6 \le CF$ – very high contamination (Bonnail et al., 2016; Håkanson, 1980).

2.4. Data preparation and the statistical analysis

Measurements below limits of quantification (LoQ) were treated as half the LoQ value of the compound considered. The data of metals (Pb, Cu, Cd, Ni, Cr, Zn, Al) in the sediments obtained by using partial and total extraction methods were compared from nine stations (Nemunas, 4, 5, 6, 7, 20A, 65, 66 and CHEMSEA2) in order to have the view on the contamination extent of the Lithuanian marine zone as reliable as possible. The comparison of the pre-treatment methods in this study is assumed to be important since: (i) the reference values (concentrations in the Earth's shale, Turekian and Wedepohl, 1961) showed the total concentrations; and (ii) it was necessary to know whether the national monitoring data on Al (partial digestion) might be used for the normalization purposes. The mean concentrations for both pre-treatment methods are shown in Table 2. The mean concentrations after partial and total leaching were compared via the parametric t-test. The post hoc Tukey HSD test was used to find out significant differences among the spatial distribution of metal concentrations. The Pearson's coefficient was used to identify the relationships among trace and major elements, TOC, carbon isotopic signatures, the particle size, water depth and salinity. The analysis was performed applying SigmaPlot 12.5 software. The PCA was used in order to identify sources of pollution with metals and to scrutinize the distribution pattern. This technique clusters variables into groups, such that variables belonging to one group are highly correlated with one another. Four datasets were analyzed separately: (1) the Curonian Lagoon; (2) the Klaipėda Strait; (3) territorial waters of the SE Baltic Sea and (4) open waters. The number of factors extracted from the variables was determined according to the Kaiser's rule. This criterion retains only factors with eigenvalues that exceed one. The analysis was performed applying Statistica 7 software.

3. Results and discussion

3.1. Assessment of sediment contamination

The nitric acid only partly leaches mineral-bounded pollutants, therefore, the real contamination of the sediments

might be not revealed (Vallius, 1999). As it was shown by Birch (2017), the sediment pre-treatment with the strong acids resulted in a 4—9 fold elevation in metal concentrations. Despite that fact, both methods are common within the HELCOM countries, and the partial leaching technique is used to evaluate the anthropogenic share of the metal concentration in sediments (e.g., Ebbing et al., 2002; Leivuori et al., 2000; Vallius, 1999). During this study, the comparison between the nitric acid extraction and the total digestion showed statistically different mean concentrations of lead and cadmium in sandy sediments, while no differences were observed in aleurites (Table 2). However, the concentrations of aluminium were about 4—8 times lower in the partial digestion than in the total leaching and, therefore, no Al-normalized enrichment factors (EFs) were calculated based on the national monitoring data. Unfortunately, no national monitoring data on metal concentrations from the silty sediments (st. CHG1, R7) were available for the methodological comparison. In general, our results demonstrated that despite different sediment pre-treatment methods, the datasets of most metals might be used in parallel in this study for the common assessment of the chemical sediment status. Spatial variations of the average contents of metals and the "metal pollution hotspots" are illustrated in Fig. 2. The comparison of metal concentrations in the water bodies revealed that the amount of elements accumulated in the Curonian Lagoon sediments was about 1.4—4.0 times higher than in the sediments of the Baltic Sea and it might show that the lagoon acts as a sink for many pollutants entering from the catchment. Among the stations, the higher concentrations of metals (Tukey HSD test, $p < 0.05$) were measured in sediments of the Klaipėda Strait (st. K1, K3A, K3B), the central part of the Curonian Lagoon (st. K10) and the open sea (st. CHEMSEA2, CHG1 and R7) (Fig. 2). The prevalent metal accumulation in sediments in most cases coincided with the increase of its organic (TOC) and mineral (Al, silt fraction) constituents (Table 3). The TOC values in sediments ranged from <1% to 10% dry weight (d.w.) with a consequently higher amount in sediments from the accumulation areas in the Curonian Lagoon (8.40% at the st. K10) and the open sea (7.59% at the st. R7). Results might be explained by the affinity of metals to the organic matter and the clay fraction of the sediment as well as the formation of e.g. organic complexes (Emelyanov et al., 2015; Pustelnikovas et al., 2007; Zalewska et al., 2015). The concentration and retention of metals in the sediments are also affected by the oxygen saturation and occurrence of hydrogen sulphide, which periodically accumulates in the bottom of the Gotland and Gdańsk Deeps (Emelyanov, 2014; Zalewska et al., 2015). In exposed and oxic waters, iron/manganese-oxides/hydroxides are important carriers of metals in sediments, while under reducing conditions some part of the iron fraction can be fixed in sediment layers in the form of iron sulphides (Emelyanov, 2014; Müller, 1999). The strong correlation

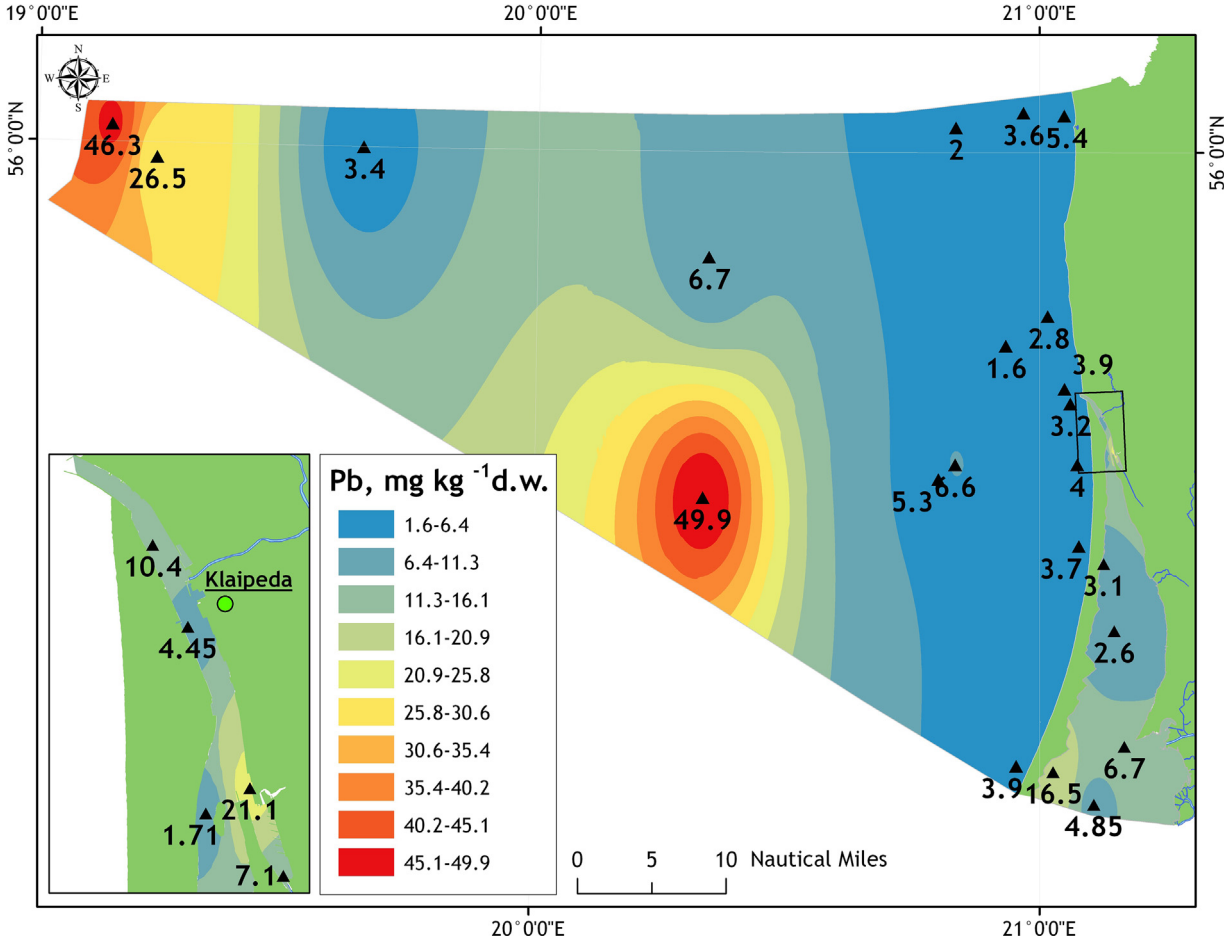

Figure 2 Distribution of Pb, Cu, Cd, Ni, Cr and Zn (the average values) in the SE Baltic Sea in 2011—2014.

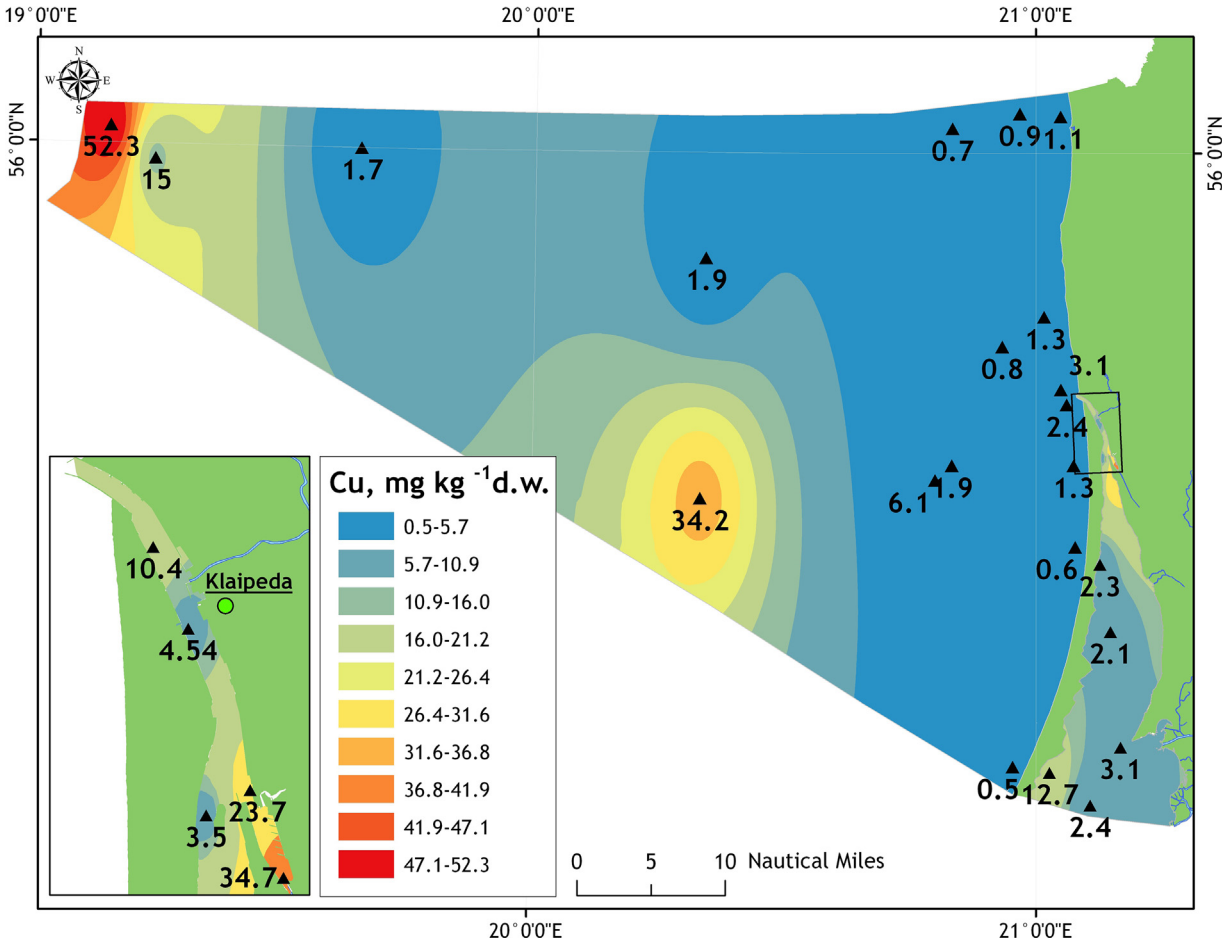

Figure 2 (*Continued*).

(Table 3) among all metals and the sulphur amount in the open sea sediments might indicate binding of metals with insoluble sulphides.

In order to quantitatively evaluate the pollution extent at the stations with the elevated metal concentrations (K1, K3A, K3B, K10, CHEMSEA2, CHG1 and R7), the contamination factors (EF, I_{geo} and CF) were calculated. In this study, the average EFs for the studied metals varied between 0.5 and 9.9 (Table 4). The mean EFs for the open sea sites were: Cd (5.5) > Pb (2.8) > Zn (1.7) > Cr, Cu (1.1) > Ni (0.6) and showed no/minor enrichment with all elements except with Cd. The EF for Cd showed a moderately severe enrichment which might be attributed to the anthropogenic sources (EF > 1.5–2.0).

The low geoaccumulation index (I_{geo}) values (<0) for Cu, Ni, Cr showed that these metals had not contaminated SE Baltic Sea sediments. The calculated I_{geo} values ($0 \leq I_{geo} < 1$) for Cd at the K10, CHEMSEA2 and R7 sites, for Pb at the CHG1 and R7 sites and for Zn (only CHG1 site) indicated that sediments from the investigated locations were uncontaminated to moderately contaminated with Cd, Pb and Zn. The highest I_{geo} value (2.3) calculated for Cd at the station CHG1 indicated moderately to highly polluted sediments (Table 4). The state of the sediment contamination based on the CF values (Table 4) showed that sediments exhibited low levels of contamination (CF < 1) for Ni and Cr; moderate ($1 \leq$ CF < 3) for Cd (K10, CHEMSEA2, R7), Cu (only CHG1), Pb (CHEMSEA2, CHG1 and R7) and Zn (CHG1 and R7); and very high contamination (6 ≤ CF) for Cd (at CHG1) (Table 4).

In summary, the values of the contamination factors (EF, I_{geo} and CF) pointed out a higher sediment pollution extent in the open sea as compared with the Klaipėda Strait (Table 4). Based on the average values of EF, I_{geo} and CF, the sediment contamination degree in the open waters was defined as moderate–considerable for Cd, minor–moderate for lead, zinc and copper and low for nickel and chromium (Table 4). The sediment pollution extent based on the EFs and I_{geo} values was comparable with the most recent data reported for the southern Baltic Sea by Zalewska et al. (2015). When comparing the average EFs values, the Baltic Sea open waters showed a higher contamination with Cd (EF = 5.5 in this study and EF = 1.7 reported by Zalewska et al., 2015), but similar contents of Pb (EF = 2.8 and EF = 2.2, respectively) and Zn (EF = 1.7 and EF = 1.5, respectively) for the SE Gotland Basin. The adjacent Gdańsk Deep was also minor contaminated with Zn and Pb (EF = 2.2 and 2.7, respectively), while the enrichment factor for Cd (EF = 7.2) indicated a moderately severe enrichment (Zalewska et al., 2015). The obtained results pointed out the similar extent of sediment pollution with Zn and Pb in the Gdańsk and Gotland Deeps, and a higher contamination with Cd in the Gdańsk Deep.

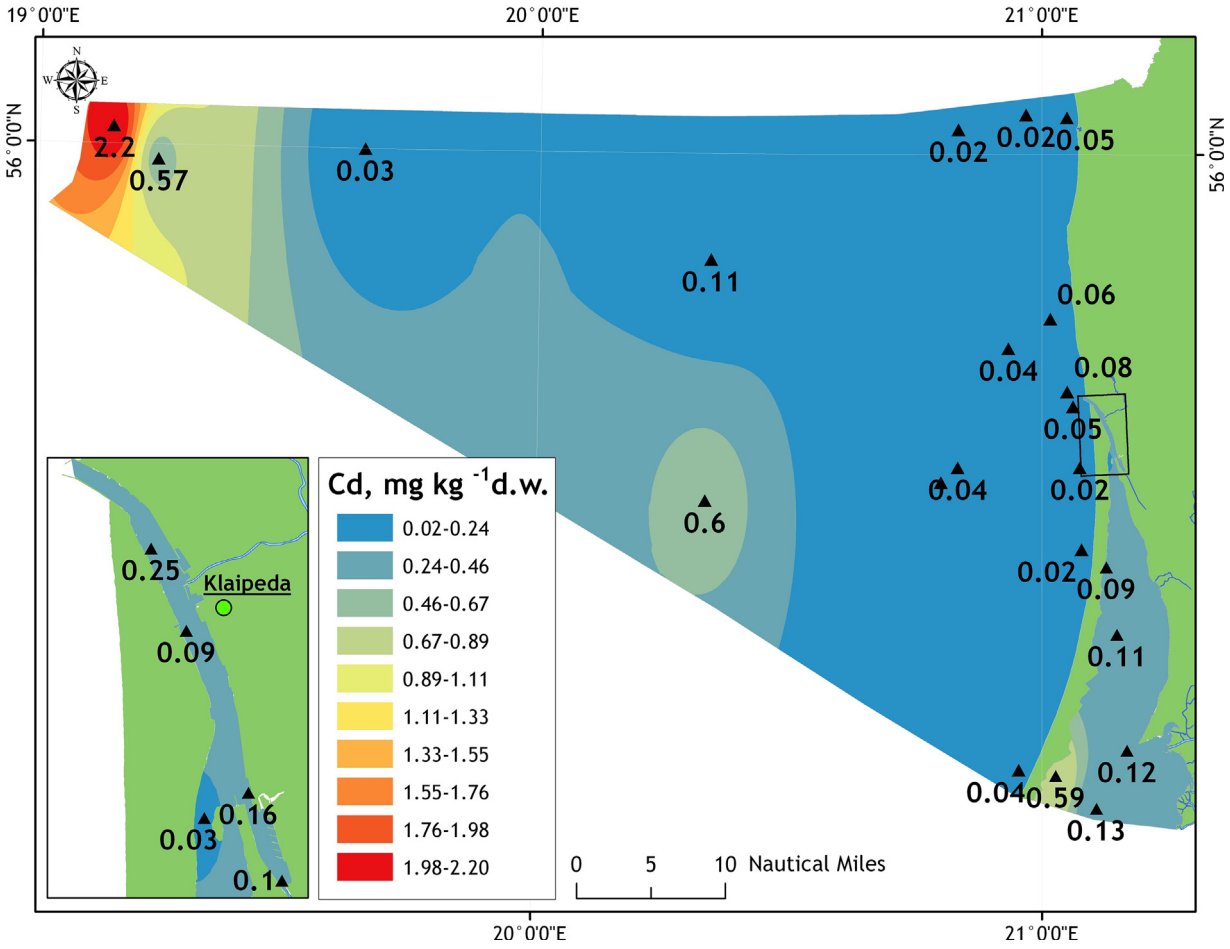

Figure 2 (*Continued*).

3.2. Identification of pollution sources

The principal component analysis (PCA) and the Pearson correlation matrix used in the study provided important tools for a better understanding of the source identification and the dynamics of the pollutants. The PCA extracted a small number of factors (Principal Components, PCs) for exploring the similarity of distribution behaviour of metals and analyzing the relationships among the observed variables (Table 3). The PCs with eigenvalues >1 were extracted for metals in sediments datasets, accounting for about 81—92% of the total variance (Table 3).

The Curonian Lagoon (without Klaipėda Strait). Only one PC (with eigenvalue >1) was extracted from the database which explained about 92% of the total variance of metals (Table 3). The PC1 was correlated with Pb, Cu, Cd, Ni, Cr, Zn, Al, TOC and the amount (%) of fine particles (<0.063 mm). The strong relationships among metals (Table 3) suggested their similar source and mechanism of distribution in sediments, while each source type was not defined. In some studies, a lithogenic (natural) origin is presumed for metals related with Al, since it is a common element in soil parent materials (e.g., Levei et al., 2014). However, the significant correlation may show the supply of aluminosilicate of the mainland origin contaminated with metals from intensive agricultural activities. The highest amount of pollutants enters the Curonian Lagoon with the riverine discharge, affected by the municipal sewage discharge, industrial and agricultural activities within catchment areas (The Nemunas River Basin District Management Plan, 2010). In 2011—2013, on the average, 11.3 t y^{-1} of Cr, 26.0 t y^{-1} of Cu, 14.6 t y^{-1} of Ni and 82.2 t y^{-1} of Zn entered the Curonian Lagoon via riverine discharge (Environmental Protection Agency data, unpublished). Pb, Cu, Cd and Zn are well-known elements of agricultural activities, specifically related to an application of pesticides and phosphate fertilizers (Wang et al., 2015). Consequently, metals originated from mainland sources accumulate in the central part of the lagoon characterized by slower dynamics and high primary production resulting in a high TOC amount. Besides the pollution of mainland origin, close to the sampling station K10 there is a marina for small boats, which may contribute to the inputs of metals and oil hydrocarbon to the sediments with the fuel residues.

The Klaipėda Strait. The PC1 explained about 70% of the total variance with high loadings of Pb, Cd, Ni, Cr, Zn, Al, TOC, salinity and amount (%) of fine particles (<0.063 mm) in sediments. On the plot of scores the relatively higher concentrations of elements appeared at the K1, K3A and K3B sites (not shown). The observed strong positive correlations for metals (Table 3) suggested that they had common geochemical behaviours and probably originated from similar pollution sources, while the possibility to identify a clear

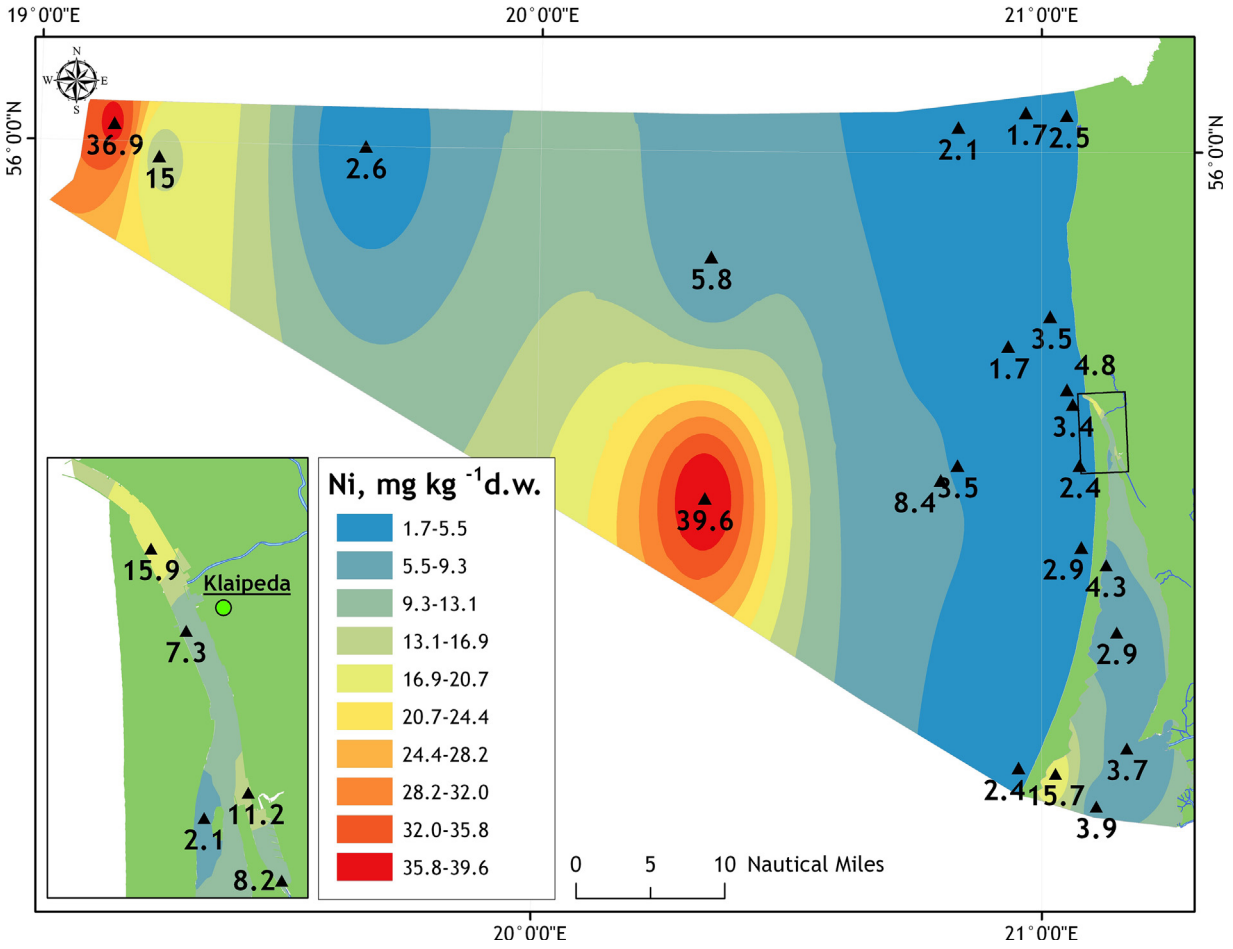

Figure 2 (*Continued*).

origin of metals was limited. On the one hand, contaminants from the rivers catchment area are carried into the harbour area, on the other hand, local pollution also appears from sources in the port itself (Galkus et al., 2012 and references therein). The increasing accumulation of trace metals in sediments at the station K1 might be greatly influenced by the flocculation processes which are often amplified by the increase of pollution. When colloidal particles move downwards from freshwater into the marine environment, flocculation causing larger particles to form and settle on the seafloor takes place. Flocculation processes in the marine water-freshwater interface have been widely reported in other studies (Karbassi et al., 2013; Palanques et al., 1995). The correlation between metal concentrations in sediments and salinity (Table 3) might support this explanation. Despite the significantly high metal concentrations at K1, K3A and 3B sites, the contamination factors (I_{geo}, CF) indicated uncontaminated/low contaminated sediments. The PC2 accounted for 19.4% of the total variance and was dominated by Cu (Table 3). Copper occurred as an important parameter at sites K3A and K3B and probably might be related to the urban and industrial activities taking place in the Klaipėda Port. The station K3B was established to track the impact of domestic and industrial effluent inputs, whereas st. K3A was located in the semi-enclosed Malku Bay in order to evaluate the impact of the floating docks of the ship repair company. Stagnation and low oxygen conditions are prevalent in the technogenic sedimentation zone of the Klaipėda Strait resulting in 5–50 times higher metal concentrations than in the natural sedimentation zone (Pustelnikovas et al., 2007). The elevated concentrations of metals in sediments and moderate pollution with copper level were indicated previously by other authors (Galkus et al., 2012).

Territorial waters. Three main PCs explained about 83% of the total variance (Table 3). The PC1 (53% of the total variance) identified a large group of variables containing all metals together with a water depth, thus confirming the distribution of elements depending on the water depth. Results (Table 3) showed that the major source for the metal accumulation in coastal sediments had a lithological material (Al), while the material of biotic origin (TOC) probably had a secondary importance. The PC2 explained 15.8% of the total variance with the moderate loadings of Cd, salinity and the water depth (Table 3). On the score plot, the elements defined by the PC1 and PC2 were related to the stations 64A1, 20, 20A and 4 (not shown) and it probably showed the mainland origin of metals: an input with the freshwater discharge (stations 4 and 64A1) as well as the sediment dumping from the Klaipėda Port area (st. 20 and 20A).

Open waters. Only one PC (with eigenvalue >1) was extracted from the database which explained about 81% of

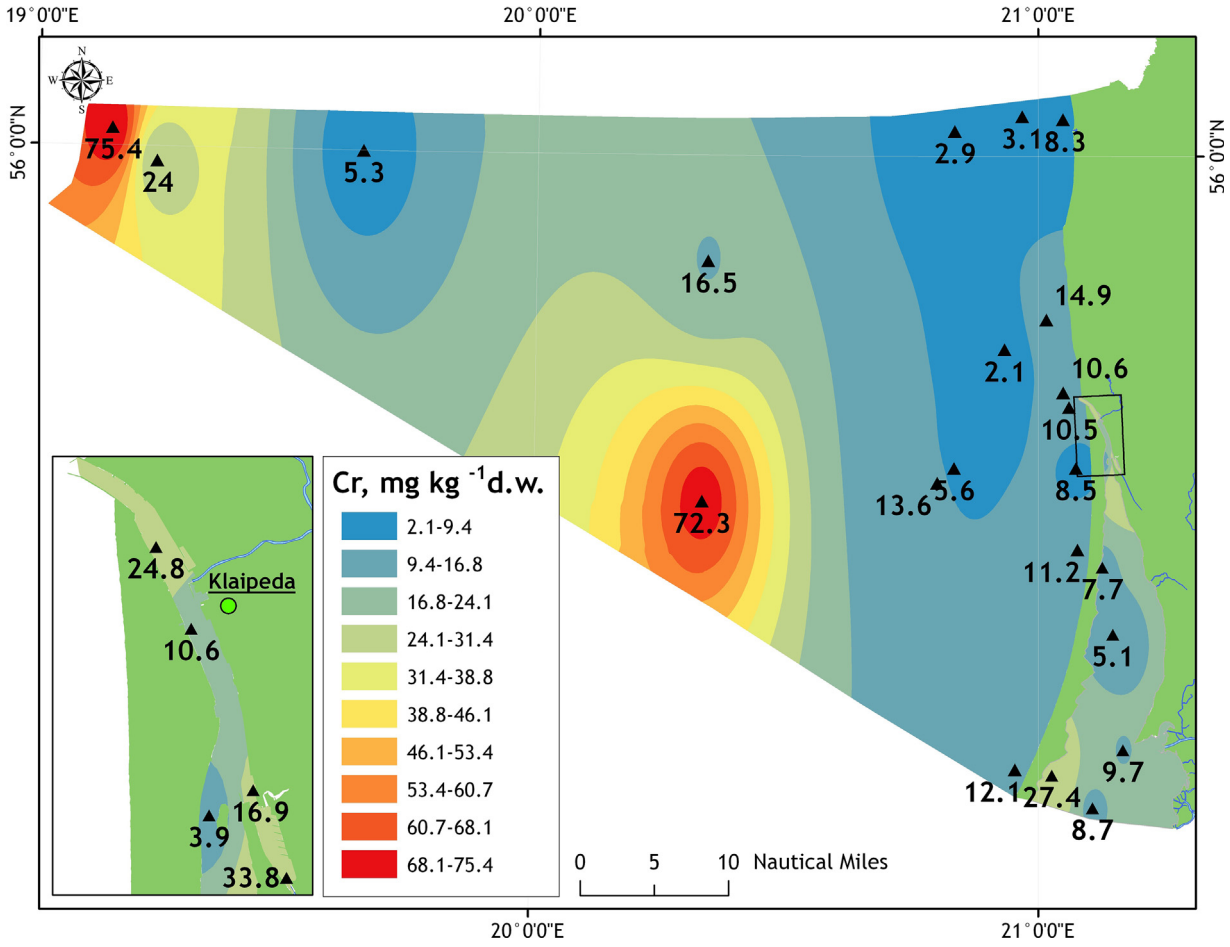

Figure 2 (*Continued*).

the total variance of metals (Table 3). The PC1 was highly correlated with all metals, TOC, water depth, the amount of sulphur and iron. Since Cd and Pb are scarce in rocks, their presence in the marine environment is usually related to anthropogenic inputs from the atmosphere and rivers (Prego et al., 1999). As it was shown, the concentrations of Pb and Cd in the open waters were clearly higher than the concentrations in the Earth's shale and showed an anthropogenic origin of pollutants (EFs >1.5—2.0). Regarding nickel, Renner et al. (1998) claimed that Ni, as well as Mn and Co, entered the southern Baltic as a result of natural erosion processes. Therefore, the strong correlations among all elements should refer to a similar distribution pattern and a combination of natural and anthropogenic sources.

The sources of metals and their distribution pathways might be indirectly identified using the C and N isotopic signatures of organic matter. The $\delta^{13}C$ and $\delta^{15}N$ signatures (from −31.3 to −23.3‰, $\delta^{15}N$ from 0.6 to 11.2‰), as well as low C N^{-1} ratio (~7), suggested that the SOM in the SE Baltic Sea was mostly derived from a contribution of marine and freshwater algae (Remeikaitė-Nikienė et al., 2016). The trace elements from water might be incorporated in living phytoplankton cells and, in this respect, phytoplankton plays an important role in the transport of metals (Aigars et al., 2014) as well as other toxic pollutants (e.g., TBT compounds, Filipkowska et al., 2014) from the water column to the bottom sediments. The presence of blooms of phytoplankton in the late spring and summer provides ideal conditions for the considerable metal accumulation from the water layer in sediments. Several studies (e.g., Lin et al., 2016; Thorsson et al., 2008) have shown that the increasing eutrophication and consequently organic matter settling to the seafloor can have a significant effect on the increasing bioaccumulation of associated contaminants in the benthic organisms. Since the decrease of the freshwater organic matter towards offshore is observed (Remeikaitė-Nikienė et al., 2016, 2017), the influence of terrestrial contaminants is believed to decrease towards open waters. The weak negative correlation between metals and $\delta^{13}C$ of SOM values (r = from −0.36 to −0.60, $p < 0.05$) in territorial waters might show a general tendency of decreasing transport of contaminants in association with freshwater phytoplankton. The correlation between metals and $\delta^{13}C$ values for the open sea was not significant. Considering an increase of the marine phytoplankton contribution at the open sea stations (Remeikaitė-Nikienė et al., 2016), it is believed that marine phytoplankton is probably not directly involved in the metal transport from terrestrial sources, although it uptakes metals deposited from the atmosphere and is likely involved in the further sedimentation and redistribution processes of fine-grained particles. An exception was R7 site which was characterized by the lowest $\delta^{13}C$ value (-31.8 ± 0.3‰) and a

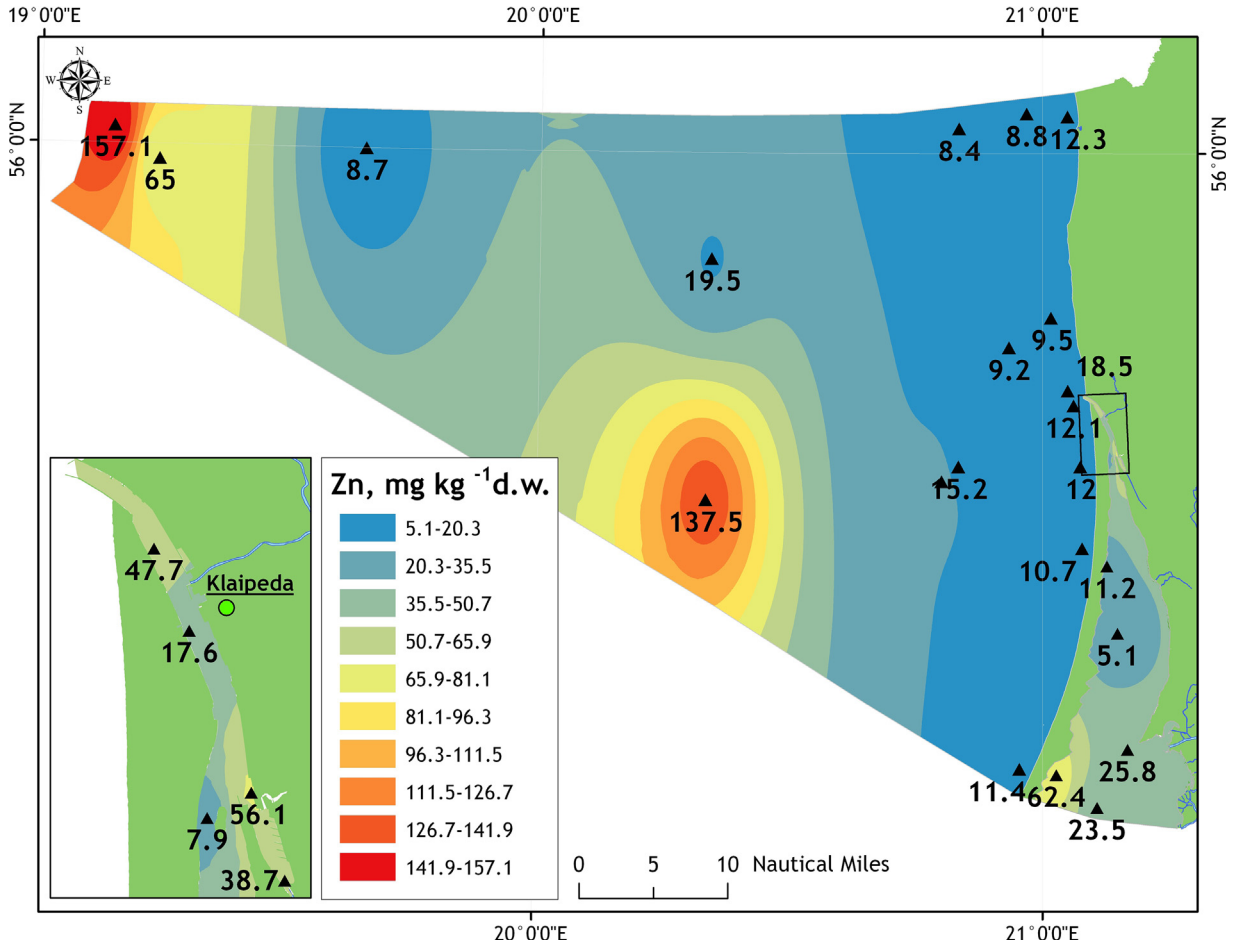

Figure 2 (*Continued*).

Table 3 Results of the PCA for the distinct research zones. The dominant loadings are given in bold.

Variables	Curonian Lagoon	Klaipėda Strait		Territorial waters			Open sea
	PC1	PC1	PC2	PC1	PC2	PC3	PC1
Pb	**−0.97**	**−0.98**	0.04	**−0.53**	−0.14	−0.24	**0.98**
Cu	**−0.99**	−0.37	**−0.84**	**−0.94**	−0.01	0.15	**0.99**
Cd	**−0.99**	**−0.96**	0.13	**−0.64**	**0.60**	−0.36	**0.99**
Ni	**−0.98**	**−0.98**	0.03	**−0.97**	−0.06	0.19	**0.99**
Cr	**−0.99**	**−0.73**	−0.38	**−0.54**	0.39	**0.56**	**0.98**
Zn	**−0.95**	**−0.84**	−0.48	**−0.99**	0.01	0.04	**0.98**
Al	**−0.98**	**−0.95**	0.27	**−0.93**	−0.12	0.29	**0.98**
TOC	**−0.98**	**−0.85**	**0.53**	−0.43	−0.10	**−0.79**	**0.99**
<0.063 [a]	**−0.71**	**−0.91**	−0.30	–	–	–	–
Depth	−0.20	−0.48	**0.66**	**−0.65**	**−0.64**	−0.31	**0.80**
Salinity	0.06	**−0.90**	0.22	0.15	**−0.77**	0.35	0.36
Fe [b]	–	–	–	–	–	–	**0.99**
S [b]	–	–	–	–	–	–	**0.99**
Eigenvalues	8.25	6.69	1.74	5.26	1.58	1.48	8.12
% of variance	91.68	69.95	18.47	52.61	15.76	14.84	81.25
Cumulative %	91.68	69.95	88.42	52.61	68.36	83.20	81.25

[a] Data on the particle size were available only for the Curonian Lagoon.
[b] Data on Fe and S were available only for the open sea stations.

Table 4 The enrichment factor (EF)[a], geoaccumulation index (I_{geo})[b] and the contamination factor (CF)[c] of trace metals in selected sediments from the SE Baltic Sea. In bold – the values >0 (I_{geo}) and >1 (EF, CF).

	Pb			Cu			Cd			Ni			Cr			Zn		
Stations	EF	I_{geo}	CF	EF	I_{geo}	CF	EF	I_{geo}	CF	EF	I_{geo}	CF	EF	I_{geo}	CF	EF	I_{geo}	CF
K10	–	−0.9	0.8	–	−2.4	0.3	–	**0.4**	**2.0**	–	−2.7	0.2	–	−2.3	0.3	–	−1.2	0.7
K3A	–	−2.1	0.4	–	−0.9	0.8	–	−2.2	0.3	–	−3.6	0.1	–	−2.0	0.4	–	−1.9	0.4
K3B	–	−2.0	0.4	–	−1.5	0.5	–	−1.5	0.5	–	−3.2	0.2	–	−3.0	0.2	–	−1.4	0.6
K1	–	−1.5	0.5	–	−2.7	0.2	–	−0.8	0.8	–	−2.7	0.2	–	−2.5	0.3	–	−1.6	0.5
CHEMSEA2	**2.3**	−0.5	**1.1**	0.8	−2.5	0.4	**4.1**	**0.3**	**1.9**	0.5	−2.8	0.2	1.0	−1.7	0.5	**1.2**	−1.4	0.6
CHG1	**3.1**	**0.6**	**2.3**	**1.6**	−0.4	**1.2**	**9.9**	**2.3**	**7.3**	0.7	−1.5	0.5	**1.2**	−0.8	0.8	**2.2**	**0.1**	**1.7**
R7	**3.1**	**0.8**	**2.5**	0.9	−0.9	0.8	**2.4**	**0.2**	**1.7**	0.7	−1.4	0.6	**1.1**	−0.9	0.8	**1.8**	−0.1	**1.5**

The EFs, I_{geo}, CFs for the open sea stations (CHEMSEA2, CHG1 and R7) calculated based on the total concentrations.

[a] EF < 1, no enrichment; 1 ≤ EF < 3, minor enrichment; 3 ≤ EF < 5, moderate enrichment; 5 ≤ EF < 10, moderately severe enrichment; 10 ≤ EF < 25, severe enrichment; 25 ≤ EF < 50, extremely severe enrichment (Zalewska et al., 2015).

[b] $I_{geo} < 0$, uncontaminated; $0 \le I_{geo} < 1$, uncontaminated to moderately contaminated; $1 \le I_{geo} < 2$, moderately contaminated; $2 \le I_{geo} < 3$, moderately to heavily contaminated; $3 \le I_{geo} < 4$, heavily contaminated; $4 \le I_{geo} < 5$, heavily to extremely contaminated; $5 \ge I_{geo}$, extremely contaminated (Müller, 1979; Zalewska et al., 2015).

[c] CF < 1, no/low contamination; 1 ≤ CF < 3, moderate; 3 ≤ CF < 6, considerable; 6 ≤ CF – very high (Håkanson, 1980; Bonnail et al., 2016).

relatively high $\delta^{15}N$ value (6.8‰) (Remeikaitė-Nikienė et al., 2016) similar to those, reported for the freshwater ecosystems (Remeikaitė-Nikienė et al., 2016, 2017). Apparently, this site is influenced by the considerable amounts of elements discharged to the sea by the Vistula River. In the Gdańsk Deep, an intensive accumulation of trace metals supplied by the Vistula River was reported in other studies (Emelyanov, 2014; Zalewska et al., 2015).

4. Conclusions

The present study showed the higher concentrations of metals in sediments of the Curonian Lagoon (stations K1, K3A, K3B in Klaipėda Strait and K10 near the Nida settlement) and the Baltic Sea open waters (stations CHEMSEA2, CHG1 and R7). Based on the average values of EF, I_{geo} and CF, the sediment contamination degree in the open waters was defined as moderate–considerable for Cd, minor–moderate for lead, zinc and copper and low for nickel and chromium. Although the PCA applied to the data set provided the qualitative information about the distribution pattern of elements, it was not adequate for supplying the quantitative information regarding the contributions of each source type. Results showed that the metal accumulation in sediments was affected by the grain-size, amount of TOC, depth variability, and thus the anthropogenic component was not easily discernible by the lithogenic one. Based on the PCA results, the only Cu in the Malku Bay might be attributed to the anthropogenic source, however, metal enrichment was not confirmed based on the values of I_{geo} and CF.

Acknowledgments

We appreciate the anonymous reviewers for their valuable comments and suggestions to improve the quality of the manuscript. The authors would like to thank all the team members from the Environmental Protection Agency, the Geology and Geography Institute of the Nature Research Centre, the Center for Physical Sciences and Technology, the crews of the vessel r/v *Vėjūnas* for their help and support during sampling and analysis.

The samples were taken and analysis was completed in the frame of the State monitoring and by implementing the projects: (1) "Application of isotope methods to assess spreading of organic substances in the Baltic Sea" which was financed by the Research Council of Lithuania" (contract No. MIP-080/2012); (2) EU part-financed project "Chemical munitions search and assessment (CHEMSEA)".

References

Abreu, I.M., Cordeiro, R.C., Soares-Gomes, A., Abessa, D.M.S., Maranho, L.A., Santelli, R.E., 2016. Ecological risk evaluation of sediment metals in a tropical Euthrophic Bay, Guanabara Bay, Southeast Atlantic. Mar. Pollut. Bull. 109 (1), 435–445, http://dx.doi.org/10.1016/j.marpolbul.2016.05.030.

Aigars, J., Poikāne, R., Jurgensone, I., Jansons, M., 2014. Impact of eutropication and climate change on Cd and other trace metal dynamic in the Gulf of Riga, Baltic Sea. Proc. Latvian Acad. Sci. Sect. B 68 (1–2), 112–117, http://dx.doi.org/10.2478/prolas-2014-0010.

Birch, G.F., 2017. Determination of sediment metal background concentrations and enrichment in marine environments – a critical review. Sci. Total. Environ. 580, 813–831, http://dx.doi.org/10.1016/j.scitotenv.2016.12.028.

Bitinas, A., Žaromskis, R., Gulbinskas, S., Damušytė, A., Žilinskas, G., Jarmalavičius, D., 2005. The results of integrated investigations of the Lithuanian coast of the Baltic Sea: geology, geomorphology, dynamics and human impact. Geol. Q. 49 (4), 355–362.

Bonnail, E., Sarmiento, A.M., Del Valls, T.A., Nieto, J.M., Riba, I., 2016. Assessment of metal contamination, bioavailability, toxicity and bioaccumulation in extreme metallic environments (Iberian Pyrite Belt) using *Corbicula fluminea*. Sci. Total. Environ. 544, 1031–1044, http://dx.doi.org/10.1016/j.scitotenv.2015.11.131.

Costa, E.S., Grilo, C.F., Wolff, G.A., Thompson, A., Figueira, R.C.L., Neto, R.R., 2015. Evaluation of metals and hydrocarbons in sediments from a tropical tidal flat estuary of Southern Brazil. Mar. Pollut. Bull. 92 (1–2), 259–268, http://dx.doi.org/10.1016/j.marpolbul.2014.11.028.

Dang, D.H., Lenoble, V., Durrieu, G., Omanović, D., Mullot, J.-U., Mounier, S., Garnier, C., 2015. Seasonal variations of coastal sedimentary trace metals cycling: insight on the effect of manganese and iron (oxy)hydroxides, sulphide and organic matter. Mar. Pollut. Bull. 92 (1—2), 113—124, http://dx.doi.org/10.1016/j.marpolbul.2014.12.048.

Ebbing, J., Zachowicz, J., Uścinowicz, S., Laban, C., 2002. Normalisation as a tool for environmental impact studies: the Gulf of Gdańsk as a case study. Baltica 15, 59—62.

Emelyanov, E.M., 2001. Biogenic components and elements in sediments of the Central Baltic and their redistribution. Mar. Geol. 172, 23—41.

Emelyanov, E.M., 2014. Biogenic components of the Baltic Sea sediments. Russ. Geol. Geophys. 55 (12), 1404—1417, http://dx.doi.org/10.1016/j.rgg.2014.11.005.

Emelyanov, E.M., Gulbinskas, S., Suzdalev, S., 2015. Biogenic components and trace elements in the sediments of river mouths and accumulation areas of the Curonian Lagoon (south-eastern Baltic Sea). Baltica 28 (2), 151—162.

Filipkowska, A., Kowalewska, G., Pavoni, B., 2014. Organotin compounds in surface sediments of the Southern Baltic coastal zone: a study on the main factors for their accumulationand degradation. Environ. Sci. Pollut. Res. Int. 21 (3), 2077—2087, http://dx.doi.org/10.1007/s11356-013-2115-x.

Galkus, A., Jokšas, K., Stakėnienė, R., Lagunavičienė, L., 2012. Heavy metal contamination of harbour bottom sediments. Pol. J. Environ. Stud. 21 (6), 1583—1594.

García, E.M., Cruz-Motta, J.J., Farina, O., Bastidas, C., 2008. Anthropogenic influences on heavy metals across marine habitats in the western coast of Venezuela. Cont. Shelf. Res. 28 (20), 2757—2766, http://dx.doi.org/10.1016/j.csr.2008.09.020.

Håkanson, L., 1980. Ecological risk index for aquatic pollution control. A sedimentological approach. Water Res. 14, 975—1001.

HELCOM, 2010. Hazardous substances in the Baltic Sea — An integrated thematic assessment of hazardous substances in the Baltic Sea. Balt. Sea Environ. Proc. No. 120B.

Ho, H.H., Swennen, R., Cappuyns, V., Vassilieva, E., Van Tran, T., 2012. Necessity of normalization to aluminum to assess the contamination by heavy metals and arsenic in sediments near Haiphong Harbor, Vietnam. J. Asian Earth Sci. 56, 29—239, http://dx.doi.org/10.1016/j.jseaes.2012.05.015.

Jakimska, A., Konieczka, P., Skóra, K., Namieśnik, J., 2011. Bioaccumulation of metals in tissues of marine animals, Part I: the role and impact of heavy metals on organisms. Pol. J. Environ. Stud. 20 (5), 1117—1125.

Karbassi, A.R., Bassam, S., Ardestani, M., 2013. Flocculation of Cu, Mn, Ni, Pb, and Zn during estuarine mixing (Caspian Sea). Int. J. Environ. Res. 7 (4), 917—924.

Levei, E., Ponta, M., Senila, M., Miclean, M., Frentiu, T., 2014. Assessment of contamination and origin of metals in mining affected river sediments: a case study of the Aries River catchment, Romania. J. Serb. Chem. Soc. 79 (8), 1019—1036, http://dx.doi.org/10.2298/JSC130501086L.

Leivuori, M., Jokšas, K., Seisuma, Z., Kulikova, I., Petersell, V., Larsen, B., Petersen, B., Floderus, S., 2000. Distribution of heavy metals in sediemnts of the Gulf of Riga, Baltic Sea. Boreal. Environ. Res. 5, 165—185.

Lin, Q., Liu, E., Zhang, E., Li, K., Shen, J., 2016. Spatial distribution, contamination and ecological risk assessment of heavy metals in surface sediments of Erhai Lake, a large eutrophic plateau lake in southwest China. Catena 145, 193—203, http://dx.doi.org/10.1016/j.catena.2016.06.003.

Loring, D.H., Rantala, R.T., 1992. Manual for the geochemical analysis of marine sediments and suspended particulate matter. Earth-Sci. Rev. 32, 235—283.

Mažeika, J., Dušauskienė-Duž, R., Radzevičius, R., 2004. Sedimentation in the eastern Baltic Sea: lead-210 dating and trace element data implication. Baltica 17 (2), 79—92.

Müller, G., 1979. Schwermetalle in den sedimenten des Rheins—veranderungen seitt 1971. Umschau 778—783.

Müller, A., 1999. Distribution of heavy metals in recent sediments in the Archipelago Sea of southwestern Finland. Boreal Environ. Res. 4, 319—330.

Palanques, A., Diaz, J.I., Farran, M., 1995. Contamination of heavy metals in the suspended and surface sediment of the Gulf of Cadiz (Spain): the role of sources, currents, pathways and sinks. Oceanol. Acta 18 (4), 469—477.

Pustelnikovas, O., Dembska, G., Szefer, P., Radke, B., Bolałek, J., 2007. Distribution of migration (state) forms of microelements in the sediments of the ports of Klaipėda and Gdańsk. Oceanol. Hydrobiol. St. 36 (4), 129—149, http://dx.doi.org/10.2478/v10009-007-0032-3.

Pustelnikovas, O., 2008. On the Eastern Baltic environment changes: a case study of the Curonian Lagoon area. Geologija 50 (2), 80—87.

Prego, R., Belzunce Segarra, M.J., Helios-Rybicka, E., Barciela, M.C., 1999. Cadmium, manganese, nickel and lead contents in surface sediments of the lower Ulla River and its estuary (northwest Spain). Bol. Inst. Esp. Oceanogr. 15 (1—4), 495—500.

Renner, R.M., Glasby, G.P., Szefer, P., 1998. Endmember analysis of heavy-metal pollution in surficial sediments from the Gulf of Gdańsk and the southern Baltic Sea off Poland. Appl. Geochem. 13, 313—318.

Remeikaitė-Nikienė, N., Lujanienė, G., Garnaga, G., Jokšas, K., Garbaras, A., Skipitytė, R., Barisevičiūtė, R., Šilobritienė, B., Stankevičius, A., 2012. Distribution of trace elements and radionuclides in the Curonian Lagoon and the Baltic Sea. In: IEEE/OES Baltic 2012 International Symposium "Ocean: Past, Present and Future. Climate Change Research, Ocean Observations & Advanced Technologies for Regional Sustainability", http://dx.doi.org/10.1109/BALTIC.2012.6249205.

Remeikaitė-Nikienė, N., Lujanienė, G., Malejevas, V., Barisevičiūtė, R., Žilius, M., Garnaga-Budrė, G., Stankevičius, A., 2016. Distribution and sources of organic matter in sediments of the southeastern Baltic Sea. J. Mar. Syst. 157, 75—81, http://dx.doi.org/10.1016/j.jmarsys.2015.12.011.

Remeikaitė-Nikienė, N., Lujanienė, G., Malejevas, V., Barisevičiūtė, R., Zilius, M., Vybernaitė-Lubienė, I., Garnaga-Budrė, G., Stankevičius, A., 2017. Assessing nature and dynamics of POM in transitional environment (the Curonian Lagoon, SE Baltic Sea) using a stable isotope approach. Ecol. Indic. 82, 217—226, http://dx.doi.org/10.1016/j.ecolind.2017.06.035.

Selvaraj, K., Parthiban, G., Chen, C.T.A., Lou, J.-Y., 2010. Anthropogenic effects on sediment quality offshore southwestern Taiwan: assessing the sediment core geochemical record. Cont. Shelf. Res. 30 (10—11), 1200—1210, http://dx.doi.org/10.1016/j.csr.2010.03.010.

The Nemunas River Basin District Management Plan, 2010. Approved by Resolution No. 1098 of the Government of the Republic of Lithuania of 21 July 2010, http://vanduo.gamta.lt/files/Nemunas%20river%20management%20plan.pdf.

Thorsson, M.H., Hedman, J.E., Bradshaw, C., Gunnarsson, J.S., Gilek, M., 2008. Effects of settling organic matter on the bioaccumulation of cadmium and BDE-99 by Baltic Sea benthic invertebrates. Mar. Environ. Res. 65, 264—281.

Trimonis, E., Gulbinskas, S., Kuzavinis, M., 2003. The Curonian Lagoon bottom sediments in the Lithuanian water area. Baltica 16, 13—20.

Turekian, K.K., Wedepohl, K.H., 1961. Distribution of the elements in Some Major Units of the Earth's Crust. Geol. Soc. Am. Bull. 72, 175—192.

Vaalgamaa, S., Conley, D.J., 2008. Detecting environmental change in estuaries: nutrient and heavy metal distributions in sediment cores in estuaries from the Gulf of Finland, Baltic Sea. Estuar. Coast. Shelf Sci. 76 (1), 45—56, http://dx.doi.org/10.1016/j.ecss.2007.06.007.

Vallius, H., 1999. Anthropogenically derived heavy metals in recent sediments of the Gulf of Finland, Baltic Sea. Chemosphere 38 (5), 945—962.

Wang, Y.Q., Yang, L.Y., Kong, L.H., Liu, E.F., Wang, L.F., Zhu, J.R., 2015. Spatial distribution, ecological risk assessment and source identification for heavy metals in surface sediments from Dongping Lake, Shandong, East China. Catena 125, 200—205, http://dx.doi.org/10.1016/j.catena.2014.10.023.

Yurkovskis, A., Poikāne, R., 2008. Biogeochemical, physical and anthropogenic transformations in the Daugava River estuary and plume, and the open Gulf of Riga (Baltic Sea) indicated by major and trace elements. J. Mar. Syst. 70 (1—2), 77—96, http://dx.doi.org/10.1016/j.jmarsys.2007.03.003.

Zalewska, T., Woroń, J., Danowska, B., Suplińska, M., 2015. Temporal changes in Hg, Pb, Cd and Zn environmental concentrations in the southern Baltic Sea sediments dated with ^{210}Pb method. Oceanologia 57 (1), 32—43, http://dx.doi.org/10.1016/j.oceano.2014.06.003.

Oceanologia (2018) 60, 207—218

Available online at www.sciencedirect.com

ScienceDirect

journal homepage: www.journals.elsevier.com/oceanologia/

ORIGINAL RESEARCH ARTICLE

Assessment of wave climate and energy resources in the Baltic Sea nearshore (Lithuanian territorial water)

Darius Jakimavičius *, **Jūratė Kriaučiūnienė, Diana Šarauskienė**

Lithuanian Energy Institute, Kaunas, Lithuania

Received 14 February 2017; accepted 11 October 2017
Available online 3 November 2017

KEYWORDS
Wave climate;
Wave modelling;
Wave power;
Baltic Sea;
MIKE 21 NSW

Summary The main task of the present research was to analyse wave climate and evaluate energy resources in the Lithuanian territorial waters of the Baltic Sea. Wave and wind parameters were analysed according to long-term measurement site data. Distribution of wave parameters in the Baltic Sea Lithuanian nearshore was evaluated according to wave modelling results. Wave energy resources were estimated for three design years (high, median and low wave intensity). The results indicated that in the coastal area of Lithuania, waves approaching from western directions prevail with mean wave height of 0.9 m. These waves are the highest and have the greatest energy potential. The strongest winds and the highest waves are characteristic for the winter and autumn seasons. In the Baltic Sea Lithuanian nearshore, the mean wave height ranges from 0.68 to 0.98 m, while the estimated mean energy flux reaches from 0.69 to 1.90 kW m^{-1} during a year of different wave intensity. Distribution of energy fluxes was analysed at different isobaths in the nearshore. Moving away from the coast, both wave height and wave power flux increases significantly when water depth increases from 5 to 20 m. Values of the mentioned parameters tend to change only slightly when the sea is deeper than 20 m. In a year of median wave intensity, the mean wave energy flux changes from 1.10 kW m^{-1} at 10 m isobaths to 1.38 kW m^{-1} at 30 m isobaths. The identified differences of wave height and energy along the selected isobaths are insignificant.

* Corresponding author at: Laboratory of Hydrology, Lithuanian Energy Institute, Breslaujos st. 3, LT444003 Kaunas, Lithuania. Tel.: +370 37 401801. Fax: +370 37 351271.
E-mail address: darius.jakimavicius@lei.lt (D. Jakimavičius).
Peer review under the responsibility of Institute of Oceanology of the Polish Academy of Sciences.

ELSEVIER Production and hosting by Elsevier

https://doi.org/10.1016/j.oceano.2017.10.004

1. Introduction

Ocean waves are considered as a clean and renewable source of energy with a tremendous worldwide potential for electricity generation. Essentially all of the energy contained in a wave (95%) is located between the water surface and the top one fourth of the wave length. This energy can be extracted in different ways, which has given rise to a large variety of available and deployed technologies (Kempener and Neumann, 2014). However, no single device or generic type has been proven superior to others and it is likely that different types will suit separate deployment zones that can be exploited (O'Hagan et al., 2016).

The highest global net power (excluding areas where $P < 5$ kW m^{-1} and potentially ice covered ones) is computed for regions of Australia and New Zealand — 574 GW, South America (W) — 324 GW and Europe (N and W) — 286 GW (Mørk et al., 2010). Since seasonal variations are generally significantly larger in the northern hemisphere, the southern coasts of South America, Africa and Australia are particularly attractive for wave energy exploitation (Falcao, 2010).

The Baltic Sea, a relatively shallow inland sea of the Atlantic Ocean, also receives increased attention when marine power resources are being discussed. One of the first attempts to evaluate a technical energy resource for the Baltic Sea was made by Swedish scientists (Bernhoff et al., 2006); the potential calculated by them is in the range of 24 TWh. The report of Henfridsson et al. (2007) stated that annual wave energy is equal to approximately 56 TWh for the Baltic Proper. This result should be considered as the gross wave energy potential for the whole Baltic Sea. The annual average energy flux is estimated to 5 kW m^{-1}. Waters et al. (2009) found that the average energy flux off the Swedish Coast is approximately between 2.4 and 5.2 kW m^{-1}.

A study by Latvian experts (Avotiņš et al., 2008) concluded that the wave potential of the Baltic Sea is satisfactory for converting energy. Soomere and Eelsalu (2014) assessed the wave energy potential of the eastern Baltic Sea and concluded that the best location for wave energy converters is in the nearshore at water depths of 15—20 m. On average, the wave energy flux is 1.5 kW m^{-1} and reaches up to 2.55 kW m^{-1} in selected locations of the north eastern Baltic Proper. The wave energy resources are much smaller (normally around 0.6—0.7 kW m^{-1}) in the interior of the Gulf of Finland and in the Gulf of Riga.

Lithuanian experts also acknowledge that the southeastern Baltic Sea provides a great potential and possibilities for electricity production from offshore renewable energy sources (Blažauskas et al., 2015). The wave power flux for annual wave heights in the Baltic nearshore at Klaipėda varies from 1.6 kW m^{-1} in a high intensity year to 0.4 kW m^{-1} in a low intensity year (Kasiulis et al., 2015).

The assessment of global wave energy potential revealed that the majority of energy can be extracted when significant wave height ranges from 1.5 to 5.5 m and when energy (mean) period is between 7 and 14 s (Mørk et al., 2010). Similar results were published in another study (Lenee-Bluhm et al., 2011): the sea states with the greatest contribution to energy have significant wave heights between 2 and 5 m and energy periods between 8 and 12 s.

High waves are rare in the Baltic as the enclosed nature of the basin means that all wave generation must take place within the basin itself and is therefore limited by the fetches of the basin. In the Baltic Sea, the longest fetches are approximately 800 km (Street et al., 2014). All-time highest significant wave height of 8.2 m was recorded in the Baltic Proper in December 2004 (Tuomi et al., 2011). However, according to most reconstructions, the long-term significant wave height in the open part of the Baltic Proper slightly exceeds 1 m (Soomere, 2016).

At the southeastern part of the Baltic Sea, southwest and west were indicated as the most frequent wave approach directions. These directions also correspond with the typical direction of the strongest and prevailing winds at the Lithuanian coast (Kelpšaitė and Dailidienė, 2011). Average annual wave heights near Klaipėda at 6 m depth for the year of different wave intensity are as follows: high intensity — 0.89 m, median intensity — 0.67 m and low intensity — 0.53 m (Kasiulis et al., 2015).

Various models can be applied to simulate wind-generated waves. One of such models is a third-generation wave model SWAN (Simulating Waves Nearshore) (Booij et al., 1999; Ris et al., 1999), developed at the Delft University of Technology. This software for computing random short-crested wind-generated waves in coastal regions and inland waters is widely used for estimation of wave energy potential (Akpınar et al., 2012; Benassai et al., 2013; Iglesias et al., 2009; Iglesias and Carballo, 2009, 2010; Tsoukala et al., 2016). Another widely used model which simulates the development of the sea state in two dimensions is WAM (Hasselmann, 1988). It was also applied in numerous studies (Iglesias et al., 2009; Mazarakis et al., 2012; Staneva et al., 2016) and is often employed in the Baltic Sea wave investigations (Kelpšaite et al., 2011; Soomere and Eelsalu, 2014; Soomere and Raamet, 2011a,b; Street et al., 2014). The model applied in the current study, the Nearshore Spectral Wind-Wave Module of MIKE 21 (MIKE 21, 2012), describes evolution of wind-generated waves in nearshore areas and was successfully used in wave studies as well (Gopaul and O'Brien-Delpesh, 2006; Johnson, 1998; Tsoukala et al., 2016; Vannucchi and Cappietti, 2016).

Analysis of different scientific publications showed that there is no detailed evaluation of wave distribution and energy resources in the Baltic Sea nearshore at the Lithuanian coast. Such evaluation would be useful when selecting the potential location for wave energy converters in the future. Therefore, the main task of this research is the analysis of wave and wind parameters according to long-term observation data, mean wave height and energy flux distribution in the Baltic Sea Lithuanian nearshore according to wave modelling results. Wave energy resources were estimated at different nearshore depths in a year of high, median and low wave intensity.

2. Research object and data

The research object is the Baltic Sea nearshore at the Lithuanian coastline. The Klaipėda Seaport, located at a navigable strait, is the northernmost ice-free port on the eastern coast of the Baltic Sea (Fig. 1). The continental coast of the Lithuanian coastline is located north of the port,

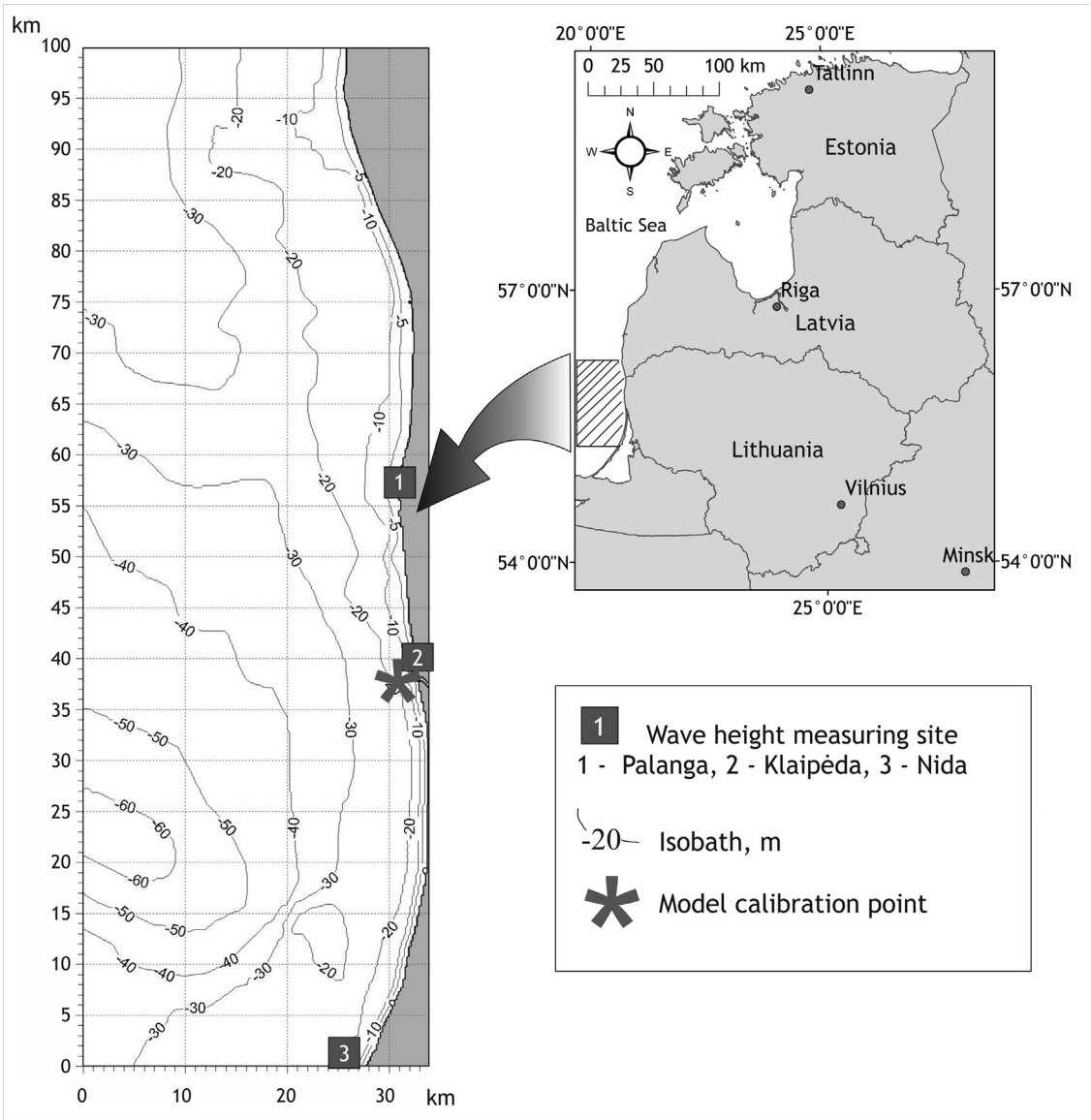

Figure 1 Bathymetry of the Baltic Sea nearshore with marked points of wave height measuring sites.

including the resort cities of Palanga and Šventoji, whereas the rest of the coast belongs to the Curonian Spit national park — a narrow peninsula of large sand dunes and pine forests, included in the UNESCO World Heritage List.

This investigation is concentrated on the wind-generated waves observed in the southeastern part of the Baltic Sea at the Lithuanian coast which can be used for electric energy generation. In order to assess wave energy potential, fluctuations of waves and wind during a long observation period had to be analysed.

In the coastal area of Lithuania, visual wave observations have been executed in three measurement sites (Fig. 1). In the 1950s, visual observations were started in Klaipėda and Nida. The observations in Palanga started in 1993. All of these observations have been continuously carried out until the present day (with some gaps in time). The present investigation is based on the observation data obtained at Klaipėda from 1970, at Nida — from 1972 and at Palanga — from 1993.

Waves are visually observed at a 500—600 m distance from the coast, in the depth of 5—6 m, 2 times a day (in spring and summer at 6:00 and 18:00 UTC + 02:00; in autumn and winter at 6:00 and 12:00 UTC + 02:00). Observations are carried out every day at the same time and in the same place. When carrying out investigations, the observer uses binoculars (with distance increments) and a stopwatch. Visual observations include the estimation of wave direction and height (mean and maximum). Mean wave height values are rounded: values up to 1.5 m height are rounded with an accuracy of 0.25 m; from 1.5 to 4.0 m — with an accuracy of 0.5 m; from 4.0 m — with an accuracy of 1.0 m. The wave period is calculated with an accuracy of 0.1 s. Together with visual wave observations, wind speed and direction are estimated at the selected sites. Wind data from Palanga, Klaipėda and Nida measurement stations (MS) is used in this research.

Wave data for model calibration were obtained from automatic wave measurement station (Fig. 1) for the period from October 2016 to May 2017. The sea depth at the

measurement site is 14.5 m. The place of measurement is 200 m west from the southern pier of Klaipėda Seaport. Hourly wave measurements were made using AWAC sensor. Range of this instrument is from −15 to +15 m, accuracy of wave height estimate <1% of measured value/1 cm, and accuracy of wave direction is 2°/0.1°.

3. Methods

The assessment of wave energy resources requires knowledge of wave climate in the researched water territory. Since the research object is wind-generated waves, a relation between wind and wave parameters was identified by applying statistical methods. The modelling of wave propagation in nearshore using Nearshore Spectral Wind-Wave Module of MIKE 21 is possible only in case a close relation between the mentioned parameters exists. Correlation and statistical analysis was applied to analyse wave and wind parameters and estimate their interdependence. Ranges of minimum, maximum, average and 25th and 75th percentiles of the analysed parameters were estimated. Wind and wave roses were created for the analysis of wind and wave parameter variation in the Baltic nearshore at the Lithuanian coast.

In the assessment of wave energy resources along the Lithuanian coast of the Baltic Sea, energy flux was estimated as follows (Saulnier et al., 2011):

$$P = 0.484 \times H^2 \times T, \quad (1)$$

where P – energy flux, W m^{-1}, H – wave height for each given point for the certain time period as a whole using the mean wave height averaged through this time period, m, T – wave period, s.

In order to assess wave energy resources, it is necessary to model wave parameters in the entire investigated area. Wave propagation modelling was performed using the 2D modelling system MIKE 21 created by the Danish Hydraulic Institute. The Nearshore Spectral Wind-Wave Module (NSW) of this system was applied for the modelling of wind-generated wave propagation parameters in the Lithuanian nearshore of the Baltic Sea. The initial data required for the NSW model (MIKE 21, 2012) includes: (1) depth of the water body (bathymetry); (2) wind speed and direction; (3) boundary conditions in the deepest part of the water area (significant wave height, mean period and direction of the wave, directional spreading index). The NSW model results in each model grid include significant wave height and period, direction of wave propagation and its standard deviation.

A 100 km long and 34 km wide sea territory was selected for the modelling (Fig. 1). A rectangular bathymetric grid of 100 m was chosen. Boundary conditions were described in the cross-section which coincided with the Y axis (in the deepest part of the water territory). Wave refraction and bed roughness that lead to dissipation of wave energy were estimated during modelling.

Wave parameters (significant wave height and period for wind of a certain speed and direction) which are required for the description of model boundary conditions in the deepest cross-section of water territory were estimated from ERA-Interim database (http://www.ecmwf.int/) in the depth of 50 m (N 55°43′55″E 21°4′20″). Hourly data set from the automatic wave measurement station (Fig. 1) and hourly wind parameters from Klaipeda MS of the period from October 2016 to May 2017 were used for model calibration. Hourly parameters of waves (significant wave height and period) induced by strong winds (≥10 m s^{-1}) of NW, W and SW directions were used for the calibration procedure. Directions of such waves and winds are usually similar or differ by no more than 20°. The analysis of wind speed and wave height for selected directions of winds showed (Fig. 2) that the measured wave heights for a specific wind speed could differ significantly (for example, if a west wind blows at a 10 m s^{-1} speed, the measured wave height can vary in the range of 1–3.3 m). Therefore, linear dependences for measured wind speed and wave height were described for the selected wind directions (Fig. 2a–c). There is a tendency that the largest waves form when the winds blow from SW and W directions. Similar tendencies were found in the analysis of the relationship between wind speed and wave period (Fig. 2d–f).

The MIKE 21 NSW model was calibrated comparing the trends of measured values of wave height and period with the modelled ones when strong winds with speeds of 10, 15 and 20 m s^{-1} are blowing from NW, W and SW directions (large circles in Fig. 2). The difference between calculated and measured wave parameters at the automatic station (Fig. 1) is small (Fig. 2), indicating a correct estimation of model boundary conditions (wave height and period).

Wave energy resources were analysed for a separate design year that starts in March of a given year and ends in February of the following year. The design years of high, median and low wave intensity were assigned according to probability distribution (of the data series of 1960–2011) for a year of 5, 50 and 95% probability. The probability of each year (from the data series of 1960–2011) was calculated according to the following equation (Weibull, 1939):

$$P = \frac{m}{n+1} \times 100\% \quad (2)$$

where P – probability, %; m – rank number, n – number of ranked years.

For further analysis, data of wave heights at Klaipėda of 1973–1974, 1994–1995 and 1976–1977 design years (which correspond to high (5%), median (50%) and low (95%) wave intensity years) was used. The mean wave heights of the selected design years are 0.90, 0.67 and 0.53 m respectively. Waves were observed in a depth of 5–6 m.

4. Results

4.1. Analysis of wave and wind parameters according to long-term observation data

Knowledge of wind regime is essential for investigations of wind-generated sea waves. The wind rose of the Baltic Sea Lithuanian nearshore (Fig. 3a) was created using the average daily data from Nida, Klaipėda and Palanga MS for the period of 1993–2011. The wind rose indicates that the westerly direction (SW, W and NW) winds prevail (46.7% of all cases), whereas winds blowing from the south and north are fairly rare. In 75.6% of all observed cases, irrespective of the direction, the winds were weak and did not exceed 6 m s^{-1}. However, when stronger winds were analysed, a tendency of westerly winds was revealed. Winds stronger than 20 m s^{-1} typically do not blow from E, SE and NE.

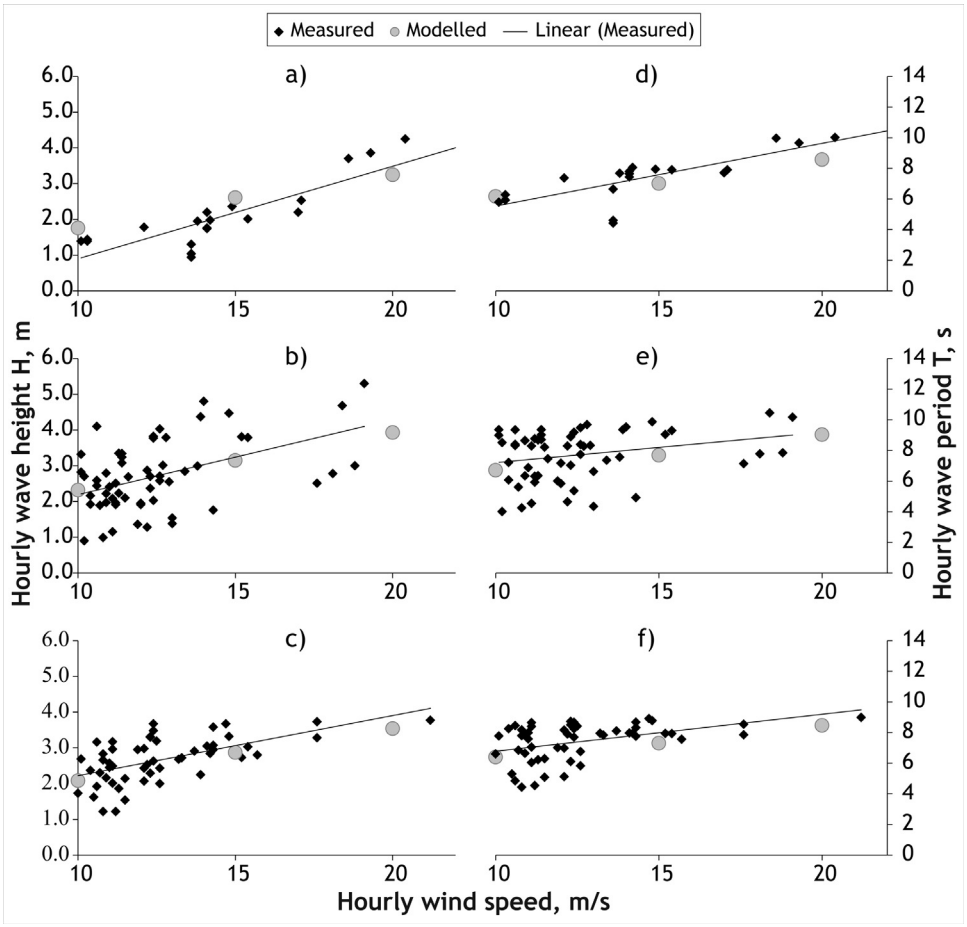

Figure 2 Relationships between wind speed and wave height for NW (a), W (b) and SW (c) wind directions and between wind speed and wave period for NW (d), W (e) and SW (f) wind directions.

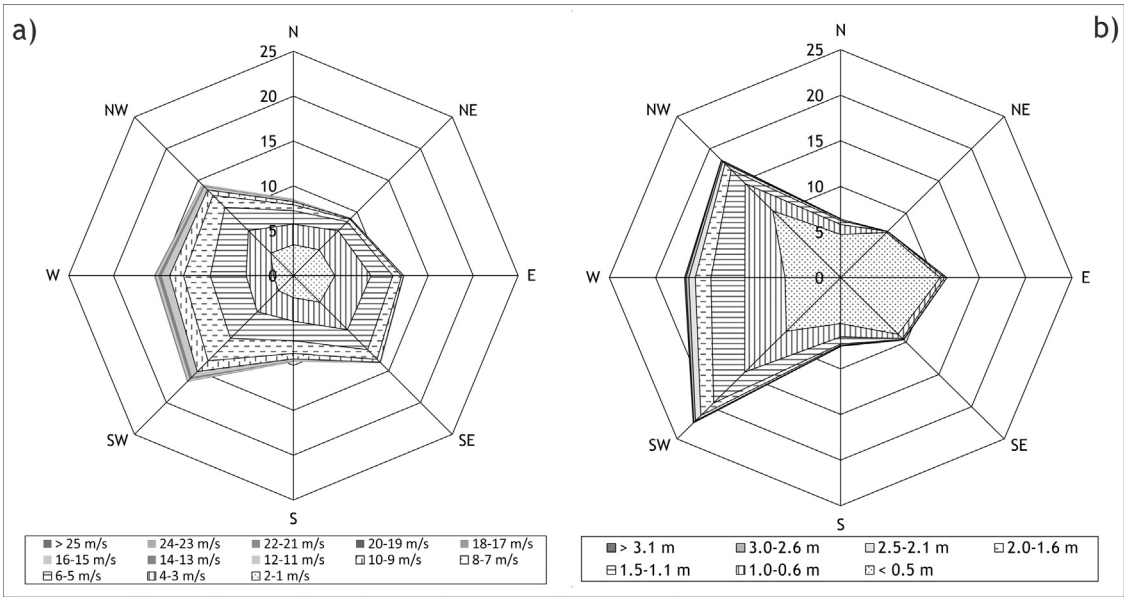

Figure 3 Wind (a) and wave (b) rose in the Baltic Sea Lithuanian nearshore (according to average daily data of Nida, Klaipėda and Palanga).

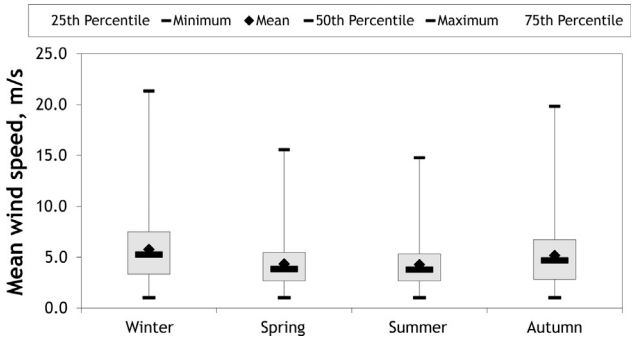

Figure 4 Mean wind speed in different seasons in the Baltic Sea Lithuanian nearshore (according to the averaged daily data of Nida, Klaipėda and Palanga MS).

The daily wind data from Nida, Klaipėda and Palanga MS was used to analyse wind speed in different seasons (Fig. 4). As shown in Fig. 4, the strongest winds are characteristic for the winter and autumn seasons. The greatest values can reach 21 m s^{-1} in winter and 20 m s^{-1} in autumn. Despite the wide range of speed extremes, the average wind speed values differ only slightly. Wind speed values of 25–75% percentile vary from 3.3 to 7.5 m s^{-1} in winter, from 2.8 to 6.7 m s^{-1} in autumn, from 2.7 to 5.4 m s^{-1} in spring and from 2.7 to 5.3 m s^{-1} in summer.

The wave rose (created according to daily wave data from Palanga, Klaipėda and Nida in 1993–2011) (Fig. 3b) shows that waves of westerly directions (SW, W, NW) are the most common (57.7% of all cases), while waves approaching from N and S directions (parallel to the shoreline) are the least frequent (28.3% of all cases). Although 12% of waves are coming from the east, the height of these waves is small (up to 0.5 m). The highest waves are of westerly directions: 7.5% of them are higher than 1 m.

This research concentrates on the analysis of wind-generated waves, therefore the correlation between mean wave height and wind speed had to be defined. Fig. 5 illustrates the variation of annual mean wave height and wind speed near Klaipėda. The variation patterns of both curves are very similar; correlation is equal to 0.84.

There is a close relation between daily data of wave height and wind speed in the investigated areas. Wave data was grouped into 8 classes according to wave directions. Then, the correlation coefficients between the wave heights of a particular direction and the wind speed were calculated. The strongest relation between these two variables was identified near Klaipėda (Table 1). Irrespective of the measurement station, the best correlation was found between the wind speed and heights of waves of western direction.

Table 1 Correlation coefficients between wave heights and wind speeds (according to daily data of 1993–2011).

Station	Wave direction							
	N	NE	E	SE	S	SW	W	NW
Nida	0.85	0.19	0.05	0.16	0.73	0.87	0.86	0.86
Klaipėda	0.75	0.58	0.69	0.75	0.82	0.86	0.87	0.80
Palanga	0.69	0.37	0.19	0.43	0.64	0.80	0.84	0.81

The seasonal and monthly regimes of mean wave height were studied in order to assess the wave energy potential, i.e. whether mean wave heights are sufficient to be successfully exploited. Scientific literature states that the minimum wave height for energy generation is 0.5 m (EPRI, 2011). The available wave observation data shows that mean wave heights are not always sufficiently high (Fig. 6). The waves along the Lithuanian coast were the highest from October to February. During these months, the average wave values exceeded 0.7 m in all MS. In March and June–September, the mean monthly wave height was close to 0.6 m, while in April and May it was close to 0.5 m.

Wave direction is another parameter important for the installation of wave energy converters. As it is presented in Fig. 7(a–c), waves approaching from western directions are the most dominant in all stations and during all seasons. During an average year, waves of these directions comprise from 54.8% (at Klaipėda) to 59.5% (at Palanga). They mostly prevail in summer (67.3%) and are sparse in autumn (53.2%). Waves of eastern direction occur twice less frequently than waves of western directions. Northern and southern waves are the most uncommon.

Durations of waves of a particular direction and height are essential for the assessment of wave energy potential as well. Fig. 8 shows only waves that are higher than 0.5 m. Waves of western directions emerge as the most intense and frequent

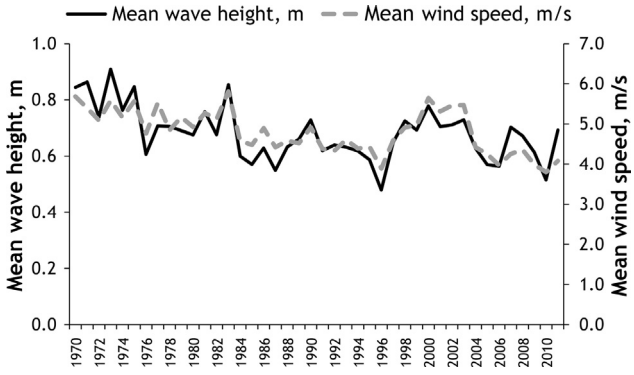

Figure 5 Variation of annual mean wave height and mean wind speed near Klaipėda.

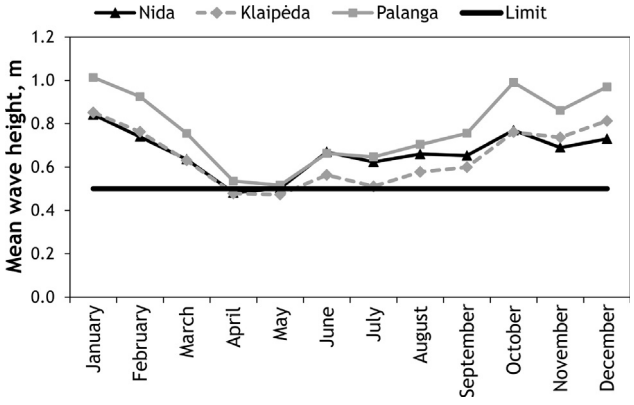

Figure 6 Mean monthly wave heights in the Baltic Sea Lithuanian nearshore (according to the data of 1993–2011).

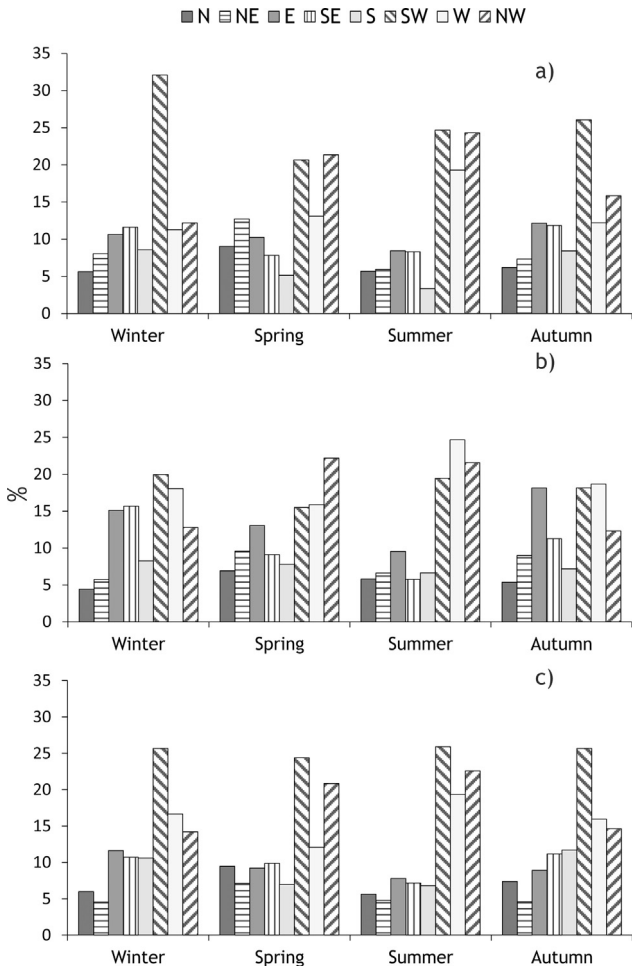

Figure 7 Seasonal variation of different wave directions (a — at Nida, b — at Klaipėda, c — at Palanga).

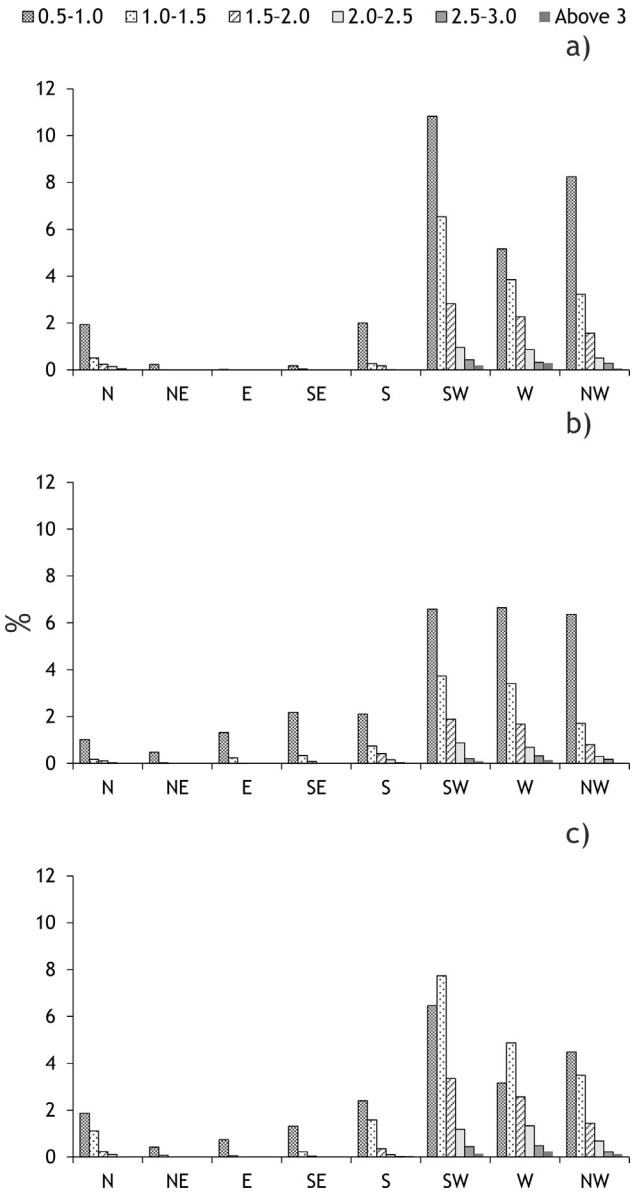

Figure 8 Wave durations (%) in the studied period, according to mean wave height and direction (a — at Nida, b — at Klaipėda, c — at Palanga).

along the Lithuanian cost. In all MS, higher than 3.0 m waves of these directions are observed in 0.5% of cases, while waves in the range of 2.0—3.0 m height occur in 3.4% of cases. Generally, lower than 2.0 m waves approaching from western directions are dominant in the Lithuanian nearshore. The amount of waves approaching from other directions is significantly lower. Daily wave height data of 1993—2011 at Nida, Klaipėda and Palanga was summarised using box diagrams (Fig. 9). Since waves of eastern directions appeared to have small heights and short durations, they were excluded from this analysis. The highest waves usually have SW and W directions. The mean height of waves reaches 1.0 m for waves of W direction, 0.9 m for waves of SW direction and 0.7 m for waves of NW direction. These heights are sufficient for energy generation.

The analysis based on long-term measurement data from three MS revealed the existence of a strong relationship between wind speed and wave height in the coastal area of Lithuania. As the available information of wave parameters from only three sites is not sufficient for a more detailed assessment of wave energy resources, a deeper investigation of propagation of waves in the entire water territory was performed using the MIKE 21 NSW model.

4.2. Mean wave height distribution in the Baltic Sea nearshore at Lithuanian coast

In order to model wave propagation in Lithuanian territorial waters, daily wind data (speed and direction) of selected three design years (corresponding to years of high, median and low wave intensity) were used. As it was determined in previous analysis (described in Section 4.1), small, energetically unusable waves (<0.5 m) are formed as a result of winds blowing from NE, E and SE. Therefore, wave propagation modelling was carried out only for the rest of wind directions and for 5, 10, 15 and 20 m s^{-1} wind speeds. Modelling results and a linear extrapolation method allowed to estimate wave parameters when wind speed changes at a 1 m s^{-1} interval from 1 to 20 m s^{-1}. Mean wave heights and periods in each modelled grid for each design year were

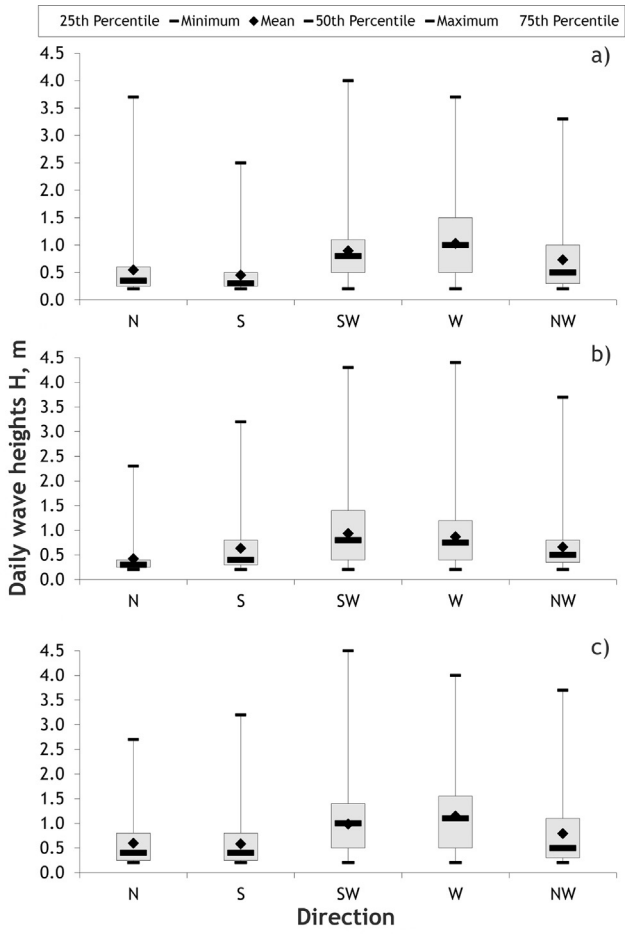

Figure 9 Variation of daily wave heights in the Baltic Sea Lithuanian nearshore (a — at Nida, b — at Klaipėda, c — at Palanga).

calculated using daily wind parameters of the selected year. The estimated wave parameters were used in the assessment of wave energy resources in the Baltic Sea Lithuanian nearshore.

During the analysis of wave propagation modelling results, it was found that wave parameters depend on water depth. Mean wave heights in the nearshore at 10 and 30 m isobaths when winds of 15 m s^{-1} are blowing from different directions are presented in Fig. 10.

To compare wave propagation in a year of high, median and low wave intensity, distribution of wave heights and periods was calculated at 10, 20 and 30 m isobaths in the selected design year (Fig. 11). The lowest waves are characteristic for low wave intensity year (Fig. 11a). In general, mean wave height in the investigated water area reaches 0.68 m and varies from 0.65 m at a 10 m isobath to 0.73 m at a 30 m isobath. In a year of high wave intensity (Fig. 11c), the mean wave height is 0.98 m, while it is equal to 0.94 m at a 10 m isobath and exceeds 1 m at 20 and 30 m isobaths along the coastline (1.03 and 1.05 m respectively). The performed modelling confirmed that regardless of the design year, the mean wave height increases more significantly when the water depth changes from 5 to 20 m, although this increase becomes much less significant if the depth grows. Wave height differences along a particular isobath are not so distinctly expressed: for example, in a year of median wave intensity, the wave height ranges between 0.76—0.82 m at a 10 m isobath and 0.88—0.90 m at a 30 m isobath.

In the assessment of wave energy potential, mean wave height seasonality is also of great importance. A year of median wave intensity was chosen to study this phenomenon in the Baltic Sea Lithuanian nearshore (Fig. 12). It was found that in the investigated area, the greatest waves prevailed in autumn and winter, while the smallest waves dominated in spring and summer.

4.3. Mean wave energy flux distribution in the Baltic Sea nearshore at Lithuanian coast

The mean wave energy flux characteristic (kW m^{-1}) which depends on mean wave height and period was used to assess the wave power potential in the Baltic Sea Lithuanian nearshore. A strong relation between wave parameters and energy flux is observed: the mean power flow increases together with the mean wave height.

Distribution of energy fluxes in the nearshore at different isobaths in a year of different wave intensity is presented in Fig. 13. In a year of high wave intensity, the mean wave energy flux was 1.75 kW m^{-1} at a 10 m isobath, 2.07 kW m^{-1} at a 20 m isobath and 2.16 kW m^{-1} at a 30 m isobath

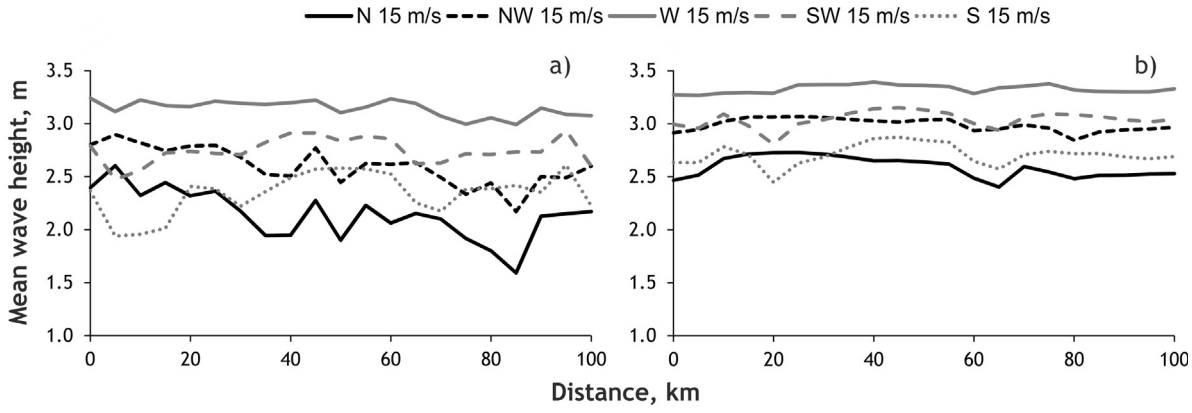

Figure 10 Mean wave heights in the Baltic Sea Lithuanian nearshore, when winds of 15 m s^{-1} of different directions are blowing: at a 10 m isobath (a), at a 30 m isobaths (b).

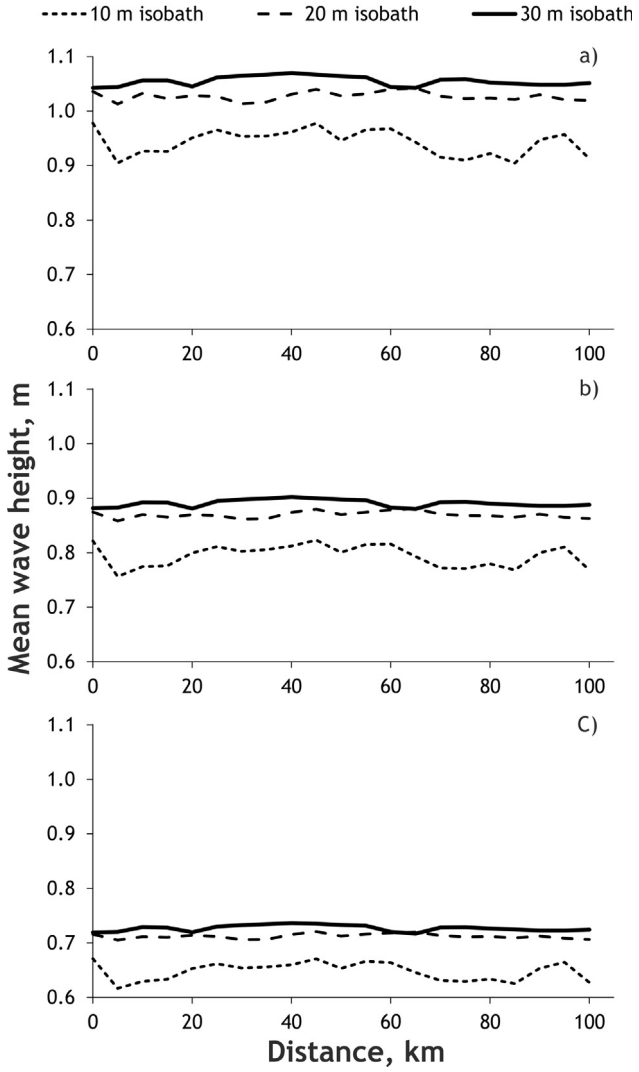

Figure 11 Distribution of mean wave heights at 10, 20 and 30 m isobaths in the Baltic Sea Lithuanian nearshore in a year of high (a), median (b) and low (c) wave intensity.

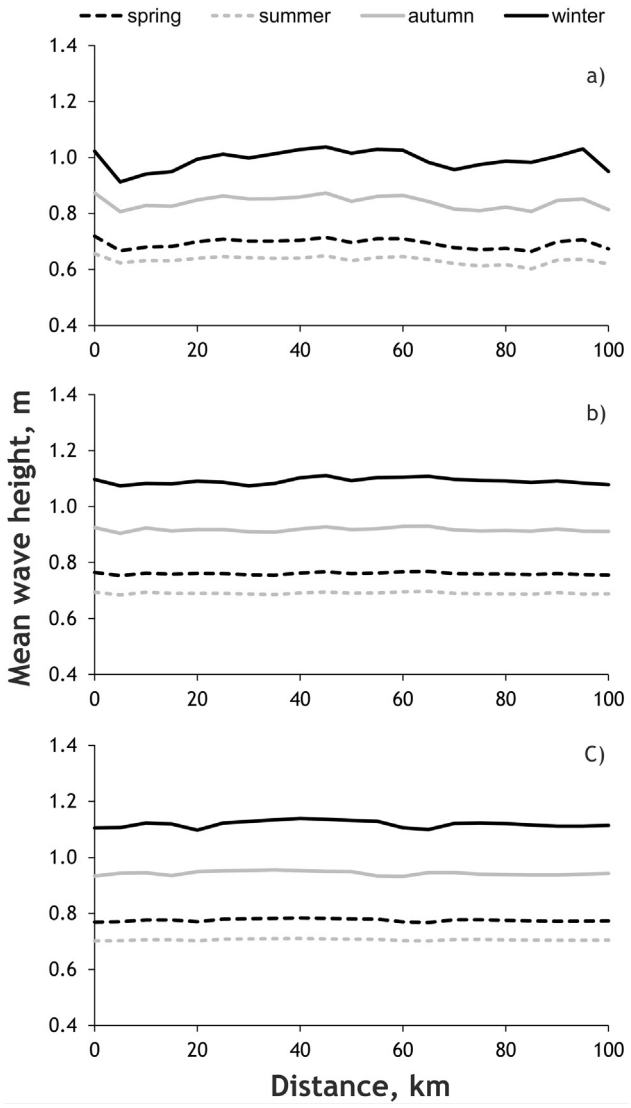

Figure 12 Seasonal distribution of mean wave height in the Baltic Sea Lithuanian nearshore in a year of median wave intensity (1994–1995): at 10 m (a), 20 m (b) and 30 m (c) isobaths.

(Fig. 13a). In a year of median wave intensity, the energy flux at the mentioned isobaths was 1.10, 1.32 and 1.38 kW m^{-1} (Fig. 13b) respectively. In a year of low wave intensity, the energy flux at the mentioned isobaths was 0.64, 0.77 and 0.80 kW m^{-1} (Fig. 13c) respectively. The mean wave energy flux of the entire investigated water territory varied from 0.69 to 1.90 kW m^{-1} in years of different wave intensity. The analysis of wave energy flux along the coastline revealed greater differences at 5 and 10 m isobaths (where deviation from the mean value comprised ±12 and ±8% respectively) than at 20 and 30 m isobaths (where these differences were insignificant, i.e. ±3%).

In the Baltic Sea nearshore, the seasonal distribution patterns of mean wave energy flux and wave height are very similar. The highest energy potential is observed during the autumn and winter seasons, while the lowest potential is observed in spring and summer (Fig. 14). For example, in winter of a year of median wave intensity at a 20 m isobath, the mean wave energy flux was 2.49, in autumn – 1.47, in spring – 0.96 and in summer – 0.96 kW m^{-1} (Fig. 14b). Similar tendencies of the seasonal distribution were identified at 10 and 30 m isobaths as well.

5. Discussion and conclusion

Wind-generated wave energy production in the Baltic Sea is only taking its first steps: most of researchers are still concentrated on theoretical assessments of the potential (Bernhoff et al., 2006; Blažauskas, 2013; Henfridsson et al., 2007; Kasiulis et al., 2015; Soomere and Eelsalu, 2014). The findings of the present study enhance our understanding of wave climate in the Lithuanian territorial waters of the Baltic Sea and could help selecting appropriate nearshore water territories for effective harvesting of sea wave energy. This study was designed to assess the wave climate and energy resources in the Baltic Sea nearshore at the Lithuanian coast.

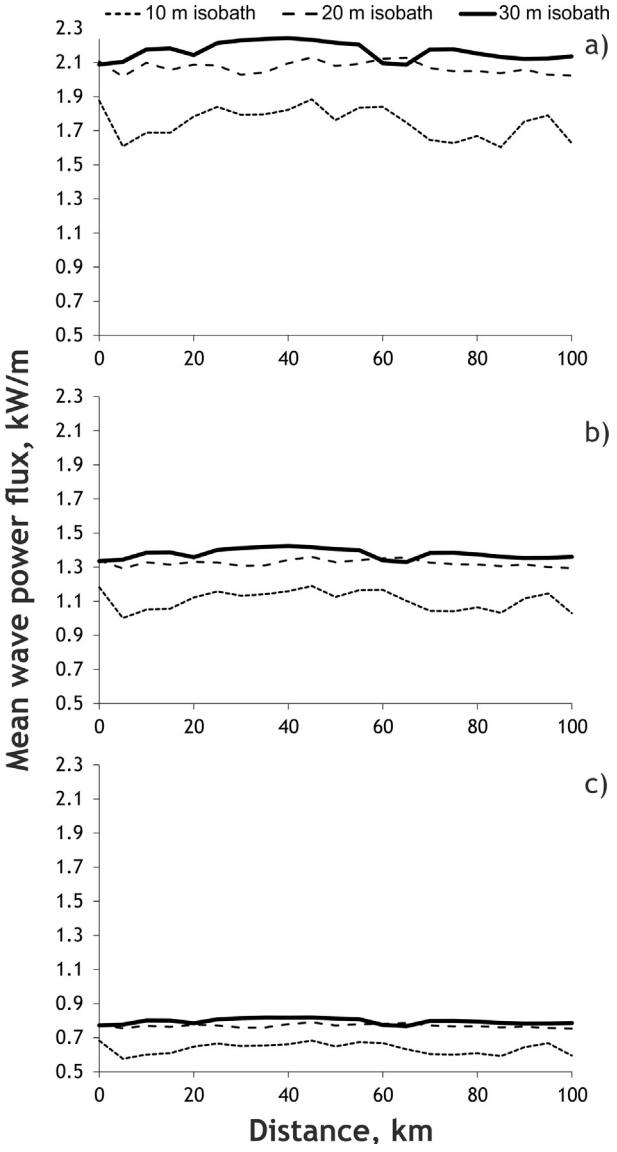

Figure 13 Distribution of mean wave energy flux at 10, 20 and 30 m isobaths in the Baltic Sea Lithuanian nearshore in a year of high (a), median (b) and low (c) wave intensity.

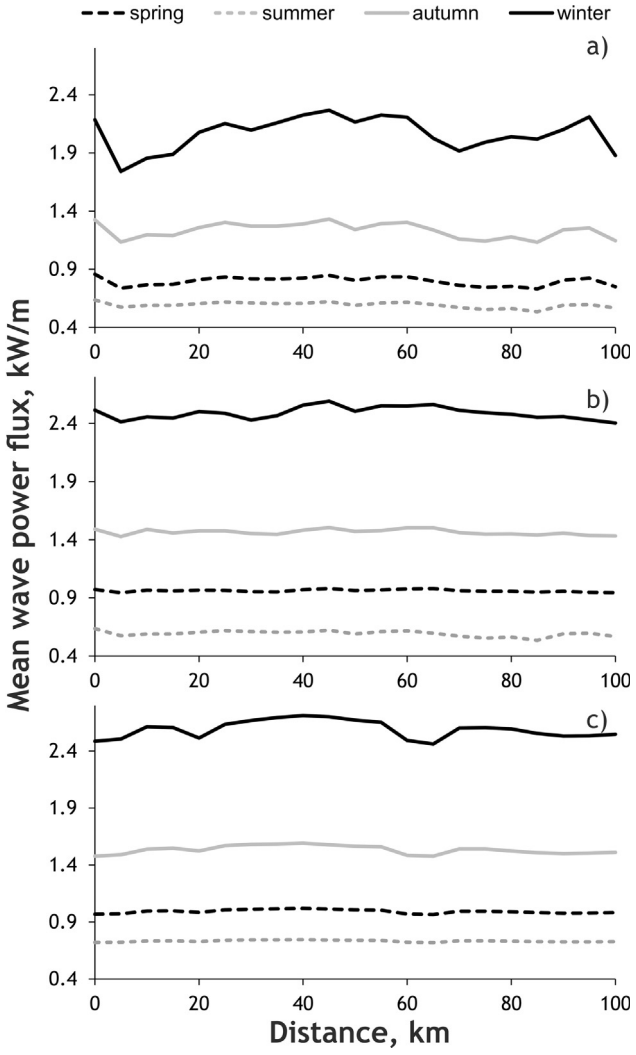

Figure 14 Seasonal distribution of mean wave energy flux in the Baltic Sea Lithuanian nearshore in a year of median wave intensity (1994–1995): at 10 m (a), 20 m (b) and 30 m (c) isobaths.

It was determined that 57.7% of the waves observed in the Baltic Sea Lithuanian nearshore are of western directions (SW, NW and W), while waves of eastern directions are less dominant (28.3%) and waves of S and N directions are the rarest (comprising 7.6% and 6.4% respectively). The mean waves approaching from western directions have the greatest heights and reach 0.9 m, whereas mean wave heights are 0.6 m for waves approaching from southern direction, 0.5 m for waves from northern direction and 0.3 m for waves from eastern direction. The predominant westerly wind directions which generate the highest waves in the eastern part of the Baltic Sea are underlined in other scientific studies (Bernhoff et al., 2006; Henfridsson et al., 2007; Kelpšaitė and Dailidienė, 2011) as well.

The analysis of observation data revealed a seasonality of wind speed and wave height: the strongest winds and the highest waves are characteristic for winter (5.7 m s^{-1} and 0.85 m) and autumn (5.1 m s^{-1} and 0.76 m), while the weakest winds and the lowest waves are inherent in spring (4.7 m s^{-1} and 0.56 m) and summer (4.7 m s^{-1} and 0.62 m). These results are also in line with those of previous studies (Street et al., 2014).

In the current study, it was determined that in a year of high wave intensity, the mean wave height reaches 0.98 m, while in a year of median wave intensity it reaches 0.83 m. In a year of low wave intensity, the mean wave height is 0.68 m. The greatest wave heights were identified in areas with water depths equal to or greater than 20 m. In a year of different wave intensity, the mean wave height in such depths ranges from 1.04 to 0.72 m, whereas in shallower waters it ranges from 0.93 to 0.63 m.

The present assessment of wave energy resources in the Baltic Sea Lithuanian nearshore indicated that the mean wave energy flux was equal to 1.21 kW m^{-1} in a year of median wave intensity. The value of wave energy flux depends on seasonality in the same way as wave height. In a year of median wave intensity, the largest energy fluxes were estimated in winter (2.38 kW m^{-1}), while smaller ones

were identified in autumn (1.41 kW m^{-1}) The smallest energy fluxes were estimated in spring and summer (0.92 and 0.68 kW m^{-1} respectively). Prior studies of the Baltic Sea wave power potential delivered similar results: about 1.5 kW m^{-1} in the nearshore regions of the eastern Baltic Proper (Soomere and Eelsalu (2014) and from 0.4 kW m^{-1} to 1.6 kW m^{-1} in the Baltic nearshore at Klaipėda (Kasiulis et al., 2015)).

The completed study confirmed that irrespective of the design year, both wave height and wave power flux increase more significantly when water depth increases from 5 to 20 m. Values of the mentioned parameters tend to change only slightly when the sea gets deeper than 20 m. These findings match those identified in other studies, such as the study performed by Soomere and Eelsalu (2014), who stated that the best location for wave energy converters is in the nearshore at water depths of 15–20 m. The identified differences of wave height and energy along the selected isobaths were insignificant.

The results obtained from the modelling of wave propagation according to the created methodology can be used for preliminary assessment of wave energy resources in the selected design year in any place of the Baltic nearshore.

Acknowledgment

The authors are grateful to the Marine Research Department under the Environmental Protection Agency of Lithuania, which so kindly facilitated the wind and wave observation data necessary for this study.

References

Akpınar, A., Van Vledder, G.Ph., Kömürcü, M.I., Özger, M., 2012. Evaluation of the numerical wave model (SWAN) for wave simulation in the Black Sea. Cont. Shelf Res. 50 (51), 80–99, http://dx.doi.org/10.1016/j.csr.2012.09.012.

Avotiņš, A., Greivulis, J., Kalniņš, L., 2008. Wave energy conversion potential of the Baltic Sea. Power Electric. Eng. 23, 213–224.

Benassai, G., Montuori, A., Migliaccio, M., Nunziata, F., 2013. Sea wave modelling with X-band COSMO-SkyMed© SAR-derived wind field forcing and applications in coastal vulnerability assessment. Ocean Sci. 9 (2), 325–341, http://dx.doi.org/10.5194/os-9-325-2013.

Bernhoff, H., Sjöstedt, E., Leijon, M., 2006. Wave energy resources in sheltered sea areas: a case study of the Baltic Sea. Renew. Energ. 31 (13), 2164–2170, http://dx.doi.org/10.1016/j.renene.2005.10.016.

Blažauskas, N., 2013. Potential of wave energy developments for the Baltic Sea Region. A case study. SUBMARINER Report 7/2013, 22 pp.

Blažauskas, N., Grigelis, A., Gelumbauskaitė, L.Ž., Gulbinskas, S., Suzdalev, S., Ferrarin, Ch., 2015. Towards sustainable use of marine resources in the south-eastern Baltic Sea (Lithuania): a review. Baltica 28 (2), 179–188, http://dx.doi.org/10.5200/baltica.2015.28.15.

Booij, N., Ris, R.C., Holthuijsen, L.H., 1999. A third-generation wave model for coastal regions – 1. Model description and validation. J. Geophys. Res. – Oceans 104 (C4), 7649–7666, http://dx.doi.org/10.1029/98JC02622.

EPRI, 2011. Mapping and Assessment of the United States Ocean Wave Energy Resources. Electric Power Research Institute, Palo Alto, CA, USA, 176 pp.

Falcao, A.F.O., 2010. Wave energy utilization: a review of the technologies. Renew. Sust. Energ. Rev. 14 (3), 899–918, http://dx.doi.org/10.1016/j.rser.2009.11.003.

Gopaul, N., O'Brien-Delpesh, C., 2006. The use of a nearshore wave model in identifying shoreline change at station beach, LaBrea, Trinidad. (Proc. 8th International Coastal Symposium). J. Coast. Res. SI39, 1474–1478.

Hasselmann, K., 1988. The WAM model – a 3rd generation ocean wave prediction model. J. Phys. Oceanogr. 18 (12), 1775–1810, http://dx.doi.org/10.1175/1520-0485(1988)0181775:TWMTGO>2.0.CO;2.

Henfridsson, U., Neimane, V., Strand, K., Kapper, R., Bernhoff, H., Danielsson, O., Leijon, M., Sundberg, J., Thorburn, K., Ericsson, E., Bergman, K., 2007. Wave energy potential in the Baltic Sea and the Danish part of the North Sea, with reflections on the Skagerrak. Renew. Energ. 32 (12), 2069–2084, http://dx.doi.org/10.1016/j.renene.2006.10.006.

Iglesias, G., Carballo, R., 2009. Wave energy potential along the Death Coast (Spain). Energy 34 (11), 1963–1975, http://dx.doi.org/10.1016/j.energy.2009.08.004.

Iglesias, G., Carballo, R., 2010. Wave energy resource in the Estaca de Bares area (Spain). Renew. Energ. 35 (7), 1574–1584, http://dx.doi.org/10.1016/j.renene.2009.10.019.

Iglesias, G., Lopez, M., Carballo, R., Castro, A., Fraguela, J.A., Frigaard, P., 2009. Wave energy potential in Galicia (NW Spain). Renew. Energ. 34 (11), 2323–2333, http://dx.doi.org/10.1016/j.renene.2009.03.030.

Johnson, H.K., 1998. On modelling wind-waves in shallow and fetch limited areas using the method of Holthuijsen, Booij and Herbers. J. Coast. Res. 14 (3), 917–932.

Kasiulis, E., Punys, P., Kofoed, J.P., 2015. Assessment of theoretical near-shore wave power potential along the Lithuanian coast of the Baltic Sea. Renew. Sust. Energ. Rev. 41, 134–142, http://dx.doi.org/10.1016/j.rser.2014.08.044.

Kelpšaitė, L., Dailidienė, I., 2011. Influence of wind wave climate change to the coastal processes in the eastern part of the Baltic Proper. (Proc. 11th International Coastal Symposium, Szczecin, Poland). J. Coast. Res., SI 64, 220–224.

Kelpšaite, L., Dailidiene, I., Soomere, T., 2011. Changes in wave dynamics at the south-eastern coast of the Baltic Proper during 1993–2008. Boreal Environ. Res. 16 (Suppl. A), 220–232.

Kempener, R., Neumann, F., 2014. Wave Energy. IRENA Ocean Energy Technology Brief 4, Irena, 28 pp.

Lenee-Bluhm, P., Paasch, R., Özkan-Haller, H.T., 2011. Characterizing the wave energy resource of the US Pacific Northwest. Renew. Energ. 36 (8), 2106–2119, http://dx.doi.org/10.1016/j.renene.2011.01.016.

Mazarakis, N., Kotroni, V., Lagouvardos, K., Bertotti, L., 2012. High-resolution wave model validation over the Greek maritime areas. Nat. Hazard. Earth Syst. 12 (11), 3433–3440, http://dx.doi.org/10.5194/nhess-12-3433-2012.

MIKE 21, 2012. Wave Modelling, Vol. 1. User Guides. MIKE by DHI, 326 pp.

Mørk, G., Barstow, S., Kabuth, A., Pontes, M.T., 2010. Assessing the global wave energy potential. In: Proc. OMAE2010 29th International Conference on Ocean, Offshore Mechanics and Arctic Engineering, June 6–11, 2010, Shanghai, China.

O'Hagan, A.M., Huerta, C., O'Callaghan, J., Greaves, D., 2016. Wave energy in Europe: views on experiences and progress to date. Int. J. Mar. Energ. 14, 180–197, http://dx.doi.org/10.1016/j.ijome.2015.09.001.

Ris, R.C., Booij, N., Holthuijsen, L.H., 1999. A third-generation wave model for coastal regions – 2. Verification. J. Geophys. Res. – Oceans 104 (C4), 7667–7681, http://dx.doi.org/10.1029/1998JC900123.

Saulnier, J.B., Prevosto, M., Maisondieu, C., 2011. Refinements of sea state statistics for marine renewables: a case study from

simultaneous buoy measurements in Portugal. Renew. Energ. 36 (11), 2853—2865, http://dx.doi.org/10.1016/j.renene.2011.04.015.

Soomere, T., 2016. Extremes and decadal variations in the Baltic Sea wave conditions. In: Pelinovsky, E., Kharif, C. (Eds.), Extreme Ocean Waves. Springer, Cham, 107—140.

Soomere, T., Eelsalu, M., 2014. On the wave energy potential along the eastern Baltic Sea coast. Renew. Energ. 71, 221—233, http://dx.doi.org/10.1016/j.renene.2014.05.025.

Soomere, T., Raamet, A., 2011a. Long-term spatial variations in the Baltic Sea wave fields. Ocean Sci. 7 (1), 141—150, http://dx.doi.org/10.5194/os-7-141-2011.

Soomere, T., Raamet, A., 2011b. Spatial patterns of the wave climate in the Baltic Proper and the Gulf of Finland. Oceanologia 53 (Suppl. 1), 335—371, http://dx.doi.org/10.5697/oc.53-1-TI.335.

Staneva, J., Wahle, K., Günther, H., Stane, E., 2016. Coupling of wave and circulation models in coastal-ocean predicting systems: a case study for the German Bight. Ocean Sci. 12 (3), 797—806, http://dx.doi.org/10.5194/os-12-797-2016.

Street, S.I., Hanson, H., Larson, M., Bertotti, L., 2014. Modelling the wave climate in the Baltic Sea. VATTEN — J. Water Manage. Res. 70, 19—29.

Tsoukala, V.K., Chondros, M., Kapelonis, Z.G., Martzikos, N., Lykou, A., Belibassakis, K., Makropoulos, C., 2016. An integrated wave modelling framework for extreme and rare events for climate change in coastal areas — the case of Rethymno, Crete. Oceanologia 58 (2), 71—89, http://dx.doi.org/10.1016/j.oceano.2016.01.002.

Tuomi, L., Kahma, K.K., Pettersson, H., 2011. Wave hindcast statistics in the seasonally ice-covered Baltic Sea. Boreal Environ. Res. 16, 451—472.

Vannucchi, V., Cappietti, L., 2016. Wave energy assessment and performance estimation of state of the art wave energy converters in Italian hotspots. Sustainability 8 (12), 1300, http://dx.doi.org/10.3390/su8121300.

Waters, R., Engstrom, J., Isberg, J., Leijon, M., 2009. Wave climate off the Swedish west coast. Renew. Energ. 34 (6), 1600—1606, http://dx.doi.org/10.1016/j.renene.2008.11.016.

Weibull, W., 1939. A statistical study of the strength of material. Ing. Vetenskaps Akad. Handl. (Stockholm) 151, 45 pp.

Oceanologia (2018) 60, 219—231

Available online at www.sciencedirect.com

ScienceDirect

journal homepage: www.journals.elsevier.com/oceanologia/

ORIGINAL RESEARCH ARTICLE

Microfouling development on artificial substrates deployed in the central Red Sea

Ahmed A. Balqadi, Adnan J. Salama, Sathianeson Satheesh *

King Abdulaziz University, Jeddah, Saudi Arabia

Received 24 April 2017; accepted 27 October 2017
Available online 15 November 2017

KEYWORDS
Biofilm;
Biofouling;
Nutrient cycling;
Diatom;
Larval settlement;
Red Sea

Summary Microfouling is the initial step in the growth of biofouling on hard substrata submerged in marine waters. In this study, microfouling development on nylon nets submerged in the central Red Sea coast of Saudi Arabia was analyzed during the winter and summer seasons for a period of 5 days each. The results showed a well-established biofilm community on nylon nets submerged for 24 h, with bacteria and diatoms being the primary colonizers. Protein was the major organic component of the biofilm that developed on the nylon nets during the winter and summer seasons. *Navicula* spp., *Nitzschia* spp., *Cylindrotheca* spp., and *Pluerosigma* spp. were the dominant diatom species settled on the nylon nets. *Pseudoalteromonas shioyasakiensis*, *Planomicrobium* sp., *Vibrio harveyi* and *Pseudoalteromonas rubra* were the dominant bacteria isolated from the nylon nets. While the abundance of bacteria showed a positive correlation with the nutrient concentration of the biofilm during both winter and summer seasons, diatom density exhibited a significant positive relationship with the biofilm nutrients during the winter season only. The results also revealed significant seasonal variations in the abundance of microfouling organisms and accumulation of nutrients on nylon nets.

* Corresponding author at: Department of Marine Biology, Faculty of Marine Sciences, King Abdulaziz University, Jeddah 21589, Saudi Arabia.
E-mail addresses: ssathianeson@kau.edu.sa, satheesh_s2005@yahoo.co.in (S. Satheesh).
Peer review under the responsibility of Institute of Oceanology of the Polish Academy of Sciences.

Production and hosting by Elsevier

1. Introduction

Microfouling development (also known as 'Biofilms) will occur within a few hours after the submersion of an artificial substratum in the sea (Dobretsov, 2009; Huggett et al., 2009; Satheesh and Wesley, 2010; Siboni et al., 2007; Wang et al., 2012). After the initial biofilm formation, the larval forms of marine organisms and macroalgal spores will settle on such surfaces (see reviews: Salta et al., 2013; Satheesh et al., 2016). Biofilm development is a process that generally

https://doi.org/10.1016/j.oceano.2017.10.006

consists of the formation of a conditioning film and the settlement of microorganisms and phytoplankton communities (Bhosle et al., 2005; Wahl, 1989). The conditioning film is composed mainly of dissolved organic materials from the surrounding medium, such as proteins and carbohydrates (Bhosle et al., 2005). Conditioning films may alter the surface properties that enable the attachment of microorganisms, primarily bacteria (Bhosle et al., 2005). After settlement, bacterial communities produce extracellular polymeric substances, which embed the cells in the biofilm and act as a glue for the firm attachment on surfaces (Stoodley et al., 2002). Photosynthetic organisms, particularly diatoms, are the secondary colonizers on surfaces in the sea (Anil et al., 2006) and considered the earliest photoautotrophs, along with cyanobacteria, to input energy in the biofilms (Nagarkar et al., 2004; Roeselers et al., 2008; Rossi and De Philippis, 2015).

Biofilm development on hard substrata in the sea, including natural surfaces, has substantial ecological significance (Sawall et al., 2012). For instance, these biofilms are important for the recruitment of benthic organisms by providing conditioned surfaces for larval settlement and metamorphosis (Dobretsov, 2009; Patil and Anil, 2005; Sneed et al., 2014; Wang et al., 2012; Whalan and Webster, 2014; Wieczorek and Todd, 1998). Biofilms are also considered to be the main source of primary production in coastal ecosystems (Thompson et al., 2004) and provide many ecosystem services, such as nutrient recycling and degradation of pollutants (Decho, 2000; Passarelli et al., 2015). Biofilm development on hard substrata may show temporal and spatial variation (Jenkins and Martins, 2010) due to changes in physical, chemical and biotic factors of the aquatic environment (Donlan, 2002; Guo et al., 2017; McElroy et al., 2016). Nutrient availability is one of the major controlling factors for the development of biofilms on hard substrata (see review: Costerton et al., 1995).

Due to their sensitivity to environmental conditions, biofilms are considered indicators for assessing the health of the environment (Baragi and Anil, 2016; Passarelli et al., 2015). As biofilm structure responds to changes in environmental conditions, it may also affect the settlement of marine invertebrate larvae (Hung et al., 2005). Many previous studies have reported on the community structure, temporal variation of conditioning film and microfouling assemblage development on different substrata submerged in marine waters (Bhosle et al., 2005; Dang and Lovell, 2000; Mitbavkar and Anil, 2008; Rampadarath et al., 2017; Satheesh and Wesley, 2010; Siboni et al., 2007; Watson et al., 2015; Wesley and Satheesh, 2009). Studies on spatial and temporal changes in biofilm community structure will improve our knowledge of biofilm community ecology in marine waters. Further, few studies in the literature relate to biofilm development on artificial substrata submerged in the Red Sea (Abdul Azis et al., 2001; Saeed et al., 2000; Zhang et al., 2014). These previous studies were mainly focused on desalination plant water intake systems. Hence, in this study, microfouling development and the seasonal changes of the biofilm community structure were assessed in the central Red Sea by submerging nylon nets. Nylon nets were selected as artificial substrates due to their wide applications in cage aquaculture. The following questions were addressed in this study: (1) How long will it take for a biofilm community to develop on artificial substratum deployed in central Red Sea coastal waters? (2) Does the biofilm community structure show any seasonal variations? (3) Do the nutrients adsorbed on the substratum have any effect on microfouling organisms, such as bacteria and diatoms? (4) Does diatom settlement on artificial substratum show temporal succession with submersion duration?

2. Material and methods

2.1. Preparation and submersion of nylon nets

Test substrata (15 cm × 15 cm) were prepared using PVC frames and nylon nets used for cage farming (black colour). Nets were submerged at a depth of 2 m at Obhur Creek (near King Abdulaziz University marine station) of the central Red Sea (north of Jeddah) region of Saudi Arabia (N21°42.562′ E039°05.764′). The PVC frames were submerged in seawater during the winter (March 2016) and summer (August 2016) seasons. The nets were washed in distilled water, dried and rinsed with 70% alcohol before submersion in the seawater (Rao, 2003; Satheesh and Wesley, 2010). Nylon nets (in replicate, $n = 5$) were retrieved from the sea after 1, 2, 3, 4 and 5 days of submersion. The nets were rinsed with filtered (Millipore, 47 μm) and sterilized (autoclaved) seawater immediately after retrieval from the sea and placed in conical flasks containing 50 ml of filtered and sterilized seawater. The conical flasks were stored in a coolbox and transported to the laboratory. In the laboratory, the biofilm that developed on the nets was removed by two methods. In the first method, the biofilm was removed using a sterile nylon brush (Wesley and Satheesh, 2009) and the scrapped biofilm assemblage was dispersed into the sterile seawater stored in the conical flask. In the second method, the nets were stored in a conical flask with a known volume of filtered seawater and the flasks were agitated by placing them in a shaker for 1 h at 300 rpm to disperse the microfouling assemblage developed on the nets. After that, the nylon nets were removed from the conical flask and the microfouling assemblage dispersed seawater was collected. The biofilm samples removed from the nylon nets using these two methods were then combined for further analysis. This microfouling assemblage dispersed water was divided into two parts; one part was used for the analysis of bacteria and diatoms and the other part was used for the analysis of nutrients.

2.2. Analysis of biofilm nutrients

The nutrient content (nitrate, nitrite, phosphate, carbohydrate and protein) analysis was carried out to analyze the temporal variability of biofilm nutrients. For an estimation of nutrients, the methods described by Wesley and Satheesh (2009) were followed. In brief, the microfouling sample dispersed seawater was filtered through a membrane filter (0.47 μm) before nutrient analysis. Total carbohydrate was determined by the phenol-sulphuric acid method (DuBois et al., 1956) using glucose as a standard. The protein content of the biofilm sample was measured by the Lowry et al. (1951) method using bovine serum albumin as is standard. For the estimation of nitrate, nitrite and phosphate the methods given by Venugopalan and Paulpandian (1989) were used.

2.3. Analysis of diatoms

The diatoms attached to the nylon nets were analyzed under a microscope (LEICA DMI 3000B) and the number of phytoplankton cells (cm^{-2} area of nylon nets) were documented using a haemocytometer. For identification of diatom species, the keys provided by Hasle and Syvertsen (1997) were used. The chlorophyll-*a* (biomass of phototrophs) in microfouling was measured after filtering the known volume of samples through GF/C glass filter (0.47 μm) paper. The filter papers were stored at −20°C before extraction using 90% acetone. The extraction was carried out overnight in a refrigerator and the chlorophyll content was measured using a spectrophotometer as previously described (Venugopalan and Paulpandian, 1989). The O.D was measured at three different wavelengths such as 630 nm, 645 nm, and 665 nm. The chlorophyll-*a* was calculated using the following formula:

$$\text{Chlorophyll-}a = 11.6\,\text{O.D}_{665} - 1.31\,\text{O.D}_{645} - 0.14\,\text{O.D}_{630}.$$

2.4. Isolation and identification of bacteria

Cultivable bacteria settled on the nylon nets were cultured using Zobell marine agar. Approximately 1 ml of dispersed biofilm was diluted (10-fold) using filtered and sterilized seawater and 0.1 ml was spread on Zobell marine agar plates. The Petri dishes were incubated at 28 ± 2°C for 48 h and the total viable colonies were counted. Bacterial colonies were selected based on colony morphology and purified by streaking on marine agar plates. The purified bacterial colonies were used for identification based on 16S rRNA gene sequencing. The bacterial genomic DNA was isolated using the InstaGene™ matrix genomic DNA isolation kit as per the protocol accompanying the kit. The isolated DNA was amplified using 16S rRNA universal primers 27F:AGAGTTTGATCMTGGCTCAG and 1492R: TACGGYTACCTTGTTACGACTT. An MJ Research Peltier Thermal cycler was used for the amplification of the DNA. PCR reactions were conducted under the following PCR conditions: Initial denaturation at 94°C for 2 min and then 35 amplification cycles at 94°C for 35 s, 55°C for 60 s and 72°C for 60 s. Final extension was at 72°C for 10 min. The DNA fragments were amplified for approximately 1400 bp using a positive control (*E. coli* genomic DNA) and a negative control in the PCR. The PCR products were purified using a Montage PCR clean-up kit (Millipore). Purified PCR products were sequenced using ABI PRISM® Big DyeTM terminator cycle sequencing kits with AmpliTaq® DNA polymerase (Applied Biosystems). Single-pass sequencing was performed using 16S rRNA universal primers 785F: GGATTAGATACCCTGGTA and 907R: CCGTCAATTCMTTTRAGTTT. Sequencing reactions were performed on an ABI 3730xl sequencer (Applied Biosystems). The resulting sequences were aligned and analyzed using NCBI blast for the identification of the bacteria. The program MUSCLE 3.7 was used for the alignment of sequences (Edgar, 2004) and the aligned sequences were cured using Gblocks 0.91b. The Tree Dyn 198.3 program was used for the construction of a phylogenetic tree (Dereeper et al., 2008).

2.5. Analysis of environmental parameters

All of the water quality parameters, such as salinity, temperature, pH, dissolved oxygen and the concentration of nutrients such as nitrite, nitrate and phosphate were analyzed at monthly intervals throughout the study using standard methods described elsewhere (Satheesh and Godwin Wesley, 2008) and the mean values for each season were calculated.

2.6. Scanning Electron Microscopic analysis (SEM) of microfouling assemblage development on nylon nets

Nylon nets were prepared as above and submerged in the Creek waters during July 2016 (summer season, experiment was conducted between 10-7-2016 and 15-07-2016) for the microfouling assemblage development. A portion of the nylon nets retrieved from the seawater each day was fixed in 2% glutaraldehyde (which was prepared in phosphate buffered saline) for 2 h. The net samples were then dehydrated through a series of ethanol gradients, starting with 20% and ending with 100% (20, 40, 60, 80 and 100%). The nets were submerged in each percentage of alcohol for approximately 30 min. Then, the nylon nets were dried by placing them on double-sided carbon tape. All samples were sputtered with 15 nm thick gold layers (JEOL JFC-1600 Auto fine coater). Finally, the nylon nets were examined with a Scanning Electron Microscope (FEI, Quanta FEG-450). The microscope was operated at an accelerating voltage of 10 kV.

2.7. Data analysis

The difference in the microfouling assemblage between two seasons (considering the abundance of bacteria and diatoms and the concentration of nutrients) was examined using a two-way ANOVA (analysis of variance), with time (days) and season (winter and summer) as factors. Correlation analysis (correlation coefficient) was also carried out using the abundance data of bacteria (CFU on culture plates) and diatoms against nylon net submersion duration [days] in winter and summer seasons. Additionally, the role of biofilm nutrients on microfouling community settlement was determined by correlation analysis between nutrient concentration in the biofilms and the abundance of microfouling communities (bacteria and diatoms) as variables. The two-way ANOVA and correlation coefficient analysis were carried out using the SPSS program. The relative abundance of dominant diatom species was calculated using the formula $(n/N) \times 100$, where '*n*' indicates the number of individuals of a particular species and '*N*' is the total number of diatoms in the biofilm.

3. Results

3.1. Environmental parameters of the creek waters

Environmental parameters of the creek waters during the study period are presented in Table 1. In general, all the parameters analyzed in this study showed higher values in the summer season except for dissolved oxygen, which was high during winter.

Table 1 Environmental parameters of the Obhur Creek during winter and summer seasons (mean ± SD).

Parameters	Winter	Summer
Temperature [°C]	26.6 ± 0.44	30.2 ± 0.68
Dissolved oxygen [mg L^{-1}]	5.66 ± 0.31	4.92 ± 0.24
pH	8.00 ± 0.10	8.3 ± 0.09
Salinity	40 ± 0.89	41 ± 0.63
Nitrite [μg l^{-1}]	0.0007 ± 0.0003	0.003 ± 0.002
Nitrate [μg l^{-1}]	0.7014 ± 0.0243	1.62 ± 0.35
Phosphate [μg l^{-1}]	0.0072 ± 0.0014	0.012 ± 0.005

3.2. Nutrient concentration of biofilm

In the microfouling assemblage developed on nylon nets, the concentration of nutrients such as nitrate, nitrite, phosphate, carbohydrate and protein showed variation with submersion time during winter and summer (Fig. 1). The nutrient concentration on nylon nets was high during the summer season. Among the nutrients, protein concentration was highest in both winter and summer seasons, followed by carbohydrate concentration (Fig. 1). Two-way ANOVA results showed significant seasonal variation in the concentration of nutrients on nylon nets (Table 2). While nitrate, nitrite and phosphate concentrations showed significant variation in relation to submersion period, protein and carbohydrate concentrations did not show a significant difference between submersion days (Table 2).

3.3. SEM analysis

Scanning electron microscope (SEM) analysis of the nylon nets submerged during the summer season is given in Fig. 2. SEM microphotographs showed progressive growth of microfouling assemblages on nylon nets in each submersion time period. The net panel submerged for 5 days was clogged with a microfouling assemblage. Bacteria and phytoplankton communities were clearly visible in the SEM microphotographs (Fig. 2).

3.4. Bacteria and photosynthetic organisms on nylon nets

The bacterial abundance (CFU on culture plates) showed an increase on nylon nets with submersion time during the winter ($r = 0.765$, $P < 0.001$) and summer seasons ($r = 0.847$, $P < 0.001$) (Fig. 3). The bacterial abundance on nylon nets showed a positive correlation during the winter and summer seasons with all of the nutrients analyzed in this study (Table 3). The two-way ANOVA revealed a significant difference in bacterial colonies on nylon nets in relation to submersion duration and season (Table 2). The 16S rRNA gene sequence results revealed the presence of four dominant bacterial strains (based on the number of colonies in each observation) on nylon nets during the study period (Fig. 4). The identified strains were *Pseudoalteromonas shioyasakiensis* (NCBI GenBank accession number: KY224086), *Planomicrobium* sp. (NCBI GenBank accession number: KY224087), *Vibrio harveyi* (NCBI GenBank accession number: KY266820) and *Pseudoalteromonas rubra* (NCBI GenBank accession number: KY266819).

The concentration of chlorophyll-*a* in the biofilm showed fluctuations with submersion duration and season. In winter, a chlorophyll-*a* content of 0.013 mg cm^{-2} was observed on nylon nets submerged for one day. However, the values declined after 2–4 days of submersion (Fig. 1). The nylon nets observed after 5 days of submersion during the winter season recorded the highest chlorophyll-*a* content, 0.038 mg cm^{-2}. In contrast, during the summer season, the chlorophyll-*a* content of nylon nets submerged for one day was 0.006 mg cm^{-2} and reached 0.015 mg cm^{-2} after 5 days of submersion. In general, the results of this study showed that the biomass of phototrophs in the biofilm developed on nylon nets was high during winter and low in summer (Fig. 1). The two-way ANOVA showed a significant variation in

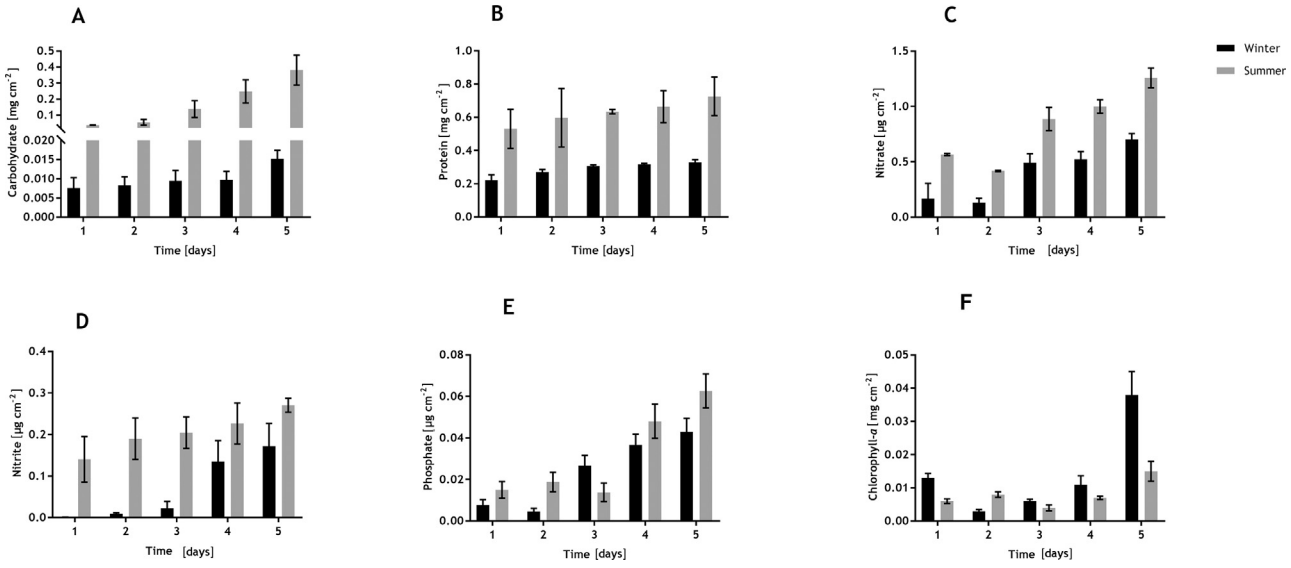

Figure 1 Seasonal changes in the concentration of nutrients and chlorophyll-*a* in the biofilm developed on nylon nets (mean ± SD, $n = 5$). Carbohydrate (a), protein (b), nitrate (c), nitrite (d), phosphate (e), chlorophyll-*a* (f).

Table 2 Two-way ANOVA (analysis of variance) of the abundance of bacteria and diatoms and concentration of nutrients in the biofilm developed on nylon nets. Nylon nets submersion duration (time, 5 days) and season (winter and summer) were considered as factors for ANOVA. Significant = $P < 0.05$. Not significant = $P > 0.05$.

Source of variation	df	Bacteria		Diatoms		Nitrate		Nitrite		Phosphate		Protein		Carbohydrate		Chlorophyll-*a*	
		F	*P*	*F*	*P*	*F*	*P*	*F*	*P*	*F*	*P*	*F*	*P*	*F*	*P*	*F*	*P*
Time [days]	4	34.06	0.000	211.16	0.000	117.19	0.000	11.7	0.000	52.13	0.000	1.74	0.160	2.064	0.104	254.64	0.000
Season	1	100.64	0.000	1054.3	0.000	441.26	0.000	181.01	0.000	12.90	0.001	526.17	0.000	216.95	0.000	155.060	0.000
Time*season	4	31.40	0.000	214.18	0.000	1.95	0.121	3.43	0.017	6.45	0.000	1.38	0.257	2.063	0.104	86.19	0.00

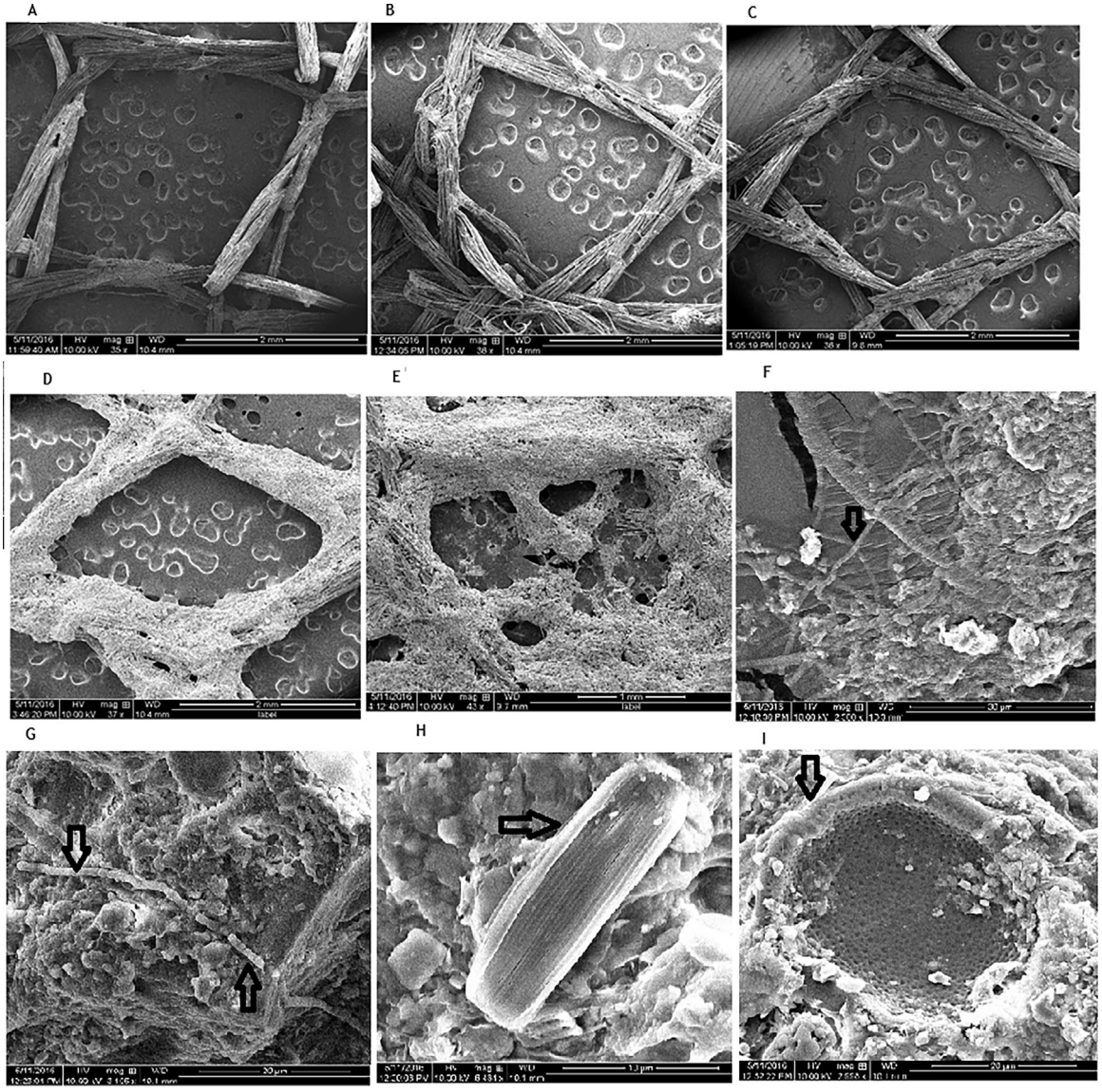

Figure 2 Scanning Electron Microscope photographs of biofilm development on nylon nets submerged in central Red Sea waters. Nylon net submerged for one day (a), nylon nets submerged for 2 days (b), nylon nets submerged for 3 days (c), nylon nets submerged for 4 days (d), nylon net submerged for 5 days (e), nylon net submerged for 24 h (one day) showing the settlement of bacteria (f and g), nylon net submerged for 24 h (one day) showing the settlement of diatoms (h and i).

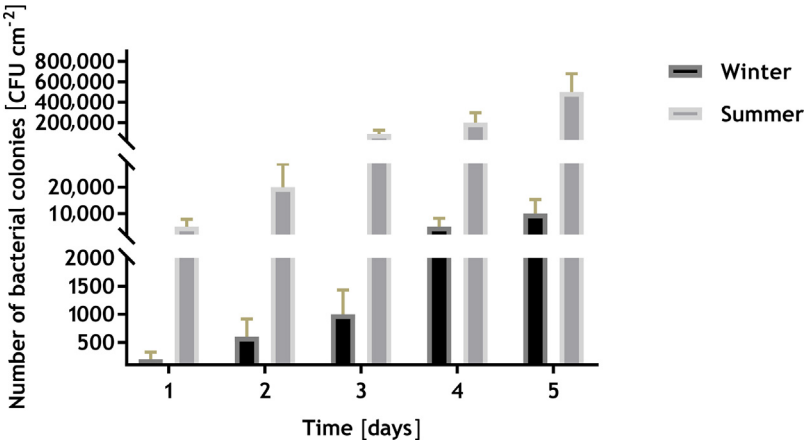

Figure 3 Colonization of bacterial communities on nylon nets submerged for 5 days during the winter and summer seasons in the central Red Sea (mean CFU ± SD, $n = 5$).

Table 3 Correlation between the abundance of microfouling organisms and concentration of nutrients in the biofilm. The abundance of diatoms and bacteria (bolded in the first column of the table) was correlated with the other parameters. $P < 0.05$ = significant, $P > 0.05$ = not significant.

Winter		*P*	Summer		*P*
Parameters	Correlation coefficient (*r*)		Parameters	Correlation coefficient (*r*)	
Total number of diatoms vs			**Total number of diatoms vs**		
Total number of bacteria	0.824	0.000	Total number of bacteria	−0.103	0.623
Nitrite	0.383	0.044	Nitrite	0.152	0.467
Nitrate	0.897	0.005	Nitrate	−0.115	0.492
Phosphate	0.810	0.000	Phosphate	0.083	0.694
Protein	0.685	0.007	Protein	−0.115	0.557
Carbohydrate	0.673	0.000	Carbohydrate	−0.115	0.218
Chlorophyll-*a*	0.704	0.000	Chlorophyll-*a*	0.038	0.066
Total number of bacteria vs			**Total number of bacteria vs**		
Nitrite	0.444	0.026	Nitrite	0.523	0.007
Nitrate	0.819	0.000	Nitrate	0.619	0.000
Phosphate	0.688	0.001	Phosphate	0.829	0.000
Protein	0.532	0.002	Protein	0.619	0.005
Carbohydrate	0.574	0.006	Carbohydrate	0.619	0.007
Chlorophyll-*a*	0.593	0.000	Chlorophyll-*a*	0.935	0.003

chlorophyll-*a* content in biofilm between winter and summer seasons (Table 2).

3.5. Settlement of diatoms on nylon nets

The diatom communities in the biofilm on the nylon nets consist of 13 species submerged during the winter season and 9 species in summer (Fig. 5, Table 4). Season-wise analysis of diatom communities showed the abundance of *Navicula* spp., *Cylindrotheca* spp., *Licmophora* spp. and *Nitzschia* spp. on nylon nets submerged during the winter season (Fig. 5, Table 4). During the summer season, *Nitzschia* spp., *Pleurosigma* spp., *Navicula* spp., *Concinodiscus* spp., *Synedra* spp. and *Gyrosigma* spp. were the abundant diatoms. Diatoms such as *Cylendrotheca* spp., *Diploneis* spp., *Amphiprora* spp. and *Cymbella* spp. were not observed on the nylon nets during the summer season (Table 4).

Diatom abundance was higher during winter than summer (Fig. 6). During the winter season, *Navicula* spp. was the most abundant diatom, with a maximum of 1221 individual cm^{-2} after 4 days (Fig. 5). *Cylindrotheca* spp. was abundant during the later stages of microfouling development on nylon nets (Fig. 5). During the summer season, *Nitzschia* spp. and *Pluerosigma* spp. were more dominant than the other species on nylon nets, with a maximum of 135 and 85 individual cm^{-2}, respectively, after 3 days (Fig. 5). In general, diatom settlement (total numbers) on nylon nets showed an increase with submersion time in both winter ($r = 0.896$, $P < 0.001$) and summer ($r = 0.227$, $P > 0.05$). Though phytoplankton abundance increased with submersion time during summer, this increasing trend was not observed on panels submerged for 4 and 5 days (Fig. 6). The relative abundance of dominant diatom species, such as *Navicula* spp., *Nitzschia* spp., *Cylindrotheca* spp. and *Pluerosigma* spp. is provided in Fig. 7. The

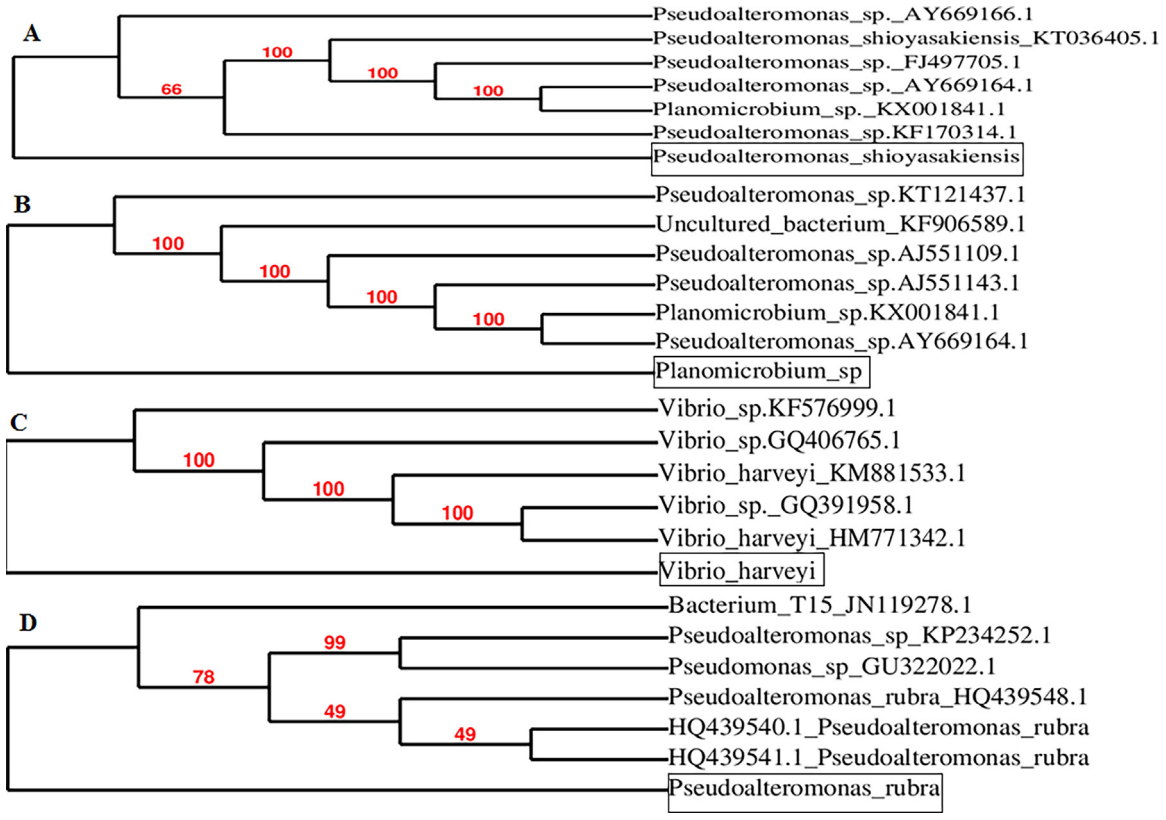

Figure 4 Phylogenetic tree of bacterial strains colonized on nylon nets submerged in the central Red Sea. The phylogenetic tree was constructed based on 16S rRNA gene sequences. *Pseudoalteromonas shioyasakiensis* (KY224086) (a), *Planomicrobium* sp. (KY224087) (b), *Vibrio harveyi* (KY266820) (c), *Pseudoalteromonas rubra* (KY266819) (d). The strains without accession numbers in the figure are recorded during this study.

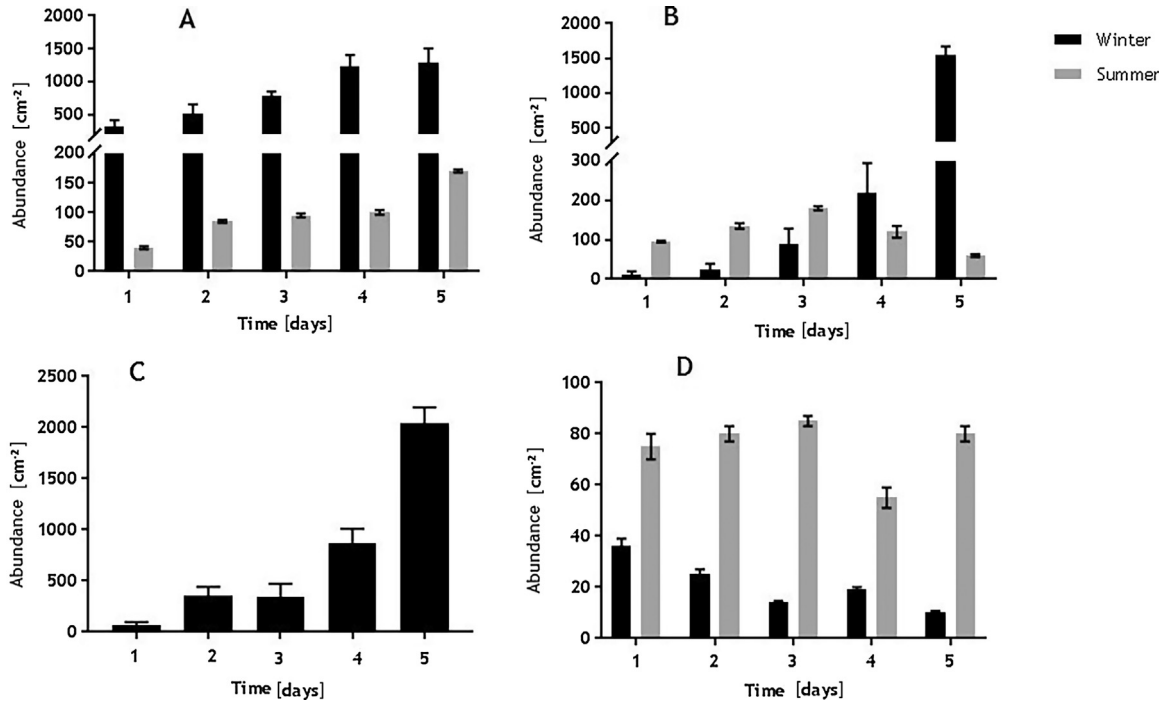

Figure 5 Abundance (mean ± SD, $n = 5$) of four dominant diatoms in the biofilm developed on nylon nets during the winter and summer seasons. *Navicula* spp. (a), *Nitzschia* spp. (b), *Cylindrotheca* spp. (c), *Pluerosigma* spp. (d).

Table 4 Density of diatom species which were not abundant in the biofilm developed on nylon nets during the winter and summer seasons (mean ± SD, $n = 5$).

Phytoplankton	Winter					Summer				
Submersion duration [days]→	1	2	3	4	5	1	2	3	4	5
Licmophora spp.	135 ± 70.92	233 ± 95.90	177 ± 53.86	175 ± 61.55	257 ± 24.73	0	11 ± 2.35	14 ± 4.18	20 ± 4.12	10 ± 1.87
Concinodiscus spp.	35 ± 10.04	75 ± 54.63	57 ± 12.17	91 ± 25.14	49 ± 18.59	30 ± 6.29	45 ± 5.87	60 ± 3.08	50 ± 5.87	40 ± 7.71
Cyclotella spp.	11 ± 13.61	4 ± 2.73	0	7 ± 2.76	0	0	0	0	4 ± 1.87	0
Pseudo-Nitzschia spp.	2 ± 4.97	2 ± 1.32	4 ± 1.56	9 ± 4.43	0	5 ± 1.87	6 ± 2.92	4 ± 1.23	9 ± 1.87	0
Gyrosigma spp.	13 ± 14.49	0	4 ± 1.66	56 ± 8.39	229 ± 28.98	25 ± 5.87	35 ± 5.87	30 ± 3.08	0	0
Diploneis spp.	2 ± 4.97	0	0	13 ± 2.04	53 ± 25.34	0	0	0	0	0
Synedra spp.	55 ± 49.18	71 ± 18.59	196 ± 34.21	442 ± 122.32	1457 ± 191.55	25 ± 3.08	30 ± 6.29	20 ± 2.74	15	10
Amphiprora spp.	43 ± 21.38	22 ± 7.86	73 ± 12.25	196 ± 81.88	465 ± 49.11	0	0	0	0	0
Symbella spp.	0	0	0	4 ± 1.10	13 ± 1.02	0	0	0	0	0
Amphora spp.	0	0	0	0	0	0	0	8	5	4

settlement of these diatom communities also showed a significant difference in relation to nylon nets submersion duration and season (Table 5). The relative abundance of *Navicula* spp. was as high as 36% and was 26% during the winter season (1-day-old nylon nets), while for *Nitzschia* spp., the relative abundance was 35.08% (after 3 days) in the summer season. The relative abundance of *Cylindrotheca* spp. showed a maximum of 24.38% (after 5 days) in winter, while this diatom was not observed during the summer season. *Pluerosigma* spp. showed a maximum relative abundance of 24.27% during the summer season. The relative abundance analysis showed a succession of diatom density, as *Navicula* spp. was dominant for up to 4 days while *Cylindrotheca* spp. was the dominant diatom on nylon nets submerged during the winter season.

The total density of diatoms showed significant variation in relation to submersion time ($F = 211.16$, $P < 0.01$) and season ($F = 1054.25$, $P < 0.01$) (Table 2). Correlation analysis revealed a positive correlation between the abundance of diatoms and bacteria ($r = 0.824$, $P < 0.001$) during the winter season. Additionally, the abundance of diatom on nylon nets showed a positive correlation with chlorophyll-*a* ($r = 0.704$, $P < 0.001$), and nutrients such as nitrate ($r = 0.897$, $P < 0.001$), nitrite ($r = 0.383$, $P < 0.05$), phosphate ($r = 0.810$, $P < 0.001$), protein ($r = 0.685$, $P < 0.001$) and carbohydrate ($r = 0.673$, $P < 0.001$) during the winter season (Table 3). However, the abundance of diatoms did not show any significant relationship with bacteria and nutrients during the summer season (Table 3).

4. Discussion

The biofilm that forms on substrates submerged in marine waters consists of organic and inorganic materials from the surrounding environment (Bhosle et al., 2005; Jain and Bhosle, 2009), in addition to microorganisms. The results of the present study indicated that protein was the major organic component in the biofilm developed on nylon nets submerged in the central Red Sea. The carbohydrate concentration was very low during the winter season. The concentration of nitrate, nitrite and phosphate in the biofilm also showed seasonal variations. The observed seasonal variations may be mainly due to the concentration of these nutrients in the coastal waters. In these waters (nylon nets submersion medium), the nutrient concentrations (data was only available for nitrate, nitrite and phosphate) were high during the summer season. As the nutrient content of the Creek waters was high during summer, accumulation of nutrients on net panels also showed higher values during this period. Previous studies by Wesley and Satheesh (2009) also confirmed that the nutrient concentration of biofilms depends on the nutrient load of the submersion medium.

The biofilms are reported to induce the attachment of microorganisms and macroorganisms (Bakker et al., 2004; Freckelton et al., 2017; Hadfield, 2011; Jain and Bhosle, 2009; Li et al., 2014; Qian et al., 2007; Whalan and Webster, 2014; Yang et al., 2016) and paves the way for the development of a biofouling assemblage on hard surfaces (Bhosle et al., 1990; Hadfield et al., 2014). In this study, the concentrations of all of the nutrients showed significant positive correlations with bacterial colonies (CFU on culture plates)

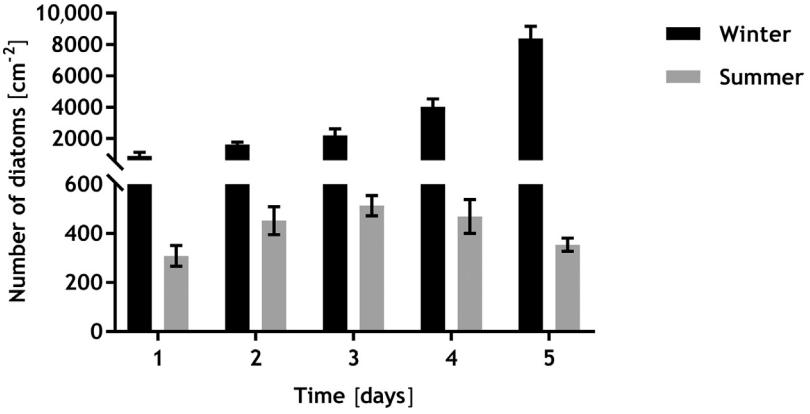

Figure 6 Total number (mean ± SD, $n = 5$) of diatoms settled on nylon nets during the winter and summer seasons.

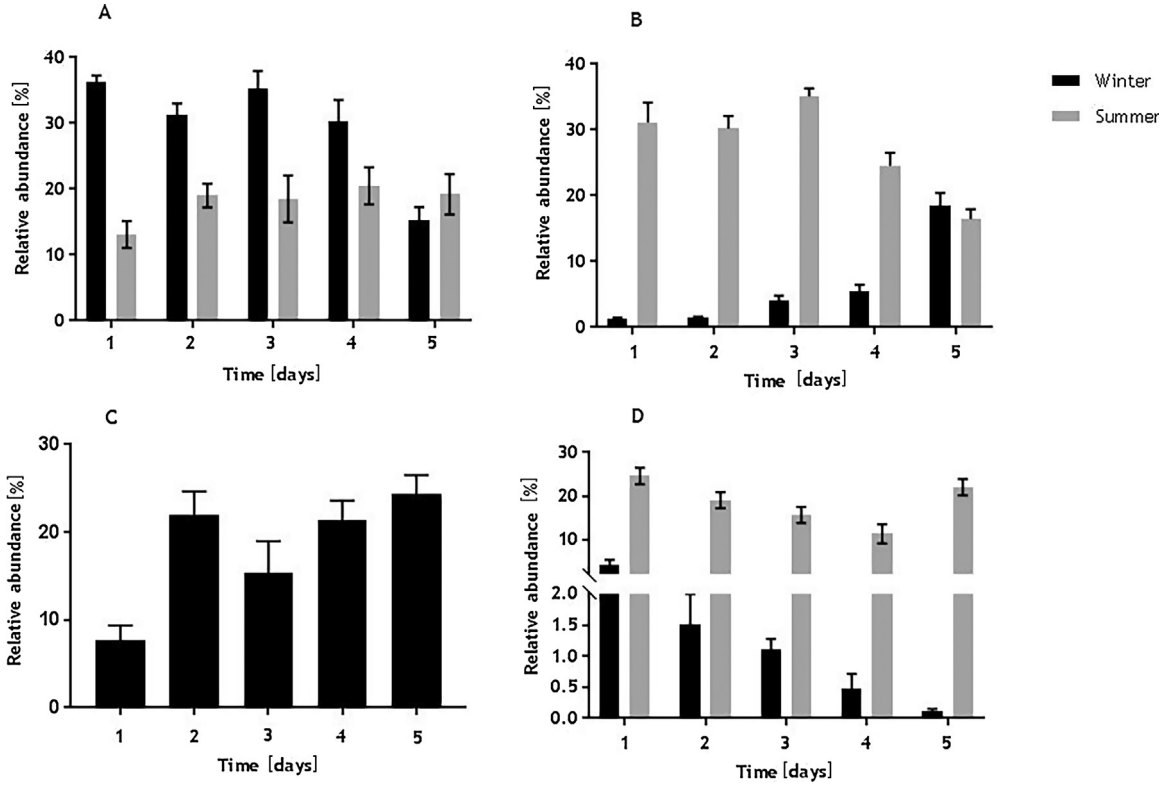

Figure 7 Relative abundance of dominant diatom species in the biofilm. *Navicula* spp. (a), *Nitzschia* spp. (b), *Cylindrotheca* spp. (c), *Pluerosigma* spp (d).

Table 5 Two-way ANOVA (analysis of variance) of the abundance of four dominant diatoms in the biofilm developed on nylon nets. Nylon nets submersion duration (time, 5 days) and season (winter and summer) were considered as factors for ANOVA. Significant = $P < 0.05$. Not significant = $P > 0.05$.

Source of variation	df	*Navicula* spp.		*Nitzschia* spp.		*Cylindrotheca* spp.		*Pleurosigma* spp.	
		F	*P*	*F*	*P*	*F*	*P*	*F*	*P*
Time [days]	4	102.90	0.000	51.93	0.000	292.57	0.000	19.79	0.000
Season	1	3175.8	0.000	1396	0.000	9499.6	0.000	833.79	0.000
Time*season	4	133.05	0.000	49.54	0.000	292.57	0.000	67.18	0.000

during winter and summer. These adsorbed nutrients may change the surface properties that enable the adhesion of microorganisms (Bakker et al., 2004; Fletcher and Marshall, 1982). The correlation analysis revealed a positive relationship between nutrients and diatoms during the winter season. However, in the summer season, there was no significant relationship between nutrients and diatom abundance on nylon nets. This showed that the seasonal factor, rather than adsorbed nutrients, plays an important role in the settlement of diatoms on surfaces.

Scanning Electron Microscopy visualization method used in this study gave better insight into the temporal sequence of microfouling development on nylon nets submerged in the marine waters. The SEM microphotographs of nylon nets confirmed the findings of previous studies which reported the settlement of bacteria and diatoms on artificial substrates submerged for a period of 24 h in the seawater (Mejdandžić et al., 2015; Satheesh and Wesley, 2010; Siboni et al., 2007). Bacterial communities form an important part of the biofilms developed on hard substrata submerged in marine waters (see reviews: Hadfield, 2011; Salta et al., 2013). In this study, the total number of cultivable bacteria (bacterial colonies on culture plates) on nylon nets showed an increase with submersion time during the winter and summer seasons. Additionally, the abundance of bacteria in biofilm was greater during summer than winter. The bacterial communities attached to the nylon nets revealed the presence of 4 dominant species. The genus *Pseudoalteromonas* is commonly found in marine biofilms on living and non-living surfaces (see review: Satheesh et al., 2016). Another prominent bacterial strain, *Vibrio harveyi*, has also been reported in marine biofilms (Henares et al., 2012) and is commonly used as a model organism for studying cell-cell communication (quorum sensing) in biofilms (Henke and Bassler, 2004). While most studies have confirmed the dominance of Alphaproteobacteria on marine biofilms (Salta et al., 2013), the bacterial strains identified in this study were Gammaproteobacteria and Firmicutes. Further, Al-Awadhi et al. (2013) highlighted the variations in bacterial identities between culture-dependent and culture-independent methods. Hence, the observed variations in bacterial identities may be due to the culture-dependent method followed in this study. In general, Gammaproteobacteria and Alphaproteobacteria have been identified as the primary colonizing bacterial groups on artificial substrata submerged in marine waters (Chung et al., 2010; Dobretsov et al., 2013; Webster and Negri, 2006).

The results of the present study showed that diatoms constitute an important part of the microfouling assemblage developed on net panels submerged in the Obhur Creek waters of the central Red Sea. The abundance of most of the diatom species on nylon nets was higher during winter than summer. The diatom community was mainly dominated by pennate diatoms, such as *Navicula* spp. and *Nitzschia* spp., during this study. Several previous studies also reported the dominance of pennate diatoms in marine biofilms (Mitbavkar and Anil, 2000; Patil and Anil, 2005; Satheesh and Wesley, 2012; Wetherbee et al., 1998). The abundance of pennate diatoms on artificial substrata may be due to the existence of a raphe along the length of the frustules that helps the pennate diatoms to attach to solid surfaces (Anil et al., 2006). *Cylindrotheca* spp. and *Pluerosigma* spp. were also abundant in the biofilm developed on the nylon nets.

The abundance of organisms in biofilms is influenced by various factors. The results clearly showed seasonal changes in microfouling communities, such as bacteria and diatoms, on nylon nets submerged in the central Red Sea coast. Seasonal variations in micro- and macrofouling community settlement on hard surfaces have been reported from tropical coastal waters by many previous researchers (Satheesh and Godwin Wesley, 2008; Satheesh and Wesley, 2011, 2012; Sawall et al., 2012; Yang et al., 2015). There are several explanations for the observed seasonal variations in microfouling community development on nylon nets. Mainly, seasonal changes in the aquatic medium may affect the development of biofilm on hard surfaces (Donlan, 2002). Further, environmental parameters such as temperature and nutrient content of the coastal waters showed considerable variations between two seasons. Other factors such as water current and wave action may also affect the settlement of microfouling assemblages. In the central Red Sea, wave action was high during winter and low during summer (Fery et al., 2015; Ralston et al., 2013). The abundance of diatoms was high during winter and low during summer but the bacterial count and nutrient concentration of the biofilm revealed an opposite trend (high in summer and low during winter). Additionally, in summer, the wind direction is northwest, driving the surface water towards the south for approximately four months at a velocity of 15—20 cm per sec. During winter, the direction is reversed, resulting in the inflow of water from the Gulf of Aden into the Red Sea (Omer, 2010). Previous studies also noted that the settlement of diatoms on hard surfaces in marine waters is affected by water velocity, size, immigration and the reproductive rate of the organisms in a specific region (Johnson et al., 1997; Satheesh and Wesley, 2012).

The abundance of diatoms in the water column may also impact their settlement on substrata. In the present study, the distribution of diatoms in the study area was not considered. However, a review of available literature shows a pronounced seasonality in the distribution phototrophic organisms the Red Sea. For instance, Raitsos et al. (2013) revealed an elevated chlorophyll-*a* content during winter and a low content in summer in the Red Sea. Previous studies in Obhur Creek (the present study area) also revealed the presence of diatoms such as *Cosinodiscus* sp. and *Nitzchia closterium* throughout the year and the absence of *Navicula* spp. during summer (Khomayis and Al-Harbi, 2003). This indicates that the abundance of diatom species in the microfouling communities in this study may mainly depend on the diatom distribution in the surrounding coastal waters, along with the environmental factors discussed earlier.

Microfouling communities interact with each other, and there may exist a strong positive or negative relationship between the organisms. In this study, the abundance of bacteria and diatoms showed a strong positive relationship during the winter season and a weak negative correlation in the summer season. Understanding the interactions between organisms settled on artificial substratum is important, as these primary colonizers (like bacteria and diatoms) are believed to induce or inhibit the settlement of marine invertebrate larvae (Hadfield and Paul, 2001; Huang et al., 2012; Jin and Qian, 2005). Due to their settlement-inhibiting or -inducing effects on marine invertebrate larvae and macroalgal spores, the marine biofilms may also influence the

structure and functioning of benthic communities in marine ecosystems (Hadfield, 2011; Russell et al., 2013).

In conclusion, bacteria and diatoms were the primary colonizers on the artificial substratum submerged in the central Red Sea. While there was a definite correlation between nutrient concentration and bacterial abundance during both seasons, this relationship was not observed for diatoms. Additionally, the interaction between microfouling organisms, such as bacteria and diatoms, showed temporal variability, highlighting the role that environmental conditions play. The results of the present study also revealed a significant seasonal variation in the abundance of microfouling organisms and the accumulation of nutrients on nylon nets.

Acknowledgements

We thank the Faculty of Marine Sciences, King Abdulaziz University for providing necessary facilities.

References

Abdul Azis, P.K., Al-Tisan, I., Sasikumar, N., 2001. Biofouling potential and environmental factors of seawater at a desalination plant intake. Desalination 135 (1—5), 69—82, http://dx.doi.org/10.1016/S0011-9164(01)00140-0.

Al-Awadhi, H., Dashti, N., Khanafer, M., Al-Mailem, D., Ali, N., Radwan, S., 2013. Bias problems in culture-independent analysis of environmental bacterial communities: a representative study on hydrocarbonoclastic bacteria. Springer plus 2 (1), 369, http://dx.doi.org/10.1186/2193-1801-2-369.

Anil, A.C., Patil, J.S., Mitbavkar, S., D'Costa, P., D'Silva, S., Hegde, S., Naik, R., 2006. Role of diatoms in marine biofouling. In: Tewari, A. (Ed.), Recent Advances on Applied Aspects of Indian Marine Algae with Reference to Global Scenario, Central Salt and Marine Chemicals Research Institute, India 1, 351—365.

Bakker, D.P., Busscher, H.J., Zanten, J.V., Veries, J.D., Klijnstra, J. W., Van Der Mei, C.H., 2004. Multiple linear regression analysis of bacterial deposition to polyurethane coatings after conditioning film formation in the marine environment. Microbiology 150 (6), 1779—1784, http://dx.doi.org/10.1099/mic.0.26983-0.

Baragi, L.V., Anil, A.C., 2016. Synergistic effect of elevated temperature, pCO_2 and nutrients on marine biofilm. Mar. Pollut. Bull. 105 (1), 102—109, http://dx.doi.org/10.1016/j.marpolbul.2016.02.049.

Bhosle, N.B., Garg, A., Fernandes, L., Citon, P., 2005. Dynamics of amino acids in the conditioning film developed on glass panels immersed in the surface seawaters of Dona Paula Bay. Biofouling 21 (2), 99—107, http://dx.doi.org/10.1080/08927010500097821.

Bhosle, N.B., Sankaran, P.D., Wagh, A.B., 1990. Carbohydrate sources of microfouling material developed on aluminium and stainless steel panels. Biofouling 2 (2), 151—164, http://dx.doi.org/10.1080/08927019009378141.

Chung, H.C., Lee, O.O., Huang, Y.L., Mok, S.Y., Kolter, R., Qian, P.Y., 2010. Bacterial community succession and chemical profiles of subtidal biofilms in relation to larval settlement of the polychaete *Hydroides elegans*. ISME J. 4 (6), 817—828, http://dx.doi.org/10.1038/ismej.2009.157.

Costerton, J.W., Lewandowski, Z., Caldwell, D.E., Korber, D.R., Lappin-Scott, H.M., 1995. Microbial biofilms. Annu. Rev. Microbiol. 49 (1), 711—745, http://dx.doi.org/10.1146/annurev.mi.49.100195.003431.

Dang, H., Lovell, C.R., 2000. Bacterial primary colonization and early succession on surfaces in marine waters as determined by amplified rRNA gene restriction analysis and sequence analysis of 16S rRNA genes. Appl. Environ. Microbiol. 66 (2), 467—475, http://dx.doi.org/10.1128/AEM.66.2.467-475.2000.

Decho, A.W., 2000. Microbial biofilms in intertidal systems: an overview. Cont. Shelf Res. 20 (10), 1257—1273, http://dx.doi.org/10.1016/S0278-4343(00)00022-4.

Dereeper, A., Guignon, V., Blanc, G., Audic, S., Buffet, S., Chevenet, F., Dufayard, J.-F., Guindon, S., Lefort, V., Lescot, M., Claverie, J.-M., Gascuel, O., 2008. Phylogeny.fr: robust phylogenetic analysis for the non-specialist. Nucleic Acids Res. 36 (2), W465—W469, http://dx.doi.org/10.1093/nar/gkn180.

Dobretsov, S., 2009. Inhibition and induction of marine biofouling by biofilms. In: Flemming, H.C., Murthy, P.S., Venkatesan, R., Cooksey, K. (Eds.), Marine and Industrial Biofouling. Springer, Berlin, 293—313, http://dx.doi.org/10.1007/7142_2008_10.

Dobretsov, S., Abed, R.M.M., Teplitski, M., 2013. Mini-review: inhibition of biofouling by marine microorganisms. Biofouling 29 (4), 423—441, http://dx.doi.org/10.1080/08927014.2013.776042.

Donlan, R.M., 2002. Biofilms: microbial life on surfaces. Emerg. Infect. Dis. 8 (9), 881—890, http://dx.doi.org/10.3201/eid0809.020063.

DuBois, M., Gilles, K.A., Hamilton, J.K., Rebers, P.A., Smith, F., 1956. Colorimetric method for determination of sugars and related substances. Anal. Chem. 28 (3), 350—356, http://dx.doi.org/10.1021/ac60111a017.

Edgar, R.C., 2004. MUSCLE: multiple sequence alignment with high accuracy and high throughput. Nucleic Acids Res. 32 (5), 1792—1797, http://dx.doi.org/10.1093/nar/gkh340.

Fery, N., Al-Subhi, A.M., Zubier, K.M., Bruss, G., 2015. Evaluation of the sea state near Jeddah based on recent observations and model results. J. Oper. Oceanogr. 8 (1), 1—10, http://dx.doi.org/10.1080/1755876X.2015.1014636.

Fletcher, M., Marshall, K.C., 1982. Bubble contact angle method for evaluating substratum interfacial characteristics and its relevance to bacterial attachment. Appl. Environ. Microbiol. 44 (1), 184—192.

Freckelton, M.L., Brian, T., Nedved, B.T., Hadfield, M.G., 2017. Induction of invertebrate larval settlement: different bacteria, different mechanisms? Sci. Rep. 7, 42557, http://dx.doi.org/10.1038/srep42557.

Guo, X., Niu, Z., Lu, D., Feng, J., Chen, Y., Tou, F., Liu, M., Yang, Y., 2017. Bacterial community structure in the intertidal biofilm along the Yangtze Estuary, China. Mar. Pollut. Bull. 124 (1), 314—320, http://dx.doi.org/10.1016/j.marpolbul.2017.07.051.

Hadfield, M.G., 2011. Biofilms and marine invertebrate larvae: what bacteria produce that larvae use to choose settlement sites. Annu. Rev. Mar. Sci. 3, 453—470, http://dx.doi.org/10.1146/annurev-marine-120709-142753.

Hadfield, M.G., Asahina, A., Hennings, S., Nedved, B., 2014. The bacterial basis of biofouling: a case study. Indian J. Mar. Sci. 43 (11), 2075—2084.http://nopr.niscair.res.in/handle/123456789/34577.

Hadfield, M.G., Paul, V.J., 2001. Natural chemical cues for settlement and metamorphosis of marine invertebrate larvae. In: McClintock, J.B., Baker, B.J. (Eds.), Marine Chemical Ecology. CRC, Boca Raton, 431—461.

Hasle, G.R., Syvertsen, E.E., 1997. Marine diatoms. In: Tomas, C.R. (Ed.), Identifying Marine Phytoplankton. Acad. Press, San Diego, 5—386.

Henares, B.M., Higgins, K.E., Boon, E.M., 2012. Discovery of a nitric oxide responsive quorum sensing circuit in *Vibrio harveyi*. ACS Chem. Biol. 7 (8), 1331—1336, http://dx.doi.org/10.1021/cb300215t.

Henke, J.M., Bassler, B.L., 2004. Three parallel quorum-sensing systems regulate gene expression in *Vibrio harveyi*. J. Bacteriol. 186 (20), 6902—6914, http://dx.doi.org/10.1128/JB.186.20.6902-6914.2004.

Huang, Y., Callahan, S., Hadfield, M.G., 2012. Recruitment in the sea: bacterial genes required for inducing larval settlement in a polychaete worm. Sci. Rep. 2, 228, http://dx.doi.org/10.1038/srep00228.

Huggett, M.J., Nedved, B.T., Hadfield, M.G., 2009. Effects of initial surface wettability on biofilm formation and subsequent settlement of *Hydroides elegans*. Biofouling 25 (5), 387–399, http://dx.doi.org/10.1080/08927010902823238.

Hung, O.S., Gosselin, L.A., Thiyagarajan, V., Wu, R.S.S., Qian, P.Y., 2005. Do effects of ultraviolet radiation on microbial films have indirect effects on larval attachment of the barnacle *Balanus amphitrite*? J. Exp. Mar. Biol. Ecol. 323 (1), 16–26, http://dx.doi.org/10.1016/j.jembe.2005.02.016.

Jain, A., Bhosle, N.B., 2009. Biochemical composition of the marine conditioning film: implications for bacterial adhesion. Biofouling 25 (1), 13–19, http://dx.doi.org/10.1080/08927010802411969.

Jenkins, S.R., Martins, G.M., 2010. Succession on hard substrata. In: Dürr, S., Thomason, J.C. (Eds.), Biofouling. Wiley-Blackwell, Oxford, UK, 60–72, http://dx.doi.org/10.1002/9781444315462.

Jin, T., Qian, P., 2005. Amino acid exposure modulates the bioactivity of biofilms for larval settlement of *Hydroides elegans* by altering bacterial community components. Mar. Ecol. Prog. Ser. 297, 169–179, http://dx.doi.org/10.3354/meps297169.

Johnson, R.E., Tuchman, N.C., Peterson, C.G., 1997. Changes in the vertical microdistribution of diatoms within a developing periphyton mat. J. North Am. Benthol. Soc. 16 (3), 503–519, http://dx.doi.org/10.2307/1468140.

Khomayis, H.S., Al-Harbi, S.M., 2003. Periphyton flora in the coastal water of Jeddah, Saudi Arabia. JKAU Mar. Sci. 14 (1), 3–18.

Li, Y.-F., Guo, X.-P., Yang, J.-L., Liang, X., Bao, W.-Y., Shen, P.-J., Shi, Z.-Y., Li, J.-L., 2014. Effects of bacterial biofilms on settlement of plantigrades of the mussel *Mytilus coruscus*. Aquaculture 433, 434–441, http://dx.doi.org/10.1016/j.aquaculture.2014.06.031.

Lowry, O.H., Rosenbrough, N.A., Farr, A.L., Randall, R.J., 1951. Protein measurement with the Folin phenol reagent. J. Biol. Chem. 193 (1), 265–275.

McElroy, D.J., Doblin, M.A., Murphy, R.J., Hochuli, D.F., Coleman, R. A., 2016. A limited legacy effect of copper in marine biofilms. Mar. Pollut. Bull. 109 (1), 117–127, http://dx.doi.org/10.1016/j.marpolbul.2016.06.011.

Mejdandžić, M., Ivanković, T., Pfannkuchen, M., Godrijan, J., Pfannkuchen, D.M., Hrenović, J., Ljubešić, Z., 2015. Colonization of diatoms and bacteria on artificial substrates in the northeastern coastal Adriatic Sea. Acta Bot. Croat. 74 (2), 407–422, http://dx.doi.org/10.1515/botcro-2015-0030.

Mitbavkar, S., Anil, A.C., 2000. Diatom colonization on stainless steel panels in estuarine waters of Goa, west coast of India. Indian J. Mar. Sci. 29, 273–276.

Mitbavkar, S., Anil, A.C., 2008. Seasonal variations in the fouling diatom community structure from a monsoon influenced tropical estuary. Biofouling 24 (6), 415–426, http://dx.doi.org/10.1080/08927010802340317.

Nagarkar, S., Williams, G.A., Subramanian, G., Saha, S.K., 2004. Cyanobacteria-dominated biofilms: a high quality food resource for intertidal grazers. Hydrobiologia 512 (1), 89–95, http://dx.doi.org/10.1023/B:HYDR.0000020313.09924.c1.

Omer, W.M., 2010. Ocean Acidification in the Arabian Sea and the Red Sea-factors Controlling pH. (Masters thesis). Faculty of Mathematics and Natural Sciences, Geophysical Institute, Chemical Oceanography, University of Bergen, 61 pp.

Passarelli, C., Meziane, T., Thiney, N., Boeuf, D., Jesus, B., Ruivo, M., Jeanthon, C., Hubas, C., 2015. Seasonal variations of the composition of microbial biofilms in sandy tidal flats: focus of fatty acids, pigments and exopolymers. Estuar. Coast. Shelf Sci. 153, 29–37, http://dx.doi.org/10.1016/j.ecss.2014.11.013.

Patil, J.S., Anil, A.C., 2005. Biofilm diatom community structure: influence of temporal and substratum variability. Biofouling 21 (3–4), 189–206, http://dx.doi.org/10.1080/08927010500256757.

Qian, P.-Y., Lau, S.C.K., Dahms, H.-U., Dobretsov, S., Harder, T., 2007. Marine biofilms as mediators of colonization by marine macroorganisms: implications for antifouling and aquaculture. Mar. Biotechnol. 9 (4), 399–410, http://dx.doi.org/10.1007/s10126-007-9001-9.

Raitsos, D.E., Pradhan, Y., Brewin, R.J.W., Stenchikov, G., Hoteit, I., 2013. Remote sensing the phytoplankton seasonal succession of the Red Sea. PLOS ONE 8, e64909, http://dx.doi.org/10.1371/journal.pone.0064909.

Ralston, D.K., Jiang, H., Farrar, J.T., 2013. Waves in the Red Sea: response to monsoonal and mountain gap winds. Cont. Shelf Res. 65, 1–13, http://dx.doi.org/10.1016/j.csr.2013.05.017.

Rampadarath, S., Bandhoa, K., Puchooa, D., Jeewon, R., Bal, S., 2017. Early bacterial biofilm colonizers in the coastal waters of Mauritius. Electron. J. Biotechnol. 29, 13–21, http://dx.doi.org/10.1016/j.ejbt.2017.06.006.

Rao, T.S., 2003. Temporal variations in an estuarine biofilm: with emphasis on nitrate reduction. Estuar. Coast. Shelf Sci. 58 (1), 67–75, http://dx.doi.org/10.1016/S0272-7714(03)00060-X.

Roeselers, G., Loosdrecht, M.C.M., van Muyzer, G., 2008. Phototrophic biofilms and their potential applications. J. Appl. Phycol. 20 (3), 227–235, http://dx.doi.org/10.1007/s10811-007-9223-2.

Rossi, F., De Philippis, R., 2015. Role of cyanobacterial exopolysaccharides in phototrophic biofilms and in complex microbial mats. Life 5 (2), 1218–1238, http://dx.doi.org/10.3390/life5021218.

Russell, B.D., Connell, S.D., Findlay, H.S., Tait, K., Widdicombe, S., Mieszkowska, N., 2013. Ocean acidification and rising temperatures may increase biofilm primary productivity but decrease grazer consumption. Philos. Trans. R. Soc. B Biol. Sci. 368 (1627), 20120438, http://dx.doi.org/10.1098/rstb.2012.0438.

Saeed, M.O., Jamaluddin, A.T., Tisan, I.A., Lawrence, D.A., Al-Amri, M.M., Chida, K., 2000. Biofouling in a seawater reverse osmosis plant on the Red Sea coast, Saudi Arabia. Desalination 128 (2), 177–190, http://dx.doi.org/10.1016/S0011-9164(00)00032-1.

Salta, M., Wharton, J.A., Blache, Y., Stokes, K.R., Briand, J.-F., 2013. Marine biofilms on artificial surfaces: structure and dynamics. Environ. Microbiol. 15 (11), 2879–2893, http://dx.doi.org/10.1111/1462-2920.12186.

Satheesh, S., Ba-akdah, M.A., Al-Sofyani, A.A., 2016. Natural antifouling compound production by microbes associated with marine macroorganisms – a review. Electron. J. Biotechnol. 21, 26–35, http://dx.doi.org/10.1016/j.ejbt.2016.02.002.

Satheesh, S., Godwin Wesley, S., 2008. Seasonal variability in the recruitment of macrofouling community in Kudankulam waters, east coast of India. Estuar. Coast. Shelf Sci. 79 (3), 518–524, http://dx.doi.org/10.1016/j.ecss.2008.05.008.

Satheesh, S., Wesley, S., 2010. Biofilm development on acrylic coupons during the initial 24 hour period of submersion in a tropical coastal environment. Oceanol. Hydrobiol. Stud. 39 (1), 27–38, http://dx.doi.org/10.2478/v10009-010-0012-x.

Satheesh, S., Wesley, S.G., 2011. Influence of submersion season on the development of test panel biofouling communities in a tropical coast. Estuar. Coast. Shelf Sci. 94 (2), 155–163, http://dx.doi.org/10.1016/j.ecss.2011.06.011.

Satheesh, S., Wesley, S.G., 2012. Temporal changes of diatoms in marine biofilm developed on acrylic panels submerged in a tropical coast. Ocean Sci. J. 47 (4), 509–517, http://dx.doi.org/10.1007/s12601-012-0046-y.

Sawall, Y., Richter, C., Ramette, A., 2012. Effects of eutrophication, seasonality and macrofouling on the diversity of bacterial biofilms in equatorial coral reefs. PLoS ONE 7, e39951, http://dx.doi.org/10.1371/journal.pone.0039951.

Siboni, N., Lidor, M., Kramarsky-Winter, E., Kushmaro, A., 2007. Conditioning film and initial biofilm formation on ceramics tiles in the marine environment. FEMS Microbiol. Lett. 274 (1), 24–29, http://dx.doi.org/10.1111/j.1574-6968.2007.00809.x.

Sneed, J.M., Sharp, K.H., Ritchie, K.B., Paul, V.J., 2014. The chemical cue tetrabromopyrrole from a biofilm bacterium induces settlement of multiple Caribbean corals. Proc. R. Soc. B Biol. Sci. 281 (1786), 20133086, http://dx.doi.org/10.1098/rspb.2013.3086.

Stoodley, P., Sauer, K., Davies, D.G., Costerton, J.W., 2002. Biofilms as complex differentiated communities. Annu. Rev. Microbiol. 56 (1), 187—209, http://dx.doi.org/10.1146/annurev.micro.56.012302.160705.

Thompson, R.C., Norton, T.A., Hawkins, S.J., 2004. Physical stress and biological control regulate the producer—consumer balance in intertidal biofilms. Ecology 85 (5), 1372—1382, http://dx.doi.org/10.1890/03-0279.

Venugopalan, V.K., Paulpandian, A.L., 1989. Methods in hydrobiology. CAS in Marine Biology. Annamalai University Publ., India, 134 pp.

Wahl, M., 1989. Marine epibiosis. I. Fouling and antifouling: some basic aspects. Mar. Ecol. Prog. Ser. 58, 175—189, http://dx.doi.org/10.3354/meps058175.

Wang, C., Bao, W.-Y., Gu, Z.-Q., Li, Y.-F., Liang, X., Ling, Y., Cai, S.-L., Shen, H.-D., Yang, J.-L., 2012. Larval settlement and metamorphosis of the mussel *Mytilus coruscus* in response to natural biofilms. Biofouling 28 (3), 249—256, http://dx.doi.org/10.1080/08927014.2012.671303.

Watson, M., Scardino, A., Zalizniak, L., Shimeta, J., 2015. Colonisation and succession of marine biofilm-dwelling ciliates in response to environmental variation. Aquat. Microb. Ecol. 74 (2), 95—105, http://dx.doi.org/10.3354/ame01731.

Webster, N.S., Negri, A.P., 2006. Site-specific variation in Antarctic marine biofilms established on artificial surfaces. Environ. Microbiol. 8 (7), 1177—1190, http://dx.doi.org/10.1111/j.1462-2920.2006.01007.x.

Wesley, S.G., Satheesh, S., 2009. Temporal variability of nutrient concentration in marine biofilm developed on acrylic panels. J. Exp. Mar. Biol. Ecol. 379 (1), 1—7, http://dx.doi.org/10.1016/j.jembe.2009.08.004.

Wetherbee, R., Lind, J.L., Burke, J., Quatrano, R.S., 1998. Mini review: the first kiss: establishment and control of initial adhesion by raphid diatoms. J. Phycol. 34 (1), 9—15, http://dx.doi.org/10.1046/j.1529-8817.1998.340009.x.

Whalan, S., Webster, N.S., 2014. Sponge larval settlement cues: the role of microbial biofilms in a warming ocean. Sci. Rep. 4, 4072, http://dx.doi.org/10.1038/srep04072.

Wieczorek, S.K., Todd, C.D., 1998. Inhibition and facilitation of settlement of epifaunal marine invertebrate larvae by microbial biofilm cues. Biofouling 12 (1—3), 81—118, http://dx.doi.org/10.1080/08927019809378348.

Yang, C., Fang, S., Chen, D., Wang, J., Liu, F., Xia, C., 2016. The possible role of bacterial signal molecules N-acyl homoserine lactones in the formation of diatom-biofilm (*Cylindrotheca* sp.). Mar. Pollut. Bull. 107 (1), 118—124, http://dx.doi.org/10.1016/j.marpolbul.2016.04.010.

Yang, C., Wang, J., Yu, Y., Liu, S., Xia, C., 2015. Seasonal variations in fouling diatom communities on the Yantai coast. Chin. J. Oceanol. Limnol. 33 (2), 439—446, http://dx.doi.org/10.1007/s00343-015-4067-0.

Zhang, W.P., Wang, Y., Tian, R.M., Bougouffa, S., Yang, B., Cao, H.L., Zhang, G., Wong, Y.H., Xu, W., Batang, Z., Al-Suwailem, A., Zhang, X.X., Qian, P.-Y., 2014. Species sorting during biofilm assembly by artificial substrates deployed in a cold seep system. Sci. Rep. 4, 6647, http://dx.doi.org/10.1038/srep06647.

Oceanologia (2018) 60, 232—243

Available online at www.sciencedirect.com

ScienceDirect

journal homepage: www.journals.elsevier.com/oceanologia/

ORIGINAL RESEARCH ARTICLE

Galveston Bay dynamics under different wind conditions

David Salas-Monreal [a,*], Ayal Anis [b], David Alberto Salas-de-Leon [c]

[a] *Universidad Veracruzana, Boca del Rio, Mexico*
[b] *Texas A&M University, Galveston, USA*
[c] *National Autonomous University of Mexico (UNAM), Ciudad Universitaria, Mexico City, Mexico*

Received 25 May 2017; accepted 17 October 2017
Available online 6 November 2017

KEYWORDS
Suspended particle dispersion;
Shallow estuarine dynamics;
Galveston Bay dynamics;
Ocean shallow water gyres

Summary The Regional Ocean Model System (ROMS) was used to simulate flow and hydrographic (temperature, salinity) patterns in a shallow, relatively flat-bottomed estuary with two subestuaries, one with an elongated shape and the other with a roughly circular shape. Simulations were used to elucidate the wind stress effect on a tidally formed cyclonic gyre in Galveston Bay, Texas (USA). The form factor suggests that Galveston Bay is a mixed, mainly diurnal system with tides that propagate out of phase by less than 1 h from side to side of the estuary. Temperature and salinity patterns suggest that the influence of the estuary extends oceanward, up to a distance commensurate with the 14 m depth isobath (~10 km offshore), during a diurnal tidal cycle. A tidally generated cyclonic gyre was observed to form in the circular subestuary, suggesting that this region may be more productive than others. This tidally formed gyre appeared to weaken and even disappear under certain wind stress conditions. Simulations suggest that the entire bay was able to flush only under northeasterly wind conditions, while for all other wind directions (northwesterly, southeasterly and southwesterly), the water appeared to pile up in the circular subestuary. Furthermore, most of the ocean-bay exchange was found to occur through the north entrance to the bay where the effects of the gyre were observed. Thus, it is expected that much of the exchange of water-borne substances, pollutants and plankton between the bay and the ocean occurs through this entrance.

* Corresponding author at: Calle Hidalgo #617, Boca del Rio, Veracruz 94290, Mexico. Tel.: +52 229 9567070.
E-mail address: davsalas@uv.mx (D. Salas-Monreal).
Peer review under the responsibility of Institute of Oceanology of the Polish Academy of Sciences.

https://doi.org/10.1016/j.oceano.2017.10.005

1. Introduction

Coastal marine ecosystems areas have been studied to understand sediment transport (Agardy, 2000; Salas-Monreal et al., 2009), zooplankton dispersion (Becerro et al., 2006; Chacon-Gomez et al., 2013; Holliday and Pieper, 1980) and the spatial and temporal variability of hydrodynamics and currents (Avendaño-Alvarez et al., 2017; Goreau and Hayes, 1994; Salas-de-Leon et al., 2004a; Wilkinson and Souter, 2008). In estuaries, gyres are commonly generated by current rectification (Storlazzi et al., 2006) due to the coastal boundaries. These gyres are one of the most important factors affecting the distribution of productive areas, sedimentation, vertical water movements, pollutants, and suspended matter concentrations (Salas-Monreal et al., 2009). Cyclonic gyres have been shown to generate highly productive areas by pumping deeper, high-nutrient, cold waters to the surface in the open ocean (Salas-de-León et al., 2008); however, in shallow waters the effects of gyres have not yet been fully described (Aretxabaleta et al., 2008; Wang et al., 1994). Cyclonic gyres in shallow waters are expected to disperse the water, pollutants, and suspended matter, since anticyclonic gyres have been found to concentrate such substances (Salas-de-Leon et al., 2004a). Thus, it is important from an ecosystem standpoint to understand the physical mechanisms associated with such gyres in shallow systems and their relation to residence time of the water-borne substances, as well as their trajectories.

The description of gyres in estuaries has been based both on *in situ* data (Cloern et al., 1983; Geyer et al., 2000; Officer, 1981; Salas-Monreal and Valle-Levinson, 2009) and model outputs (Dalrymple et al., 1990; Spiteri et al., 2008). The Regional Oceanic Modeling System (ROMS), which is a free-surface, hydrostatic, primitive equation model has been successfully used to describe currents and channel dynamics in estuaries. Xinyu and Valle-Levinson (2007) performed numerical experiments to simulate river discharge, with and without the influence of tides, in a shallow estuary and to describe the buoyancy effects on the circulation. Using the ROMS, Scully et al. (2009) found that the dominant along-channel momentum balance in estuaries is not always between the pressure gradient and the bottom stress. The nonlinear advective acceleration term can be on the same order of magnitude. The ROMS has also been used to study lateral circulation and to estimate sediment transport in estuaries (Chen and Sanford, 2009). The suspension (or resuspension) and deposition of matter are processes of particular importance in estuarine systems and arise mainly due to the presence of cyclonic and anticyclonic gyres, respectively.

The goal of this study is to advance the understanding of flow patterns and gyres generated in shallow flat estuaries under the influence of winds, tides, and river discharges. A recent oil spill in Galveston Bay, Texas (USA) ($>635\ m^3$ on March 23, 2014), resulting from a barge and cargo ship collision in the Houston Ship Channel, provided the impetus for the present study (Houston Chronicle, April 6, 2014). Model simulations and comparison to *in situ* data were carried out for the month of April 2014 in Galveston Bay to elucidate the relative importance of the terms in the momentum equation and to describe the variability of tidally generated gyres under different wind forcing conditions. The Galveston Bay estuary represents an ideal set up for the present study since it includes two differently shaped sub-estuaries (Fig. 1) directly influenced by two rivers.

Galveston Bay, the second largest estuary in the Gulf of Mexico (Fig. 1), has a surface area of 1600 km^2, is 50 km long, and is 27 km wide. The bathymetry is relatively flat with a mean depth of 3 m, except in the northern entrance (Houston Ship Channel), where a 12 m deep channel is located (Dupuis and Anis, 2013). The bay has an intertidal range of 0.5 m. The bay is connected to the Gulf of Mexico *via* two inlets (southern entrance and northern entrance) and has two major freshwater sources, the San Jacinto and Trinity Rivers (Fig. 1). The estuary is one of the most important shipping hubs in the USA and home to the Port of Houston, the largest port in the USA, and based on foreign tonnage, this estuary is the sixth largest in the world. More than one-third of the USA chemical production facilities and oil refineries are located around the bay, and one-third of commercial fishing income and one-half of sport fishing expenditures in Texas come from the estuary. Previous studies have already described the general dynamics of the bay using model simulations to reproduce the general circulation (Rayson et al., 2015), the effect of hurricanes within the bay (Rego and Li, 2010), and the effect of varying fresh water inputs on the oyster population within Galveston Bay (Klinck et al., 2002).

This manuscript reports the results of a study that explores the dynamics of tidally formed cyclonic gyres in a shallow estuary. This manuscript incorporates field observations and model simulation results and addresses the following three main objectives: (1) the variability of tidally generated gyres under different wind forcing conditions, (2) the distance of the river influence on the estuary and (3) the relative importance of the terms in the momentum equation.

2. Material and methods

The ROMS has been used to model internal tides and to estimate tidal fields, mixing and current patterns (Robertson, 2006; Salas-de-Leon et al., 2004a; Scully et al., 2009; Sutherland et al., 2011; Xinyu and Valle-Levinson, 2007). According to Robertson (2006), the semidiurnal baroclinic tides are well simulated with ROMS. The free-surface, hydrostatic, primitive equation ocean model uses sigma coordinates in the vertical (Haidvogel et al., 2000) to increase the accuracy of the simulations. In this study, the ROMS was setup following the basic configuration described in Salas-Monreal et al. (2012) to elucidate the effect of the wind stress in a shallow estuary and the influence of fresh water inputs on flow dynamics. The model was configured for the domain shown in Fig. 1. At the locations of freshwater inflow into the estuary (San Jacinto and Trinity Rivers), salinity was assumed to be zero and temperature equal to 15°C. River velocity discharges were set to $0.40\ m\ s^{-1}$ for both rivers ($\sim 100\ m^3\ s^{-1}$), which are representative values for this time of the year according to O'Donnell (2005). Tidal sea surface elevations, used to force the model at the external boundary, were obtained from the North Jetty station located at the entrance of the Galveston Bay (Fig. 1; http://tidesandcurrents.noaa.gov/harcon.html?id=8771341). Initial ocean salinity and temperature (inside and outside of the

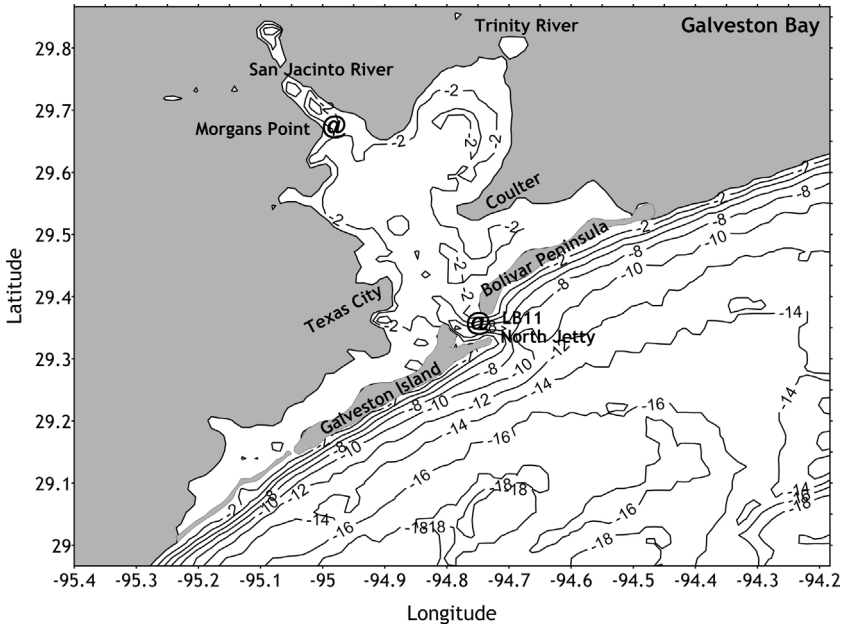

Figure 1 Galveston Bay and locations of the northern and southern entrances and the San Jacinto and Trinity Rivers. The @ symbols represent the location of the Morgans Point, LB11, and North Jetty tide stations. Two subestuaries are visible, one off the San Jacinto River with an elongated shape, and the second off the Trinity River with a roughly circular shape.

bay) were uniformly set throughout the entire domain to 22 and 34°C, respectively. The vertical eddy diffusivity uses a Mellor-Yamada closure scheme, as has typically been used in estuaries and bays (Fong, 1998).

The model domain has 64 × 84 grid points with 10 sigma coordinates. Using these sigma coordinates, the vertical resolution varies from <0.5 m in the flat part of the estuary to ~1 m at the channel (northern entrance). The resolution 64 × 84 grid points (~1.5 × 1 km of horizontal resolution) were chosen since gyres are often masked by insufficient grid resolution (Lynch et al., 1995). The free surface elevation, which uses the "Flather condition" (Marchesiello et al., 2001), the salinity, temperature, and water velocities at each grid point were recorded at 0.5 hourly intervals after the model had reached stability. Bottom stress was assumed to be a quadratic function of the bottom velocity with a drag coefficient of 2.5×10^{-3}. The tidally averaged potential and kinetic energy were calculated for each grid point. Once the normalized differences in energy from successive iterations were on the order of 10^{-3} or lower ($((E_{i+1}-E_i)/E_i \leq 0.001)$, the model was considered stable; this occurred after 28 simulation days.

A total of five experiments were conducted. The first experiment was conducted assuming a zero wind velocity to elucidate the circulation within the estuary resulting solely due to tidal forcing. The next four experiments were conducted assuming a constant wind speed of 10 m s^{-1} blowing from a southeastern, southwestern, northeastern and northwestern direction, respectively, to elucidate the residual flow under relatively strong and sustained wind conditions. These winds were chosen based on the conclusion of Park et al. (2001) that the winds that most significantly affect the estuary blow from the southeast with speeds of ~8 m s^{-1}. The wind speed in this study was set to 10 m s^{-1} based on observations of the seasonal wind velocities observed from the simulation period in the estuary, as reported by the National Weather Service (http://www.srh.noaa.gov/hgx/).

2.1. Initial model simulations and calibration

Tidal components and phases were obtained at four NOAA stations (Table 1) to classify the tides within the estuary. Based on the tide information from these stations, the form factor (F = (K1 + O1)/(M2 + S2)) (Salas Pérez et al., 2012) classifies the estuary itself as diurnal ($F > 3$), while at the entrance of the estuary, tides are classified as mixed, mainly diurnal ($1.5 < F < 3$). To obtain residual flows from *in situ* observations, it is thus necessary to perform at least six measurements per day (Nyquist frequency = 3 cyc day^{-1}) to reproduce a semidiurnal sinusoidal signal. At least twelve measurements will allow for the reproduction of the inflexion points of a tidally mixed (mainly diurnal) signal (Chacon-Gomez et al., 2013), as well as for the obtaining of subtidal flows from *in situ* data within the estuary.

The model was forced at the external ocean boundary with tidal components and phases calculated from the sea-level observations at the North Jetty station (Fig. 1). Here, only the seven largest tidal amplitudes (Table 2) were used, as they could accurately reproduce the observed tidal signal at the North Jetty station (Fig. 2; correlation of 0.82 and a p-value < 0.05, which imply the matching of phase). These tidal components were calculated using a two-year time series at the North Jetty station.

Tidal simulations, recorded hourly, were compared to measured sea surface elevations obtained from the North Jetty and Morgans Point stations, as seen in Fig. 2. A higher correlation (0.82) was present between the simulated sea level and the observed time series at the North Jetty station than between the simulated harmonics and the Morgans Point station time series (0.73). This finding maybe attributed to river discharges from the San Jacinto River (causing the sea elevation to rise), to the amplification/attenuation of the diurnal/semidiurnal tides due to the relative shallowness of the bay or simply as a result of using the North Jetty tides to

Table 1 Amplitudes, form factor (F = (K1 + O1)/(M2 + S2)), and classification for the four main tide constituents at the four NOAA stations in Galveston Bay.

Station	Latitude	Longitude	K1 (m)	O1 (m)	M2 (m)	S2 (m)	F	Tide classification
North Jetty	29°21.4′N	94°43.5′W	0.466	0.420	0.381	0.095	1.86	Mixed, mainly diurnal
Port Bolivar	29°21.5′N	94°47.5′W	0.464	0.459	0.260	0.080	2.71	Mixed, mainly diurnal
Eagle Point	29°28.9′N	94°55.0′W	0.384	0.374	0.113	0.038	5.02	Diurnal
Morgans Point	29°40.9′N	94°59.1′W	0.473	0.454	0.208	0.053	3.55	Diurnal

Table 2 The seven major tide constituents (North Jetty tide station) used to force the model at the external ocean boundary.

Constituent	Amplitude (m)	Phase	Speed (m s^{-1})
M2	0.381	108.1	28.984
S2	0.095	117.5	30.000
N2	0.105	87.0	28.439
K1	0.466	307.0	15.041
O1	0.420	313.2	13.943
SSA	0.282	55.1	0.082
SA	0.217	155.4	0.041

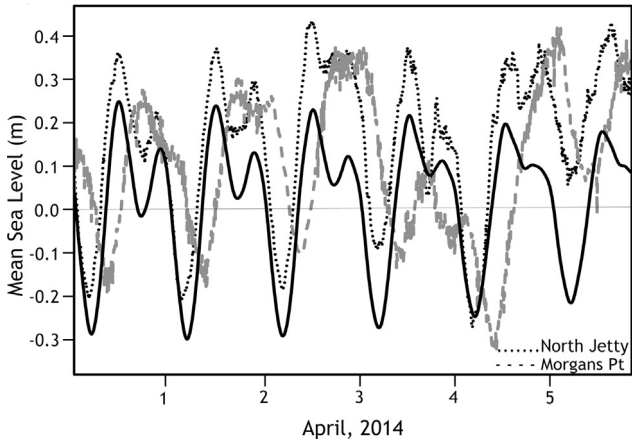

Figure 2 Time series of observed hourly mean sea level (m) at the North Jetty (dotted lines), Morgans Point (dashed lines) and the simulated sea level (solid line).

force the model (http://www.srh.noaa.gov/hgx). In addition, a time lag of 0.42 h was observed between the two stations.

Since the ROMS (3D model) is a hydrostatic model, two conditions were tested, the first condition being (Ro) $(alpha)^2 \ll 1$ and the second condition being (Fr)^2 $(alpha)^2 \ll 1$. Here, $alpha = H\,L^{-1}$ is the aspect ratio of the motion, Ro is the Rossby number (U/fL) and Fr is the Froude number (U/NH), in which U is the velocity scale, L and H are the length and depth scale, respectively, f is the Coriolis parameter, and N is the Brunt–Vaisala frequency. Finally, the Ekman layer thickness $(2k/f)^{1/2}$ (where k is the eddy viscosity scale) is approximately 4.5 m, and since the depth of the bay is ~3 m, its dynamics could be considered frictional (surface and bottom). As shown in Fig. 3, the model could reproduce the temperature time series at both stations ($r^2 > 0.79$ and a

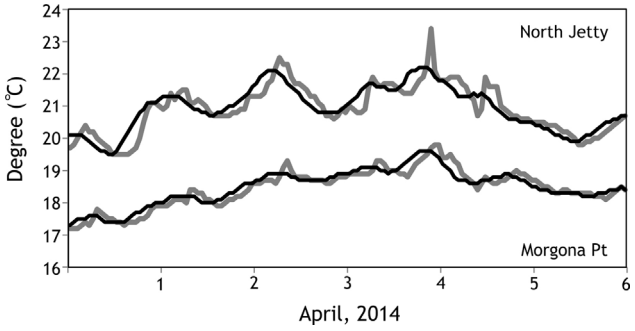

Figure 3 Time series of observed surface temperature (°C) at North Jetty, and Morgans Point (gray) and simulated surface temperature (solid black line) at the same locations.

p-value < 0.05). However, a time lag was noted between the observed and simulated temperatures, which was attributed to an increase in cold river inflow of fresher water to the estuary, as a result of several rain events during this period. The lag would thus not be simulated by the model since constant values were used for river water discharge, salinity, and temperature. Once the model was validated, the outputs were used to describe the temperature, salinity and current fields throughout the bay.

3. Results and discussion

3.1. Model simulations with no wind conditions

Once the model was calibrated, five experiments were performed. The first experiment was performed assuming no winds to describe the tidal effects on sea surface temperature (SST), salinity and current fields (1 m depth). The simulated temperature field for April 4th, 2014, exhibits a surface gradient of up to 4°C between the northern entrance and San Jacinto River during ebb (Fig. 4b) and up to 3°C during flood (Fig. 4a). The difference in SST gradient of ~1°C, observed between ebb and flood tides, was also evident up to a distance offshore corresponding to the 14 m depth isobaths or 10 km offshore (Isotherms of ~22.5°C). The simulations suggest that this is roughly the offshore distance of influence of the discharges of the San Jacinto and Trinity Rivers and thus likely the offshore distance where estuarine-borne matter might be directly affected by the diurnal tidal cycle. This can be corroborated by satellite images which show a color gradient (sediment gradient) at this location. The simulated residual temperature (Fig. 4c), obtained after filtering the diurnal tidal signal, suggests that the temperature in the estuary was modified at both bay entrances

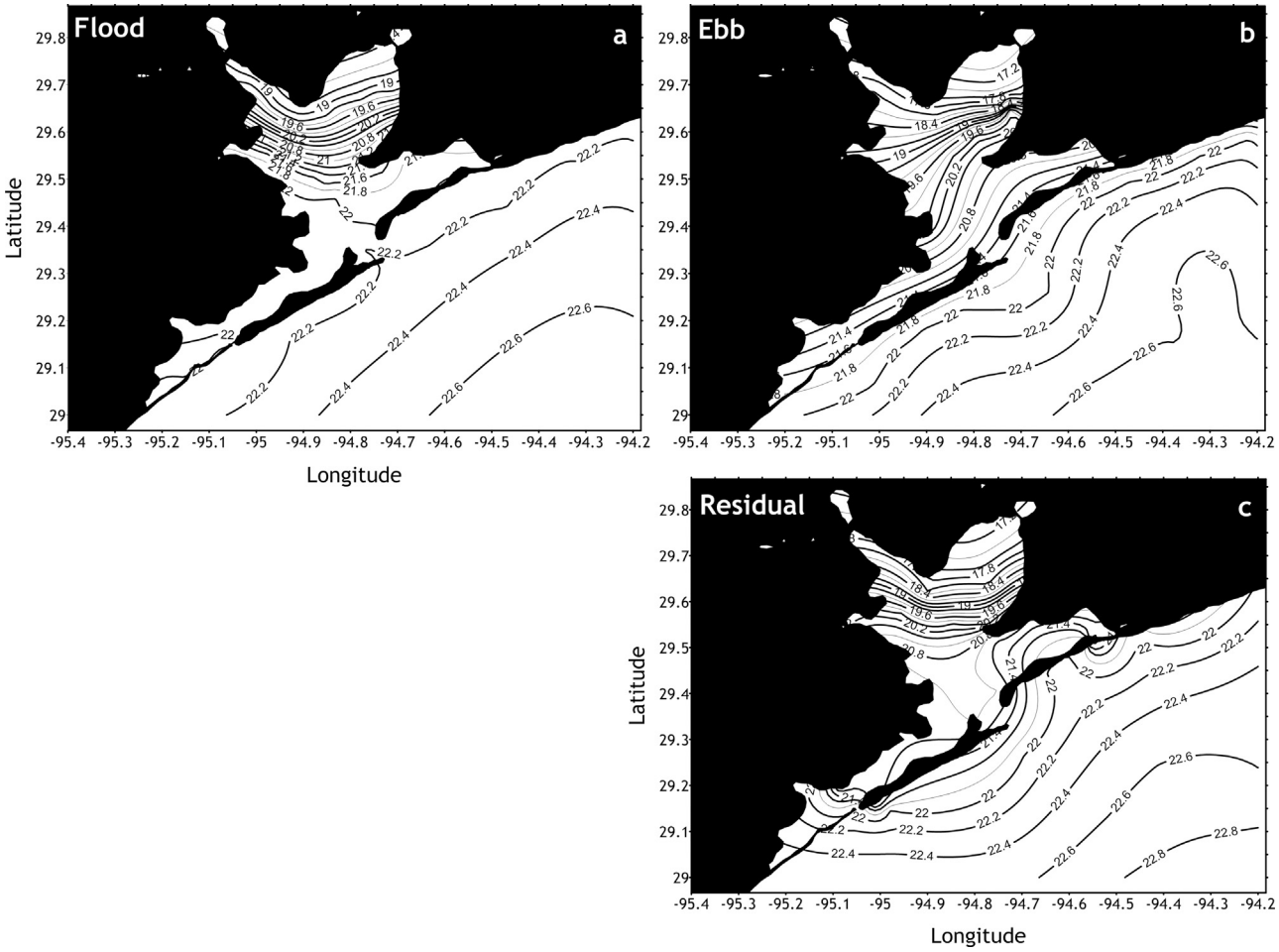

Figure 4 Surface temperature fields (contour lines are at 0.2°C intervals) obtained from model simulations during flood (a), ebb (b), and the residual (c) for April 4th, 2014.

(Fig. 1). The southern entrance exhibited a higher spatial temperature gradient ($\sim 4.0 \times 10^{-5}$°C m^{-1}) than that observed at the northern entrance ($\sim 1.1 \times 10^{-5}$°C m^{-1}). This finding may appear opposite to what one may expect, since the northern entrance shows a higher influence by the river discharge (*e.g.*, lower temperatures) compared to the southern entrance. However, lower mixing rates, associated with the lower volume transport at the southern entrance compared to that observed at the northern entrance, may provide a plausible explanation for the difference in the temperature gradients. Inside the estuary, a stronger temperature gradient was observed at a latitude near the Coulter "tongue" (29.55°N, Fig. 1). At this latitude, the discharges of the San Jacinto and Trinity Rivers have the largest influence within the estuary. This area is expected to be one with relatively higher concentrations of organisms, due to nutrient transport by the rivers, and organic pollutants originating from the Houston metropolitan area. This was also confirmed by Chlorophyll-*a* satellite images (Zhang et al., 2014).

Surface salinity differences between the entrances and the river mouths during flood (Fig. 5a) and ebb (Fig. 5b) tides had a vertical salinity gradient of $\sim 27 \times 10^{-5}$ and $\sim 21 \times 10^{-5}$, respectively. Lower salinities were found near the Trinity River (14) and higher salinities were observed near the southern entrance of the bay (>26). The higher salinities observed at the southern entrance may be attributed to a combined influence of the open ocean and the larger distance from the San Jacinto and Trinity Rivers compared to that of the northern entrance. Although planktonic organisms can be biologically active at times (for which the present simulations do not account), there are similarities between the diffusion and advection of salt and plankton (Valle-Levinson et al., 2004). In such cases, it may be assumed that plankton will move in and out of the estuary following patterns similar to those of salinity. Thus, it seems reasonable to expect that in the present scenario, plankton will move out and into the estuary at a latitude near Coulter (Fig. 1).

The influence of the rivers, based on salinity values obtained from model simulations, was observed seaward to a distance where the 14 m depth isobath is located or ~10 km offshore (isohaline of ~32). This is also the distance where satellite images show a color gradient (sediment gradient). Thus, based on the hydrographic properties from the simulations, it is suggested that the influence of the rivers may be observed to a distance offshore of ~10 km, commensurate with the 14 m depth isobath. This is also the distance offshore that water-borne matter from the estuary may reach during a tidal cycle under calm (no winds) conditions. The simulated residual surface salinity exhibits a difference of 12 between the entrance and the river mouth (Fig. 5c).

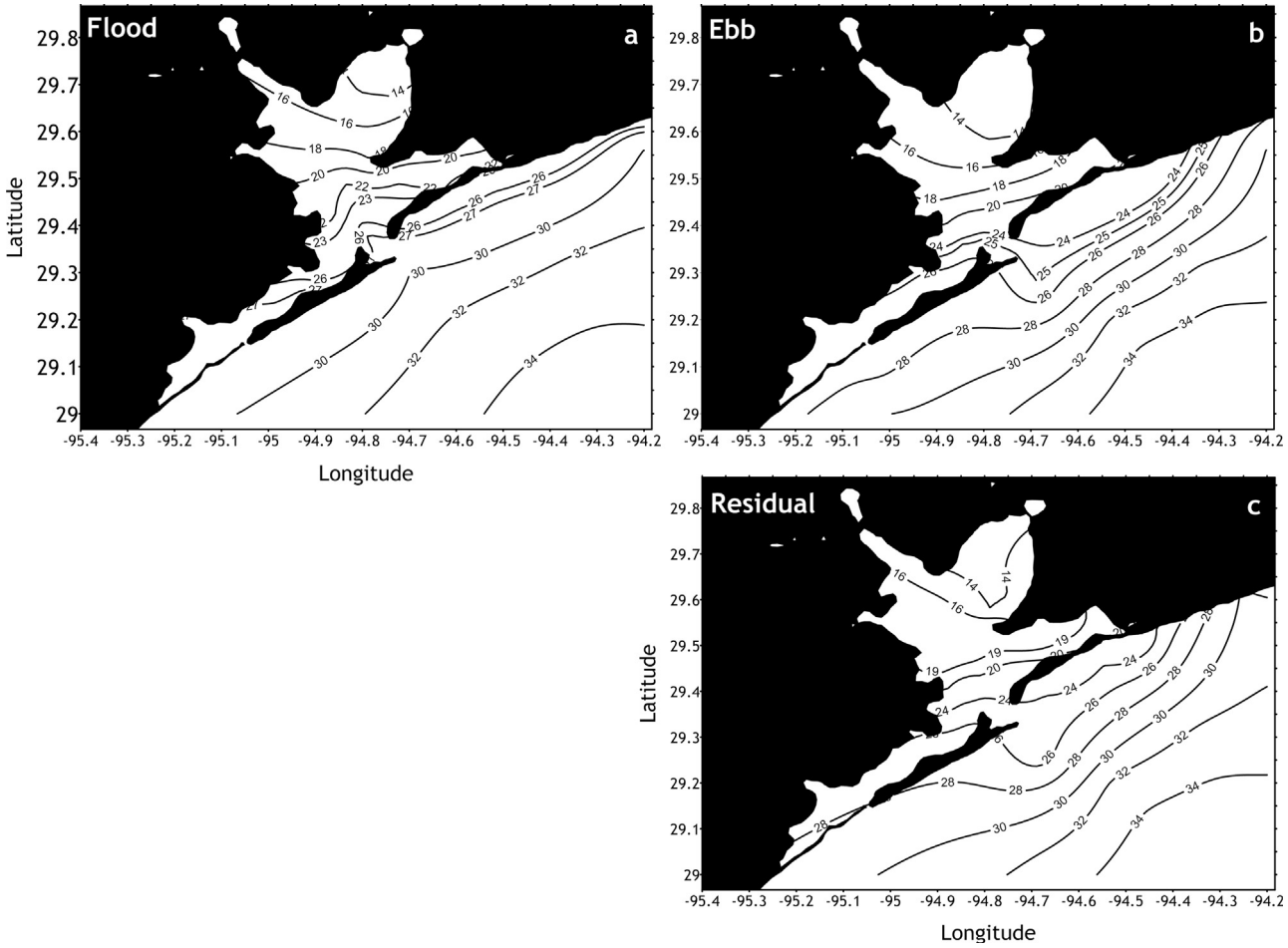

Figure 5 Surface salinity fields (contour lines are at 2 intervals) obtained from model simulations during flood (a), ebb (b) and the residual (c) for April 4th, 2014.

An interesting feature is an increase in salinity from 14 to 16 near Trinity River toward Coulter (a horizontal gradient of 6×10^{-5}). This feature appears to be attributed to a cyclonic gyre and is supported here by the pattern of the residual velocity currents shown in Fig. 6c. High productivity areas have been associated with cyclonic gyres through the pumping of nutrient-rich deep water in coastal areas (Salas Pérez et al., 2012; Salas-de-Leon et al., 2004b; Salas-Monreal et al., 2009). In the case of Galveston Bay, a cyclonic gyre is expected to be highly productive since the current trajectories confine river discharges from the San Jacinto and Trinity Rivers into this area. Such a confluence of currents may also concentrate a variety of water-borne substances and suspended particles, including oil derivatives and pollutants, as is suggested by the satellite images (high dark color or sediments in this area).

During flood tides the gyre appears to be displaced northward toward the Trinity River mouth, while during ebb, it is displaced southward toward the Coulter "tongue" (Fig. 6a, b). In contrast, the San Jacinto River area exhibits a bidirectional flow, with inflow during flood and outflow during ebb. The difference in current fields might be attributed to the shapes of these bays; while the San Jacinto subestuary has an elongated shape, the Trinity subestuary has a circular shape that allows the cyclonic gyre to develop during a tidal cycle. In general, water velocity simulations never reached speeds above 0.7 m s^{-1}. These values are consistent with the flow velocity previously reported by Klinck et al. (2002) and reported by the Gulf of Mexico Foundation (http://www.gulfmex.org/).

The residence time of the estuary, calculated using the velocity simulations, was estimated to be ~18.5 h. Velocities were also used to calculate volume fluxes at the estuary entrances. Most of the water was found to exit the estuary through the northern entrance (55,200 m^3 s^{-1}) while only 18% exits through the southern entrance (12,400 m^3 s^{-1}). However, due to the gyre and the shape of the coastline, it is expected that areas with residence times larger than 18.5 h may exist, such as in the northern part of the bay (Rayson et al., 2015) or at the gyre location. These regions are expected to be locations with high biological productivity and high concentrations of water-borne substances such as pollutants and suspended particles.

The cyclonic gyre is not expected to generate a highly productive area through the commonly observed pumping mechanism of deep nutrient-enriched waters due to the shallowness of the subestuary (~3 m depth; Fig. 1). However, the gyre may introduce nutrients through resuspension of the bottom sediments and/or by concentrating higher nutrient content waters from the rivers into the subestuary. This

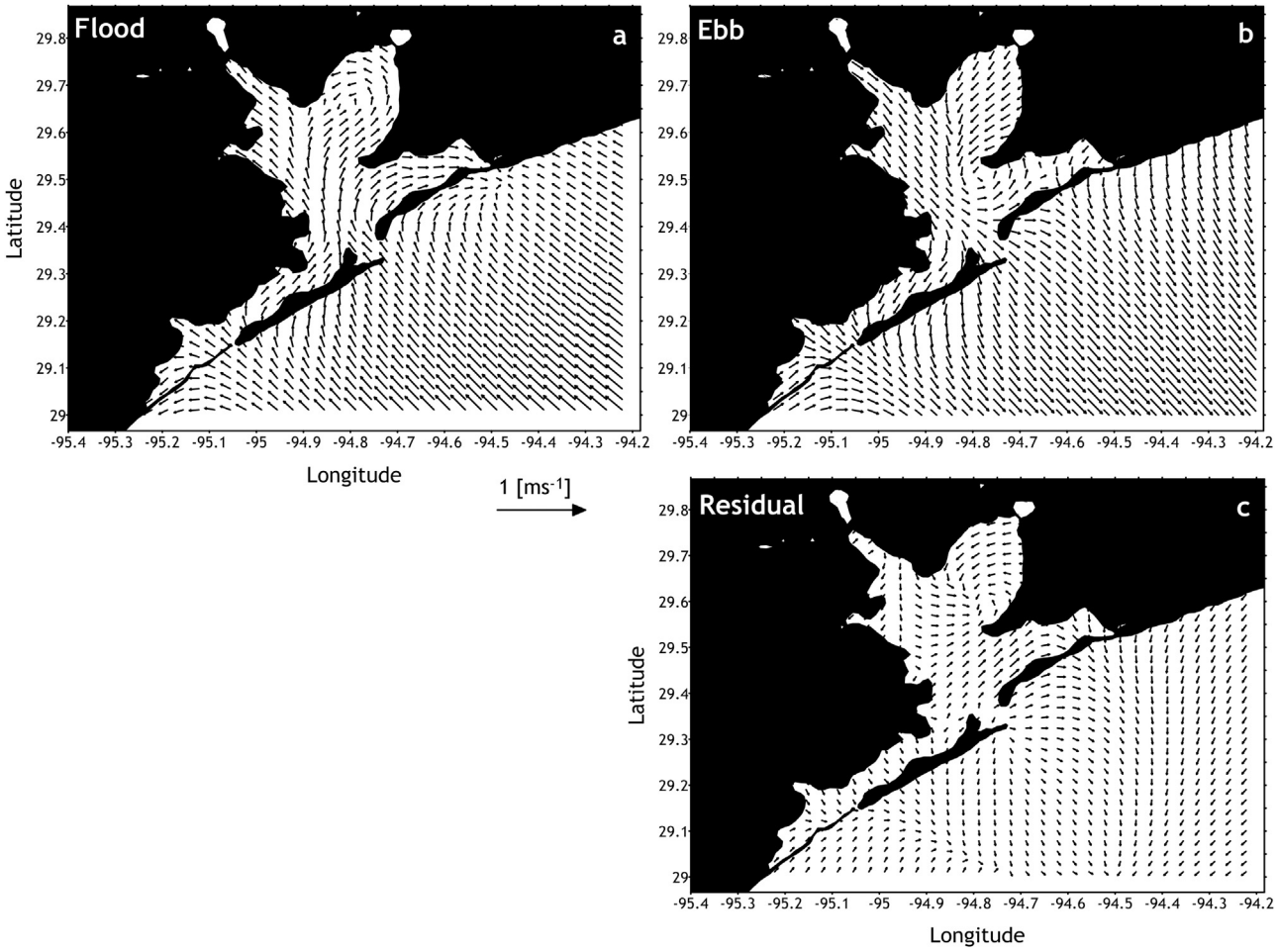

Figure 6 Surface velocity fields (m s^{-1}) obtained from model simulations during flood (a), ebb (b) and the residual (c) for April 4th, 2014.

finding was also suggested by means of satellite images (Zhang et al., 2014).

3.2. Two-layer flow

Even though Galveston Bay is a shallow and relatively flat micro-tidal estuary, the flow at the northern entrance forms a two-layer system (Fig. 7) and is influenced by the Coriolis acceleration, as can be observed from the upward tilt at the northern end of the bottom-layer inflow (Fig. 7c, right side). Bottom friction plays an important role since the core of the inflow (0.5 m s^{-1}) is located at a depth of 6 m, which is about three-quarters of the overall water depth at the estuary northern entrance. The strongest outflows were observed near the surface at the southern end of the northern entrance due to the Coriolis acceleration. The maximum cross-channel flow speed (Fig. 7b) at the northern entrance was ~0.2 m s^{-1}, which is less than 30% of the along-channel flow speed (Fig. 7a; ~0.5 m s^{-1}). When flow scales in an estuary are much larger than the Rossby radius of deformation, the circulation within the estuary can be considered in geostrophic balance. The Rossby radius of deformation (Gill, 1982) for Galveston Bay is $\sim 1.4 \times 10^5$ m, while the estuary scale is $< 1 \times 10^5$ m. Thus, it is expected that friction will play a significant role in the momentum balance. Here, the influence of the Coriolis acceleration term appears to be evident in the two-layer residual flow structure from the upward tilt of the bottom flow at the right side of the channel (~30°N), while the influence of friction is evident from the vertical location of the core of the inflow.

The model does not account directly for zooplankton concentrations since it does not contain an ecosystem model. However, it is commonly noted that in estuaries with irregular bathymetry, planktonic organisms concentrate close to the pycnocline depth (Lennert-Cody and Franks, 1999; Ryan et al., 2005; Shanks, 1983; Zeldis and Jillett, 1982). In this case, a large fraction of organisms will be located at a depth of ~5 m at the entrance of the estuary. Nevertheless, zooplankton has been observed to cross the pycnocline depending on the hour of the day and the state of turbulence levels in the water (Heywood, 1996).

Since the flow exchange through the northern entrance is approximately 4 times that through the southern entrance, it is expected that most of the estuarine-ocean exchange of water-borne constituents will occur through the northern entrance. In addition, since the tides are mainly diurnal (Table 1), it may be expected that organisms (*e.g.*, plankton) will enter and exit the estuary once a day following the diurnal tidal cycle.

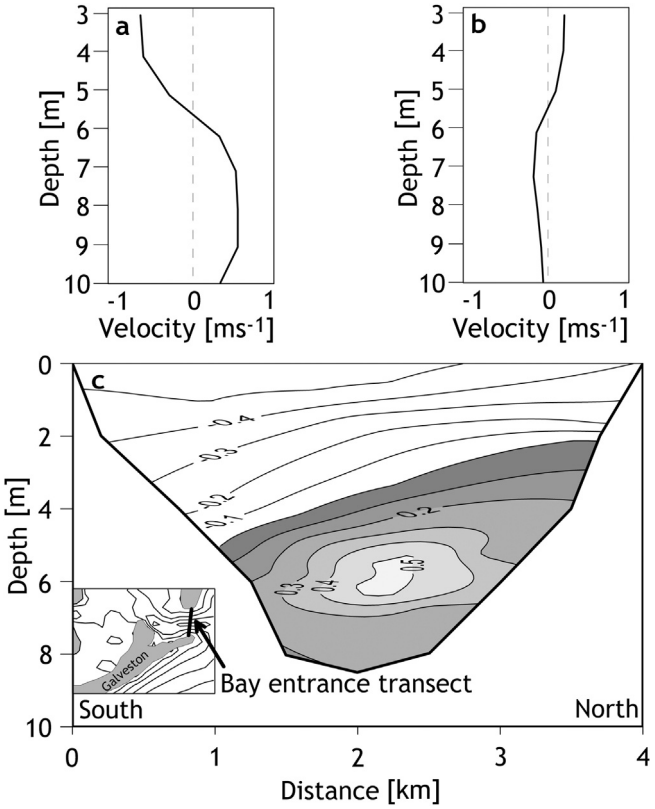

Figure 7 Simulated residual velocities at the northern entrance. (a) Along-channel; (b) cross-channel; (c) along-channel flow through a cross channel transect. Positive values indicate inflow, while negative values indicate outflow, for April 4th, 2014.

During a diurnal tidal cycle, the bulk of oceanic organisms is expected to be concentrated near the northern end of each of the two entrances, while estuarine organisms may concentrate near the southern ends of the entrances due to the Coriolis acceleration. Fig. 8 represents simulations of Lagrangian surface drifters/particles released at the southern part of the model domain (Fig. 8a) and at both estuary entrances (Fig. 8b). The drifters/particles were released at each grid point of the border domain (84 points) and at the bay entrances (8 points); however, due to the number of points, only 10 drifters/particles are shown in Fig. 8a and only 3 drifters/particles are shown in Fig. 8b. Simulations suggest that more than 60% of the drifters/particles released at a distance of up to 30 km from the northern entrance (Fig. 8a) will enter and leave the estuary during a single diurnal tidal cycle. Therefore, even though the river influence was observed to a distance of ∼10 km seaward from the mouth of the estuary, most of the water-borne constituents located at a distance of ∼30 km may be expected to enter and exit the estuary during a diurnal tidal cycle. This is of particular importance to our understanding of the ecosystem of Galveston Bay, since the estuarine-ocean exchange of nutrients, planktonic organisms, and other water-borne biota is likely to follow patterns similar to those of the Lagrangian drifters. Furthermore, Fig. 8b shows that even though the particles released at the northern entrance were very close to each other, they have two different paths, showing that the trajectories are quite sensitive to the initial position of the particles.

3.3. Model simulations under seasonal wind conditions

Since Galveston Bay is a shallow micro-tidal system, winds (surface stress) are expected to play an important role in the local dynamics. To examine this further, four experiments were performed by forcing the model with tides and constant winds of 10 m s^{-1} blowing from four different directions: southeasterly (SE; Fig. 9a), southwesterly (SW; Fig. 9b), northeasterly (NE; Fig. 9c) and northwesterly (NW; Fig. 9c). All the experiments showed differences between one another; however, in all cases, the tidally formed gyre diminished in strength, or even disappeared, under these winds conditions. Under SE and SW wind-stress forcing, the cyclonic gyre (positive vorticity) was observed in the Trinity subestuary (Fig. 9a, b) but diminished in strength with the vorticity reduced by $\sim 1 \times 10^{-4}$ s^{-1}, compared to the vorticity value obtained under no wind conditions ($\sim 3 \times 10^{-4}$ s^{-1}). Due to the wind direction (for both SW and SE), water piled up at the estuary region located between the Coulter "tongue" and the Bolivar Peninsula forming a pressure gradient, $((1/\rho)(\partial P/\partial y))$, larger than 0.9×10^{-5} m s^{-2}, along the subestuary. This is significantly higher than the pressure gradient (0.2×10^{-5} m s^{-2}) observed when the model was forced solely by tides. Under NE and NW wind-stress forcing (Fig. 9c, d), the cyclonic gyre formation was not observed. However, during NW winds, water piled up at the region located between the Coulter "tongue" and the Bolivar

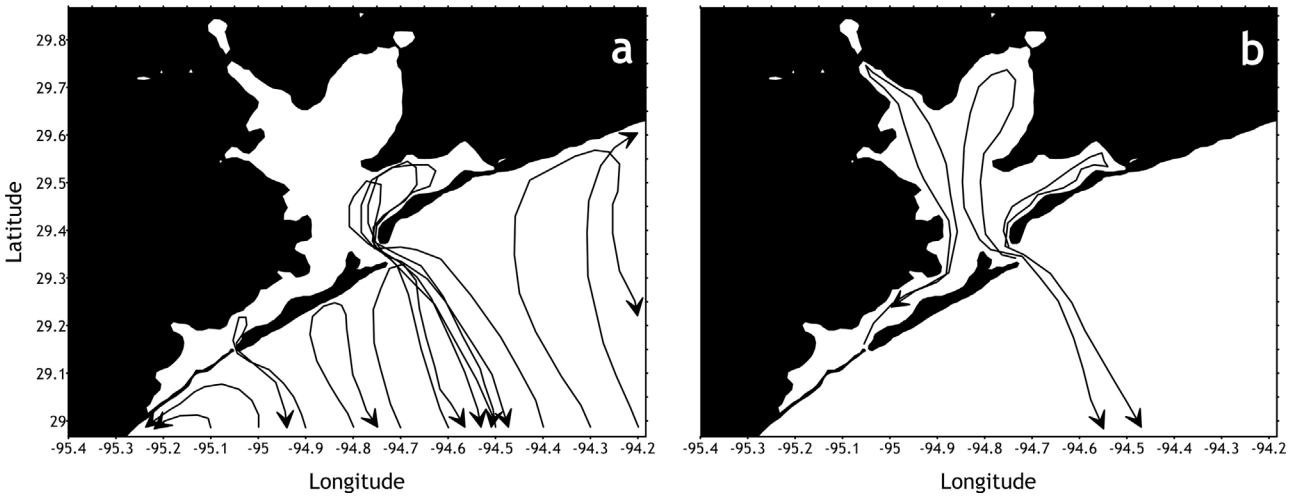

Figure 8 Simulations of Lagrangian surface drifters/particles. (a) Paths of drifters released at intervals of 0.1° longitude, starting at the southern edge of the domain, during one diurnal cycle; (b) three Lagrangian surface drifters/particles followed during one diurnal tidal cycle. Two drifters were released at the northern entrance and one at the southern entrance to the bay. Filled arrow heads represent the location of the drifters at the end of the diurnal tidal cycle for April 4th, 2014.

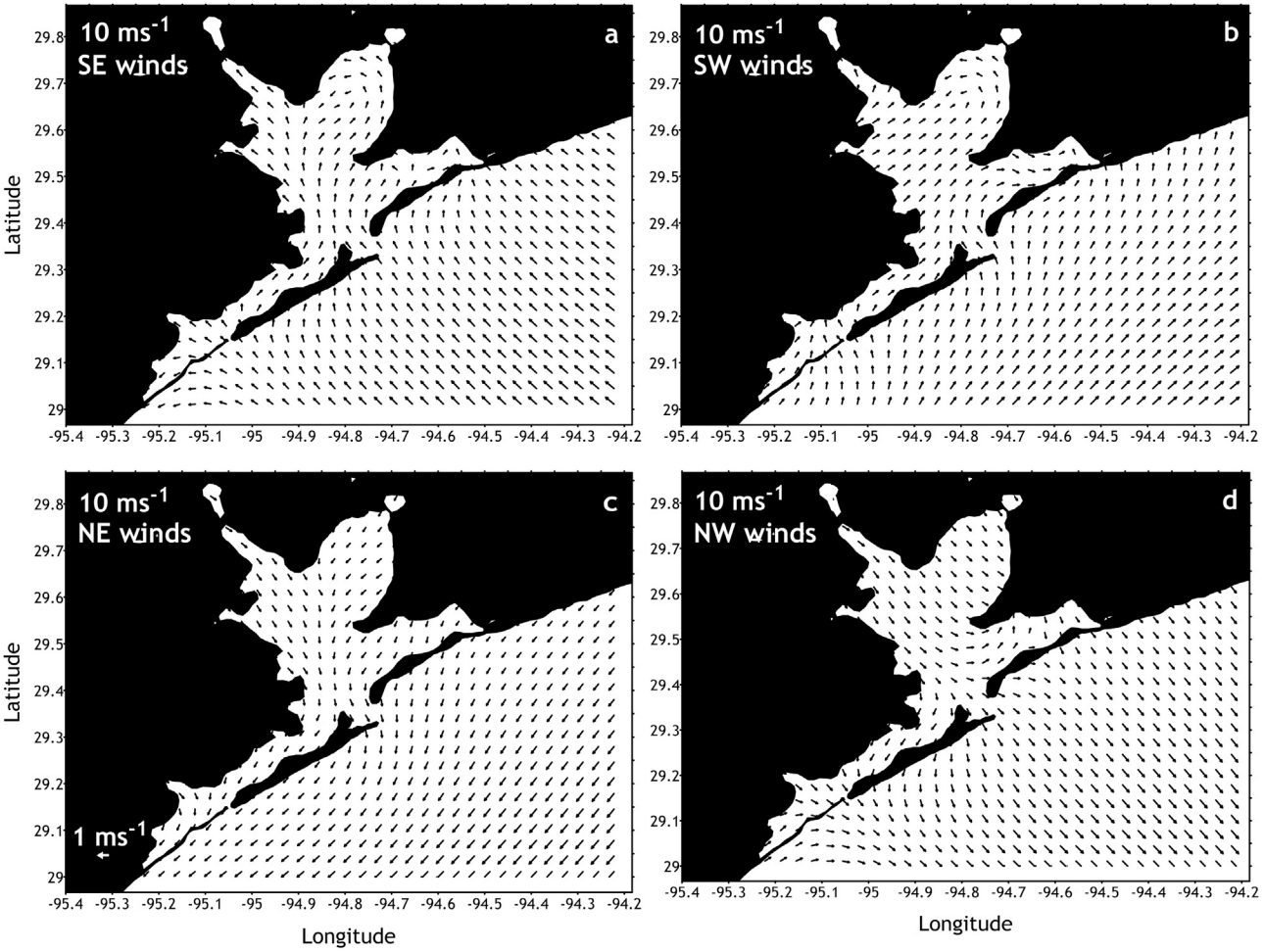

Figure 9 Residual velocity fields (m s^{-1}) obtained from model simulations under sustained southeasterly (a), southwesterly (b), northeasterly (c), and northwesterly (d) wind conditions. Wind speed for all cases was set to 10 m s^{-1}.

Peninsula. This pile-up appears to be associated with the current trajectories advecting water from the San Jacinto River to this region (Fig. 9d). The pressure gradient formed along the estuary was found to be weaker (0.7×10^{-5} m s^{-2}) than that under either SE or SW wind conditions. Under NE wind conditions, the entire estuary could flush, providing a means for water-borne substances, pollutants, and planktonic organisms to exit the estuary through both entrances. The NE winds constituted the only wind forcing conditions allowing the entire bay to flush. Due to the geometry of the San Jacinto subestuary (elongated shape), only NE and NW winds could flush it, while the Trinity subestuary (circular shape) was observed to fully flush only under NE winds. Southeasterly winds, with speeds of ~8 m s^{-1}, are the most common winds in Galveston Bay (Park et al., 2001). Thus, the observed cyclonic gyre is likely to be present most of the time, possibly creating a region with elevated concentrations of suspended particles and planktonic organisms. Under NE and SE wind conditions, the influence of the rivers was observed up to 6 km offshore, while under SW and NW wind conditions, the influence of the rivers was observed up to 12 km; therefore, the SW wind conditions create the farthest influence of the river offshore. Using the National Weather Service data at Galveston, it could be inferred that from October to April, the dominant southerly winds will not allow the entire bay to flush out, while from May to September, the dominant northerly winds may favor flushing of the entire bay.

3.4. Scale analysis

To describe the dynamics at Galveston Bay, a scale analysis of the momentum equation (Eq. (1)) was performed following (Emery and Thomson, 2001).

$$\frac{\partial V}{\partial t} + u\frac{\partial V}{\partial x} + v\frac{\partial V}{\partial y} + W\frac{\partial V}{\partial z} + fu = \frac{1}{\rho}\frac{\partial P}{\partial y} + \frac{\partial}{\partial z}\left(k\frac{\partial V}{\partial z}\right). \quad (1)$$

In Eq. (1), t is time; u, v, and w are velocity components in the x (east), y (north) and z (down) directions, respectively; f is the Coriolis parameter; ρ is seawater density; P is total pressure; and k is the vertical eddy viscosity. Eq. (1) presents the tidal current plus the residual current; therefore, an average process of 25 h was applied to remove the tidal stresses (advection terms of tidal current) in the momentum equation. The magnitude of the terms in the momentum Eq. (1) for the residual flow were computed by vertically and horizontally averaging over the elongated and circular estuary and resulted in the following values: [0.6 + 1.1 + 0.6 + 0.3 + 0.1 = 1.2 + 1.5] $\times 10^{-5}$ m s^{-2} for the elongated estuary and [0.4 + 0.8 + 1.2 + 0.1 + 0.2 = 0.8 + 1.9] $\times 10^{-5}$ m s^{-2} for the circular estuary. Friction along the surface and bottom had a more pronounced effect in shallow waters because friction can affect the entire water column (<3 m on average for Galveston Bay), whereas advection had a larger effect near the river mouths (Fig. 10). Thus, the local dynamics appear to be governed mainly by friction, due to the shallowness of the bay, and advection, due to the river discharges. However, once the wind relaxes, the pressure gradient terms, $\partial P/\partial y$ and $\partial P/\partial x$, become important in the local dynamics due to water piling up in the region between the Coulter "tongue" and the Bolivar Peninsula. Therefore, the dynamics of both subestuaries were the same regardless of the subestuary shape and the distance to the Galveston Bay mouth. Finally, at the northern entrance, Coriolis acceleration appears to play an important role in the local dynamics. As noted above, this can be clearly observed from the intensification and upward tilt of both the inflow and outflow at the northern side of the entrance (Fig. 7c, right side) and as further confirmed by the scale analysis.

4. Conclusions

Model outputs and *in situ* data from Galveston Bay, Texas (USA), a shallow, relatively flat estuary with two subestuaries, one elongated and one roughly circular, were used to elucidate the wind-stress effects on a tidally formed cyclonic gyre in the circular subestuary. Tidal amplitudes were used to calculate the form factor, which suggested that the estuary is a diurnal system with tides that have a phase difference of less than 1 h within the estuary. The simulated hydrographic data (temperature and salinity) showed that the river influence can be observed up to a distance commensurate with the 14 m depth isobath (~10 km offshore) during a diurnal

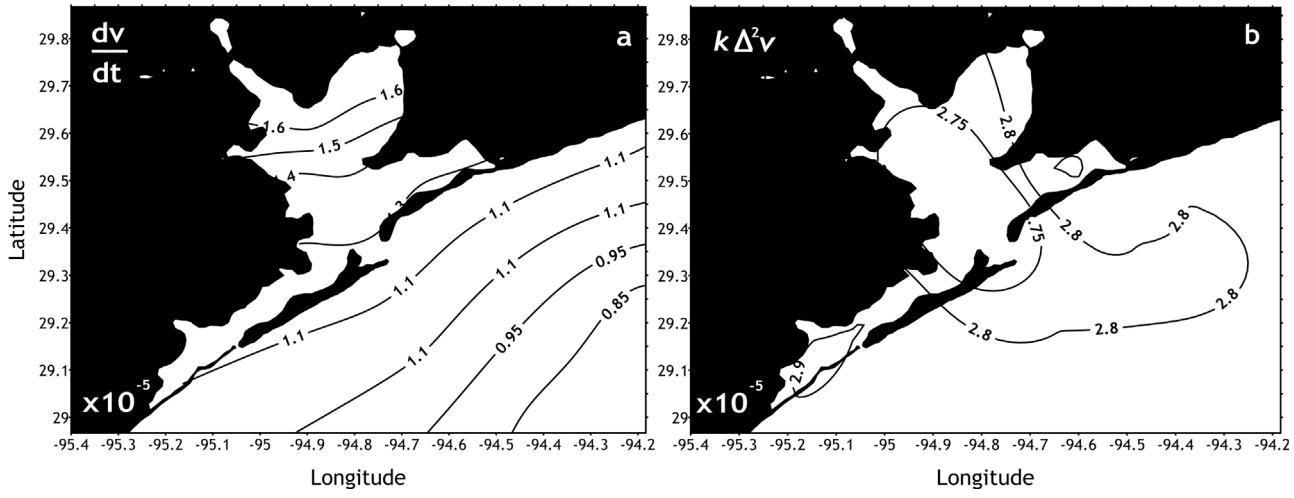

Figure 10 Residual acceleration terms: (a) advection (dv/dt) and (b) friction under southeasterly wind conditions ($k\Delta^2 v$).

tidal cycle and up to 12 km offshore under SW wind conditions. However, the most significant influence of the main rivers (San Jacinto and Trinity) was observed in the region where the two subestuaries meet (at the Coulter Peninsula latitude), which is also the region where the cyclonic gyre was observed.

The tidally formed gyre appeared to be further enhanced through the combined effect of the circular shape of the subestuary and the confluence of the river outflow. The current trajectories of the gyre confine the river discharges from the San Jacinto and Trinity Rivers into this area as well. Thus, it is expected that elevated concentrations of nutrients may be found in this area, resulting in higher productivity rates than elsewhere in the bay, as described in previous studies with chlorophyll-*a* data (Zhang et al., 2014). Adding wind forcing to the simulations showed a general weakening of the gyre when winds were applied from various directions. In particular, the gyre was observed to disappear under northerly wind conditions.

More than 82% of the inflow-outflow transport was observed to occur through the northern entrance of the estuary while less than 18% occurred through the southern entrance. The residence time of the bay, calculated using the water velocity simulations, was found to be less than 18.5 h. However, due to the tidally formed cyclonic gyre and the shape of the coast line, water may reside for a longer period of time in the area influenced by the gyre. Rayson et al. (2015) described the residence time in the upper bay area to be up to 50 days. The estuary was found to flush completely only under the forcing of northeasterly winds, mostly from October to April. These were also the wind conditions under which the gyre was observed to disappear completely.

Based on a scale analysis of the momentum equation, friction (at the surface and the bottom) and advection were found to be the dominant terms in the estuary. However, the pressure gradient and Coriolis acceleration terms were found to be particularly significant near the northern entrance to Galveston Bay.

Acknowledgements

This project was supported by a sabbatical grant from CONACYT number 232872. We also acknowledge the National Oceanic and Atmospheric Administration (NOAA) for data availability.

Appendix A. Supplementary data

Supplementary data associated with this article can be found, in the online version, at doi:10.1016/j.oceano.2017.10.005.

References

Agardy, T., 2000. Effects of fisheries on marine ecosystems: a conservationist's perspective. ICES J. Mar. Sci. 57 (3), 761—765, http://dx.doi.org/10.1006/jmsc.2000.0721.

Aretxabaleta, A.L., McGillicuddy, D.J., Smith, K.W., Lynch, D.R., 2008. Model simulations of the Bay of Fundy Gyre: 1. Climatological results. J. Geophys. Res. Oceans 113 (C10), C10027, http://dx.doi.org/10.1029/2007JC004480.

Avendaño-Alvarez, O., Salas-Monreal, D., Marin-Hernandez, M., Salas-de-Leon, D.A., Monreal-Gomez, M.A., 2017. Annual hydrological variation and hypoxic zone in a tropical coral reef system. Reg. Stud. Mar. Sci. 9, 145—155, http://dx.doi.org/10.1016/j.rsma.2016.12.007.

Becerro, M.A., Bonito, V., Paul, J.V., 2006. Effects of monsoon-driven wave action on coral reefs of Guam and implications for coral recruitment. Coral Reefs 25 (2), 193—199, http://dx.doi.org/10.1007/s00338-005-0080-7.

Chacon-Gomez, I.C., Salas-Monreal, D., Riveron-Enzastiga, M.L., 2013. Current pattern and coral larval dispersion in a tropical coral reef system. Cont. Shelf Res. 68, 23—32, http://dx.doi.org/10.1016/j.csr.2013.08.014.

Chen, S.N., Sanford, L.P., 2009. Lateral circulation driven by boundary mixing and the associated transport of sediments in idealized partially mixed estuaries. Cont. Shelf Res. 29 (1), 101—118, http://dx.doi.org/10.1016/j.csr.2008.01.001.

Cloern, J.E., Alpine, A.E., Cole, B.E., Wong, R.L., Arthur, J.F., Ball, M.D., 1983. River discharge controls phytoplankton dynamics in the northern San Francisco Bay estuary. Estuar. Coast. Shelf Sci. 16 (4), 415—429, http://dx.doi.org/10.1016/0272-7714(83)90103-8.

Dalrymple, R.W., Knight, R., Zaitlin, B.A., Middleton, G.V., 1990. Dynamics and facies model of a macrotidal sand-bar complex, Cobequid Bay—Salmon River Estuary (Bay of Fundy). Sedimentology 37 (4), 577—612, http://dx.doi.org/10.1111/j.1365-3091.1990.tb00624.x.

Dupuis, K.W., Anis, A., 2013. Observations and modeling of wind waves in a Shallow Estuary: Galveston Bay, Texas. J. Waterw. Port C-ASCE 139 (4), 314—325, http://dx.doi.org/10.1061/(ASCE)WW.1943-5460.0000160.

Emery, W.J., Thomson, R.E., 2001. Data Analysis Methods in Physical Oceanography. Elsevier Sci., New York, 638 pp.

Fong, D.A., 1998. Dynamics of freshwater plumes: observations and numerical modeling of the wind-forced response and alongshore freshwater transport. (Ph.d. thesis). Massachusetts Institute of Technology and Woods Hole Oceanographic Institution, http://dx.doi.org/10.1575/1912/4784.

Geyer, W.R., Trowbridge, J.H., Bowen, M.M., 2000. The dynamics of a partially mixed estuary. J. Phys. Oceanogr. 30 (8), 2035—2048, http://dx.doi.org/10.1175/1520-0485(2000)030<2035:TDOAPM>2.0.CO;2.

Gill, A.E., 1982. Atmosphere-Ocean Dynamics. Acad. Press, Orlando, 662 pp.

Goreau, T.J., Hayes, R.L., 1994. Coral bleaching and ocean "hot spots". Ambio 23, 176—180.

Haidvogel, D.B., Arango, H.G., Hedstrom, K., Beckmann, A., Malanotte-Rizzoli, P., Shchepetkin, A.F., 2000. Model evaluation experiments in the North Atlantic Basin: simulations in nonlinear terrain-following coordinates. Dyn. Atmos. Oceans 32 (3—4), 239—281, http://dx.doi.org/10.1016/S0377-0265(00)00049-X.

Heywood, K.J., 1996. Diel vertical migration of zooplankton in the Northeast Atlantic. J. Plankton Res. 18 (2), 163—184, http://dx.doi.org/10.1093/plankt/18.2.163.

Holliday, D.V., Pieper, R.E., 1980. Volume scattering strengths and zooplankton distributions at acoustic frequencies between 0.5 and 3 MHz. J. Acoust. Soc. Am. 67 (1), 135—146, http://dx.doi.org/10.1121/1.384472.

Houston Chronicle, April 6, 2014. Oil spills in Galveston Bay a routine occurrence, http://www.houstonchronicle.com/news/science-environment/article/Oil-spills-in-Galveston-Bay-a-routine-occurrence-5381283.php.

Klinck, J.M., Hofmann, E.E., Powell, E.N., Dekshenieks, M.M., 2002. Impact of channelization on oyster production: a hydrodynamic-oyster population model for Galveston Bay, Texas. Environ. Model. Assess. 7 (4), 273—289.

Lennert-Cody, C.E., Franks, P.J., 1999. Plankton patchiness in high-frequency internal waves. Mar. Ecol.-Prog. Ser. 186, 59—66.

Lynch, D.R., Justin, T.C.I.P., Naimie, C.E., Werner, F.E., 1995. Convergence studies of tidally-rectified circulation on Georges bank. In: Lynch, D.R., Davies, A.M. (Eds.), Quantitative Skill Assessment for Coastal Ocean Models. AGU, 153—174.

Marchesiello, P., McWilliams, J.C., Shchepetkin, A., 2001. Open boundary conditions for long-term integration of regional oceanic models. Ocean Model. 3, 1—20, http://dx.doi.org/10.1016/S1463-5003(00)00013-5.

O'Donnell, H.W., 2005. Investigation of flood induced pipeline failures on lower San Jacinto River. In: Pipelines 2005. Optimizing Pipeline Design, Operations, and Maintenance in Today's Economy. 451—463, http://dx.doi.org/10.1061/40800(180)35.

Officer, C.B., 1981. Physical dynamics of estuarine suspended sediments. Mar. Geol. 40 (1—2), 1—14, http://dx.doi.org/10.1016/0025-3227(81)90039-6.

Park, J.S., Wade, T.L., Sweet, S., 2001. Atmospheric distribution of polycyclic aromatic hydrocarbons and deposition to Galveston Bay, Texas, USA. Atmos. Environ. 35 (19), 3241—3249, http://dx.doi.org/10.1016/S1352-2310(01)00080-2.

Rayson, M.D., Gross, E.S., Fringer, O.B., 2015. Modeling the tidal and sub-tidal hydrodynamics in a shallow, micro-tidal estuary. Ocean Model. 89, 29—44, http://dx.doi.org/10.1016/j.ocemod.2015.02.002.

Rego, J., Li, C., 2010. Storm surge propagation in Galveston Bay during Hurricane Ike. J. Mar. Syst. 82 (4), 265—279, http://dx.doi.org/10.1016/j.jmarsys.2010.06.001.

Robertson, R., 2006. Modeling internal tides over Fieberling Guyot: resolution, parameterization, performance. Ocean Dyn. 56 (5—6), 430—444.

Ryan, J.P., Chavez, F.P., Bellingham, J.G., 2005. Physical—biological coupling in Monterey Bay, California: topographic influences on phytoplankton ecology. Mar. Ecol.-Prog. Ser. 287, 23—32.

Salas Pérez, J.J., Salas-Monreal, D., Monreal-Gómez, M.A., Riveron-Enzastiga, M.L., Llasat, C., 2012. Seasonal absolute acoustic intensity, atmospheric forcing and currents in a tropical coral reef system. Estuar. Coast. Shelf Sci. 100, 102—112, http://dx.doi.org/10.1016/j.ecss.2012.01.002.

Salas-de-Leon, D.A., Diaz-Flores, M.A., Monreal-Gómez, M.A., 2004a. Circulation and vorticity in the Southern Gulf of Mexico. In: Schroeder, W. (Ed.), Hans Ertel Memorial Book, German Commission of History of Geophysics and Cosmical Physics. p. 229.

Salas-de-Leon, D.A., Monreal-Gomez, M.A., Signoret, M., Aldeco, J., 2004b. Anticyclonic-cyclonic eddies and their impact on near-surface chlorophyll stocks and oxygen supersaturation over the Campeche Canyon, Gulf of Mexico. J. Geophys. Res. Oceans 109, C05012, http://dx.doi.org/10.1029/2002JC001614.

Salas-de-León, D.A., Monreal-Gómez, M.A., Díaz-Flores, M.A., Salas-Monreal, D., Velasco-Mendoza, H., Riverón-Enzástiga, M.L., Ortiz-Zamora, G., 2008. Role of near-bottom currents in the distribution of sediments within the Southern Bay of Campeche, Gulf of México. J. Coastal Res. 24 (6), 1487—1494, http://dx.doi.org/10.2112/07-0857.1.

Salas-Monreal, D., Valle-Levinson, A., 2009. Continuously stratified flow dynamics over a hollow. J. Geophys. Res. Oceans 114 (C3), http://dx.doi.org/10.1029/2007JC004648.

Salas-Monreal, D., Salas-de-León, D.A., Monreal-Gómez, M.A., Riverón-Enzástiga, M.L., 2009. Current rectification in a tropical coral reef system. Coral Reefs 28 (4), 871—879, http://dx.doi.org/10.1007/s00338-009-0521-9.

Salas-Monreal, D., Salas-de-Leon, D.A., Monreal-Gomez, M.A., Riveron-Enzastiga, M.L., Mojica-Ramirez, E., 2012. Hydraulic jump in the Gulf of California. Open J. Mar. Sci. 2, 141—149, http://dx.doi.org/10.4236/ojms.2012.24017.

Scully, M.E., Geyer, W.R., Lerczak, J.A., 2009. The influence of lateral advection on the residual estuarine circulation: a numerical modeling study of the Hudson River estuary. J. Phys. Oceanogr. 39 (1), 107—124, http://dx.doi.org/10.1175/2008JPO3952.1.

Shanks, A.L., 1983. Surface slicks associated with tidally forced internal waves may transport pelagic larvae of benthic invertebrates and fishes shoreward. Mar. Ecol. Prog. Ser. 13 (2), 311—315.

Spiteri, C., Slomp, C.P., Tuncay, K., Meile, C., 2008. Modeling biogeochemical processes in subterranean estuaries: effect of flow dynamics and redox conditions on submarine groundwater discharge of nutrients. Water Resour. Res. 44 (2), W02430, http://dx.doi.org/10.1029/2007WR006071.

Storlazzi, C.D., Mc Manus, M.A., Logan, J.B., Mc Laughlin, B.E., 2006. Cross-shore velocity shear, eddies and heterogeneity in water column properties over fringing coral reefs: West Maui, Hawaii. Cont. Shelf Res. 26 (3), 401—421, http://dx.doi.org/10.1016/j.csr.2005.12.006.

Sutherland, D.A., MacCready, P., Banas, N.S., Smedstad, L.F., 2011. A model study of the Salish Sea Estuarine circulation. J. Phys. Oceanogr. 41 (6), 1125—1143, http://dx.doi.org/10.1175/2011JPO4540.1.

Valle-Levinson, A., Trasvina-Castro, A., Gutierrez-de-Velasco, G., Gonzalez-Armas, R., 2004. Diurnal vertical motions over a seamount of the southern Gulf of California. J. Mar. Syst. 50, 61—77.

Wang, J., Mysak, L.A., Ingram, R.G., 1994. A three-dimensional numerical simulation of Hudson Bay summer ocean circulation: topographic gyres, separations, and coastal jets. J. Phys. Oceanogr. 24 (12), 2496—2514, http://dx.doi.org/10.1175/1520-0485(1994)024<2496:ATDNSO>2.0.CO;2.

Wilkinson, C., Souter, D. (Eds.), 2008. Status of Caribbean Coral Reefs After Bleaching and Hurricanes in 2005. Global Coral Reef Monitoring Network, and Reef and Rainforest Research Centre, Townsville. 148 pp.

Xinyu, G., Valle-Levinson, A., 2007. Tidal effects on estuarine circulation and outflow plume in the Chesapeake Bay. Cont. Shelf Res. 27 (1), 20—42, http://dx.doi.org/10.1016/j.csr.2006.08.009.

Zeldis, J.R., Jillett, J.B., 1982. Aggregation of pelagic *Munida gregaria* (Fabricius) (Decapoda, Anomura) by coastal fronts and internal waves. J. Plankton Res. 4 (4), 839—857, http://dx.doi.org/10.1093/plankt/4.4.839.

Zhang, S., Zheng, G., Gao, H., Roelke, D., 2014. Satellite remote sensing of chlorophyll-*a* concentrations in the Galveston Bay, Texas. In: AGU Fall Meeting Abstracts 1. p. 232.

Oceanologia (2018) 60, vii—viii

Available online at www.sciencedirect.com

ScienceDirect

journal homepage: www.journals.elsevier.com/oceanologia/

CORRIGENDUM

Corrigendum to "Aerosol physical properties in Spitsbergen's fjords: Hornsund and Kongsfjorden during AREX campaigns in 2014 and 2015" [Oceanologia 59 (2017) 460—472]

Piotr Markuszewski [a,b,*], Anna Rozwadowska [a], Małgorzata Cisek [a], Przemysław Makuch [a], Tomasz Petelski [a]

[a] *Institute of Oceanology, Polish Academy of Sciences, Sopot, Poland*
[b] *Centre for Polar Studies National Leading Research Centre, Sosnowiec, Poland*

The publisher regrets that the following mistakes appeared in this paper:

1. In the caption of Fig. 1 descriptions of subregions "1" and "3" have been inverted. Fig. 1 with the correct caption is printed below.
2. In Eq. (5) on page 464, "$\lambda\lambda_0$" was mistakenly replaced with "*e*". Moreover, the words "of the scattering coefficient spectrum" and "resolution" were unnecessarily added to the sentence containing Eq. (5).

   The correct sentence including Eq. (5) is reproduced below:

   In the paper, aerosol scattering properties are characterized by scattering coefficient at light wavelength of 550 nm, b, and Ångström exponent, AE, representing the slope of the scattering coefficient spectrum, $b(\lambda)$, in a log—log scale:

$$b(\lambda) = b(\lambda_0)\left(\frac{\lambda}{\lambda_0}\right)^{-AE} \quad (5)$$

   where λ_0 is a selected wavelength, usually $\lambda_0 = 1$ μm.
3. Several errors occurred in the second paragraph of Section 4.2, on page 466:

   on line 7 of this paragraph read "mean particle diameter was higher in 2015 (its value" instead of "medium particle diameter was higher than in 2015 (where values",

DOI of original article: https://doi.org/10.1016/j.oceano.2017.03.012.
* Corresponding author at: Institute of Oceanology, Polish Academy of Sciences, Powstańców Warszawy 55, 81-712 Sopot, Poland. Tel.: +48 58 7311901; fax: +48 58 551 21 30.
E-mail address: pmarkusz@iopan.da.pl (P. Markuszewski).

https://doi.org/10.1016/j.oceano.2017.11.004

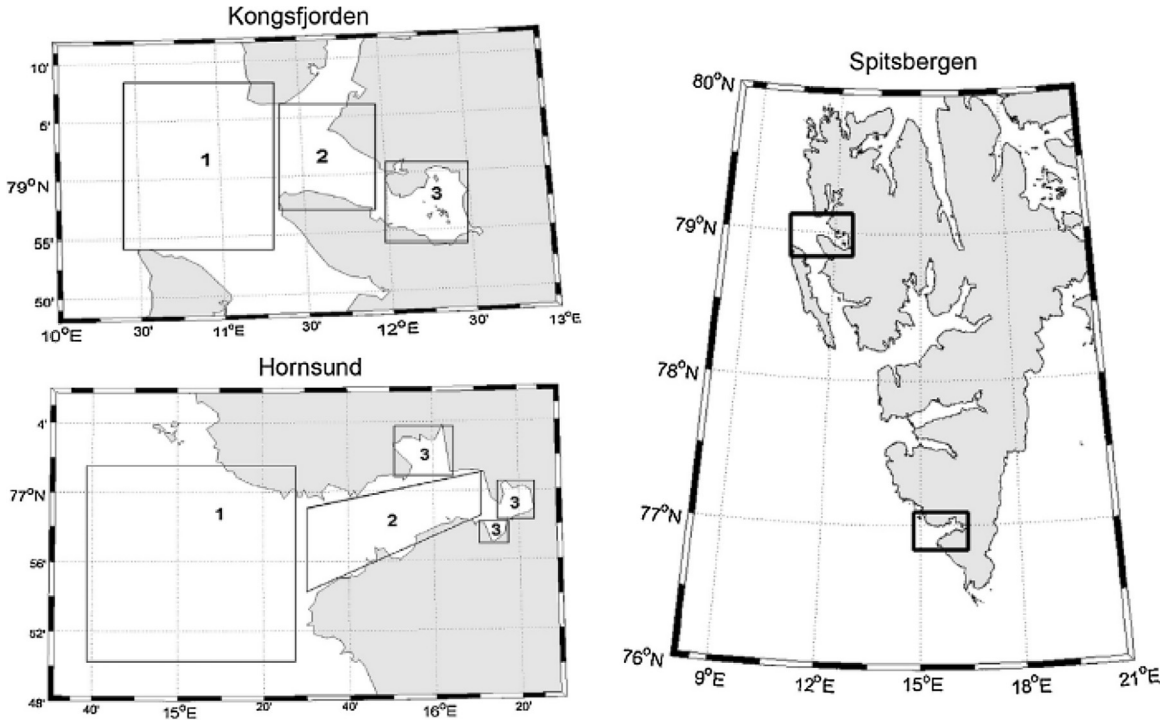

Figure 1 Location of Hornsund and Kongsfjorden and fjords' subregions where the measurements were performed during the AREX campaigns in 2014 and 2015. Numbers represent the fjord subregions: 1 — fjord mouth and the sea outside the fjord, 2 — central part, 3 — innermost part of the fjord.

on line 10 of this paragraph read “dominated in 2015” instead of “dominated in 2014”,

on lines 14 and 15 of this paragraph read “were larger than in Hornsund by less than 0.4 μm” instead of “were larger by approximately 0.7 μm”.

4. On page 470, on lines 17 and 18 (the last sentence of the first paragraph) the words “east” and “west” have been inverted. The correct text is given below:

“i.e. from west (subsection 1, leftmost point) to east (subsection 3, rightmost point)”

The publisher would like to apologize for any inconvenience caused.